

HYDRODYNAMICS OF SINGLE- AND TWO-PHASE FLOW
IN INCLINED ROD ARRAYS

by

DEREK BRAM EBELING-KONING

B.S. Rensselaer Polytechnic Institute
(1977)

S.M. Massachusetts Institute of Technology
(1979)

Submitted to the Department of
Nuclear Engineering
in Partial Fulfillment of the
Requirements for the Degree of

DOCTOR OF PHILOSOPHY

at the

• MASSACHUSETTS INSTITUTE OF TECHNOLOGY

February 1984

Signature of the Author

Derek Bram Ebeling-Koning

Department of Nuclear Engineering

September 16, 1983

Certified by

Neil E. Todreas

Professor Neil E. Todreas

Thesis Supervisor

Accepted by

A. F. Henry

Allen F. Henry

Chairman, Departmental
Graduate Committee

MASSACHUSETTS INSTITUTE
OF TECHNOLOGY

APR 09 1984

LIBRARIES

ARCHIVES

HYDRODYNAMICS OF SINGLE- AND
TWO-PHASE FLOW IN INCLINED ROD ARRAYS

by

Derek Bram Ebeling-Koning

Submitted to the Department of Nuclear Engineering
on September 16, 1983, in partial fulfillment of the
requirements of the Degree of Doctor of Philosophy
in Nuclear Engineering.

ABSTRACT

Required inputs for thermal-hydraulic codes are constitutive relations for fluid-solid flow resistance, in single-phase flow, and interfacial momentum exchange (relative phase motion), in two-phase flow.

An inclined rod array air-water experiment was constructed to study the hydrodynamics of multidimensional porous medium flow in rod arrays. Velocities, pressures, and bubble distributions were measured in square rod arrays of $P/d = 1.5$, at 0, 30, 45, and 90 degree inclinations to the vertical flow direction.

Constitutive models for single-phase flow resistance are reviewed, new comprehensive models developed, and an assessment with previously published and new data made. The principle of superimposing one-dimensional correlations proves successful for turbulent single-phase inclined flow.

For bubbly two-phase incline flow a new flow separation phenomena was observed and modeled. Bubbles of diameters significantly smaller than the rod diameter travel along the rod axis, while larger diameter bubbles move through the rod array gaps. The outcome is a flow separation not predictable with current interfacial momentum exchange models. A two-region liquid velocity model is developed to explain the experimentally observed phenomena. Fundamental data for bubbles rising in rod arrays were also taken.

Thesis Supervisor: Neil E. Todreas
Title: Professor of Nuclear Engineering

Thesis Reader: Peter Griffith
Title: Professor of Mechanical Engineering

To my Family: Mom, Dad, Bob, Tasha, Gwen,
Trebor, Blanche, and Hap.

ACKNOWLEDGEMENTS

First of all, I would like to give my sincere thanks to my supervisor Professor Neil E. Todreas for his guidance, suggestions, endless concern, and demand for quality, while still giving me creative freedom. Thanks are also extended to my reader, Professor Peter Griffith, for helping to keep this ambitious task in perspective and sharing his wealth of insight.

Thanks are due to Dr. Richard T. Lahey, Jr., Dr. Lothar Wolf, Prof. John E. Meyer, Mr. Yves Coëffé, and Prof. Warren M. Rohsenow for their expert advise and comments.

The experimental portion of this research could not have been accomplished without the help of: Joseph (Tiny) A. Caloggero and Frederick R. Johnson for their continuous assistance and advise; to Hugo R. (Bob) Barra, Aubrey R. Rigby, Peter B. Roemer, and Maureen R. Hayes; and to Yehia Khalil for designing the test loop. Also thanks to Ernesto Faillace, Victor Iannello, Chi-Ming (George) Or, and William Ijams for their assistance in data collection.

To my dearest friends, I give my wholehearted thanks for sharing the peaks and pulling me out of the valleys:

Walter H. Strohmayer,

Linda P. Nelson,

Thomas J. Downar,

Paul D. Symolon,

Richard P. Burke,

- Steven P. MacCabe, and
- Joseph A. Sefcik.

For the hours of discussions, consultations, and criticism, thanks to my colleagues and office mates: Shih-Ping K., Tolis E., Steven A., Tsing-Tung H., Shih-Kuei C., Hugo D., Marty V., Bahman A., and Roy K.

Very special thanks to James T. Robinson for his fresh interest in this research and countless suggestions at the most crucial end.

To Clare Egan, Sofia Caloggero, and Elenore Kehoe, thanks for making the Nuclear Engineering Department an enjoyable working environment.

I am indebted to Duk-Haeng (David) R. Rhee for typing this manuscript in the wee hours. Also thanks to Gregory K. Branan and Dr. Andrei L. Schor for proofing parts of this manuscript.

This research was partially supported by Northeast Utilities through the Sherman R. Knapp Fellowship, U.S. Department of Energy Basic Energy Science Contract No. DE-AC02-82ER12075, and under appointment to the Nuclear Science and Engineering and Health Physics Fellowship program administered by Oak Ridge Associated Universities for the U.S. Department of Energy.

TABLE OF CONTENTS

	<u>Page</u>
ABSTRACT	2
ACKNOWLEDGEMENTS	4
LIST OF FIGURES.	13
LIST OF TABLES	19
LIST OF PLATES	21
NOMENCLATURE	22
CHAPTER 1: INTRODUCTION	28
1.1 Objective and Scope.	30
1.2 Motivation	31
1.3 Contribution	32
1.4 Outline.	33
CHAPTER 2: THERMAL-HYDRAULIC MODEL METHODOLOGY.	34
2.1 General Model Development.	34
2.2 General Hydrodynamic Conservation Equations.	36
2.3 Constitutive Relations	38
2.4 Practical Conservation Model	39
CHAPTER 3: HYDRODYNAMIC MODEL	40
3.1 Single-Phase Hydrodynamic Model.	40
3.2 Two-Phase Hydrodynamic Model	42
CHAPTER 4: EXPERIMENT	46
4.1 Design Base.	46
4.2 Test Sections.	46
4.3 Test Duct.	48

	<u>Page</u>
4.4	Flow Loop. 56
4.5	Instrumentation. 59
4.5.1	Turbine Meter 59
4.5.2	Orifice Meter 61
4.5.3	Rotameter 61
4.5.4	Loop Pressure and Temperature 63
4.5.5	Pitot-Static Tube 63
4.5.6	Photography 67
4.5.7	Single Bubble Measurements. 69
CHAPTER 5:	SINGLE-PHASE FLOW MODELING 73
5.1	Flow Field Description 73
5.2	Multidimensional Flow Resistance Formulation 79
5.2.1	General Formulation 79
5.2.2	Model Constraints 83
5.2.3	Secondary Variables 84
5.2.4	Modeling Formulation. 90
5.3	Parallel Flow Resistance 91
5.4	Crossflow Resistance 94
5.5	Inclined Flow Resistance 105
5.5.1	Single Cylinder Superposition Model 105
5.5.2	Rod Array Superposition Models. 107
5.5.2.1	Parallel Flow Component. 107
5.5.2.2	Crossflow Component. 112
5.5.2.3	Summary. 114
5.6	Lift/Drag Flow Resistance Components 118

	<u>Page</u>
5.6.1	Coordinate System 118
5.6.2	Composite Superposition Models 119
5.7	Published Data Base 122
5.7.1	Kazakevich 122
5.7.2	Groehn 125
5.7.3	Möller 125
5.7.4	Böttgenbach. 127
5.7.5	Data Summary 127
5.7.6	Drag Component Correlations. 127
5.8	Experimental Data 134
5.8.1	Flow Fields. 134
5.8.2	Flow Resistance. 138
5.9	Model, Correlation, and Data Comparison 152
5.9.1	Correlation and Composite Superposition Model Evaluation 152
5.9.2	Recommendations. 158
5.10	Individual Superposition Factor Evaluation. 162
5.11	Summary 167
CHAPTER 6:	TWO-PHASE FLOW MODELING 169
6.1	Model Formulation 170
6.1.1	General Formulation. 170
6.1.2	Drag Force Formulation 172
6.2	Flow Environments 174
6.3	One-Dimensional Drag Coefficient Models 176
6.3.1	Single Bubble in Infinite Medium 176
6.3.2	Multiple Bubbles in Infinite Medium. 184

	<u>Page</u>
6.3.3 Single bubble in Finite Geometry	187
6.3.3.1 Round Tubes	190
6.3.3.2 Parallel Array.	194
6.3.3.3 Crossflow Array	200
6.3.4 Multiple Bubbles in Finite Geometry.	203
6.3.5 Liquid Flow.	203
6.4 Inclined Array Flow Observations.	204
6.4.1 Single Bubble in Inclined Array.	204
6.4.1.1 Zero Liquid Flow.	204
6.4.1.2 Liquid Flow	208
6.4.2 Stream of Bubbles in Inclined Array.	208
6.4.3 Two-Phase Flow in Inclined Array	213
6.4.3.1 Previous Work	213
6.4.3.2 Bubbly Flow Observations in Inclined Array	216
6.5 Multidimensional Drag Coefficient	224
6.5.1 Current Code Models.	224
6.5.2 Isotropic Model.	228
6.5.3 Superposition Model.	228
6.5.4 Two-Region Model	233
6.5.4.1 Liquid Velocity Model	233
6.5.4.2 Drag Force Formulation.	236
6.5.4.3 Mainstream Drag Coefficient	236
6.5.4.4 Recirculating Region Drag Coefficient.	239
6.5.4.5 Weighting Function λ	240
6.5.4.6 Model Validation.	242

	<u>Page</u>
6.5.5 Summary	246
6.6 Summary and Conclusion	248
CHAPTER 7: SUMMARY, CONCLUSIONS, AND FUTURE WORK	251
APPENDIX A: DERIVATION OF THE TIME/VOLUME-AVERAGED MASS AND MOMENTUM CONSERVATION EQUATIONS	254
A.1 Mathematical Theorems	254
A.1.1 Leibnitz's Rule	254
A.1.2 Gauss' Theorem	254
A.2 Local Instantaneous Conservation Equations	256
A.2.1 Local Instantaneous Mass Equation	256
A.2.2 Mass Jump Condition	257
A.2.3 Local Instantaneous Momentum Equation	258
A.2.4 Momentum Jump Condition	259
A.2.5 Summary	260
A.3 Local Time-Averaged Conservation Equation Equations	260
A.3.1 Time-Averaging Definitions and Theorems	260
A.3.2 Time-Averaged Mass Equation	261
A.3.3 Time-Averaged Mass Jump Condition	263
A.3.4 Time-Averaged Momentum Equation	264
A.3.5 Time-Averaged Momentum Jump Condition	265
A.3.6 Summary	266
A.4 Time/Volume-Averaged Conservation Equations	266
A.4.1 Volume-Averaging Definitions and Theorems	268
A.4.2 Time/Volume-Averaged Mass Equation	269
A.4.3 Time/Volume-Averaged Mass Jump Condition	270
A.4.4 Time/Volume-Averaged Momentum Equation	270

	<u>Page</u>
A.4.5	Time/Volume-Averaged Momentum Jump Equation. . . 272
A.4.6	Summary. 272
A.5	Time/Surface-Area-Averaged Conservation Equations . . . 273
A.5.1	Conversion of Volume to Surface-Averaged Equations 273
A.5.2	Comments on Surface-Averaged Equations 273
A.6	Partitioning of Constitutive Variables in the Time/Volume-Averaged Momentum Equation. 275
A.6.1	Total Stress Tensor. 275
A.6.2	Volumetric Flow Resistance 275
A.6.3	Interfacial Momentum Exchange. 275
A.6.4	Summary. 277
APPENDIX B:	TEST ASSEMBLY BLUEPRINTS. 278
APPENDIX C:	INSTRUMENT CALIBRATION. 291
C.1	Turbine Meter Calibration 291
C.2	Orifice Meter Calibration 292
C.3	Rotameter Calibration 295
C.4	Pitot-Static Tube Calibration 301
APPENDIX D:	MODELS FOR CROSSFLOW MAINSTREAM VELOCITY. 304
APPENDIX E:	SINGLE-PHASE RESISTANCE DATA. 316
APPENDIX F:	SINGLE BUBBLE VELOCITY AND TRAJECTORY DATA. 325
APPENDIX G:	DERIVATION OF MULTIPLE BUBBLE DRAG MODEL. 335
G.1	Single Bubble Model 335
G.2	Multiple Bubble Model 337
G.2.1	Viscous Regime 337
G.2.2	Distorted Regime 338
G.2.3	Churn-Turbulent Regime 341

	<u>Page</u>
G.3 Summary	342
APPENDIX H: THERMIT-2 MODIFICATIONS	344
APPENDIX I: BUBBLE VELOCITY AND TRAJECTORY CALCULATIONS	345
I.1 Isotropic Model	345
I.2 Two-Region Model.	348
REFERENCES.	355
BIOGRAPHICAL NOTE	361

LIST OF FIGURES

		<u>Page</u>
1.1	Cross sections of heat transfer components.	29
2.1	Thermal-hydraulic model development	35
4.1	Parallel test section cross section	49
4.2	Test duct cross section	54
4.3	Cross-sectional view of test section/test duct/diffuser assembly.	55
4.4	Air-water test loop	58
4.5	Air orifice calibration curves.	62
4.6	Velocity and differential pressure measurement system	65
4.7	Photographic lighting arrangements (a) back reflecting, (b) front reflecting, (c) back shadow	68
4.8	Collimated perpendicular lighting arrangement	70
5.1	Observed rod array streamlines.	76
5.2	Postulated rod array streamlines.	78
5.3	Regular rod array geometry and coordinate definitions	80
5.4	Coordinate system transformation.	82
5.5	Two-dimensional flow coordinate definitions--(a) crossflow independent resistance, (b) symmetric crossflow direction	85
5.6	Crossflow mainstream porosity models.	87
5.7	Velocity vector definitions	89
5.8	Parallel flow resistance for round tube and square array of $P/d = 1.5$	93
5.9	Crossflow correlations for square array of $P/d = 1.5$	98
5.10	Circumferential variation in crossflow resistance	99
5.11	Geometry and Reynolds dependence of Gunter-Shaw [G.2] and Jakob [J.1] crossflow correlations.	101

	<u>Page</u>
5.12 Geometry and Reynolds dependence of Idel'chik [I.2] and Chilton-Genereaux [C.2] crossflow correlations.	102
5.13 Array independent crossflow correlation	104
5.14 Principle of independence for inclined cylinder	106
5.15 Inclined flow mainstream velocity model	110
5.16 Parallel flow superposition models.	115
5.17 Crossflow superposition models.	116
5.18 (x,y) coordinate system	120
5.19 Range of parallel/crossflow ratio	121
5.20 Superposition model prediction of drag resistance component .	123
5.21 Superposition model prediction of lift resistance component .	124
5.22 Groehn's (a) experimental setup and (b) sample data [G.1] . .	126
5.23 Bottgenbach's test apparatus [B.4].	128
5.24 Bottgenbach's reduced data (a) crossflow component and (b) parallel flow component [B.4]	129
5.25 Normalized drag flow resistance correlations.	133
5.26 45 degree test section flow profile, $Re_v = 7,450$ (bottom) . .	135
5.27 45 degree test section flow profile, $Re_v = 7,450$ (middle) . .	135
5.28 45 degree test section flow profile, $Re_v = 7,450$ (top). . . .	135
5.29 Effect of Reynolds number on velocity and pressure profile, 45 degree test section.	139
5.30 30 degree test section flow profile, $Re_v = 7,450$	140
5.31 Parallel and crossflow test section velocity profile, $Re_v = 7,450$	141
5.32 Measured variables and locations.	143
5.33 Parallel flow resistance, drag component.	144
5.34 30 degree test section flow resistance, drag component. . . .	145
5.35 30 degree test section flow resistance, lift component. . . .	146

	<u>Page</u>
5.36 45 degree test section flow resistance, drag component. . . .	147
5.37 45 degree test section flow resistance, lift component. . . .	148
5.38 Crossflow resistance, drag component.	149
5.39 Flow resistance curve fits.	150
5.40 Angle and geometry dependence of flow resistance, drag component ($Re_d = 10^4$).	153
5.41 Angle and geometry dependence of flow resistance, lift component ($Re_d = 10^4$).	154
5.42 Reynolds number dependence of flow resistance, drag component ($\gamma_v = 0.65$).	156
5.43 Reynolds number dependence of flow resistance, lift component ($\gamma_v \approx .65$).	157
5.44 Data, correlation, and model comparison, drag component . . .	159
5.45 Data and model comparison, lift component	160
5.46 Parallel and crossflow resistance components.	163
5.47 Data, crossflow superposition model comparison.	165
5.48 Data, parallel flow superposition model comparison.	166
6.1 Single bubble drag coefficient in an infinite medium (Insert from Ref. [C.3]).	181
6.2 Bubble shape regimes for buoyancy flow in infinite medium (adapted from Ref. [C.3])	182
6.3 Bubble rise velocity in test duct	183
6.4 Comparison of bubble rise velocity in infinite medium of this study with previous work [C.3]	185
6.5 Multiple bubble drag coefficient for infinite medium.	189
6.6 Slug velocity in round tube [C.3]	193
6.7 Effect of round tube on bubble rise velocity.	195
6.8 Bubble rise velocity in parallel test section	196
6.9 Effect of parallel rod array on bubble rise velocity.	198

	<u>Page</u>
6.10 Definition of characteristic length for square rod array (a) volumetric hydraulic diameter, (b) inscribe diameter, and (c) average gap width	199
6.11 Bubble rise velocity in crossflow section	201
6.12 Effect of crossflow rod array on bubble rise velocity	202
6.13 Bubble (a) force and (b) velocity vector definitions.	205
6.14 Bubble rise velocity in 45 degree test section for zero liquid flow.	206
6.15 Bubble trajectory in 45 degree test section for zero liquid flow.	207
6.16 Two step description of bubble trajectory in inclined rod array of standing liquid.	209
6.17 Bubble trajectory in 45 degree test section for 0.36 ft/sec (0.11 m/sec) liquid velocity.	210
6.18 Bubble trajectory in 45 degree test section for 0.56 ft/sec (0.17 m/sec) liquid velocity.	211
6.19 Bubble velocity in 45 degree test section for two liquid flow rates	212
6.20 Test section designs of (a) Baush and Lahey [B.10] and (b) Osakabe and Adachi [O.1].	217
6.21 Map of flow conditions photographed	218
6.22 Void distribution predictions of 45 degree test section with THERMIT-2 (a) coordinate mesh, (b) low, and (c) high liquid flow rate.	227
6.23 Bubble trajectory prediction with isotropic model for large bubbles	229
6.24 Bubble rise velocity in parallel and crossflow test sections	231
6.25 Bubble coordinate variable definitions (a) general and (b) for zero liquid flow.	232
6.26 Two-region velocity model	234
6.27 Construction of mainstream and recirculation region velocities	237

	<u>Page</u>
6.28 Model/data comparison of single bubble trajectory in 45 degree test section	243
6.29 Bubble trajectory prediction with two-region model for large bubbles	244
6.30 Model/data comparison of bubble velocity in 45 degree test section	245
A.1 Control volume definitions.	255
A.2 Time interval definition.	262
A.3 Stationary spatial averaging control volume	267
B.1 Test section isometric.	279
B.2 Parallel test section--cutaway side view.	280
B.3 30 degree test section--cutaway side view	281
B.4 45 degree test section--cutaway side view	282
B.5 Crossflow test section--cutaway side view	283
B.6 Cutaway top view--(a) parallel test section, (b) 45 degree test section.	284
B.7 Test section assembly	285
B.8 Test duct isometric.	286
B.9 Test duct isometric detail.	287
B.10 Probe penetration detail.	288
B.11 Inlet flow diffuser/straightener.	289
B.12 Instrument calibration tube	290
C.1 Turbine flow meter calibration curve.	293
C.2 Air orifice metering system	294
C.3 Air orifice meter calibration curve	297
C.4 12 FS rotameter calibration curve	299
C.5 20 FS rotameter calibration curve	300

	<u>Page</u>
C.6 Pitot-static tube calibration velocity profiles	302
C.7 Pitot-static tube calibration curve	303
D.1 Definition of average mainstream flow area.	305
D.2 Definition of (a) minimum and (b) average clearance area (model (A) and (B), respectively).	307
D.3 Path length with constant minimum clearance area model for mainstream volume (model (C))	309
D.4 Crossflow mainstream porosity model (A) for principle crossflow directions.	311
D.5 Crossflow mainstream porosity model (C) for principle crossflow directions.	312
D.6 Crossflow mainstream porosity model (B) for principle crossflow directions.	313
F.1 Measured quantities for determining bubble velocity and trajectory.	326
I.1 Isotropic and two-region model for $D_b = 0.02$ ft (0.61 cm).	349

LIST OF TABLES

	<u>Page</u>
4.1 Test Section Geometry	52
4.2 Test Duct Geometry	57
4.3 Test Loop Conditions	60
4.4 Average Bubble Diameter Generated at Orifice	72
5.1 Flow Regime Classifications.	75
5.2 Parallel Flow Correlations (for smooth surfaces)	92
5.3 Crossflow Correlations	95
5.4 Superposition Models	117
5.5 Published Inclined Flow Data	130
5.6 Linear Fits for Flow Resistance Data	151
6.1 Drag Coefficient Models for Single Bubble in Infinite Medium .	179
6.2 Multiple Bubble Drag Coefficient	188
6.3 Round Tube Relative Velocity Ratio	192
6.4 Two-Region Model	241
6.5 Multidimensional Interfacial Drag Models	247
C.1 Orifice Meter Calibration Curve.	296
D.1 Models for Crossflow Mainstream Porosity, δ_v	315
E.1 Flow Resistance for Parallel Test Section, Drag Component. . .	318
E.2 Flow Resistance for 30 Degree Test Section, Drag Component . .	319
E.3 Flow Resistance for 30 Degree Test Section, Lift Component . .	320
E.4 Flow Resistance for 45 Degree Test Section, Drag Component . .	321
E.5 Flow Resistance for 45 Degree Test Section, Lift Component . .	322
E.6 Flow Resistance for Crossflow Test Section, Drag Component . .	323

	<u>Page</u>
E.7 Estimated Measurement Error Bars	324
F.1 Bubble Velocity in Test Duct	327
F.2 Bubble Velocity in Parallel Test Section	328
F.3 Bubble Velocity in Crossflow Test Section.	329
F.4 Bubble Trajectory in 45 Degree Test Section: $ \langle \underline{v}_l \rangle = 0$	330
F.5 Bubble Velocity in 45 Degree Test Section: $ \langle \underline{v}_l \rangle = 0$	331
F.6 Bubble Trajectory in 45 Degree Test Section: $ \langle \underline{v}_l \rangle = 0.36$ ft/sec	332
F.7 Bubble Trajectory in 45 Degree Test Section: $ \langle \underline{v}_l \rangle = 0.56$ ft/sec	333
F.8 Bubble Velocity in 45 Degree Test Section: $ \langle \underline{v}_l \rangle > 0$	334
G.1 Multiple Bubble Drag Coefficient	343
I.1 Two-Region Model Program Input/Output.	350
I.2 Two-Region Model Program Listing	351

LIST OF PLATES

		<u>Page</u>
4.1	30 Degree Test Section (a) Parts, (b) Half Assembled, (c) Side View, (d) End View	50
4.2	(a) Parallel, 30 Degree, and Crossflow Test Sections--End View, (b) Mounted Test Duct with Crossflow Section, (c) Flow Loop, (d) Flow Diffuser/Straightener	51
4.3	(a) Differential Pressure Measuring System, (b) Pitot-Static Tube and Small Bubble Generating Orifices in Parallel Test Section, (c) Large Bubble Release Cup.	66
6.1	(a) Spherical, (b) Distorted, and (c) Capped Bubbles in Infinite Medium; (d) Distorted and (e) Slug Bubbles in Parallel Array; (f) Slug Bubble in Crossflow Array.	178
6.2	Bubble Trajectories for a Stream of Bubbles in 45 Degree Test Section with (a) $Re_v = 00$, (b) $Re_v = 1,600$, and (c) $Re_v = 2,750$	214
6.3	Bubble Trajectories for a Stream of Bubbles in 45 Degree Test Section (a) For Small Bubbles at $Re_v = 1,600$, (b) Close-up of Spiral Motion at $Re_v = 5,150$	215
6.4	Flow Pattern in 45 Degree Test Section for Low Liquid Flow Rate.	219
6.5	Flow Pattern in 45 Degree Test Section for High Liquid Flow Rate	220
6.6	Flow Distribution at Exit Plenum of 45 Degree Test Section for $j_g = 0.013$ ft/sec (0.0038 m/sec).	221
6.7	Flow Distribution at Exit Plenum of 45 Degree Test Section for $j_g = 0.047$ ft/sec (0.014 m/sec)	222
6.8	Flow Distribution at Exit Plenum of 45 Degree Test Section for $j_g = 0.87$ ft/sec (0.27 m/sec)	223

NOMENCLATURE

<u>Variable</u>	<u>Definition</u>
A	Area
A, B, B ₀	Friction factor constants
a	Constant in Groehn's correlation
a _p	3/(2 D _b)
b	Total crossflow resistance coefficient
C _m	Momentum covariance coefficient
C	Pitot-static tube calibration constant
C _D	Bubble drag coefficient
c	Form drag resistance coefficient
D	Tube diameter
D _v	Volumetric hydraulic diameter
D _b	Bubble equivalent spherical diameter
d	Rod diameter
E ₀	Eötvös Number
<u>e</u>	Unit vector
F _B	Body force
F _D	Total steady state drag force
F _G	Buoyancy force
F _R	Resistance force
f	Friction factor
f	Arbitrary variable of definition
f'[α]	Function in Ishii's model
g	Acceleration of gravity

<u>Variable</u>	<u>Definition</u>
$g_1(\theta)$	Parallel superposition factor
$\underline{\underline{H}}$	Surface to volume transformation tensor
H_{21}	Radius of curvature
$h_1(\theta)$	Crossflow superposition factor
$\underline{\underline{I}}$	Identity tensor
$\underline{\underline{J}}$	Directional mainstream drag tensor
j	Superficial velocity
$\underline{\underline{K}}, K$	Flow resistance coefficient tensor
k	Constant in Darcy Law
k'	Orifice meter calibration constant
L	Length
\overline{L}_{gap}	Average gap width, $S_T - \gamma_v d$
l_j	Line coordinate length
M	Interfacial momentum exchange
\hat{M}	Dimensionless viscosity number
m, m', n, n'	Exponential constants
\dot{m}	Mass flow rate
N_b	Number of bubbles
N_μ	Alternate definition of viscosity number
\underline{n}	Interface normal vector
P	Pitch of equilateral rod arrangement
p	Pressure
Δp	Differential pressure
Q	Volumetric flow rate
R	Flow resistance
RA	Rod arrangement

<u>Variable</u>	<u>Definition</u>
Re_v	Liquid Reynolds number, $\rho_l D_v \langle \underline{v} \rangle / \mu_l$
Re_d	Liquid Reynolds number, $\rho_l d \underline{v}_{ms} / \mu_l$
Re_b	Bubble Reynolds number, $\rho_l D_b \underline{v}_r / \mu_l$
\underline{r}	Coordinate vector
S_L	Longitudinal pitch
S_L'	Staggered pitch
S_T	Transverse pitch
\underline{T}	Total stress tensor
T	Temperature
t	Time
Δt	Time interval
u	Characteristic velocity
V	Volume
v	Velocity
v_r	Relative velocity
w	Arbitrary weighting variable
x, y, z	Cartesian coordinates
x, y, z	Principle coordinates of test section
α	Void fraction
α_m	Maximum packing void fraction
β	Volumetric flow fraction
Γ	Interfacial mass exchange
γ	Porosity
δ	Interface region thickness
δ_v	Crossflow mainstream porosity

<u>Variable</u>	<u>Definition</u>
ϵ	Roughness
η	Crossflow plane flow inclination
$\eta'(\theta)$	Function in Todreas-Coëffé model
θ	Inclination from rod axis
λ	Mainstream/recirculating region weighting function
μ	Viscosity
π	3.14159
ρ	Density
σ	Surface tension
τ	Shear stress
ϕ	Inclination from vertical
χ	Phase density function
ψ	Angle between rod axis and total drag force

<u>Subscript</u>	<u>Definition</u>
b	Bubble
b'	Multiple bubble
c	Characteristic
D'	Multiple bubble drag
f	Fluid
ff	Fluid-fluid interface
fs	Fluid-solid interface
g	Gas phase
gj	Drift velocity
i	Interface

<u>Subscript</u>	<u>Definition</u>
j	Interface index
k, 1, 2	Phase
l	Liquid phase
m	Mixture
ms	Mainstream
S	System
s	Surface
V	Volume
w	Wall
x, y, z	Cartesian coordinate components
xs	Cross section
θ	Multidimensional component
$\parallel, \perp 1, \perp 2$	Three-dimensional rod array principal coordinate components
\parallel, \perp	Two-dimensional rod array principal coordinate components
①	Mainstream region
②	Recirculation region
∞	Infinite medium

<u>Superscript</u>	<u>Definition</u>
C	Capped/churned-turbulent regime
D	Distorted regime
DC	Distorted-capped transition
e	Combined viscous and turbulent shear
ff	Averaged over fluid-fluid interface

SuperscriptDefinition

fs	Averaged over fluid-solid interface
i	Averaged over interface
j	Averaged over area
T	Turbulent shear stress
us	upstream
V	Viscous regime
VD	Viscous-distorted transition
VN	Viscous-Newton transition

SymbolDefinition

\bar{f}	Average
\overline{f}	Time average
$\overline{\overline{f}}$	Phase-weighted time average
$\overline{\overline{f}}$	Density-weighted time average
\underline{f}	Vector
$\underline{\underline{f}}$	Tensor
$ f $	Absolute value
$\nabla \cdot$	Divergence
$\langle f \rangle$	Volume average
$\langle\langle f \rangle\rangle$	Phase-weighted volume average
$\langle\langle f \rangle\rangle$	Phase-density weighted volume average
$\{f\}$	Surface average
$\{\{f\}\}$	Phase-weighted surface average
$\{\{f\}\}$	Phase-density weighted surface average
$f[], ftn[]$	Functional dependence
Δ	Definition
f^*	Dimensionless variable

CHAPTER 1

INTRODUCTION

Efficient heat transfer is an essential part of the power generating and chemical process industries. Heat transfer components such as condensers, boilers, steam generators, baffled heat exchangers, and nuclear reactors, are used extensively in these industries. The most widely used heat transfer geometry is a shell enclosing a tube array with heat exchange between the fluid within the tubes and the fluid within the shell surrounding the tubes. Arrays of tubes are widely used because they provide a large surface area for heat transfer while still furnishing structural strength, low flow resistance, and ease of construction. Schematics of several heat transfer components are shown in Fig. 1.1.

A detailed understanding of heat transfer components is desired to maintain good operational performance with maximum efficiency over a long lifetime. Thermal-hydraulic computer codes have been developed to aid in the design and performance analysis. These codes solve the finite difference fluid conservation equations along with problem specific geometry, boundary conditions, initial conditions, and constitutive relations. The advent of high-speed digital computers and advanced numerical methods have expanded thermal-hydraulic codes from one-dimensional mixture models to a two- and three-dimensional, nonequilibrium, two-fluid models. A partial list of these codes are: COBRA-TF [C.4], TRAC [T.3], THERMIT [R.3, K.3], URSULA-2 [U.1], COMMIX-2 [S.2]. The application of these codes has been hampered by the

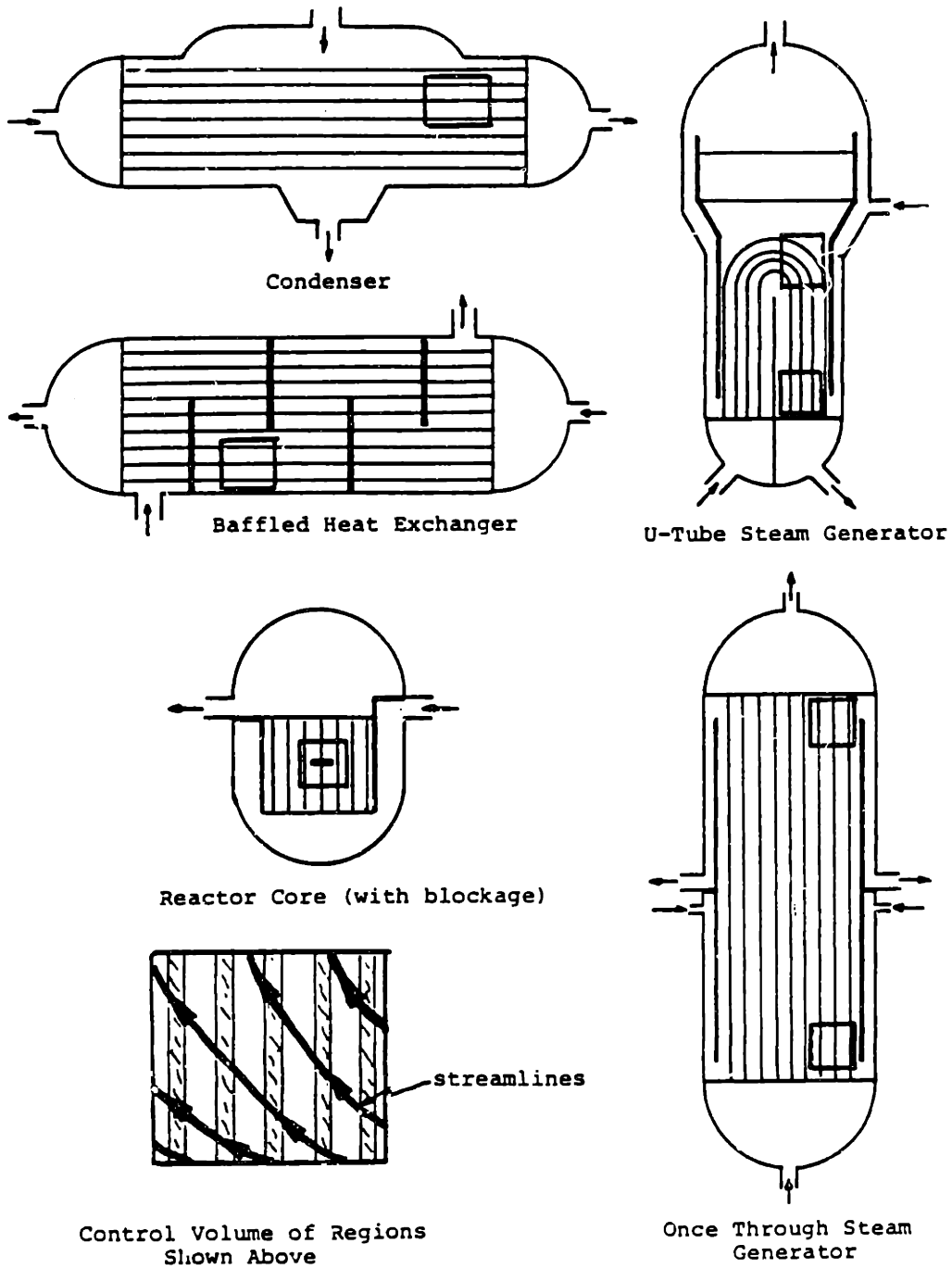


Figure 1.1 Cross sections of heat transferring components.

insufficient development of multidimensional constitutive relations.

Analysis with advanced thermal-hydraulic codes provide detailed descriptions of flow distributions and heat transfer rates which are essential to solving current heat transfer component problems. For example, in the U-tube steam generator, regions of flow stagnation cause temperature increases, voidage, and sludge accumulation, leading to tube denting, cracking, and corrosion, limiting the component lifetime in addition to decreasing its efficiency [W.2].

Also of importance in a nuclear power plant, is the steam generator heat transfer rate under transient conditions. In some reactor transients (i.e., loss of auxiliary feed water) the response of the primary coolant system is contingent on the heat transfer (removal) rate of the steam generators. Therefore the more accurately the steam generator transient performance can be predicted, the safer and more economically the entire plant can be operated.

A third application of advanced thermal-hydraulic codes is in the design of new heat exchangers. Many new rod array concepts are being proposed [G.4, G.5] which costly experimental programs can only partially address. Code analysis enables relatively less expensive scoping and sensitivity studies to be performed so that judicious choices of validating experiments may be made.

1.1 Objective and Scope

A fundamental part of thermal-hydraulic codes is the constitutive relations describing the fluid interaction with its environment. Constitutive relations have been well formulated for one-dimensional flows in round tubes and some for rod array geometries, but very little

work has been done for multidimensional flows in rod arrays. The objective of this research is to explore, assess, and identify the limitations of current multidimensional hydrodynamic constitutive models and propose new formulations where warranted. The specific constitutive variables addressed here are: for single-phase flow, the fluid-solid flow resistance (skin friction and form drag), and for two-phase flow, the liquid-gas interfacial resistance (relative motion between phases). The focus of this study is on the influence of flow direction with respect to the rod array axis, applied on a porous medium scale (as opposed to a subchannel or distributed parameter scale). Current unsubstantiated models have been developed by superimposing one-dimensional correlations for the three principal orthogonal directions.

An experimental investigation of flow inclined to a rod array is performed to help assess the applicability and limits of current constitutive models and direct research in the areas of needed model improvement. The experimental program consist of pressure, velocity, and flow distribution measurements for air-water at zero, 30, 45, and 90 degree inclinations to the axis of a square pitch rod array.

1.2 Motivation

The principle motivation for this work is the lack of substantiating experimental data of multidimensional effects predicted by the current multidimensional models. Single-phase flow at incline angles exhibits not only a drag resistance force in the average flow direction but also a lift force perpendicular to the flow direction. Four researchers [K.2, G.1, B.4, M.3] have measured the drag resistance

component through inclined rods. However, of these four, only two [B.4, M.3] attempted to measure the lift resistance component. Even with this sparse published data a comprehensive comparison with multidimensional resistance correlations has not been made.

Two-phase experiments of inclined flows in rod arrays is also sparse. Two researchers [B.10, O.1] have published flow regime observations in inclined array flow, but little has been done about validating current interfacial models. Current bubbly flow interfacial models are based on drag forces for a single bubble rising in a large liquid pool. Clearly the introduction of a rod array will change the flow field, and consequently alter the bubble drag forces from that in a large pool.

The goal of this research is to identify the important physical phenomena not incorporated in current constitutive models and propose new methods to include these phenomena.

1.3 Contributions

Previewed here are several important contributions arising from this research:

- (1) Confirmation of the superposition formulation for single-phase turbulent flow resistance.
- (2) Identification of the questionable application of superposition formulations for single-phase laminar flow.
- (3) Observation of a phase separation phenomena in bubbly flow and a physical model to describe these observations.
- (4) Addition of new data for the fundamental understanding of bubble kinematics in parallel, crossflow, and inclined rod arrays.

1.4 Outline

The general development methodology for a thermal-hydraulic model is presented in Chapter 2. Practical single- and two-phase models are presented in Chapter 3. Chapter 4 describes the experimental apparatus and instrumentation. Single-phase flow resistance models are discussed in Chapter 5 and two-phase interfacial force models in Chapter 6. Finally an evaluation of this exploratory study and the areas requiring further research are presented in Chapter 7.

CHAPTER 2

THERMAL-HYDRAULIC MODEL METHODOLOGY

2.1 General Model Development

Thermal-hydraulic computer codes are a tool developed to solve the flow field within a defined system for a specified set of boundary and initial conditions. The codes solve the conservation equations in conjunction with constitutive laws describing the interaction of the fluid(s) with its surrounding environment. Universal, intrinsic constitutive laws valid for all environments is beyond the current knowledge of thermal-hydraulics, therefore constitutive relations applicable for a limited environment have been used extensively in developing thermal-hydraulic models.

Figure 2.1 shows the general procedure used in developing a thermal-hydraulic model for a specific problem. Starting with the conservation laws, a set of generalized conservation equations are developed by time and volume averaging. These generalized equations are then simplified to a set of practical equations by making constraining assumptions chosen for the specific problem of interest (i.e., one-dimensional, steady state, incompressible, equal phasic pressures, thermal equilibrium, etc.). Still, relations for the remaining constitutive variables are required.

Constitutive relations are developed by first starting with phenomenological models; then correlating and/or validating the individual models with separate effects experiments. Finally the individual models are collectively validated with global experiments.

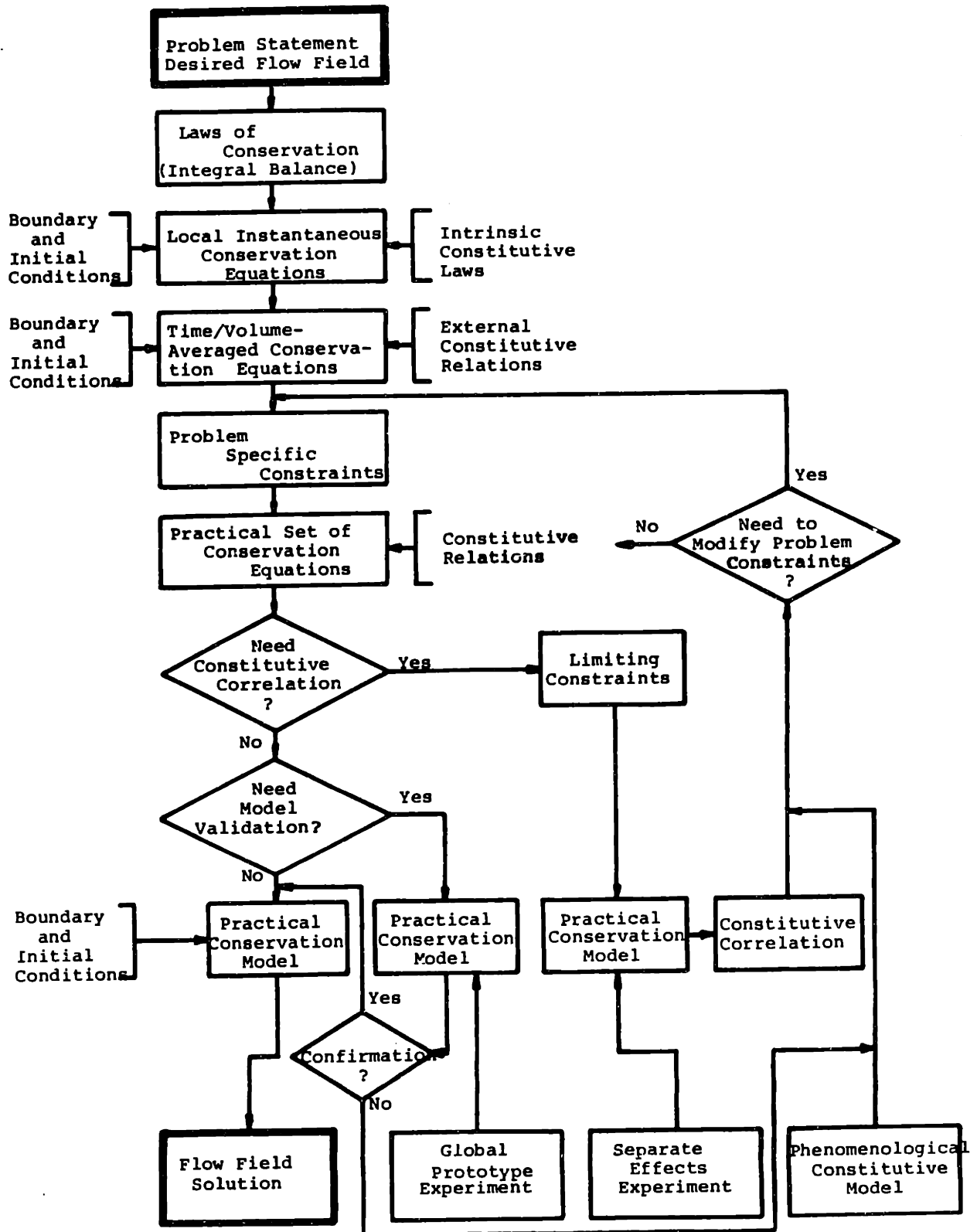


Figure 2.1 Thermal-hydraulic model development.

Separate effects experiments are designed to identify, isolate, and correlate a single phenomena. Global experiments are primarily to confirm the integral effects predicted by several constitutive relations developed from separate effects experiments. In some instances developing constitutive relations from separate effects experiments is not feasible and global experiments have to be used directly for correlation of the integral effect. Once confirmed constitutive relations have been developed the flow solutions may be solved for the desired boundary and initial conditions.

A key component in the solution methodology is the choice and modeling form of the constitutive variables. With proper models, extrapolation and integration of the constitutive relations to conditions outside the range of correlation may be done with confidence. Unambiguous experimental data for the environmental conditions of interest is a major contributor to comprehensive constitutive models.

In the remainder of this chapter the generalized conservation equations for the hydrodynamics of porous medium flow and corresponding constitutive variables are presented.

2.2 General Hydrodynamic Conservation Equations

The local instantaneous hydrodynamic conservation equations for phase k are

$$\frac{\partial \rho_k}{\partial t} + \nabla \cdot \rho_k \mathbf{v}_k = 0 \quad (2.1)$$

$$\frac{\partial}{\partial t} (\rho_k \mathbf{v}_k) + \nabla \cdot \rho_k \mathbf{v}_k \mathbf{v}_k - \rho_k \mathbf{F}_B - \nabla \cdot \mathbf{T}_k = 0 \quad (2.2)$$

$$\sum_k \rho_k (\mathbf{v}_k - \mathbf{v}_i) \cdot \mathbf{n}_k = 0 \quad (2.3)$$

$$\sum_k (\rho_k \mathbf{v}_k (\mathbf{v}_k - \mathbf{v}_i) \cdot \mathbf{n}_k - \mathbf{n}_k \cdot \mathbf{T}_k) = 2H_{21} \sigma \mathbf{n}_i \quad (2.4)$$

where Eqs. (2.3) and (2.4) are the interfacial jump conditions. In the above, the state variables are the phasic density ρ_k , and velocity \underline{v}_k ; and the intrinsic constitutive variables are σ , \underline{F}_B , \underline{T}_k , and \underline{v}_i .

These equations, derived from the integral mass and momentum balances (as shown in Appendix A), are intermittently applicable at a point depending on the phase present. Because of the complicated interface structure of two-phase flow, solving the local instantaneous equations in general flow systems is impractical except for simple, well-defined flow situations. Clearly a more useful set of equations is one where the high frequency spatial and temporal fluctuations are averaged out. Time and volume averaging the local instantaneous equations through a control volume including solid structures, yields the time/volume-averaged porous medium conservation equations

$$\begin{aligned} \frac{\partial}{\partial t} [\gamma_v \langle \alpha_k \rangle \langle \langle \bar{\rho}_k \rangle \rangle] + \nabla \cdot [\gamma_v \langle \alpha_k \rangle \langle \langle \bar{\rho}_k \rangle \rangle \langle \underline{\bar{v}}_k \rangle] \\ = \gamma_v \langle \Gamma_k \rangle \end{aligned} \quad (2.5)$$

$$\begin{aligned} \frac{\partial}{\partial t} [\gamma_v \langle \alpha_k \rangle \langle \langle \bar{\rho}_k \rangle \rangle \langle \underline{\bar{v}}_k \rangle] + \nabla \cdot [\gamma_v \langle C_{km} \rangle \langle \alpha_k \rangle \langle \langle \bar{\rho}_k \rangle \rangle \langle \underline{\bar{v}}_k \rangle \langle \underline{\bar{v}}_k \rangle] \\ - \gamma_v \langle \alpha_k \rangle \langle \langle \bar{\rho}_k \rangle \rangle \langle \underline{\bar{F}}_B \rangle - \nabla \cdot [\gamma_v \langle \alpha_k \rangle \langle \langle \underline{\bar{T}}_k \rangle \rangle + \langle \langle \underline{\bar{T}}_k \rangle \rangle] \\ + \gamma_v \langle R_k \rangle = \gamma_v \langle M_k \rangle \end{aligned} \quad (2.6)$$

where the jump and closure conditions are

$$\sum_k \langle \Gamma_k \rangle = 0 \quad (2.7)$$

$$\sum_k \langle M_k \rangle = \langle M_m \rangle \quad (2.8)$$

$$\sum_k \langle \alpha_k \rangle = 1 \quad (2.9)$$

(See Appendix A for a detailed derivation.)

Although mathematically similar to the local instantaneous equations, these equations introduce new global state variables, $\{\underline{v}_k^m\}$ and $\langle\langle \underline{\rho}_k^m \rangle\rangle$, which are weighted temporally and spatially averages of the local state variables \underline{v}_k and ρ_k . In the averaging process new external constitutive variables (i.e., $\langle \Gamma_k \rangle$, $\langle \alpha_k \rangle$, $\langle\langle \underline{T}_k^m \rangle\rangle$, $\langle\langle \underline{T}_k^T \rangle\rangle$, $\langle \underline{R}_k \rangle$, $\langle \underline{M}_m \rangle$, $\langle \underline{M}_k \rangle$, \underline{C}_{km} and, $\{\underline{F}_B^m\}$) are introduced.

2.3 Constitutive Relations

Some of the external constitutive variables are definable in terms of local state and intrinsic constitutive variables (i.e., $\langle \Gamma_k \rangle$, $\langle\langle \underline{T}_k^m \rangle\rangle$, $\langle \underline{R}_k \rangle$, $\{\underline{F}_B^m\}$, $\langle \underline{M}_m \rangle$, and $\langle \underline{M}_k \rangle$). However through spatial and temporal integration they also become dependent on the surrounding environment. New constitutive variables are also introduced (i.e., $\langle \alpha_k \rangle$, $\langle\langle \underline{T}_k^T \rangle\rangle$, and \underline{C}_{mk}) which incorporate the topological characteristics lost by averaging the state variables. The local variables appearing in the formal definitions of the constitutive variables are not available when the generalized conservation equations are solved, hence models for the constitutive variables ultimately must be dependent on only the environmental geometry and global state variables.

In developing models for the constitutive variables, fundamental relations are desired for wider application and extrapolation. The drawback of fundamental models is that they generally rely on many separate effects experiments as building blocks for more elaborate flow situations. The compilation of many fundamental models can become quite complex and have the potential for many sources for error. Lumped constitutive models are simple to develop and have good accuracy in the range of correlation, but are limited to that range, since without a

physical fundamental basis extrapolation outside the validation range is unwise.

2.4 Practical Conservation Model

Employing the generalized conservation equations directly, with its many required constitutive relations and elaborate state variable definitions, is still an involved task. To transform these time/volume-averaged equations into a practical set of equations several justifiable simplifying assumptions, for the problem of interest, should be made. With careful choices of the restricting assumptions the number of constitutive relations required can be reduced and the physical interpretation of the global state variables may be simplified.

By always starting first with Eq. (2.5) through (2.9) and stating the restricting assumptions clearly, an unambiguous practical conservation model can be developed. If experimental observations warrant relaxing one of the restrictions, then a new practical conservation model can be easily constructed. Clearly the experiments used for validation should reflect the same degree of restrictive assumptions as the model being used. For example one-dimensional flow data cannot fully validate a three-dimensional constitutive model.

In Chapter 3 a practical set of conservation equations for single- and two-phase flow in inclined rod arrays is presented and the required constitutive variable identified. In Chapter 4 the validating experiment is described. Then in Chapter 5 and 6 constitutive relations for inclined flows are developed.

CHAPTER 3

HYDRODYNAMIC MODEL

Practical hydrodynamic models for single- and two-phase porous medium flow in rod arrays are developed here and the required constitutive relations identified.

3.1 Single-Phase Hydrodynamic Model

For single-phase flow the void fraction $\langle \alpha_k \rangle$, is unity, and the interfacial conditions and k-phase subscripts may be dropped, hence the generalized conservation equations, Eq. (2.5) through (2.9), reduce to

$$\frac{\partial}{\partial t} [\gamma_v \langle \bar{\rho} \rangle] + \nabla \cdot [\gamma_v \langle \bar{\rho} \rangle \{ \underline{\bar{v}} \}] = 0 \quad (3.1)$$

$$\begin{aligned} \frac{\partial}{\partial t} [\gamma_v \langle \bar{\rho} \rangle \{ \underline{\bar{v}} \}] + \nabla \cdot [\gamma_v \underline{c}_m \langle \bar{\rho} \rangle \{ \underline{\bar{v}} \} \{ \underline{\bar{v}} \}] \\ - \gamma_v \langle \bar{\rho} \rangle \{ \underline{\bar{F}}_B \} - \nabla \cdot [\gamma_v (\langle \underline{\bar{T}} \rangle + \langle \underline{\bar{T}}^T \rangle)] \\ + \gamma_v \langle \underline{R} \rangle = 0 \end{aligned} \quad (3.2)$$

Now a practical conservation model can be developed by making some reasonable restricting assumptions:

- The flow is incompressible

$$\begin{aligned} \langle \bar{\rho} \rangle &= \rho \\ \{ \underline{\bar{v}} \} &= \langle \underline{\bar{v}} \rangle \\ \{ \underline{\bar{F}}_B \} &= \langle \underline{\bar{F}}_B \rangle \end{aligned} \quad (3.3)$$

- The only body force is the constant gravitational field,

$$\langle \underline{\bar{F}}_B \rangle = \underline{g} \quad (3.4)$$

- The total shear tensor may be modeled in terms of pressure and shear forces (See Appendix A.6.1)

$$\langle \underline{\underline{\tau}} \rangle = - \langle \underline{\underline{p}} \rangle \underline{\underline{I}} + \langle \underline{\underline{\tau}} \rangle \quad (3.5)$$

- The averaging volume is large and includes enough distributed solids such that the viscous and turbulent shear stresses $\langle \underline{\underline{\tau}} \rangle$ and $\langle \underline{\underline{\tau}} \underline{\underline{\tau}} \rangle$, respectively, are negligible compared to the fluid-solid flow resistance $\langle \underline{\underline{R}} \rangle$.
- The spatial covariance is negligible

$$\underline{\underline{C}}_{\underline{\underline{m}}} = \underline{\underline{I}} \quad (3.6)$$

- The spatial coordinates are the Cartesian system (x,y,z).

Introducing the above assumptions into Eq. (3.1) and (3.2) gives

$$\frac{\partial}{\partial t} [\gamma_v \rho] + \frac{\partial}{\partial x} [\gamma_v \rho v_x] + \frac{\partial}{\partial y} [\gamma_v \rho v_y] + \frac{\partial}{\partial z} [\gamma_v \rho v_z] = 0 \quad (3.7)$$

$$\begin{aligned} \frac{\partial}{\partial t} [\gamma_v \rho v_x] + \frac{\partial}{\partial x} [\gamma_v \rho v_x v_x] + \frac{\partial}{\partial y} [\gamma_v \rho v_x v_y] \\ + \frac{\partial}{\partial z} [\gamma_v \rho v_x v_z] - \gamma_v \rho g_x + \gamma_v \frac{\partial}{\partial x} [\gamma_v \langle \underline{\underline{p}} \rangle] + \gamma_v \langle R_x \rangle = 0 \end{aligned} \quad (3.8)$$

$$\begin{aligned} \frac{\partial}{\partial t} [\gamma_v \rho v_y] + \frac{\partial}{\partial x} [\gamma_v \rho v_y v_x] + \frac{\partial}{\partial y} [\gamma_v \rho v_y v_y] \\ + \frac{\partial}{\partial z} [\gamma_v \rho v_y v_z] - \gamma_v \rho g_y + \gamma_v \frac{\partial}{\partial y} [\gamma_v \langle \underline{\underline{p}} \rangle] + \gamma_v \langle R_y \rangle = 0 \end{aligned} \quad (3.9)$$

$$\begin{aligned} \frac{\partial}{\partial t} [\gamma_v \rho v_z] + \frac{\partial}{\partial x} [\gamma_v \rho v_z v_x] + \frac{\partial}{\partial y} [\gamma_v \rho v_z v_y] \\ + \frac{\partial}{\partial z} [\gamma_v \rho v_z v_z] - \gamma_v \rho g_z + \gamma_v \frac{\partial}{\partial z} [\gamma_v \langle \underline{\underline{p}} \rangle] + \gamma_v \langle R_z \rangle = 0 \end{aligned} \quad (3.10)$$

where

$$\langle \underline{\underline{v}} \rangle = v_x \underline{\underline{e}}_x + v_y \underline{\underline{e}}_y + v_z \underline{\underline{e}}_z \quad (3.11)$$

and

$$\underline{\underline{g}} = g_x \underline{\underline{e}}_x + g_y \underline{\underline{e}}_y + g_z \underline{\underline{e}}_z \quad (3.12)$$

The remaining constitutive variables are $\langle \bar{p} \rangle$ and $\langle \underline{R} \rangle$. Assuming the equation of state intrinsic constitutive relations can be applied to temporal/spatial-averaged state variables gives a relation between the pressure $\langle \bar{p} \rangle$, and density ρ ,

$$\rho = \text{fn}[\langle \bar{p} \rangle, T_g]$$

where T_g is the system temperature. Because pressure is an easier quantity to measure than density, $\langle \bar{p} \rangle$ is generally referred to as the state variable and ρ the correlated constitutive variable.

The one remaining constitutive variable is the flow resistance $\langle \underline{R} \rangle$. Correlations for $\langle \underline{R} \rangle$ can be developed by measuring the state variables for a specified flow field and solving Eq. (3.7) through (3.10) for $\langle \underline{R} \rangle$. In Chapter 5 correlations for $\langle \underline{R} \rangle$ for single-phase flow inclined to rod arrays are discussed in detail.

3.2 Two-Phase Hydrodynamic Model

A practical two-fluid conservation model is developed by making a set of restricting assumptions and applying them to the generalized conservation equations. Presented here is a set of assumptions used widely in current two-fluid codes [R.3, T.3, C.4, S.2].

Starting with Eq. (2.5) through (2.9),

- Partitioning the total stress tensor into a pressure and shear stress term

$$\langle \langle \bar{T}_{\underline{k}} \rangle \rangle = - \langle \langle \bar{p}_{\underline{k}} \rangle \rangle \underline{I} + \langle \langle \bar{T}_{\underline{k}} \rangle \rangle$$

and

- Partitioning the interfacial force $\langle \underline{M}_{\underline{k}} \rangle$, into a mass transfer force $\langle \underline{M}_{\underline{k}}^\Gamma \rangle$, steady state drag and transient

force $\langle \underline{M}_k^d \rangle$, and a pressure fluctuation term,

gives

$$\frac{\partial}{\partial t} [\gamma_v \langle \alpha_k \rangle \langle \langle \bar{\rho}_k \rangle \rangle] + \nabla \cdot [\gamma_v \langle \alpha_k \rangle \langle \langle \bar{\rho}_k \rangle \rangle \{ \underline{v}_k \}^{\bar{m}}] = \gamma_v \langle \Gamma_k \rangle \quad (3.13)$$

$$\begin{aligned} \frac{\partial}{\partial t} [\gamma_v \langle \alpha_k \rangle \langle \langle \bar{\rho}_k \rangle \rangle \{ \underline{v}_k \}^{\bar{m}}] + \nabla \cdot [\gamma_v \langle \alpha_k \rangle \langle \langle \bar{\rho}_k \rangle \rangle \{ \underline{v}_k \}^{\bar{m}} \{ \underline{v}_k \}^{\bar{m}}] \\ - \gamma_v \langle \alpha_k \rangle \langle \langle \bar{\rho}_k \rangle \rangle \{ \underline{F}_{-B} \}^{\bar{m}} - \nabla \cdot [\gamma_v \langle \alpha_k \rangle \langle \langle \bar{\tau}_{ik} \rangle \rangle + \langle \langle \bar{\tau}_{ik}^T \rangle \rangle] \\ + \langle \alpha_k \rangle \nabla \cdot [\gamma_v \langle \langle \bar{p}_k \rangle \rangle] + \gamma_v \langle R_k \rangle = \gamma_v \langle \underline{M}_k^T \rangle \\ + \gamma_v \langle \underline{M}_k^d \rangle - \gamma_v \Delta p_k^i \nabla \langle \alpha_k \rangle \end{aligned} \quad (3.14)$$

(See Appendix A.6 for a detailed derivation).

The simplifying assumptions are:

- The phasic densities are constant

$$\begin{aligned} \langle \langle \bar{\rho}_k \rangle \rangle &= \rho_k \\ \{ \underline{v}_k \}^{\bar{m}} &= \langle \langle \bar{\underline{v}}_k \rangle \rangle \\ \{ \underline{F}_{-B} \}^{\bar{m}} &= \langle \langle \bar{\underline{F}}_{-B} \rangle \rangle \end{aligned} \quad (3.15)$$

- The only body force is the gravitation field

$$\langle \langle \bar{\underline{F}}_{-B} \rangle \rangle = \underline{g} \quad (3.16)$$

- The mixture momentum due to surface tension forces is negligible

$$\langle \underline{M}_{-m} \rangle = 0 \quad (3.17)$$

- The phasic viscous and turbulent shear stresses, $\langle \langle \bar{\tau}_{ik} \rangle \rangle$ and $\langle \langle \bar{\tau}_{ik}^T \rangle \rangle$, respectively, are negligible.

- The liquid phase only contacts the solid surfaces, so

$$\langle \underline{R}_{-g} \rangle = 0 \quad (3.18)$$

- The spatial covariance is negligible

$$C_{km} = I \quad (3.19)$$

- The phasic pressure fluctuations are negligible, such that

$$\langle\langle \bar{p} \rangle\rangle = \langle\langle \bar{p}_g \rangle\rangle = \langle\langle \bar{p}_l \rangle\rangle \quad (3.20)$$

and

$$\Delta p_l^i = \Delta p_g^i = 0 \quad (3.21)$$

The simplifying definitions made possible by using the jump and closure conditions (Eq. (2.7), (2.8), and (2.9)) are:

$$\langle \Gamma \rangle \stackrel{\Delta}{=} \langle \Gamma_g \rangle = - \langle \Gamma_l \rangle \quad (3.22)$$

$$\langle \underline{M}_i^d \rangle \stackrel{\Delta}{=} \langle \underline{M}_g^d \rangle = - \langle \underline{M}_l^d \rangle - (\langle \underline{M}_g^\Gamma \rangle + \langle \underline{M}_l^\Gamma \rangle) \quad (3.23)$$

$$\langle \alpha \rangle \stackrel{\Delta}{=} \langle \alpha_g \rangle = - \langle \alpha_l \rangle \quad (3.24)$$

$$\langle \underline{M}_i^\Gamma \rangle \stackrel{\Delta}{=} \langle \underline{M}_g^\Gamma \rangle \quad (3.25)$$

Substituting the simplifying assumptions and definitions into Eq. (3.13) and (3.14) yields the two-fluid hydrodynamic model:

$$\frac{\partial}{\partial t} [\gamma_v \langle \alpha \rangle \rho_g] + \nabla \cdot [\gamma_v \langle \alpha \rangle \rho_g \langle\langle \bar{v}_g \rangle\rangle] = \gamma_v \langle \Gamma \rangle \quad (3.26)$$

$$\frac{\partial}{\partial t} [\gamma_v (1 - \langle \alpha \rangle) \rho_l] + \nabla \cdot [\gamma_v (1 - \langle \alpha \rangle) \rho_l \langle\langle \bar{v}_l \rangle\rangle] = - \gamma_v \langle \Gamma \rangle \quad (3.27)$$

$$\begin{aligned} & \frac{\partial}{\partial t} [\gamma_v \langle \alpha \rangle \rho_g \langle\langle \bar{v}_g \rangle\rangle] + \nabla \cdot [\gamma_v \langle \alpha \rangle \rho_g \langle\langle \bar{v}_g \rangle\rangle \langle\langle \bar{v}_g \rangle\rangle] \\ & - \gamma_v \langle \alpha \rangle \rho_g \underline{g} + \langle \alpha \rangle \nabla \cdot [\gamma_v \langle\langle \bar{p} \rangle\rangle] \\ & = \gamma_v \langle \underline{M}_i^\Gamma \rangle + \gamma_v \langle \underline{M}_i^d \rangle \end{aligned} \quad (3.28)$$

$$\begin{aligned} & \frac{\partial}{\partial t} [\gamma_v (1 - \langle \alpha \rangle) \rho_l \langle\langle \bar{v}_l \rangle\rangle] + \nabla \cdot [\gamma_v (1 - \langle \alpha \rangle) \rho_l \langle\langle \bar{v}_l \rangle\rangle \langle\langle \bar{v}_l \rangle\rangle] \\ & - \gamma_v (1 - \langle \alpha \rangle) \rho_l \underline{g} + (1 - \langle \alpha \rangle) \nabla \cdot [\gamma_v \langle\langle \bar{p} \rangle\rangle] + \gamma_v \langle \underline{R}_l \rangle \\ & = - \gamma_v \langle \underline{M}_i^\Gamma \rangle - \gamma_v \langle \underline{M}_i^d \rangle \end{aligned} \quad (3.29)$$

In this model the state variables are: ρ_g , ρ_l , $\langle\langle\bar{v}_g\rangle\rangle$, and $\langle\langle\bar{v}_l\rangle\rangle$. The constitutive variables are: $\langle\Gamma\rangle$, $\langle\alpha\rangle$, $\langle\langle\bar{p}\rangle\rangle$, $\langle\bar{M}_i^\Gamma\rangle$, $\langle\bar{M}_i^d\rangle$, and $\langle\bar{R}_l\rangle$. Hence six constitutive relations are still required. For a two-component system there is no phase change so

$$\langle\Gamma\rangle = 0 \quad (3.30)$$

and

$$\langle\bar{M}_i^\Gamma\rangle = 0 \quad (3.31)$$

Analogous to the single-phase flow model, the intrinsic equations of state for each phase are applied to the average variables, giving

$$\rho_g = \text{ftn}[\langle\langle\bar{p}\rangle\rangle, T_s] \quad (3.32)$$

$$\rho_l = \text{ftn}[\langle\langle\bar{p}\rangle\rangle, T_s] \quad (3.33)$$

With Eq. (3.32) and (3.33), ρ_g and ρ_l become known constitutive variables and $\langle\alpha\rangle$ and $\langle\langle\bar{p}\rangle\rangle$ become the new state variables. (Strictly speaking the constraint $\langle\langle\bar{p}_g\rangle\rangle = \langle\langle\bar{p}_l\rangle\rangle$ is the topological constitutive relation replacing the required relation for $\langle\alpha\rangle$.)

All that remains are constitutive relations for $\langle\bar{M}_i^d\rangle$ and $\langle\bar{R}_l\rangle$. In Chapter 6 we consider models for $\langle\bar{M}_i^d\rangle$ in multidimensional rod array geometries. Models for $\langle\bar{R}_l\rangle$ are not addressed in this study, but do require further development for multidimensional rod array flows.

CHAPTER 4

EXPERIMENT

An experimental apparatus was designed and constructed to study the fundamental behavior of single- and two-phase flow in inclined rod arrays. The apparatus consists of: four test sections of a single rod array geometry at various inclinations to the average flow direction; a test duct to house the individual test sections; an atmospheric air-water flow loop; and flow instrumentation.

4.1 Design Base

Two basic categories of experiments are generally performed: prototype experiments, where a scaled version of a particular component design is used to study the overall design performance; and separate effects experiments, where an experiment is designed to amplify one particular flow phenomena for detailed understanding and modeling. Both types of experiments are needed. Prototype experiments are used extensively to confirm the aggregate effects predicted by combined individual models developed from separate effects experiments.

In this research we are interested in modeling a specific phenomena, influence of flow to rod array orientation. Therefore the experiment described below is a design structured to amplify the effect of rod array inclination on fluid flow.

4.2 Test Sections

Four test sections of identical rod array geometry were designed

with each differing only in the direction of the array axis with respect to the test section housing. The four array/housing inclinations are zero degrees (parallel flow), 30, 45, and 90 degrees (crossflow). A square array arrangement was chosen to allow visual observation and instrument probe penetration through the rod array. The test loop maximum flow rates and desired maximum velocities (Sec. 4.4) constrained the test section flow area to less than 0.50 inch^2 (3.2 cm^2). A trade-off between the desire for a large test array--small rod diameter and pitch--and large gap spacing for visual observation and instrumentation--large rod diameter and pitch--resulted in a chosen rod diameter of 0.25 inch (0.318 cm) and pitch to diameter ratio of 1.5.

Each inclined rod array is set in a rectangular housing 15 pitches wide and 3 pitches deep: 5.625 inch (14.3 cm) in the direction of rod inclination and 1.125 inch (2.36 cm) perpendicular to the axis of inclination. Half-round rods were placed on the housing walls to minimize the presence of a finite depth. (The smallest perturbation from an array of infinite extent results when the solid boundaries are located through the rod centers.) Half-round rods on the walls and a gap required in the center for instrumentation, limited the array depth to only odd numbers of pitches. One pitch would create too strong a wall effect. Five pitches with the total flow area constraint of 0.50 inch^2 would restrict the width to only twice the depth. Hence the test housing was designed 3 pitches deep allowing for a width five times the depth (15 pitches).

A cross-sectional view of the parallel test section is shown in Fig. 4.1. The wide side walls and imbedded rods are both made of plexiglass to allow visual observation from the side and keep the construction of half-round rods simple. The center rods are stainless steel for structural rigidity not obtainable with plexiglass. The center rods are supported by stainless steel pins in the plexiglass sides and holes drilled in the short sides of the housing. The housing short sides are made of brass because it is more rigid than plexiglass, less corrosive than aluminum, and easier to machine than stainless steel.

The four test sections are all 3 feet long (0.91 m) which corresponds to approximately 80 equivalent diameters. This long length was chosen to ensure ample distance for flow development in both single- and two-phase flow. At the top and bottom of the 30 and 45 degree test sections partial rods are inserted to retain identical, well-defined boundary conditions for all test sections (a very helpful feature when making simulations with a computer code). Views of the 30 degree test section are shown partially assembled in Plate 4.1 (c) and (d). End views of the other three test sections are shown in Plate 4.2 (a). More detailed blue prints of each test section are given in Appendix B.

The test section basic dimensions are summarized in Table 4.1.

4.3 Test Duct

A single test duct was constructed to mount the individual test sections in the test loop. This method eliminated the need for each test section to be watertight. A cross-sectional view of the test duct is

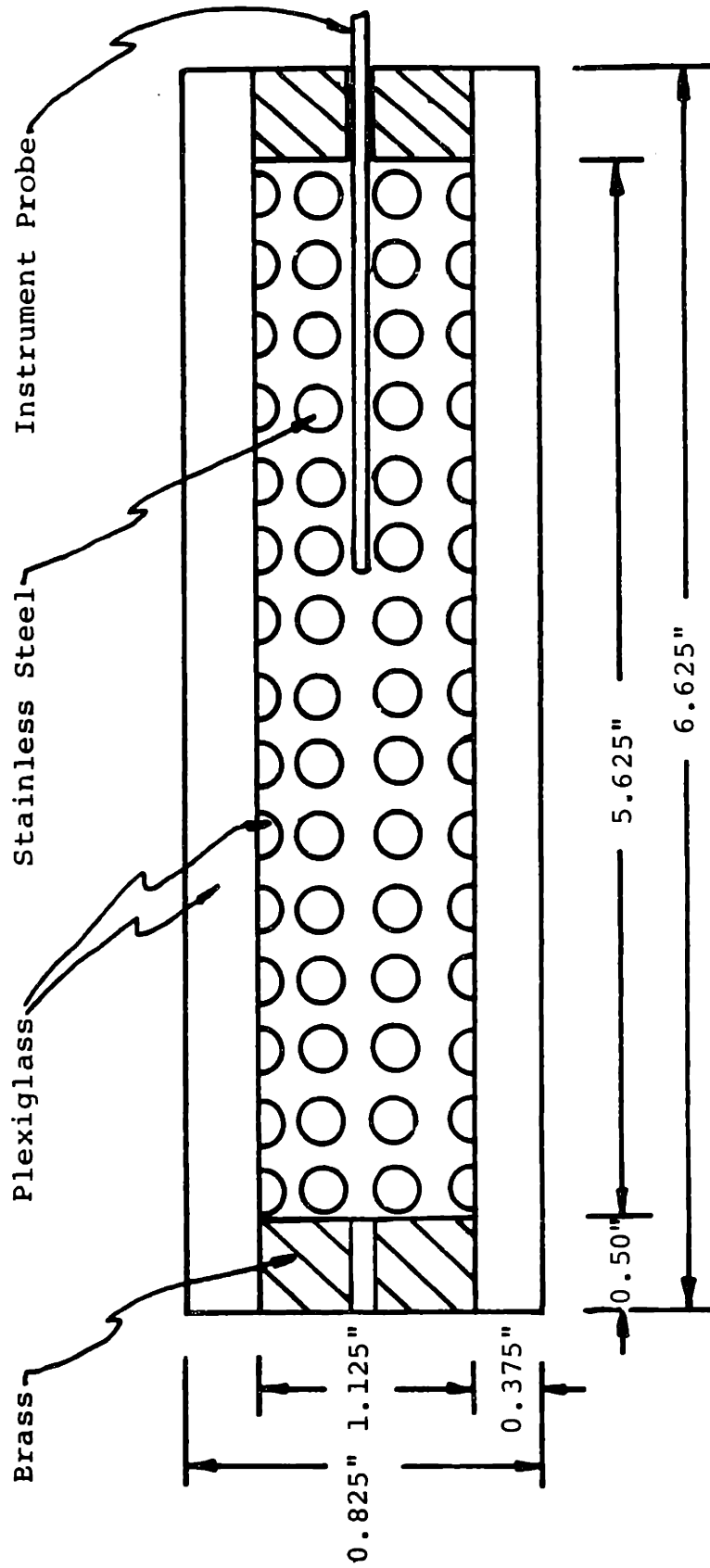
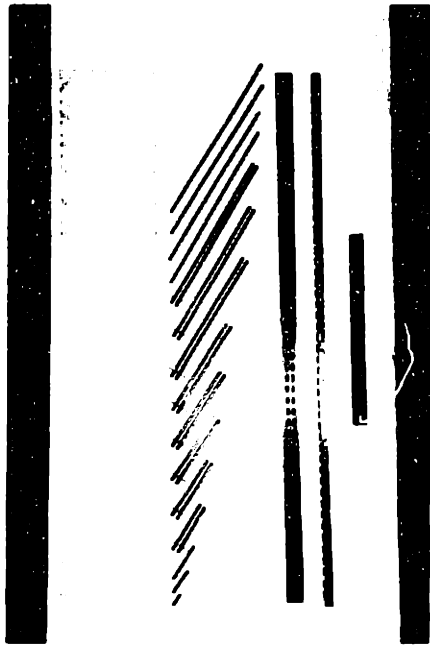
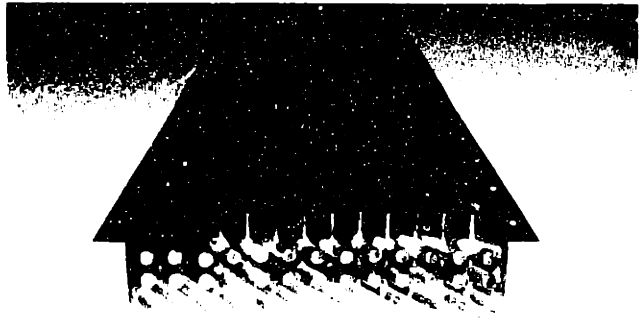


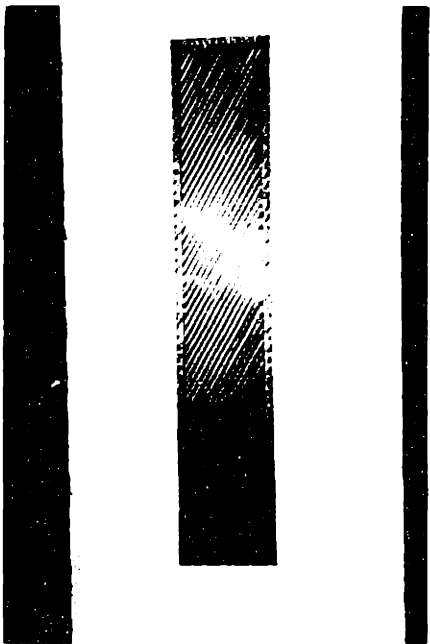
Figure 4.1 Parallel test section cross section.



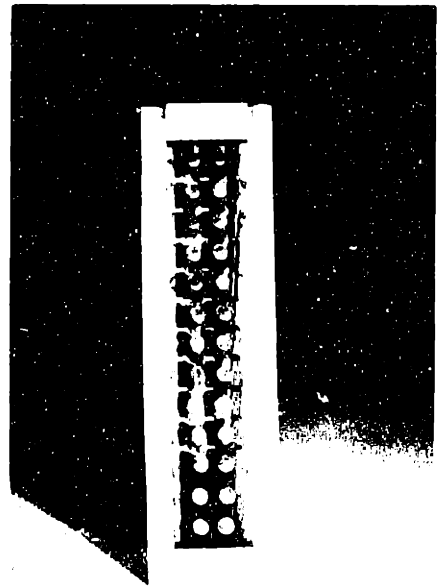
(A)



(B)

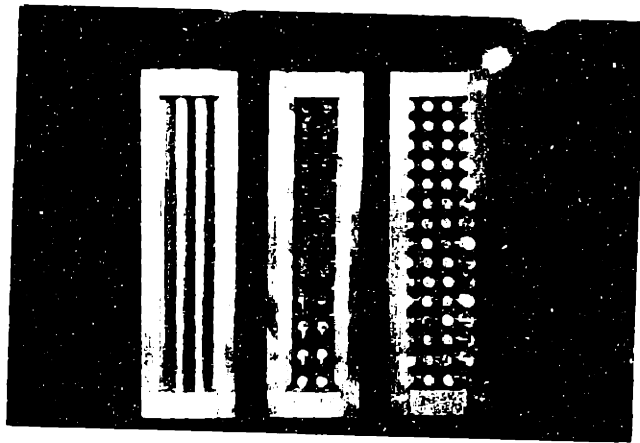


(C)

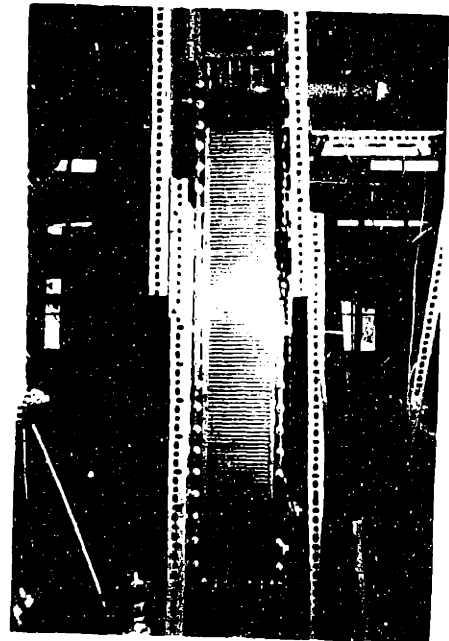


(D)

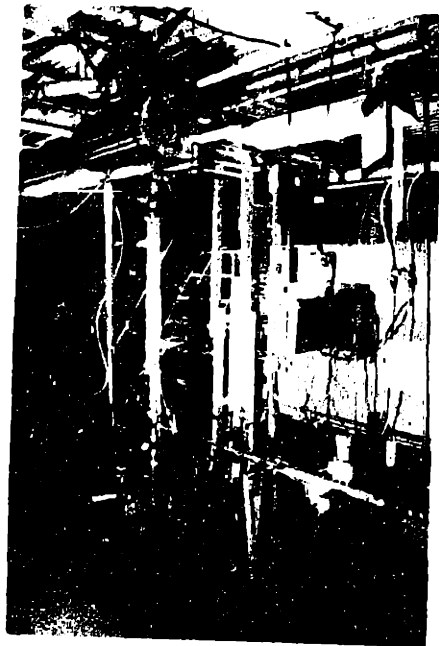
PLATE 4.1 30 DEGREE TEST SECTION (A) PARTS, (B) HALF ASSEMBLED, (C) SIDE VIEW, (D) END VIEW.



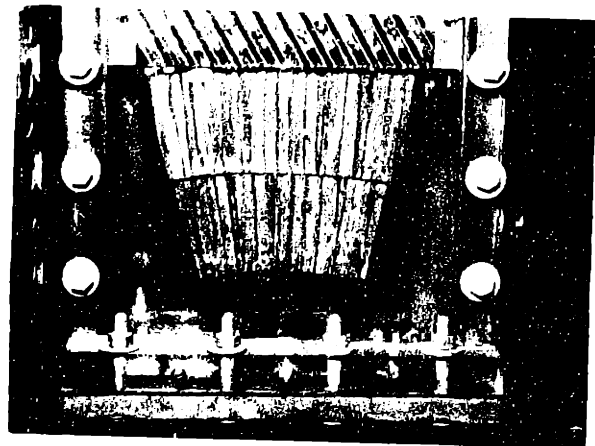
(A)



(B)



(C)



(D)

PLATE 4.2 (A) PARALLEL, 30 DEGREE, AND CROSSFLOW TEST SECTIONS--END VIEW, (B) MOUNTED TEST DUCT WITH CROSSFLOW TEST SECTION, (C) FLOW LOOP, (D) FLOW DIFFUSER/STRAIGHTENER.

TABLE 4.1

Test Section Geometry

Number of Test Sections	4	--
Rod Array Inclination, θ	0, 30, 45, 90	degrees
Length, L_x	36 (91.4)	in (cm)
Inside Width, $L_y = 15 P$	5.625 (14.3)	in (cm)
Inside Depth, $L_z = 3 P$	1.125 (2.86)	in (cm)
Rod Pitch, P	0.375 (0.953)	in (cm)
Rod Diameter, d	0.250 (0.635)	in (cm)
Pitch to Diameter Ratio, P/d	1.5	--
Gap, $P-d$	0.125 (0.318)	in (cm)
Length to Hydraulic Diameter, L_x/D_v	-80	--
Rod Arrangement, RA	Square	--
Fluid Flow Area, \bar{A}_f	4.12 (26.6)	in ² (cm ²)
Hydraulic Diameter, D_v (infinite array)	0.466 (1.18)	in (cm)
Hydraulic Diameter, D_v (parallel test section)	0.399 (1.01)	in (cm)
Hydraulic Diameter, D_v (30°, 45°, and 90° test sections)	0.406 (1.03)	in (cm)

shown in Fig. 4.2. The short sides are made of brass. Round rubber gaskets set in grooves in the brass sides maintain a watertight seal. The wide sides are plexiglass to allow viewing through the entire test section and duct assembly.

The duct is 4.0 ft (1.22 m) long, one foot longer than the test sections. The test sections, supported by six keyway pins are mounted in the center of the duct to allow for a 6.0 inch (15.2 cm) inlet and outlet plenum. A plexiglass diffuser containing an aluminum honeycomb flow straightener is inserted in the inlet plenum to provide a smooth transition into the test section. Brass end caps couple the test duct housing to the flow loop. Figure 4.3 shows a cross-sectional view of the test section/duct/diffuser assembly. The diffuser and mounted test duct (with the crossflow test section) are also shown in Plate 2(b) and (d). The assembly is always mounted vertically with flow introduced from the bottom.

Also shown in Fig. 4.3 are twelve penetrations for instrumentation, six located on each side of the test duct. Ten of these penetrations coincide with the top half of the test sections, hence corresponding slots are also located on each test section. The penetrations allow flow measurements along the center of each test section (See Fig. 4.1) at various elevations. Because of the symmetry of both the duct and test sections, measurements in the bottom half may be obtained simply by inverting the entire housing and relocating the diffuser at the bottom.

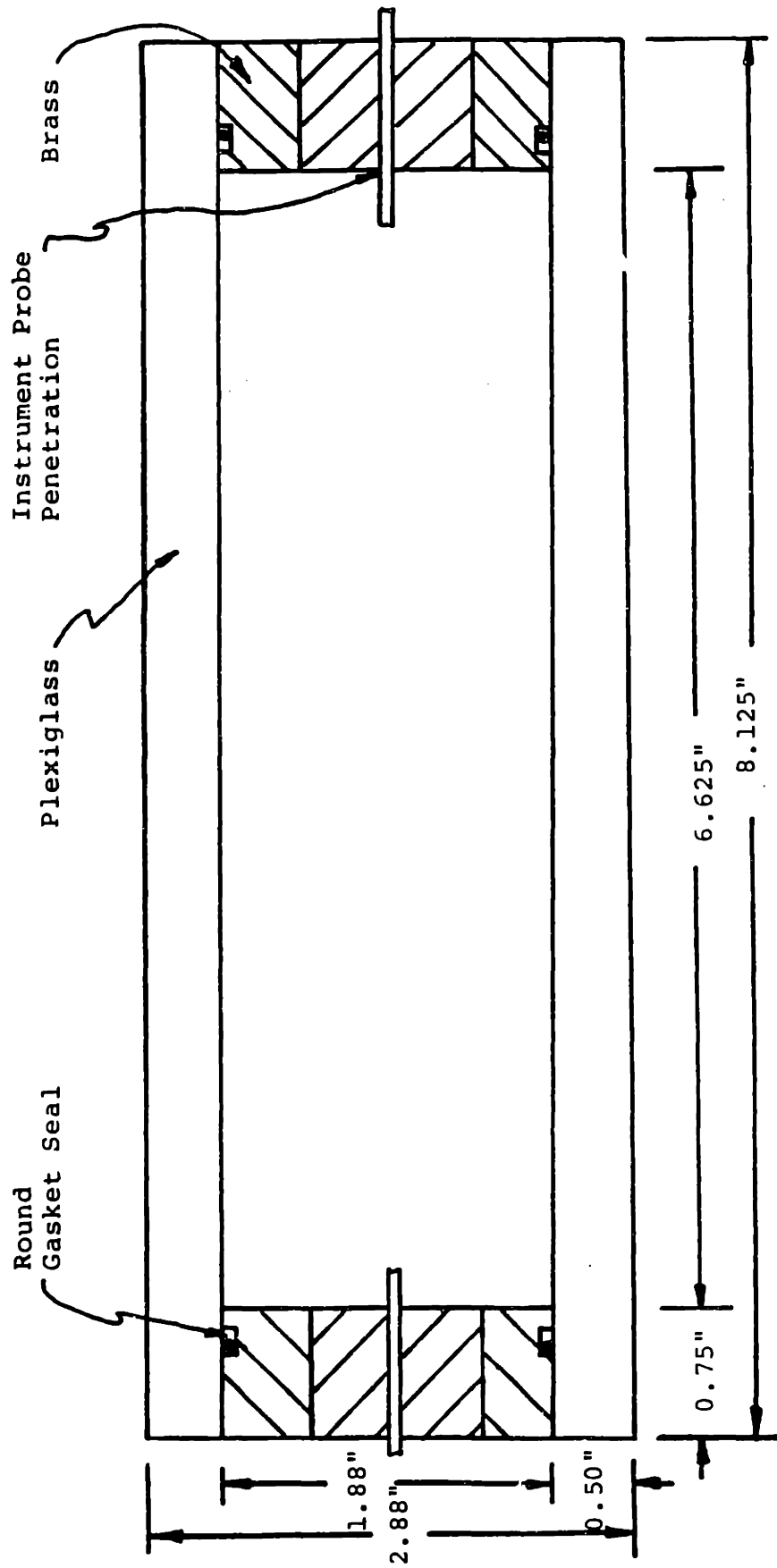


Figure 4.2 Test duct cross section.

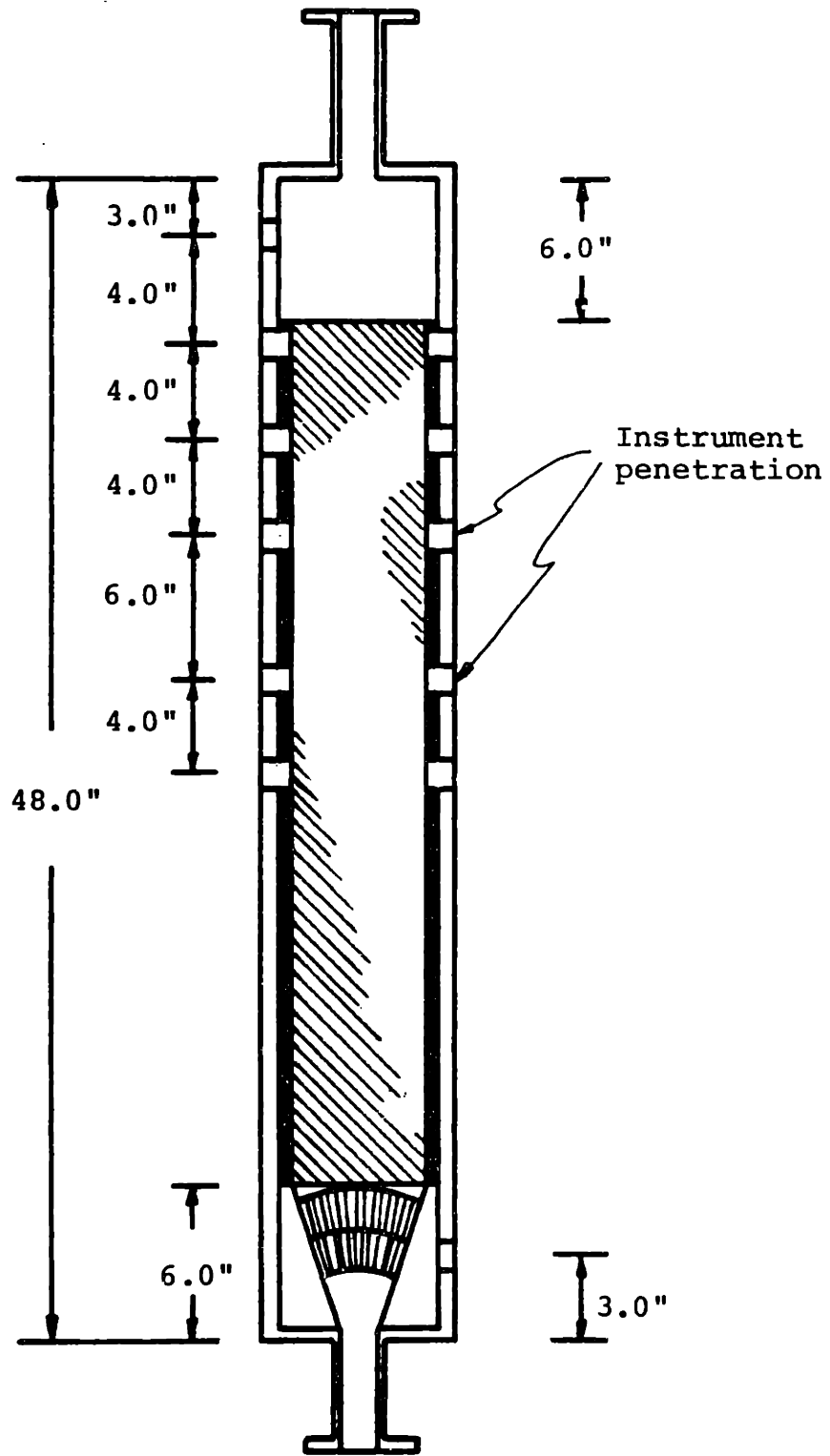


Figure 4.3 Cross-sectional view of test section/test duct/diffuser assembly.

Table 4.2 summarizes the test duct geometry. Detailed drawings of the test duct and diffuser are given in Appendix B.

4.4 Flow Loop

The test assembly is mounted vertically in an atmospheric air-water loop. Water and air are used for the liquid and gas phases because they are different components eliminating phase change, and they make handling and instrumenting simple and inexpensive. Air-water is also a reasonable model for most commercial two-phase flows (i.e., steam-water).

The system, shown schematically in Fig. 4.4, consists of a closed water loop circulated by a 1.5 horsepower Bell and Gossett pump. Air from the laboratory compressor is metered through either a high or low flow rate system and introduced into the water loop through a mixer just upstream of the test assembly. The mixer is a capped off piece of copper pipe set in the center of the water pipe with an array of 0.0625 inch (0.159 cm) holes drilled around the pipe circumference. The air after passing through the test assembly, enters a separation tank and then is exhausted to the ambient. The tank is normally maintained at atmospheric pressure, but can be increased by throttling the exhausting air. In practice pressures higher than two atmospheres absolute produced leaks in the separation tank welds, so the loop was generally operated at atmospheric pressure. A short bypass loop is provided to permit low flow rates without damaging the pump. A picture of the flow loop is shown in Plate 4.2(c).

TABLE 4.2

Test Duct Geometry

Length	48.0	(12.9)	in (cm)
Inside Width	6.625	(16.8)	in (cm)
Inside Depth	1.88	(4.78)	in (cm)
Entrance Plenum Length	6.0	(15.2)	in (cm)
Exit Plenum Length	6.0	(15.2)	in (cm)
Cross-Sectional Area	12.46	(31.6)	in ² (cm ²)
Hydraulic Diameter	2.93	(7.44)	in (cm)

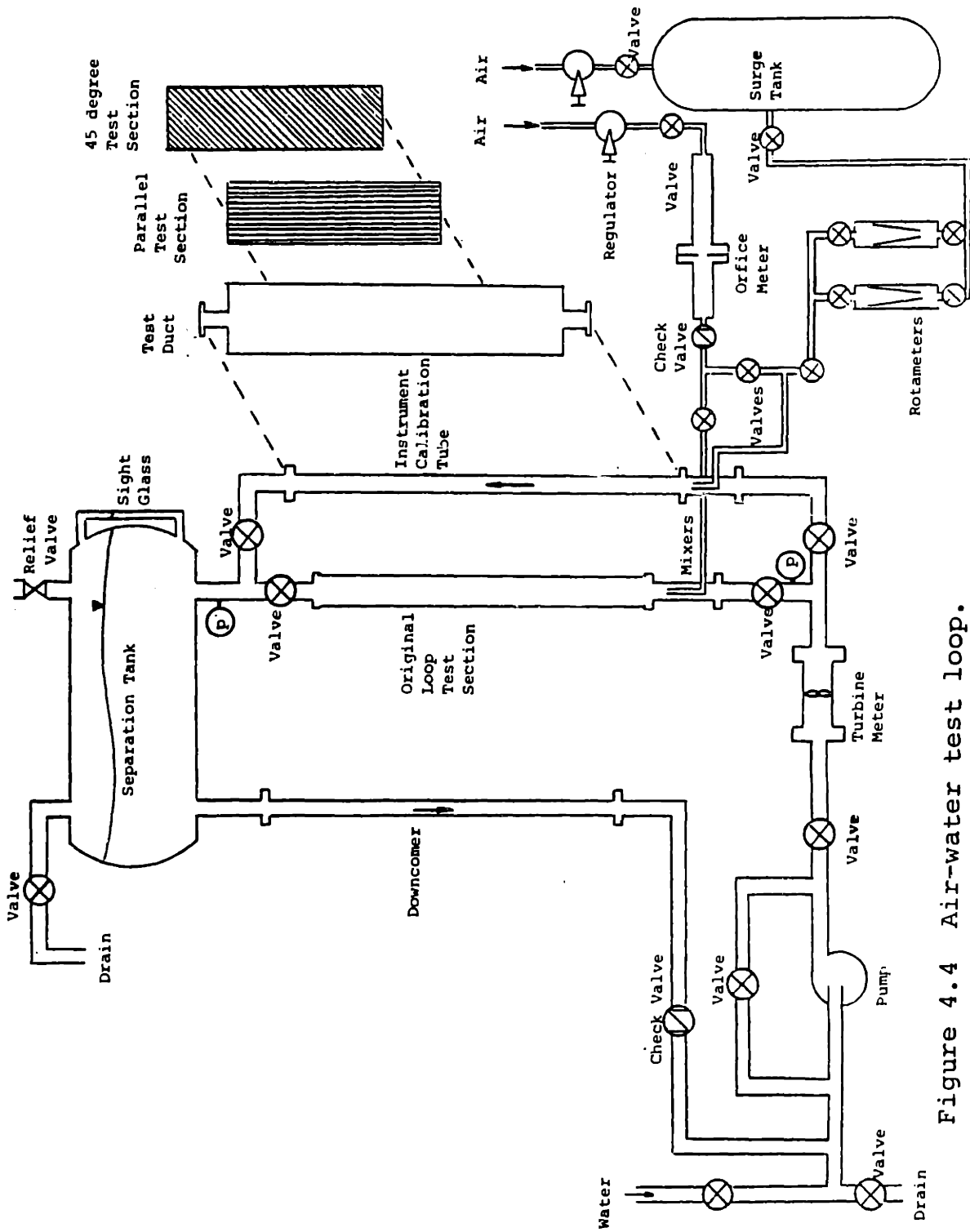


Figure 4.4 Air-water test loop.

The loop operating conditions are summarized in Table 4.3. The desired maximum liquid and gas velocities of 6.0 ft/sec (1.83 m/sec) and 60 ft/sec (18.3 m/sec), respectively, set the test section cross-sectional flow area of 4.12 inch² (26.6 cm²). The maximum liquid velocity was chosen to enable normal commercial component flow conditions to be reached. The maximum gas velocity was chosen to allow simulation of annular flow. The flow metering systems along with the local measuring instrumentation are described in the next section.

4.5 Instrumentation

Good reviews of single- and two-phase fluid measuring techniques are given in References [B.9, L.1, and H.2]. In this experiment the liquid flow rate was measured with a turbine flow meter; and the gas flow rate was measured at high flow rates, with a sharp-edged orifice, and at lower flow rates, with two rotameters. The loop pressure and temperature were monitored with Bourdon gauges and a thermometer. Local velocity and differential pressure measurements within the test sections, were made with pitot-static tubes and an electric manometer system. Lastly, two-phase flow was studied with photographs, a single-bubble release system, and transit-time measurements.

4.5.1 Turbine Meter

A Fischer-Porter industrial turbine flow meter was used to measure the loop liquid flow rate. A turbine flow meter consists of a small propeller encased in a pipe housing and inserted in the loop. The meter requires 15 straight pipe diameters upstream and 4 diameters downstream.

TABLE 4.3

Test Loop Conditions

Water Flow Rate, Q_l	0 - 0.17 (0 - 0.0048)	ft ³ /sec (m ³ /sec)
Water Superficial Velocity, Q_l / \bar{A}_f	0 - 6.0 (0 - 1.83)	ft/sec (m/sec)
Air Flow Rate, Q_g	0 - 1.72 (0 - 0.0486)	ft ³ /sec (m ³ /sec)
Air Superficial Velocity, Q_g / \bar{A}_f	0 - 60 (0 - 18.3)	ft/sec (m/sec)
Temperature, T	60 - 100 (15 - 38)	°F (°C)
Pressure at Separation Tank, p	14.7 - 30 (0.1 - 0.2)	psia (MPa)

An oscillator and magnetic pick up measures the propeller's rotational frequency. This frequency is directly proportional to the liquid flow rate through the meter. The calibrated flow rate is

$$Q_l(\text{gpm}) = 36.08 (V - 0.996) \quad (4.1)$$

where V is the D.C. output voltage. The meter was calibrated from 4.0 to 144 gpm. Details of the calibration are given in Appendix C.1.

4.5.2 Orifice Meter

An orifice meter and two rotameters are used to span the five decade range in gas flow rate required to encompass all two-phase flow regimes from bubbly to annular flow (See Fig. 4.5).

A orifice meter measures the differential pressure drop across a sharp-edged orifice placed in the flow stream. The gas flow rate is proportional to the square root of the orifice pressure drop. Curves for the gas mass flow rate as a function of the upstream pressure and orifice diameter are given in Fig. 4.5. These were constructed from calibration curves for ASME flange-tap sharp-edged orifices and checked with volume integral measurements (See Appendix C.2).

4.5.3 Rotameters

Two Fischer-Porter rotameters were used to measure low gas flow rates. A rotameter is simply a vertical graduated glass tube of increasing cross-sectional area with a float of specified mass and size inside. The float rises to a height in the tube proportional to the flow rate passing through the tube. The resulting calibration curves for both flow meters are:

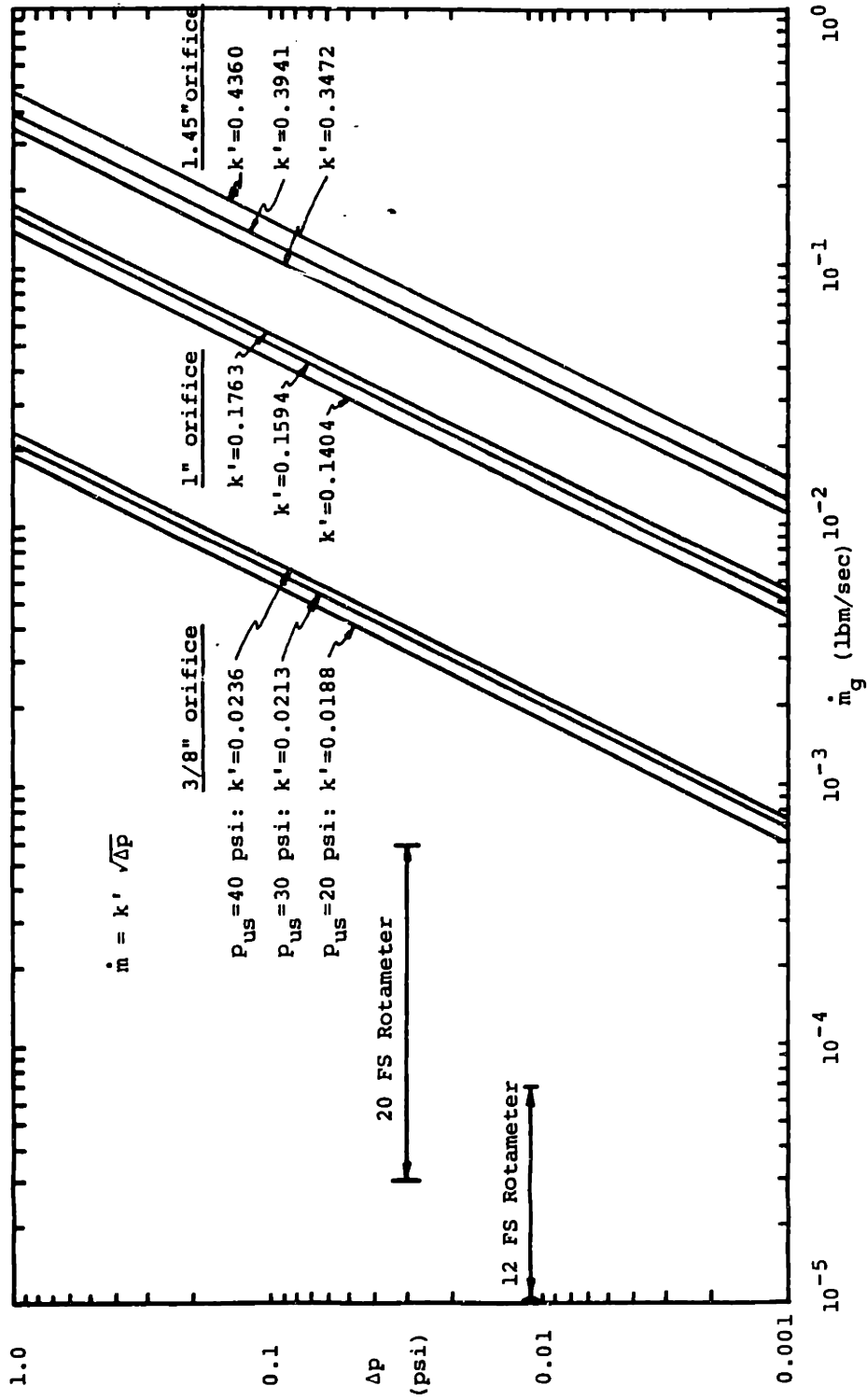


Figure 4.5 Air orifice meter calibration curves.

For the 12 full scale (FS) rotameter

$$\dot{m} \text{ (lbm/sec)} = 4.57 \times 10^{-6} \text{ RD} \sqrt{\frac{p_{us} + 14.7}{14.7}} - 1.50 \times 10^{-5} \quad (4.2)$$

where $2.0 \times 10^{-6} \leq \dot{m} \leq 6.9 \times 10^{-5}$; and for the 20 FS rotameter

$$\dot{m} \text{ (lbm/sec)} = 2.36 \times 10^{-5} \text{ RD} \sqrt{\frac{p_{us} + 14.7}{14.7}} - 1.08 \times 10^{-4} \quad (4.3)$$

where $3.0 \times 10^{-5} \leq \dot{m} \leq 5.9 \times 10^{-4}$. In both equations RD is the scale reading, and p_{us} is the upstream gauge pressure (regulator pressure) in psi. (See Appendix C.3 for more details.)

The air flow through all the air meters are controlled by downstream valves so that the pressure through the meter always equals the regulator pressure.

4.5.4 Loop Pressure and Temperature

The loop pressure is monitored with two Bourdon gauges, one located just before the separation tank inlet and the other located between the turbine meter and mixer (See Fig. 4.4). The loop temperature is measured in the outlet plenum of the test duct with a thermometer. The thermometer can be seen in the top of Plate 4.2(b).

4.5.5 Pitot-Static Tube

Local velocity and pressure measurements are made with a pitot-static tube and electric manometer system. A pitot-static tube is an L-shaped probe constructed of two concentric tubes pointing in the direction of the flow. Holes at the probe tip and circumferentially around the outer tube measure respectively the stagnation and static pressures. Differential pressure drops are measured between static taps

of two pitot-static tubes (See Fig. 4.6).

The local flow velocity is determined from the dynamic pressure of a single pitot-static tube. The dynamic pressure is the difference between the stagnation and static pressure

$$\Delta p_{\text{dyn}} = \frac{1}{C^2} \frac{\rho_{\ell} v_{\ell}^2}{2} \quad (4.4)$$

or

$$v_{\ell} = C \sqrt{\frac{2\Delta p_{\text{dyn}}}{\rho_{\ell}}} \quad (4.5)$$

The calibration constant C corrects for nonideal (nonisentropic) slowing down of the fluid at the probe tip. As described in Appendix C.4 the pitot-static tubes were calibrated giving

$$v_{\ell} \text{ (ft/sec)} = 11.6 \sqrt{\Delta p_{\text{dyn}} \text{ (psi)}} \quad (4.6)$$

which corresponds to $C = 0.95$. One pitot-static tube inserted in the parallel test section is shown in Plate 4.3(a).

Differential pressure was measured with an electric manometer and time-averaging voltmeter shown in Plate 4.3(b) and schematically in Fig. 4.5. The system consist of a Datametric multi-range differential pressure transducer which measures full scale pressures from 0.002 to 20.0 psi (0.1 to 1000 Torr). The transducer is connected to a silicon oil loop which is linked to the measuring environment by two diaphragms. Water was used as the medium in the piping (air was also tried, but produced slow response times and required constant purging as water entered from the test section). With water in both the test section and piping, the measured differential pressure excludes any gravitation head

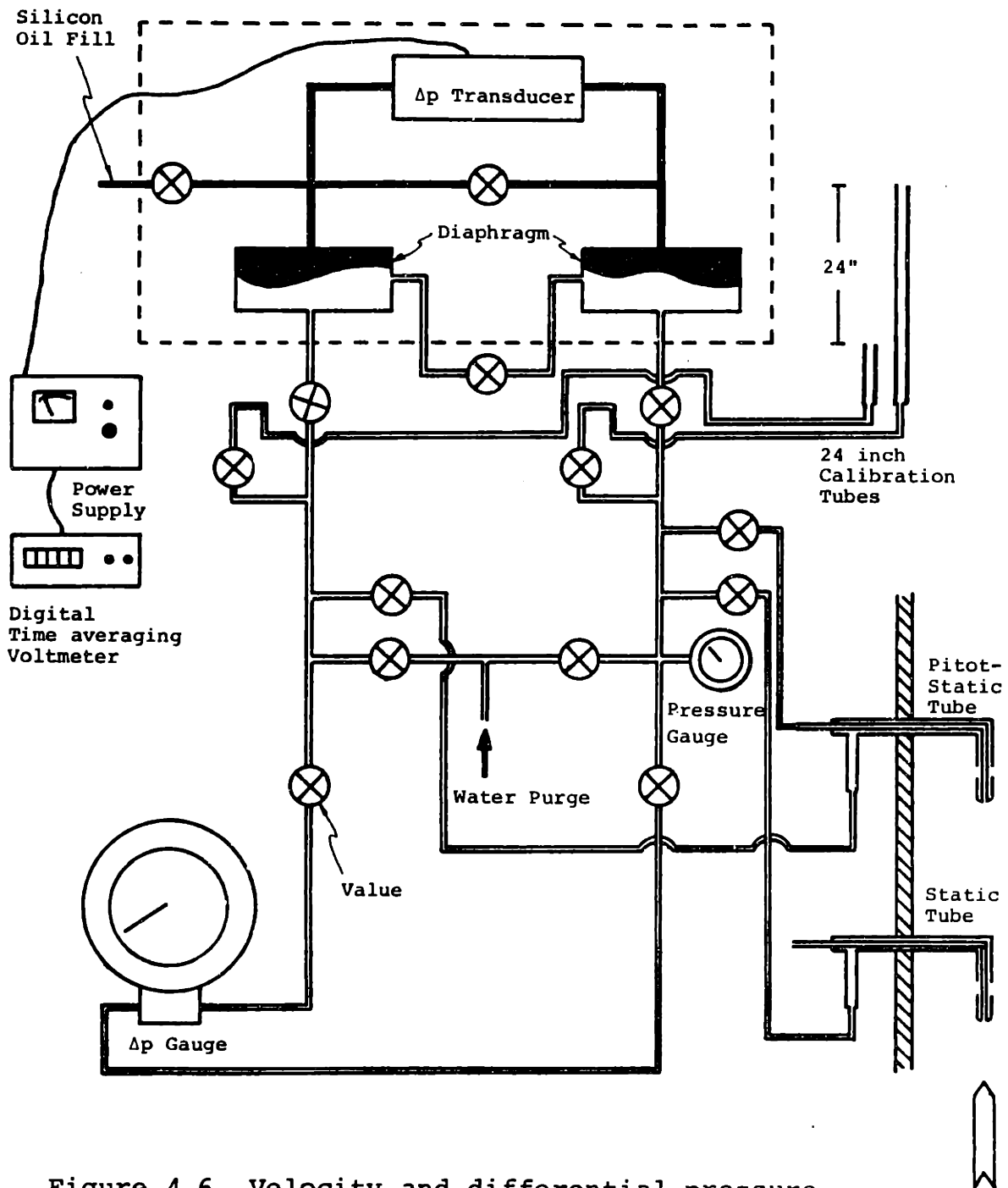
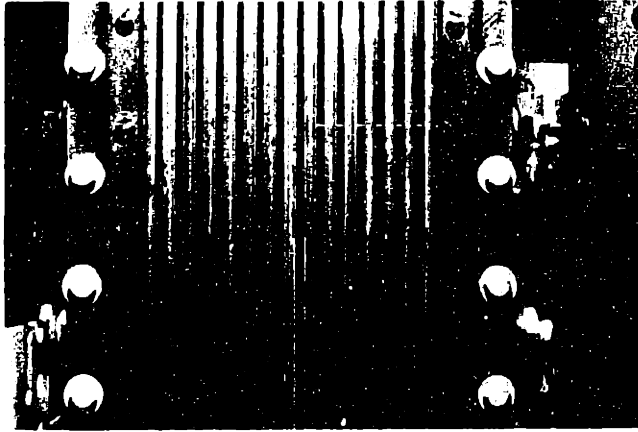
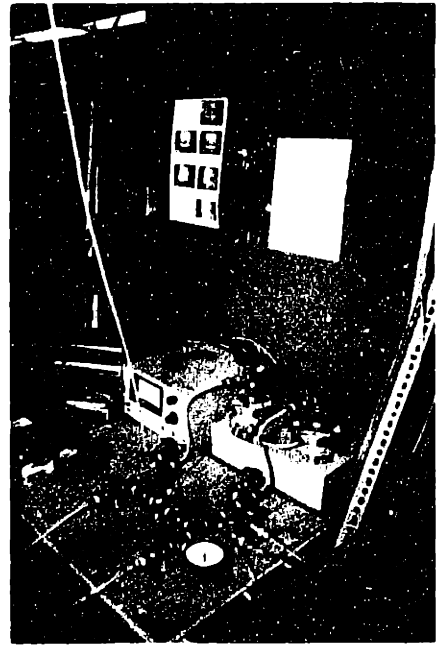


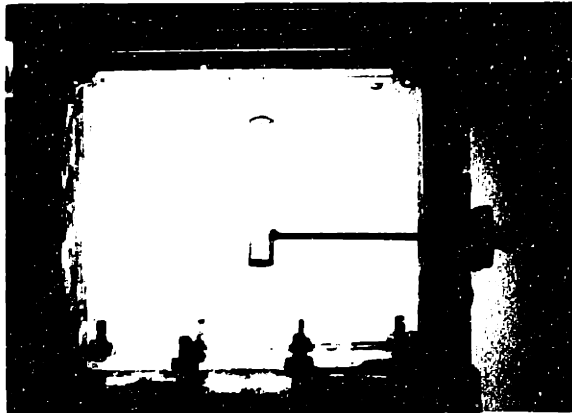
Figure 4.6 Velocity and differential pressure measurement system.



(A)



(B)



(C)

PLATE 4.3 (A) DIFFERENTIAL PRESSURE MEASURING SYSTEM, (B) PITOT-STATIC TUBE AND SMALL BUBBLE GENERATING ORFICES IN PARALLEL TEST SECTION, (C) LARGE BUBBLE RELEASE CUP.

and hence is independent of the probe locations in the test assembly. Thus the recorded differential pressure is only caused by friction, form, and acceleration pressure drops, not elevation. Instantaneous pressure readings were averaged over 10 to 100 seconds with a TSI time-averaging digital voltmeter. The averaging interval was governed by the fluctuations in the reading.

The electric manometer system was convenient because the single unit could cover a large range of differential pressures. One quirk of the system is it is very sensitive to ambient temperature changes. It has to be warmed up for several hours before using and has a significant drift from the zero setting when operated at the lower two scales. Best results were obtained when the system was left on continuously and lowest differential pressure data were taken first, right after zeroing the meter.

4.5.6 Photography

Two-phase flow regimes were studied and documented with photographs. A 35 mm camera, tripod, tungsten lights, and back drop were used. Several lighting arrangements were employed to capture specific regime characteristics and minimize light scattering of the plexiglass rods and windows (See Fig. 4.7).

A front reflecting technique was used for still photographs of flow regimes both within the test sections and in the exit plenum. A back shadow method was used to photograph the shape of single bubbles. Last a back reflecting technique was used to obtain multiple bubble trajectories

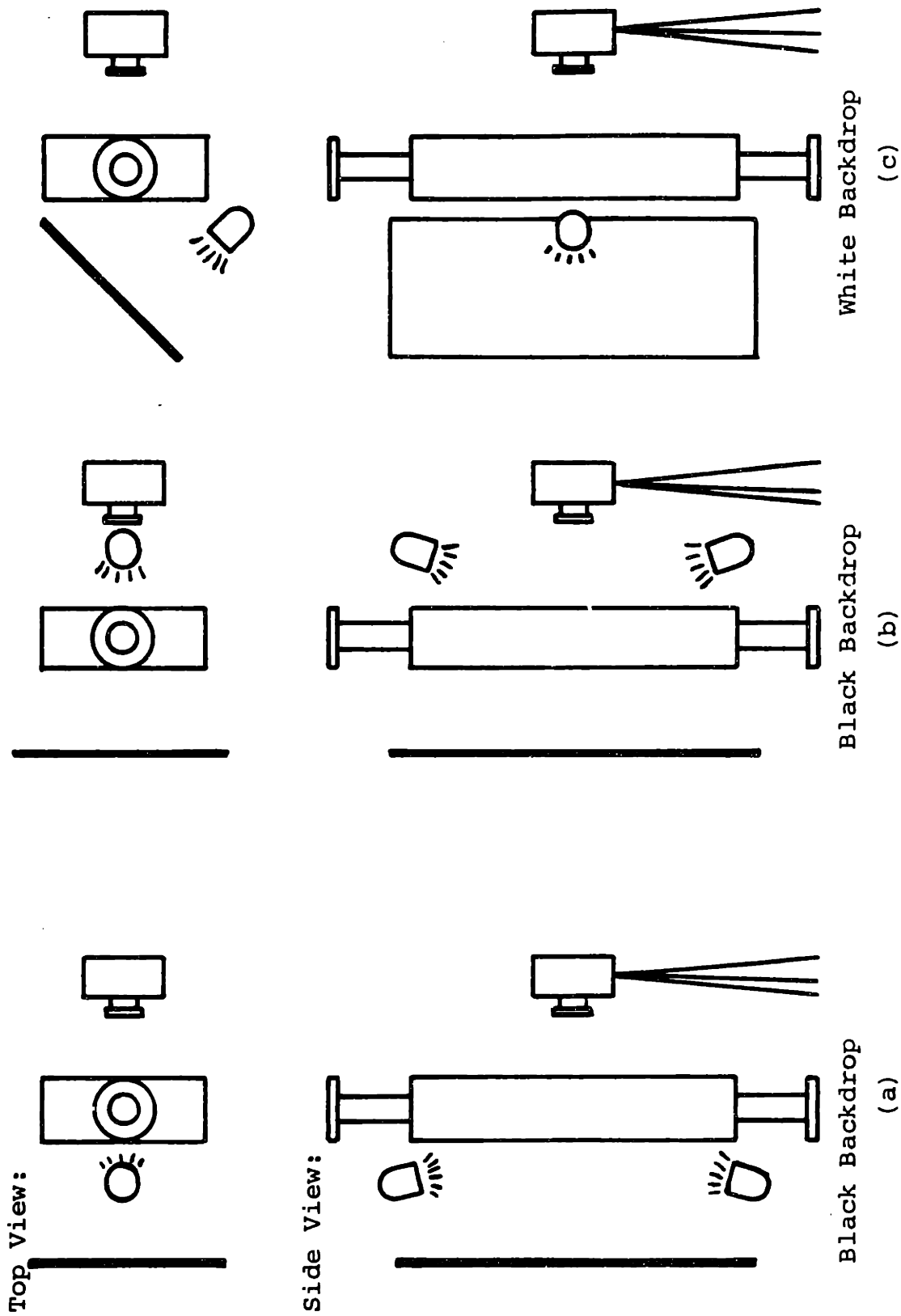


Figure 4.7 Photographic lighting arrangements (a) back reflecting, (b) front reflecting, (c) back shadow.

by time exposing the illuminating bubbles. Long exposure times are desired to obtain long bubble track lengths. However the maximum exposure time possible is limited by the contrast between the bright bubbles and dark background. If the time is too long, then the tracks become washed out by the background light. Best results were obtained for short exposures of many bubbles producing a lot of short tracks showing the average trajectories of the bubbles. Trajectories of a single bubble were not obtainable because the required exposure times were too long. Photographs employing the above lighting techniques are shown and analyzed in Chapter 6.

To obtain single bubble trajectory photographs a fourth lighting arrangement was explored. This lighting arrangement shown in Fig. 4.8, increased the bubble/background contrast, but limited the area of illumination to only the first 6 inches of the test section. Because the illuminated area was small and only in the developing flow region photographic single bubble trajectory data were not obtained. With a high intensity coherent light source this technique could be perfected.

4.5.7 Single Bubble Measurements

To study the dynamics of bubbles in inclined rod arrays two single-bubble release systems were developed.

At very low gas flow rates the bubble size that forms at an orifice (tube) is dependent only on the tube diameter [C.3]. Thus a spectrum of bubble diameters can be generated by using different diameter tubes. The bubble equivalent volumetric diameter for a given tube was determined by

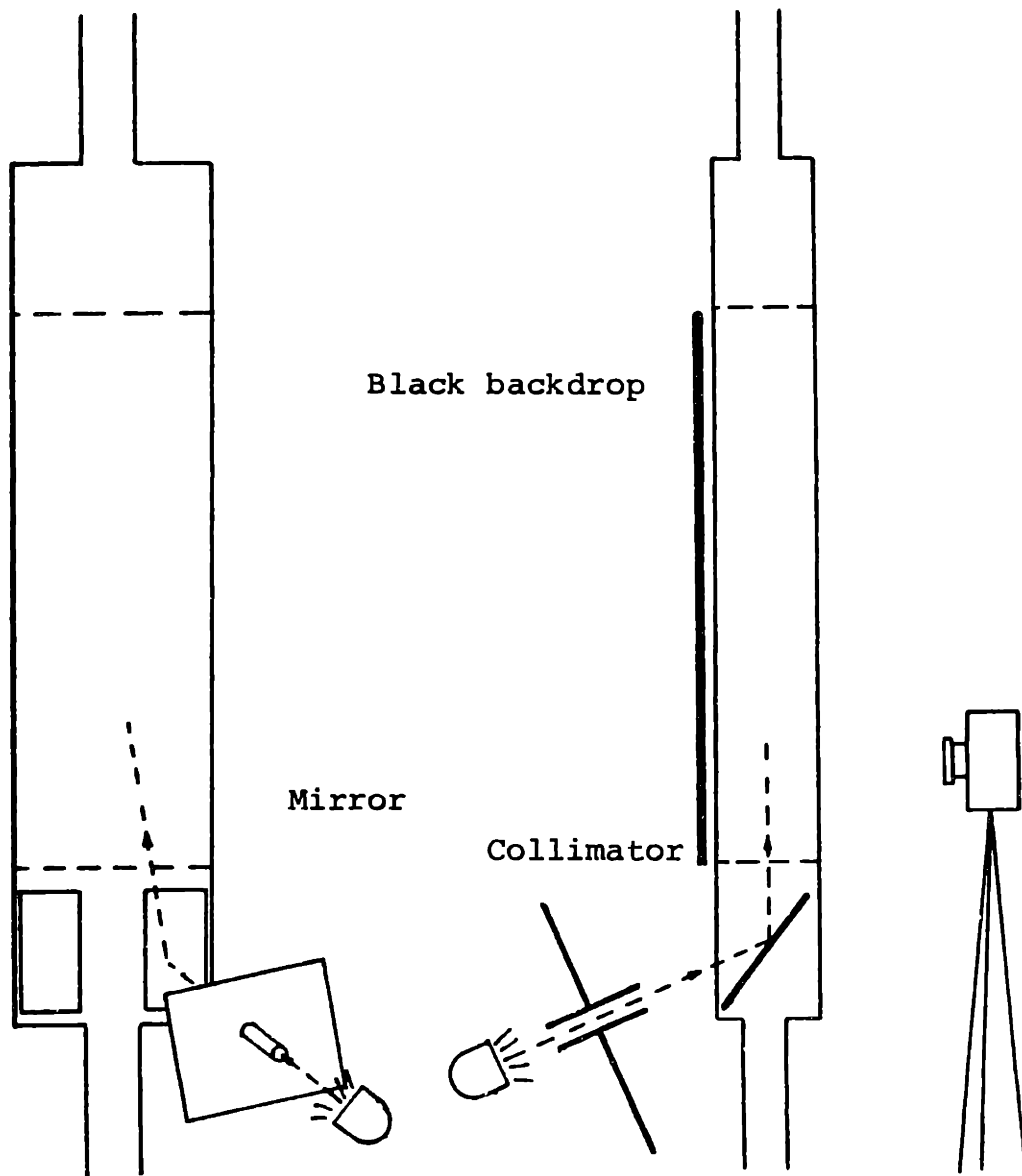


Figure 4.8 Collimated perpendicular lighting arrangement.

scaled photographs and by counting the number of bubbles required to fill a known volume. Table 4.4 lists the tubes and calibrated diameters. Plate 4.3(b) shows two tubes inserted in the parallel test section.

Larger bubbles were created by releasing a known volume of air in the lower plenum from a rotatable cup. A slug of air is placed in a water filled horizontal glass tube. The air volume is determined from the slug length and glass tube inside diameter (0.090 inch, 0.229 cm). Next the air is transferred through a hollow support tube to a small inverted cup in the center of the lower plenum. Finally the bubble is released by quickly uprighting the cup (See Plate 4.3(c)). Single bubble velocities were determined by transit-time measurements. The time of flight of a bubble over a known path length was determined with a stop watch, giving

$$v_g = \frac{\ell}{\Delta t} \quad (4.7)$$

The actual path length ℓ , was determined by visually marking the starting and stopping locations within the test section. Larger distances, from 2 to 3 feet, were used to minimize the error of starting and stopping time.

Single bubble trajectories were determined by measuring the vertical (x) and horizontal (y) components of path length ℓ . Then the bubble trajectory ϕ_b , is simply

$$\phi_b = \text{Tan}^{-1} \frac{\ell_y}{\ell_x} \quad (4.8)$$

where $\phi_b = 0$ for a vertical rising bubble.

The two-phase flow regime and single bubble data are presented in Chapter 6.

TABLE 4.4

Average Bubble Diameter Generated at Orifice

Tube	Outside Diameter (inch)	Inside Diameter (inch)	Equivalent Volumetric Bubble Diameter (inch) ± 0.01
A	0.010	0.005	0.03
B	0.018	0.0095	0.06
C	0.022	0.011	0.08
D	0.35	0.023	0.11
E	0.065	0.045	0.12
F	0.072	0.054	0.12

CHAPTER 5

SINGLE-PHASE FLOW MODELING

The principal constitutive relation for a single-phase, porous medium flow is the flow resistance. Single-phase flow resistance is the average skin friction, form drag, and form lift forces on a fluid flowing through a porous, nondeformable solid medium; mathematically

$$\langle \underline{R} \rangle = \frac{\Delta}{V_f} \int_{A_{fs}} (\overline{pI} - \overline{T}) \cdot \underline{n} \, dA \quad (5.1)$$

where the first term in the integral results in the form drag and lift and the second in the skin friction. Form drag is the component force parallel to the average flow direction and lift is the perpendicular component.

The introduction of volumetric flow resistance enables the distributed fluid-solid momentum interaction, which is dependent on the flow conditions independent of geometry, to be lumped as a single force correlated to the average flow conditions for a specific geometry. Before going into explicit mathematical models for flow resistance we shall examine the fundamental flow field within a rod array.

5.1 Flow Field Description

Much insight into constitutive modeling can be gained from a full understanding of the flow field within rod arrays. We define five flow regimes comprised of laminar or turbulent flow within three

regions. In laminar flow all momentum exchange is transmitted by viscous forces; in turbulent flow fluid eddies also contribute to momentum exchange. The presence of a boundary layer and flow separation around a submerged solid allows three distinct regions to be defined: The mainstream region--comprised of the bulk fluid flowing around the submerged solid, the boundary layer region--consisting of the slower fluid which blankets the solid surface, and the drag region--which is the recirculating fluid region between the separated boundary layer and trailing edge of the solid surface. The five regimes are listed in Table 5.1. Below we shall restrict our discussion of flow patterns to the laminar through subcritical-turbulent regimes for which the patterns in rod arrays are relatively unchanged.

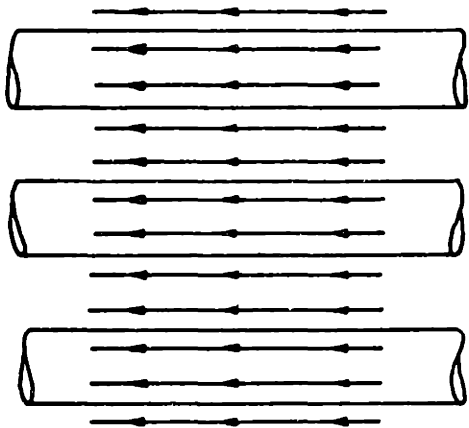
Parallel flow in rod arrays experiences no flow area change, hence no boundary layer separation or drag region, Figure 5.1(a) shows the evenly spaced, parallel streamlines for parallel flow. (A streamline is the path of a continuum fluid element which for turbulent flow may be interpreted as the average path.) In parallel flow because there is no drag region the five regimes discussed above reduce to just laminar, laminar-turbulent transition, and turbulent flow.

For flow across a cylinder (Fig. 5.1(b)) the laminar boundary layer separates at about 82 degrees from the leading edge resulting in two vortices behind the cylinder [H.1, V.2]. At high flow velocities these vortices start shedding in a periodic fashion. For an array of cylinders (rod array) a similar flow pattern exists even at higher velocities where the vortices remain attached because of a flow

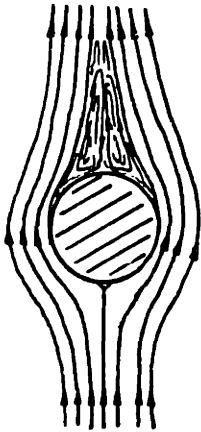
TABLE 5.1

Flow Regime Classifications

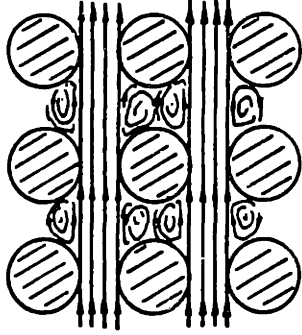
<u>Flow Regime</u>	<u>Description</u>	<u>Mainstream Region</u>	<u>Boundary Layer Region</u>	<u>Drag Region</u>
Creep	No separation, negligible inertial forces, viscous forces dominate.	Laminar	Laminar	-----
Laminar	Separations due to inertial forces creates drag region.	Laminar	Laminar	Laminar
Laminar/ Turbulent Transition	Turbulent eddies introduced into main stream.	Turbulent	Laminar	Laminar
Sub- critical Turbulent	Turbulent eddies in drag region.	Turbulent	Laminar	Turbulent
Super- critical Turbulent	Turbulence in boundary layer before separation.	Turbulent	Turbulent	Turbulent



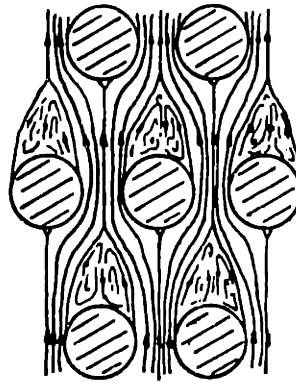
(a) Parallel flow



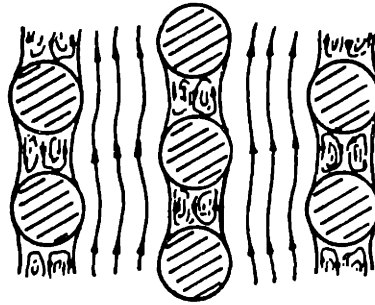
(b) Single cylinder crossflow



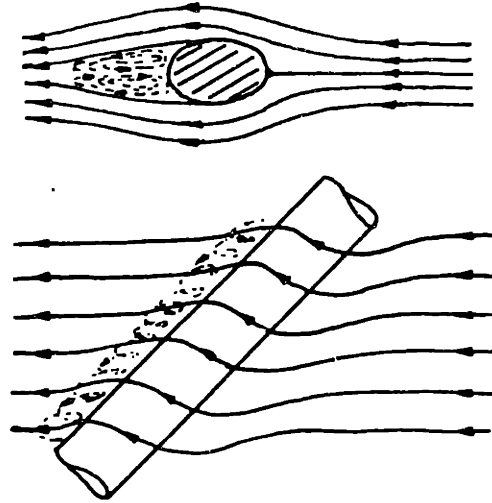
(c) In-line array crossflow



(d) Staggered array crossflow (tight transverse pitch)



(e) Staggered array crossflow (tight longitudinal pitch)



(f) Single inclined cylinder flow

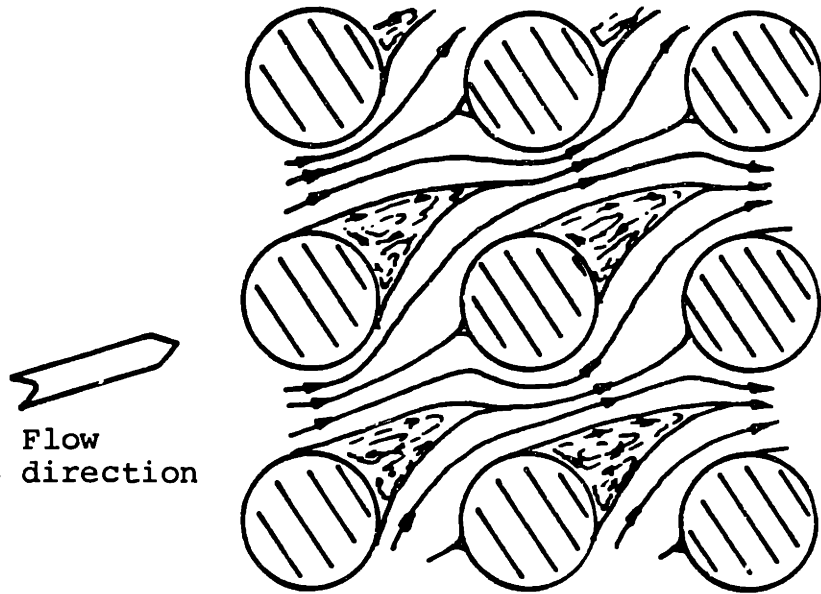
Figure 5.1 Observed rod array streamlines.

restriction downstream. Figure 5.1(c), (d), and (e) sketch the observed crossflow patterns for in-line and two limiting staggered rod arrangements [H.1, V.2, W.3]. Hoerner [H.1] found that the distance at which interference between two rods begins is about five pitch to diameters.

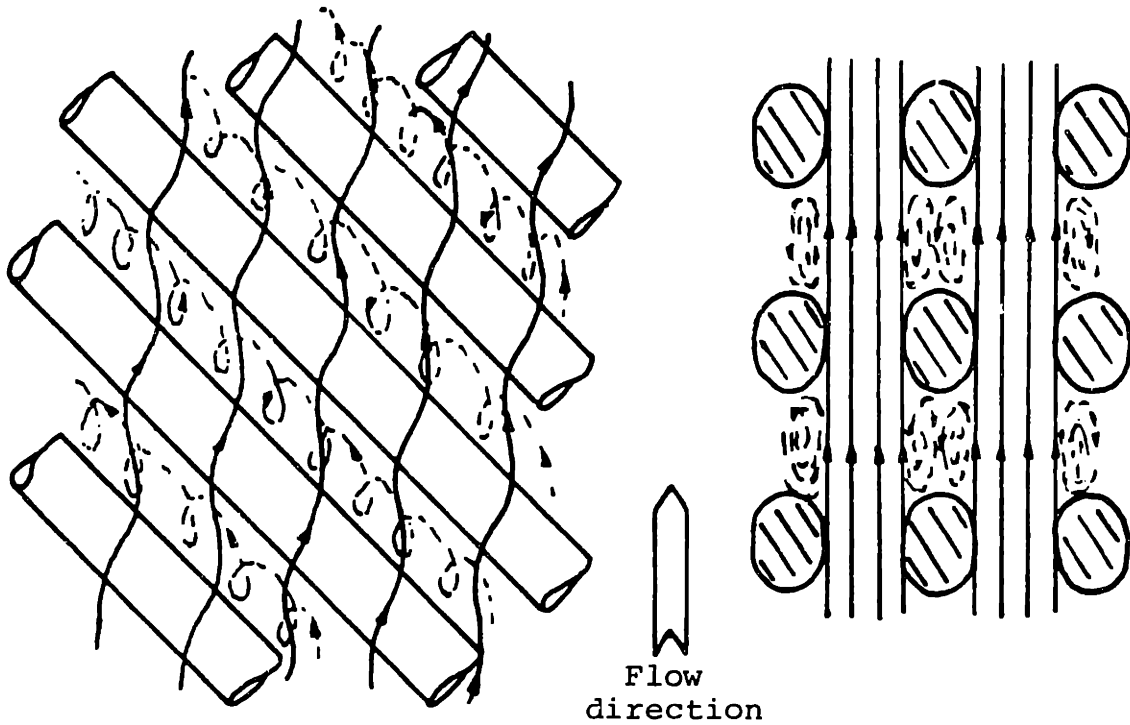
The last pertinent observation is of flow across an inclined (yaw) cylinder (Fig. 5.1(f)). As a streamline approaches an inclined rod it deflects towards the rod axis, then across the rod along the shortest path and finally resumes its original flow direction. The vortex generated behind the cylinder moves along the cylinder axis.

From the above observations we postulate two additional flow patterns of situations which have not yet been documented visually. For crossflow in an arbitrary direction, the mainstream flow periodically subdivides and rejoins as in the principal flow direction cases, except not in a symmetric fashion (Fig. 5.2(a)). For inclined flow in a rod array the mainstream flow does not maintain the average flow direction but slants towards crossflow while the recirculating flow moves along the rod axis resulting in a net vertical average flow. This postulated flow pattern description will be very useful when formulating two-phase flow models in Chapter 6. Although both of the above described flow patterns are illustrated for a square array in Fig. 5.2, analogous patterns can be envisioned for staggered arrays.

Now with a physical picture of single-phase flow in any direction in rod arrays, let us proceed with the development of flow resistance models.



(a) Arbitrary direction crossflow.



(b) Arbitrary direction incline flow.

Figure 5.2 Postulated rod array streamlines.

5.2 Multidimensional Flow Resistance Formulation

5.2.1 General Formulation

The flow resistance vector $\langle \underline{R} \rangle$ is modeled in the general form of a loss coefficient matrix \underline{K} times the characteristic average velocity \underline{u} within the porous medium,

$$\langle \underline{R} \rangle = \underline{K} \underline{u} \quad (5.2)$$

This formulation originated from extending the Darcy scalar law used for isotropic, viscous flows in porous media

$$R = \frac{\mu}{k} u \quad (5.3)$$

(where k is a constant) to higher velocity, anisotropic flows where μ/k becomes dependent on the flow speed and direction [B.2, W.1].

Regular rod array geometries have three orthogonal axes of symmetry ($\parallel, \perp 1, \perp 2$) as shown in Fig. 5.3. In this coordinate system the loss coefficient matrix becomes diagonal

$$\begin{bmatrix} R_{\parallel} \\ R_{\perp 1} \\ R_{\perp 2} \end{bmatrix} = \begin{bmatrix} K_{\parallel} & 0 & 0 \\ 0 & K_{\perp 1} & 0 \\ 0 & 0 & K_{\perp 2} \end{bmatrix} \begin{bmatrix} u_{\parallel} \\ u_{\perp 1} \\ u_{\perp 2} \end{bmatrix} \quad (5.4)$$

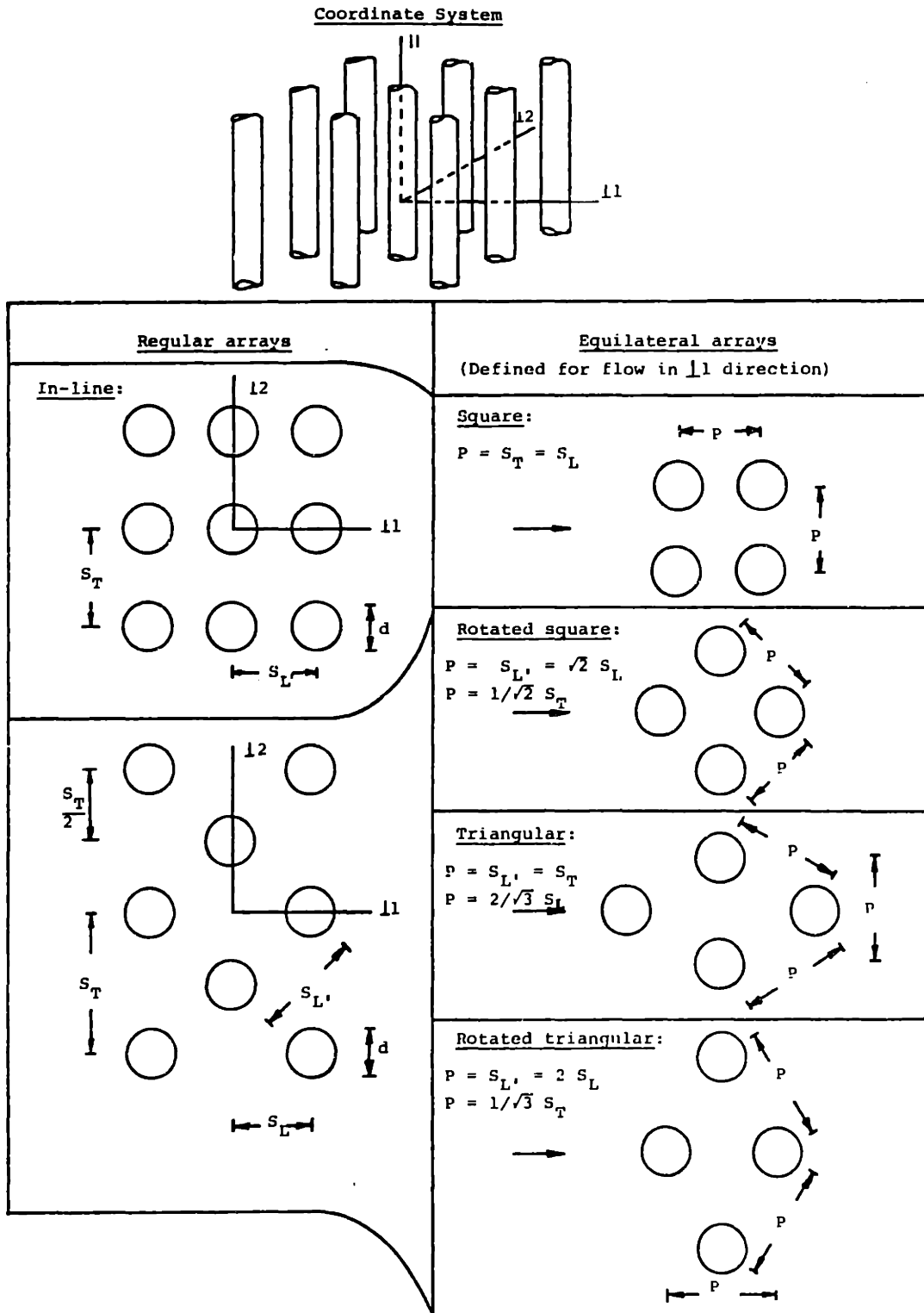


Figure 5.3 Regular rod array geometry and coordinate definitions.

since the resistance and velocity vectors are collinear for each of these principal component directions, there is no lift force. Equation (5.4) also can be written in terms of scalar components

$$\begin{aligned} \langle \underline{R} \rangle &= R_{||} \underline{e}_{||} + R_{\perp 1} \underline{e}_{\perp 1} + R_{\perp 2} \underline{e}_{\perp 2} \\ &= K_{||} u_{||} \underline{e}_{||} + K_{\perp 1} u_{\perp 1} \underline{e}_{\perp 1} + K_{\perp 2} u_{\perp 2} \underline{e}_{\perp 2} \end{aligned} \quad (5.5)$$

where \underline{e} is the unit vector. Equation (5.4) may be transformed into any desired coordinate system by a coordinate transformation matrix \underline{T} .

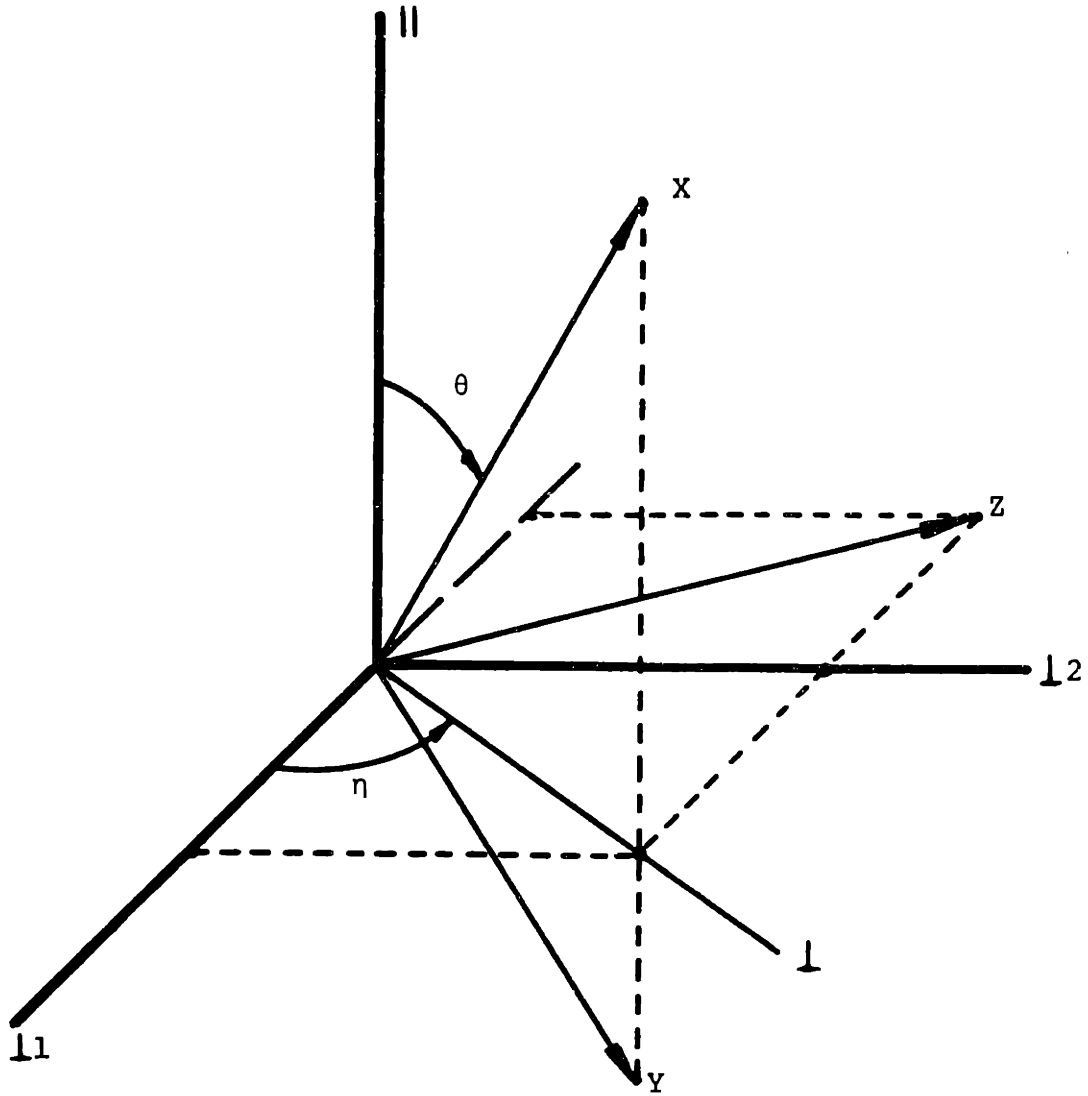
$$\langle \underline{R}' \rangle = (\underline{T} \langle \underline{R} \rangle) = (\underline{T} \underline{K} \underline{T}^{-1}) (\underline{T} \underline{u}) = \underline{K}' \underline{u}' \quad (5.6)$$

A specific example of \underline{T} where the z-axis is restricted to the crossflow plane is given in Fig. 5.4. Tensor \underline{K}' is no longer a diagonal matrix signifying the presence of both drag and lift components of resistance for flow in any of the coordinate directions x, y, or z. This coordinate system with the flow in the x-direction will be used extensively.

In general, the resistance vector depends on the flow conditions, geometry, and fluid properties. For flow in regular rod arrays

$$\langle \underline{R} \rangle = \text{ftn} [\underline{u}, \nabla \underline{u}, S_L, S_T, d, RA, \epsilon, \rho, \mu] \quad (5.7)$$

where ϵ denotes the surface roughness and RA the rod arrangement (i.e., in-line, staggered, square, etc.).



$$\begin{bmatrix} e_x \\ e_y \\ e_z \end{bmatrix} = \begin{bmatrix} \cos \theta & \sin \theta \cos \eta & \sin \theta \sin \eta \\ -\sin \theta & \cos \theta \cos \eta & \cos \theta \sin \eta \\ 0 & \sin \eta & \cos \eta \end{bmatrix} \begin{bmatrix} e_{l_2} \\ e_{l_1} \\ e_l \end{bmatrix}$$

$\underbrace{\hspace{10em}}_{\substack{\Delta \\ \underline{\underline{T}}}}$

Figure 5.4 Coordinate system transformation.

5.2.2 Model Constraints

The model development and validation presented here will be concerned with two-dimensional, turbulent, fully developed flow through smooth rod arrays. For fully-developed flow in smooth arrays the ∇u and ϵ dependence in Eq. (5.7) may be eliminated. The three-dimensional flow can be reduced to a two-dimensional inclined flow problem by either of two independent assumptions:

- (1) The crossflow resistance is independent of flow direction in the crossflow plane

$$K_{\parallel} = K_{\perp 1} = K_{\perp 2} \quad (5.8)$$

or,

- (2) The crossflow velocity is in a symmetric direction of the rod array. All symmetric directions can be represented by a rod arrangement where $\perp 1$ is the flow direction, so

$$u_{\perp 2} = 0 \quad \text{and} \quad K_{\perp 1} = K_{\perp} \quad (5.9)$$

For both cases the crossflow velocity and resistance become collinear.

For a two-dimensional flow we define the crossflow velocity as

$$u_{\perp} \triangleq \sqrt{u_{\perp 1}^2 + u_{\perp 2}^2}, \quad \eta \triangleq \tan^{-1} \left(\frac{u_{\perp 2}}{u_{\perp 1}} \right) \quad (5.10)$$

so Eq. (5.5) reduces to

$$\begin{aligned} \langle \underline{R} \rangle &= R_{\parallel} \underline{e}_{\parallel} + R_{\perp} \underline{e}_{\perp} \\ &= K_{\parallel} u_{\parallel} \underline{e}_{\parallel} + K_{\perp} u_{\perp} \underline{e}_{\perp} \end{aligned} \quad (5.11)$$

where

$$\underline{u} = u_{||} \underline{e}_{||} + u_{\perp} \underline{e}_{\perp} \quad (5.12)$$

Finally, we also define \underline{u} in terms of polar components

$$|\underline{u}| \triangleq \sqrt{u_{||}^2 + u_{\perp 1}^2 + u_{\perp 2}^2} = \sqrt{u_{||}^2 + u_{\perp}^2} \quad (5.13)$$

$$\theta \triangleq \tan^{-1} \left(\frac{\sqrt{u_{\perp 1}^2 + u_{\perp 2}^2}}{u_{||}} \right) = \tan^{-1} \left(\frac{u_{\perp}}{u_{||}} \right) \quad (5.14)$$

These vectors are summarized for the two independent assumptions, in Fig. 5.5.

Applying the above constraints, the independent variables of the flow resistance (Eq. (5.7)) reduces to

$$\langle R \rangle = \text{ftn} [|\underline{u}|, \theta, S_L, S_T, d, RA, \rho, \mu] \quad (5.15)$$

5.2.3 Secondary Variables

Some useful secondary variables are defined for regular rod arrays as follows

- The volume porosity

$$\gamma_v \triangleq \frac{\text{Fluid Volume}}{\text{Total Volume}} = \left[1 - \frac{\pi}{4} \left(\frac{d}{S_L} \right) \left(\frac{d}{S_T} \right) \right] \quad (5.16)$$

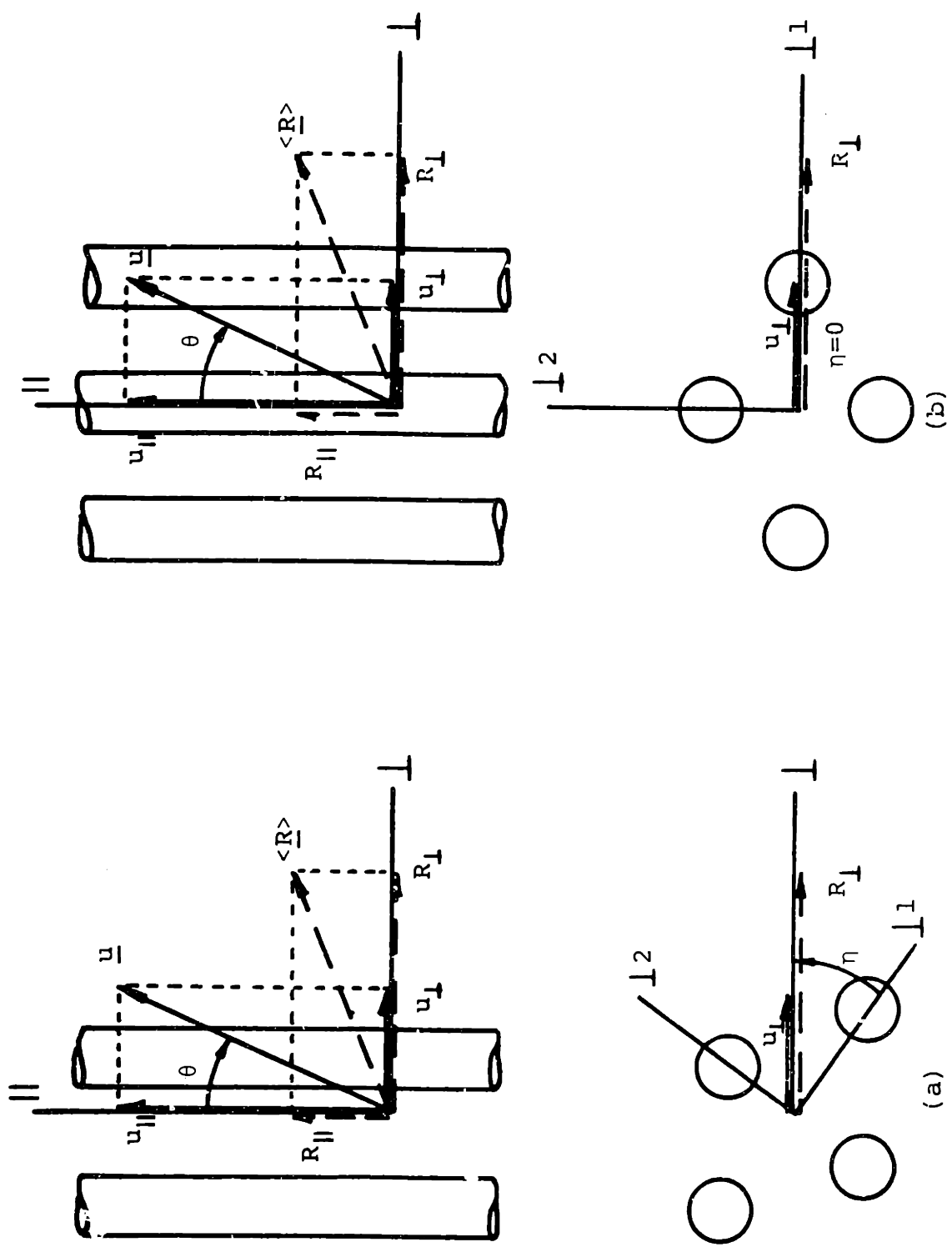


Figure 5.5 Two-dimensional flow coordinate definitions---(a) crossflow independent resistance, (b) symmetric crossflow direction.

- The volumetric hydraulic diameter

$$D_v \stackrel{\Delta}{=} \frac{4 \text{ (Fluid Volume)}}{\text{Wetted Surface Area}} = \frac{4 (S_L S_T - \frac{\pi}{4} d^2) L_{||}}{\pi d L_{||}} \quad (5.17)$$

$$= d \left(\frac{\gamma_v}{1 - \gamma_v} \right)$$

Note that for a rod array D_v is equal to the equivalent hydraulic diameter of parallel flow, based on flow area and wetted perimeter. Also notice D_v is a length scale independent of rod arrangement or flow direction.

- Crossflow mainstream porosity

$$\delta_v \stackrel{\Delta}{=} \frac{\text{Crossflow Mainstream Volume}}{\text{Fluid Volume}} \quad (5.18)$$

The crossflow mainstream porosity is used to define the crossflow mainstream velocity discussed below. Explicit relations for δ_v depend on how the mainstream flow volume is modeled. A detailed discussion of various models is given in Appendix D. The most widely used model ((A)) defines the mainstream volume as the area at the minimum flow clearance times the straight length S_L . In this model, δ_v is dependent on the rod arrangement. An approximate model ((D)) independent of rod arrangement is introduced here, $\delta_v = \gamma_v$. Model ((D)) is used with generalized crossflow correlations that have rod arrangement dependence averaged out. These two models are shown for staggered and in-line arrays in Fig. 5.6.

Three characteristic flow velocities $|\underline{u}|$ are defined:

Model	Staggered Array	
	In-line Array	Staggered Array
A	<p>Diagram A: In-line array of four circles with a central shaded rectangle. Labels: s_L, s_T, and the equation $\delta_v = \frac{1}{2} \left(1 - \frac{d}{s_T}\right) \gamma_v$.</p>	<p>Diagram A (Staggered): $2(s_{L'} - d) \geq (s_T - d)$</p> <p>Diagram A (Staggered): Staggered array of four circles with a central shaded rectangle. Labels: s_L, $s_{L'}$, s_T, $2s_{L'} - d$, and the equation $\delta_v = \frac{1}{2} \left(1 - \frac{d}{s_T}\right) \gamma_v$.</p>
	<p>Diagram A: In-line array of four circles with a central shaded rectangle. Labels: s_L, s_T, and the equation $\delta_v = \gamma_v$.</p>	<p>Diagram A (Staggered): $2(s_{L'} - d) \leq (s_T - d)$</p> <p>Diagram A (Staggered): Staggered array of four circles with a central shaded rectangle. Labels: s_L, $s_{L'}$, s_T, $2s_{L'} - d$, and the equation $\delta_v = \frac{2(s_{L'} - d)}{\gamma_v}$.</p>
D	<p>Diagram D: In-line array of four circles with a central shaded rectangle. Labels: s_L, s_T, and the equation $\delta_v = \gamma_v$.</p>	<p>Diagram D (Staggered): $2(s_{L'} - d) \geq (s_T - d)$</p> <p>Diagram D (Staggered): Staggered array of four circles with a central shaded rectangle. Labels: s_T, $s_T \gamma_v^2$, and the equation $\delta_v = \gamma_v$.</p>
	<p>Diagram D: In-line array of four circles with a central shaded rectangle. Labels: s_T, $s_T \gamma_v^2$, and the equation $\delta_v = \gamma_v$.</p>	<p>Diagram D (Staggered): $2(s_{L'} - d) \leq (s_T - d)$</p> <p>Diagram D (Staggered): Staggered array of four circles with a central shaded rectangle. Labels: s_T, $s_T \gamma_v^2$, and the equation $\delta_v = \gamma_v$.</p>

Figure 5.6 Crossflow mainstream porosity models.

- The superficial velocity

$$|\underline{v}_{\infty}| \triangleq \frac{\text{Volumetric Flow Rate}}{\text{Total Cross-sectional Area}} = \frac{Q}{A_{xs}} \quad (5.19)$$

- The average velocity

$$|\langle \underline{v} \rangle| \triangleq \frac{\text{Volumetric Flow Rate}}{\text{Average Flow Area}} = \frac{Q}{A_{xs} \gamma_v} = \frac{|\underline{v}_{\infty}|}{\gamma_v} \quad (5.20)$$

- The crossflow mainstream velocity

$$\begin{aligned} |\underline{v}_{-ms}| &\triangleq \frac{\text{Volumetric Flow Rate}}{\text{Average Mainstream Flow Area}} \\ &= \frac{Q}{A_{xs} \delta_v \gamma_v} = \frac{|\langle \underline{v} \rangle|}{\delta_v} = \frac{|\underline{v}_{\infty}|}{\delta_v \gamma_v} \end{aligned} \quad (5.21)$$

The velocity magnitudes as defined are independent of the flow direction (See Fig. 5.7).

Last we define the dimensionless Reynolds number group

$$Re \triangleq \frac{\rho |\underline{u}| L}{\mu} \quad (5.22)$$

where $|\underline{u}|$ and L are a characteristic velocity and length respectively.

The Reynolds numbers used here are

$$Re_v \triangleq \frac{\rho |\langle \underline{v} \rangle| D_v}{\mu} \quad (5.23)$$

$$Re_d \triangleq \frac{\rho |\underline{v}_{-ms}| d}{\mu} = Re_v \left(\frac{1 - \gamma_v}{\delta_v \gamma_v} \right) \quad (5.24)$$

The first definition is recommended for use in porous media. The second has been used by many authors to correlate crossflow data.

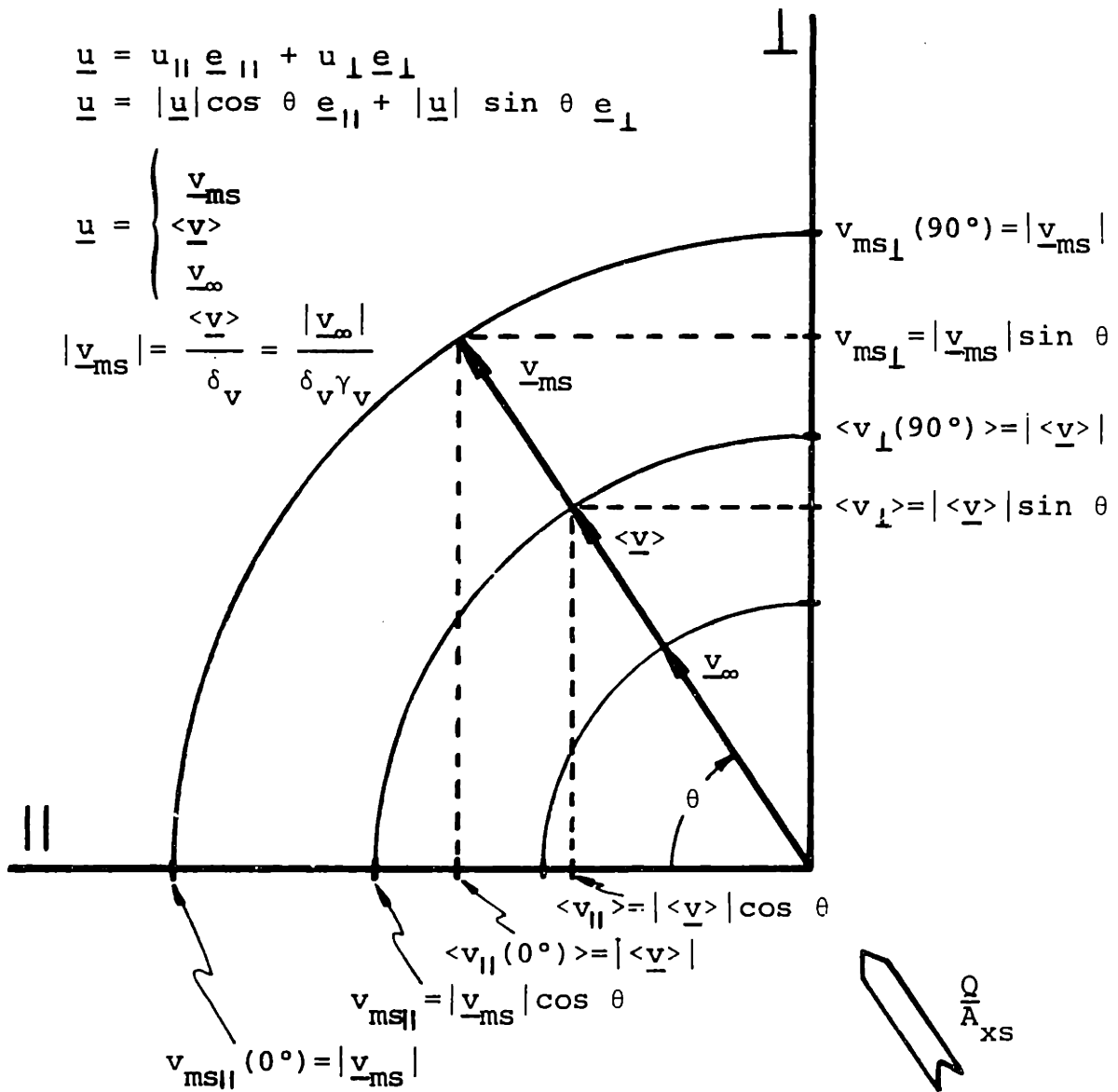


Figure 5.7 Velocity vector definitions.

5.2.4 Modeling Formulation

We postulate correlating $K_{||}$ and K_{\perp} of Eq. (5.11) by forms analogous to those used in one-dimensional correlations

$$\begin{aligned} \langle \underline{R} \rangle = & \left(f_{\theta||}[\underline{u}] \frac{1}{D_v} \frac{\rho|\underline{u}|}{2} \right) u_{||} \underline{e}_{||} + \\ & \left(f_{\theta\perp}[\underline{u}] \frac{1}{D_v} \frac{\rho|\underline{u}|}{2} + c_{\theta\perp}[\underline{u}] \frac{1}{D_v} \frac{\rho|\underline{u}|}{2} \right) u_{\perp} \underline{e}_{\perp} \end{aligned} \quad (5.25)$$

This form reduces simply to the one-dimensional limits of parallel and crossflow. The coefficient f denotes skin friction and c denotes form drag. Remember that there is no form drag for parallel flow. Generally for crossflow, only the sum of the skin friction and form drag is known, hence we define a total drag coefficient $b_{\theta\perp}$, giving the modeling formula

$$\begin{aligned} \langle \underline{R} \rangle = & R_{||}(\theta) \underline{e}_{||} + R_{\perp}(\theta) \underline{e}_{\perp} \\ = & \left(f_{\theta||}[\underline{u}] \frac{1}{D_v} \frac{\rho|\underline{u}|}{2} \right) u_{||} \underline{e}_{||} + \left(b_{\theta\perp}[\underline{u}] \frac{1}{D_v} \frac{\rho|\underline{u}|}{2} \right) u_{\perp} \underline{e}_{\perp} \end{aligned} \quad (5.26)$$

Equation (5.26) can be put in a dimensionless form by multiplying by $D_v^2/\mu|\underline{u}|$. Thus

$$\begin{aligned} \langle \underline{R}^* \rangle \triangleq & \frac{D_v^2}{\mu|\underline{u}|} \langle \underline{R} \rangle = R_{||}^*(\theta) \underline{e}_{||} + R_{\perp}^*(\theta) \underline{e}_{\perp} \\ = & \frac{f_{\theta||}[\underline{u}]}{2} \left(\frac{\rho|\underline{u}|D_v}{\mu} \right) \frac{u_{||}}{|\underline{u}|} \underline{e}_{||} + \frac{b_{\theta\perp}[\underline{u}]}{2} \left(\frac{\rho|\underline{u}|D_v}{\mu} \right) \frac{u_{\perp}}{|\underline{u}|} \underline{e}_{\perp} \end{aligned} \quad (5.27)$$

where the asterisk (*) denotes the dimensionless form.

In the remainder of this chapter, we shall review correlations for $f_{\theta_{\parallel}}$ and $b_{\theta_{\perp}}$ for the limiting cases of parallel and crossflow, then present superposition models relating $f_{\theta_{\parallel}}$ and $b_{\theta_{\perp}}$ for inclined flows to the one-dimensional limits, and finally evaluate the multidimensional models with published data and new data taken in this study.

5.3 Parallel Flow Resistance

For the limiting case of parallel flow, $\theta = 0^\circ$, the resistance vector reduces to

$$\langle \underline{R} \rangle = R_{\parallel}(0^\circ) \underline{e}_{\parallel} + R_{\perp}(0^\circ) \underline{e}_{\perp} \quad (5.28)$$

where

$$R_{\parallel}(0^\circ) = f_{\parallel} \left[\left| \underline{v} \right| \right] \frac{1}{D_v} \frac{\rho \left| \langle \underline{v} \rangle \right|}{2} \langle v_{\parallel}(0^\circ) \rangle \quad (5.29)$$

$$R_{\perp}(0^\circ) = 0$$

and the characteristic velocity \underline{u} has been taken as the average velocity, $\langle \underline{v} \rangle$. Note that for parallel flow $\langle v_{\parallel}(0^\circ) \rangle = \left| \langle \underline{v} \rangle \right|$.

A wealth of data and correlations for f_{\parallel} are available in the literature. Knudsen and Katz [K.1] have summarized round tube corrections; Marek et. al. [M.2] have related round tube correlations to square arrays. Rehme [R.2] has related round tube correlations to triangular arrays and also has developed a generalized model for all noncircular geometries [R.1]. Sparrow and Loeffler [S.4] have analytically solved the laminar flow solution for both square and triangular arrays. All these models are summarized in Table 5.2 and plotted for a round tube and square array of $P/d = 1.5$ in Figure 5.8. Note that the rod array friction for turbulent flow is only about 7 percent higher than that for an equivalent round tube.

TABLE 5.2

Parallel Flow Correlations (for smooth surfaces)

$$f_{||} \triangleq \frac{2D_v R_{||} (0^*)}{\rho |\langle v \rangle|^2}$$

Reference	Skin Friction Factor	Geometry	Range
[K.1]	$f_{ } = \frac{64}{Re_v}$	Round tube	Laminar flow solution
Nikaradse [K.1]	$\frac{1}{\sqrt{f_{ }}} = 2.0 \log \left(\frac{Re_v}{2} \sqrt{f_{ }} \right) - 0.2$	Round tube	$4 \times 10^3 < Re_v < 3.2 \times 10^6$
Blasius [B.3]	$f_{ } = \frac{0.316}{(Re_v)^{0.25}}$	Round tube	$3 \times 10^3 < Re_v < 1 \times 10^5$
McAdam [M.1]	$f_{ } = \frac{0.184}{(Re_v)^{0.20}}$	Round tube	$5 \times 10^3 < Re_v < 2 \times 10^5$
Maubach [M.3]	$\frac{1}{\sqrt{f_{ }}} = 2.035 \log (Re_v \sqrt{f_{ }}) - 0.989$	Round tube	Turbulent flow
Sparrow and Loeffler [S.4]	$f_{ } = \text{ftn} [RA, \delta_v]$	Square and triangular array	Analytical laminar flow solution
Rehme [R.2]	$\frac{f_{ }}{f_{ }(\text{round tube})} = \frac{1.045 + 0.071(\frac{P}{d} - 1)}{1.036 + 0.054(\frac{P}{d} - 1)}$	Triangular arrays	$Re_v = 10^4$ $Re_v = 10^5$
Rehme [R.1]	$f_{ } = \text{ftn}[f_{ }(\text{round tube}), f_{ }(\text{laminar}), \text{geometry}]$	All rod arrangements	Laminar and turbulent flow
Marek et. al. [M.2]	$\frac{f_{ }}{f_{ }(\text{round tube})} = 1.04 + 0.06(\frac{P}{d} - 1)$	Square arrays	$Re_v = 10^5$

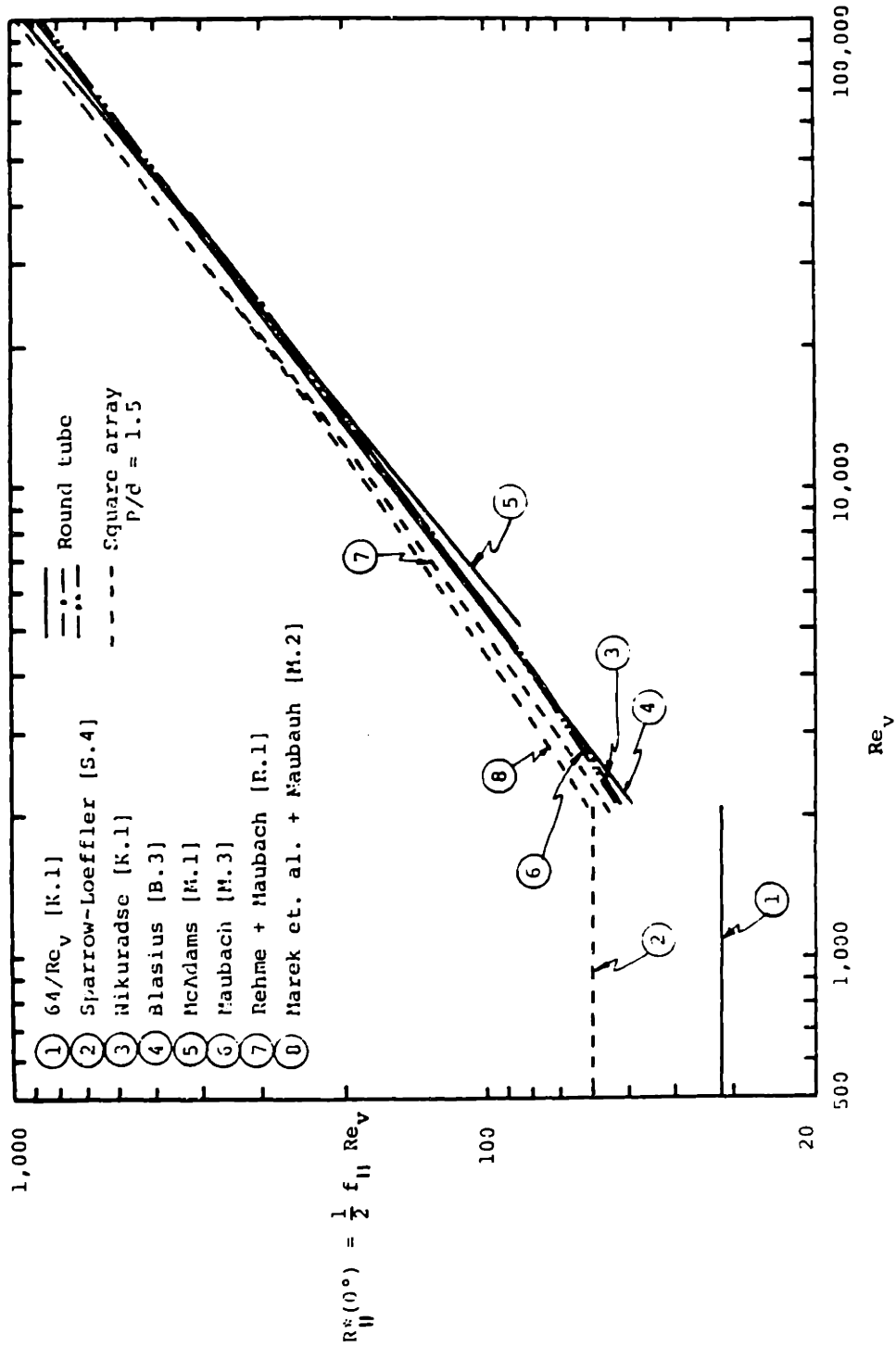


Figure 5.6 Parallel flow resistance for round tube and square array of $P/d = 1.5$.

In the developments to follow we shall use the form

$$f_{\parallel} = \frac{A}{(\text{Re}_v)^n} \quad (5.30)$$

and when numerical values are needed the Blasius correlation ($A = 0.316$, $n = 0.25$) shall be used. This model is sufficient because, as will be seen later, f_{\parallel} has a minimal effect on the total flow resistance for inclined flows.

5.4 Crossflow Resistance

The other one dimensional limit is pure crossflow, $\theta = 90^\circ$. For crossflow the resistance vector becomes

$$\langle \underline{R} \rangle = R_{\parallel}(90^\circ) \underline{e}_{\parallel} + R_{\perp}(90^\circ) \underline{e}_{\perp} \quad (5.31)$$

where

$$R_{\parallel}(90^\circ) = 0$$

$$R_{\perp}(90^\circ) = b_{\perp} [|\underline{v}_{ms}|] \frac{1}{D_v} \frac{\rho |\underline{v}_{ms}|}{2} v_{ms\perp}(90^\circ) \quad (5.32)$$

and now the characteristic velocity is v_{ms} , and $v_{ms\perp}(90^\circ) = |\underline{v}_{ms}|$. Ample crossflow data and correlations are available in the literature. Unlike parallel flow, however, there is considerable variation in correlating forms, characteristic lengths, mainstream velocity definitions, and the predicted flow resistance itself.

Knudsen and Katz [K.1] summarized some of the simple, earlier correlations. More elaborate piecewise correlations were developed by Idel'chik [I.2] and more recently by Bossier [B.6], VDI-Wärmeatlas [V.1], Zūkauskas and Ulinakas [Z.1] and Toborek [T.1]. Table 5.3

TABLE 5.3

Crossflow Correlations

$$b_{\perp} \triangleq \frac{2D_v \delta_v^2 R_{\perp}(90^\circ)}{\rho |\langle v \rangle|^2}$$

Reference	Total Drag Coefficient	δ_v model*	Geometry	Range
Gunter and Shaw [G.2]	$b_{\perp} = \frac{180}{(Re_v/\delta_v)} \left(\frac{D_v}{S_T}\right)^{0.4} \left(\frac{S_L}{S_T}\right)^{0.6}$	(A)	Rod arrays and extended surfaces	$(Re_v/\delta_v) < 500$
	$b_{\perp} = \frac{1.92}{(Re_v/\delta_v)^{0.145}} \left(\frac{D_v}{S_T}\right)^{0.4} \left(\frac{S_L}{S_T}\right)^{0.6}$		1.25 < S_T/d < 5.0 1.25 < S_L/d < 5.0	500 < (Re_v/δ_v) < 200,000
Jakob [J.1]	$b_{\perp} = \frac{4.0}{(Re_v/\delta_v)^{0.16}} \left(\frac{D_v}{d}\right)^{0.16} \left(\frac{D_v}{S_L}\right) \left[0.25 + \frac{0.1175}{\left(\frac{S_T}{d} - 1\right)^{1.08}} \right]$	(A)	Staggered 0.6 < S_L/d < 3.0 1.25 < S_T/d < 3.5	5,000 <
	$b_{\perp} = \frac{4.0}{(Re_v/\delta_v)^{0.15}} \left(\frac{D_v}{d}\right)^{0.15} \left(\frac{D_v}{S_L}\right) \left[0.044 + \frac{0.08 \left(\frac{S_L}{d}\right)}{\left(\frac{S_T}{d} - 1\right) (0.43 + 1.13 d/S_L)} \right]$		In-line 1.25 < S_L/d < 3.0 1.25 < S_T/d < 3.0	(Re_v/S_v) < 40,000
Chilton and Genereaux [C.2]	$b_{\perp} = \frac{106}{(Re_v/\delta_v)}$	(A)	Staggered and in-line	$(Re_v/\delta_v) < 100$
	$b_{\perp} = \frac{3.0}{(Re_v/\delta_v)^{0.2}} \left(\frac{D_v}{S_T - d}\right)^{0.2}$		Staggered	100 <
	$b_{\perp} = \frac{1.32}{(Re_v/\delta_v)^{0.2}} \left(\frac{D_v}{S_T - d}\right)^{0.2}$		In-line	$\left(\frac{Re_v}{\delta_v}\right) \left(\frac{S_T - d}{D_v}\right) < 20,000$

TABLE 5.3 (continued)

Crossflow Correlations

Idel'chik [I.2]	$b_{\perp} = \frac{\text{ftn} \left[\frac{S_T}{d}, \frac{S_L}{d} \right]}{(Re_v/\delta_v)^m}; m = \frac{0.2}{\left(\frac{S_T}{S_L} - d \right)^2}$ $b_{\perp} = \frac{\text{ftn} \left[\frac{S_T}{d}, \frac{S_L}{d} \right]}{(Re_v/\delta_v)^{0.27}}$	(A)	In-line Staggered	$3,000 <$ $(Re_v/\delta_v) \left(\frac{d}{D_v} \right)$ $< 10,000$
Boisser [B.6]	$b_{\perp} = \text{ftn} [Re_v, \delta_v, P/d]$	assume $v_{ms} = v_m$ or $\delta_v = \frac{1}{\gamma_v}$	Square arrays	Turbulent flow
VDI- Wärmetlas [V.1]	$b_{\perp} = \text{ftn} \left[(Re_v/\delta_v), \frac{S_T}{d}, \frac{S_L}{d} \right]$	(B)	In-line and staggered	$2 <$ (Re_v/δ_v) $< 1,000,000$
Zūkauskas [Z.1]	$b_{\perp} = \text{ftn} \left[(Re_v/\delta_v), \frac{S_T}{d}, \frac{S_L}{d} \right]$	(A)	In-line and staggered	$3 <$ $(Re_v/\delta_v) \left(\frac{d}{D_v} \right)$ $< 1,000,000$
Toborek [T.1]	$b_{\perp} = \text{ftn} [(Re_v/\delta_v), P/d]$	(A)	Square and triangular	$1 <$ $(Re_v/\delta_v) \left(\frac{d}{D_v} \right)$ $< 1,000,000$
This Study	$b_{\perp} = \frac{6.0 \delta_v^{1.85}}{(Re_v/\delta_v)^{0.15}}$	(D)	All rod arrays	$1,000 <$ Re_v $< 10,000$
Hoerner [H.1]	$b_{\perp} = \frac{4}{\pi} C_D; C_D = \text{ftn} [Re_v]$	$\delta_v = 1$	Isolated single cylinder $S_L/d > 5$ $S_T/d > 5$	All Re_v

* Models shown in Appendix D

summarizes the reviewed correlations. The majority use the area of minimum flow clearance in defining the mainstream velocity (Model (A) of Fig. 5.6), however the characteristic length and Reynolds number dependence postulated by each author vary considerably. Figure 5.9 shows a comparison of the crossflow resistance predictions for a square array of $P/d = 1.5$. The correlations span a ± 35 percent band for this particular geometry. The newer, more elaborate correlations of VDI-Wärmeatlas, Žukauskas, and Toborek, however, are in closer agreement.

For a well defined, symmetric crossflow geometry (flow direction), the flow resistance should be evaluated from a comprehensive correlation such as Žukauskas, or a correlation based on data for the particular geometry and velocity of interest (or better yet on the data base itself). For three-dimensional flows and irregular rod arrangements the above method becomes inadequate. For these applications an averaged correlation independent of rod arrangement (crossflow direction) is desired. Figure 5.10 shows graphically the desired constant flow resistance which is an average of the circumferential variation. Generally only the resistances in the symmetric flow directions are known.

Attempts to predict the circumferential variation in flow resistance are not practical because, as is shown below, the absolute accuracy of the crossflow resistance measurements and correlations are less than the circumferential variation being predicted. Hence we propose using an average correlation for a given porosity independent of the rod arrangement (flow direction).

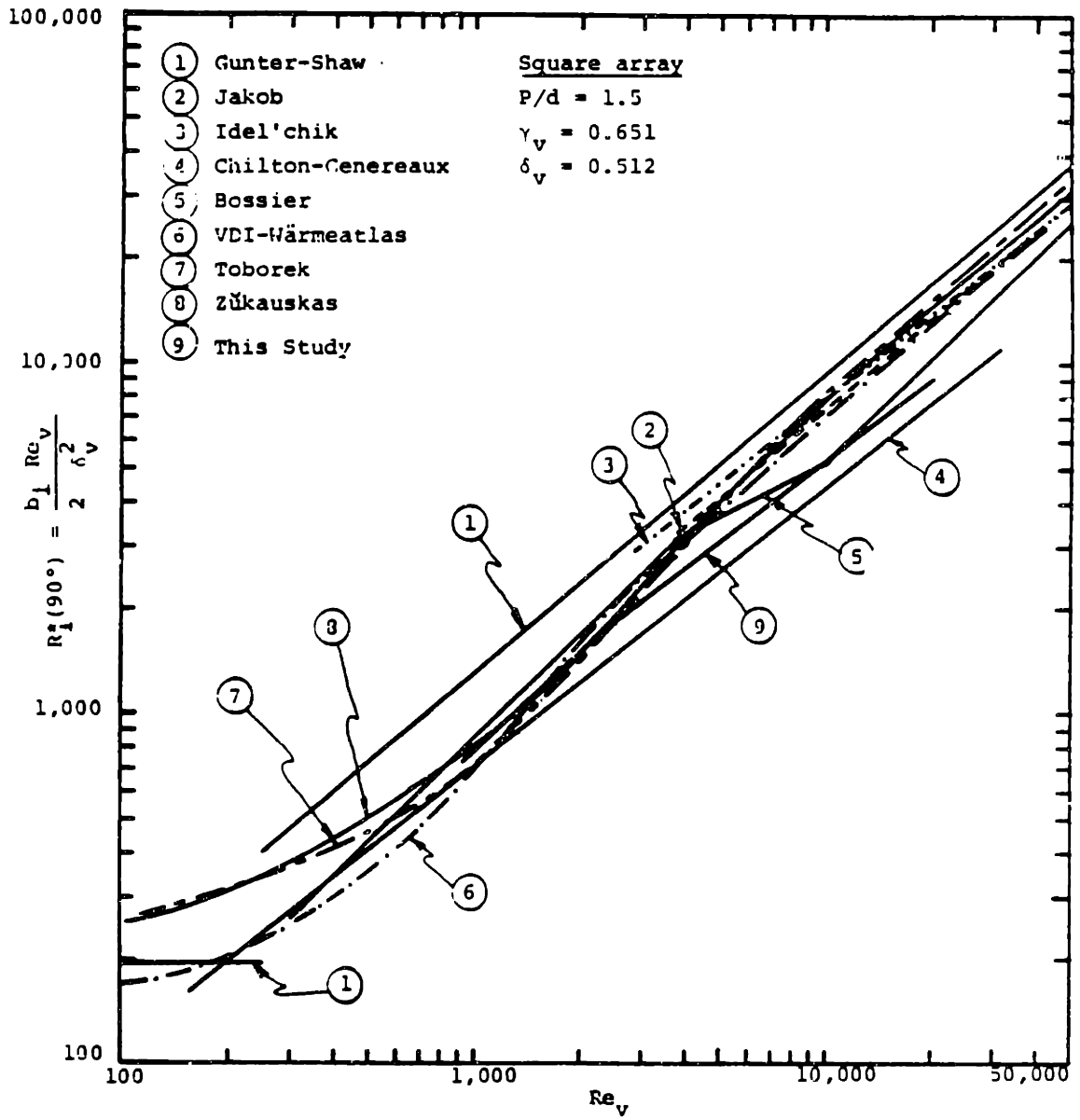
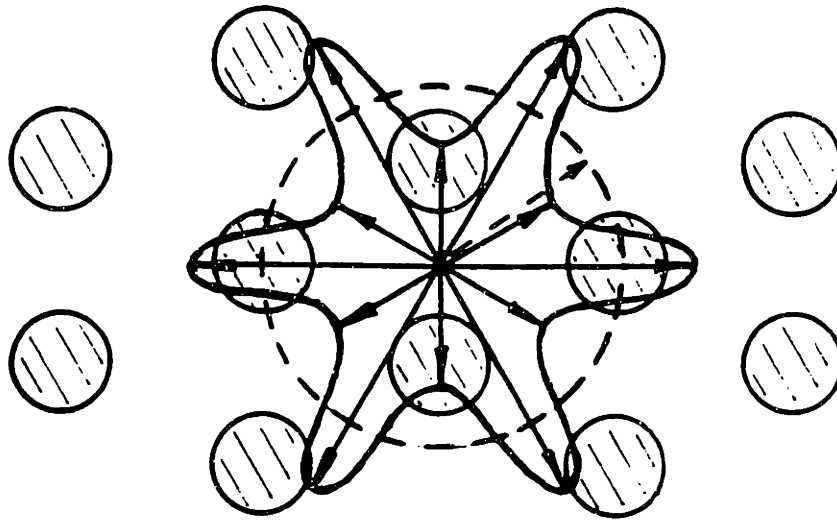
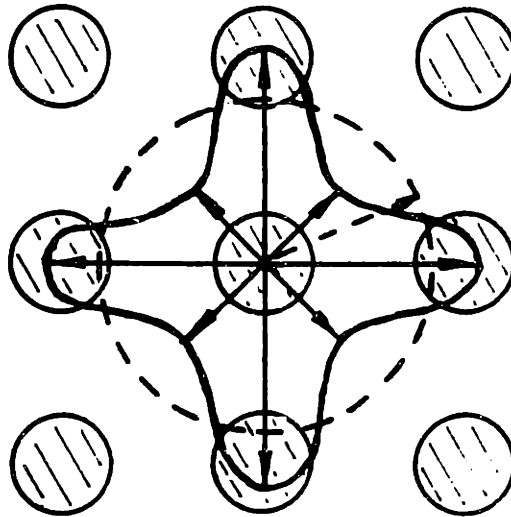


Figure 5.9 Crossflow correlations for square array of $P/d = 1.5$.



(a) Triangular array



(b) Square array

- ↑ Known flow resistance for symmetric directions.
- Locus of local flow resistance vectors.
- ↑ Average flow resistance.
- - - Locus of average flow resistance vectors.

Figure 5.10 Circumferential variation in crossflow resistance.

A simple generalized crossflow correlation is created by averaging out the variations in Reynolds number and geometric arrangement of the simpler correlations. (This is sufficient for the analysis performed here. A more precise correlation based on the complete crossflow data base should be developed for implementation in thermal-hydraulic codes.)

The chosen generalized form is

$$b_{\perp} = \frac{B_o [\gamma_v]}{(Re_v / \delta_v)^{0.15}} \quad (5.33)$$

where (1) the rod arrangement independent model (\textcircled{D}) is used for the mainstream porosity, $\delta_v = \gamma_v$; (2) a mean Reynolds number dependence of 0.15 is used; (3) the only length scale is the array independent volumetric hydraulic diameter, D_v ; and (4) B_o is assumed only a function of the volume porosity, γ_v .

Figures 5.11 and 5.12 show plots of B_o as evaluated from the four simpler correlations for four equilateral rod arrangements (See Fig. 5.3). Comparison of these curves show no consistent rod arrangement dependence. For a given porosity, the accuracy of predicting the resistance as shown by the variation between correlations for a given rod arrangement is as great as the rod arrangement dependence predicted by each author. The curves in Fig. 5.11 and 5.12 are for a Reynolds number of 10^4 . The arrows show the translations of each curve for Reynolds numbers ranging from 10^3 to 10^5 . Clearly the inconsistent array dependence exists for all Reynolds numbers. Butterworth [B.2] reaffirmed this point for a limited set of experimental data. He found no arrangement dependence when comparing data for square and rotated

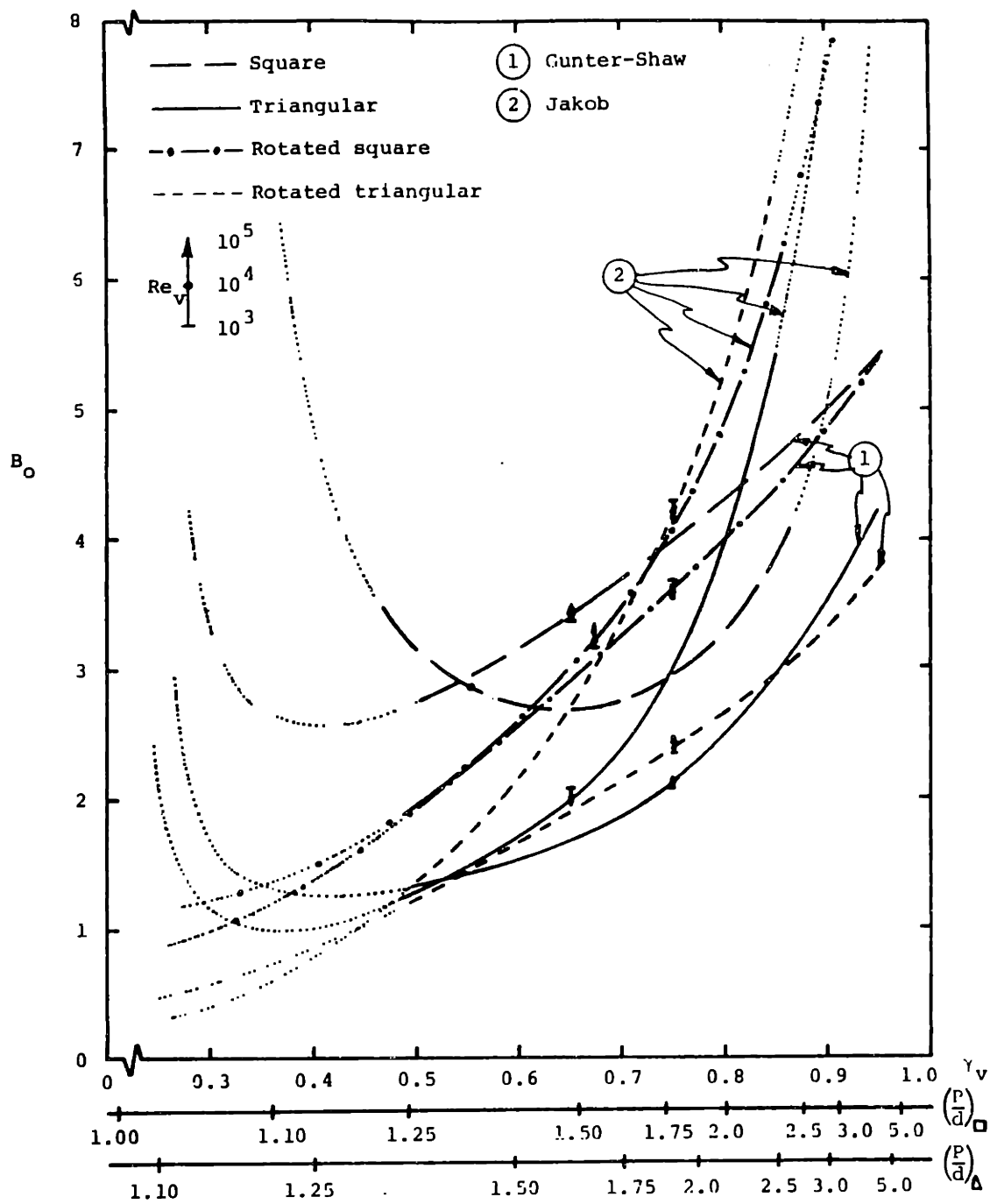


Figure 5.11 Geometry and Reynolds dependence of Gunter-Shaw [G.2] and Jakob [J.1] crossflow correlations.

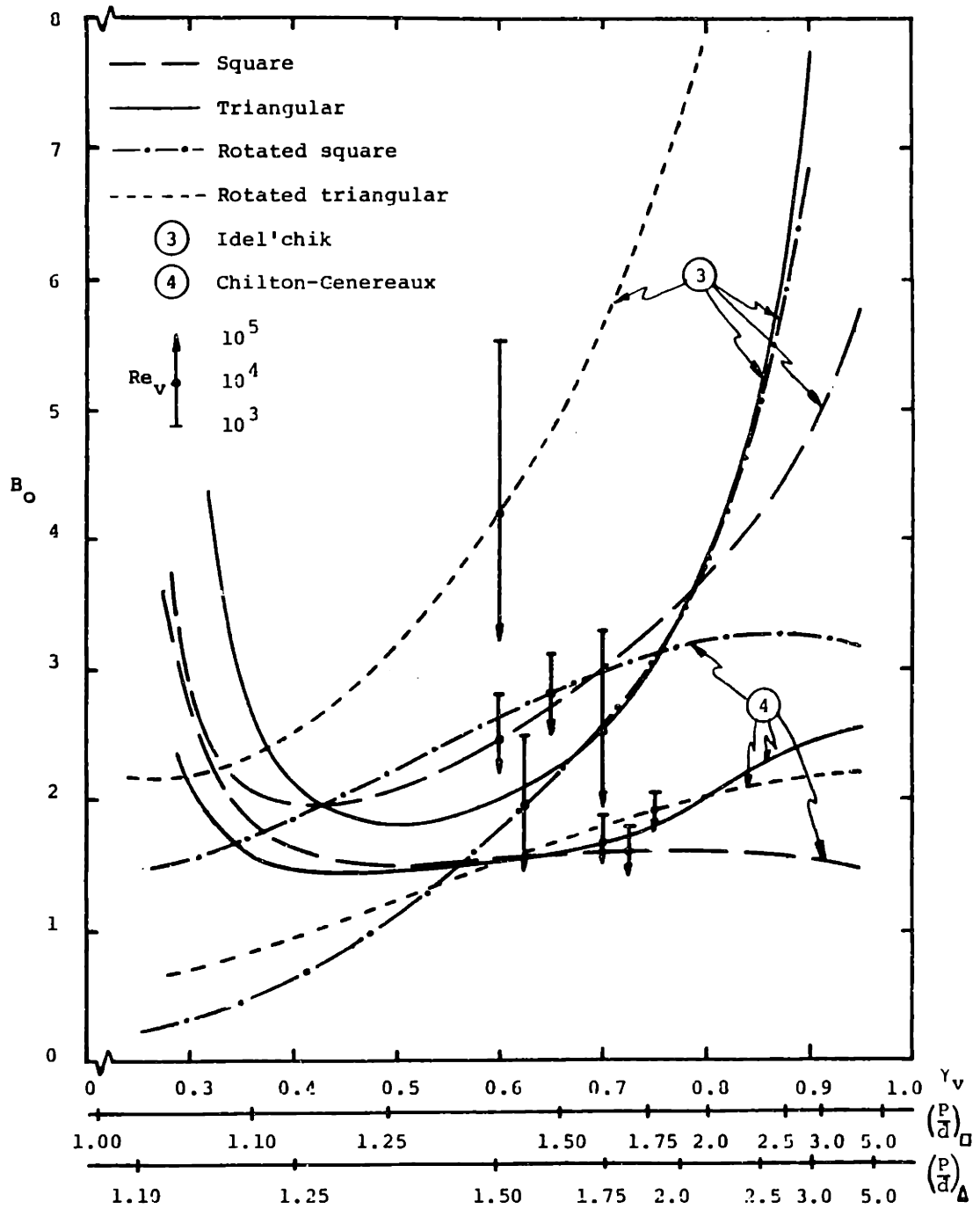


Figure 5.12 Geometry and Reynolds dependence of Idel'chik [I.2] and Chilton-Genereaux [C.2] crossflow correlations.

square arrays of $P/d = 1.5$ in laminar flow; and comparing triangular and rotated triangular arrays of $P/d = 1.25$ and 1.33 in both the laminar and turbulent flow.

Considering the curves collectively, a monotonically increasing porosity dependence is apparent. We propose a simple, array independent crossflow resistance model where B_o in Eq. (5.33) is

$$B_o = 6.0 \delta_v^{1.85} \quad (5.34)$$

This model is a smooth curve through the mean of the correlations as shown in Fig. 5.13. This approximate model is based on two constraints (1) the model approaches a single cylinder resistance as the volume porosity approaches one; and (2) the model is only a function of the volumetric hydraulic diameter and average velocity. Thus

$$R_{\perp} (90^\circ) = \frac{6.0}{(Re_v)^{0.15}} \frac{1}{D_v} \frac{\rho |\langle v \rangle|}{2} \langle v_{\perp} (90^\circ) \rangle \quad (5.35)$$

This model is not very accurate. It was developed here to emphasize the limitations of rod arrangement dependent correlations, help motivate the development of more precise array independent crossflow correlations, and furnish an average crossflow correlation for use in the inclined flow development to follow.

The crossflow correlation form used subsequently is

$$b_{\perp} = \frac{B}{(Re_v)^m} \quad (5.36)$$

When numerical values are required we shall use $B = 6.0 \delta_v^2$ and $m = 0.15$.

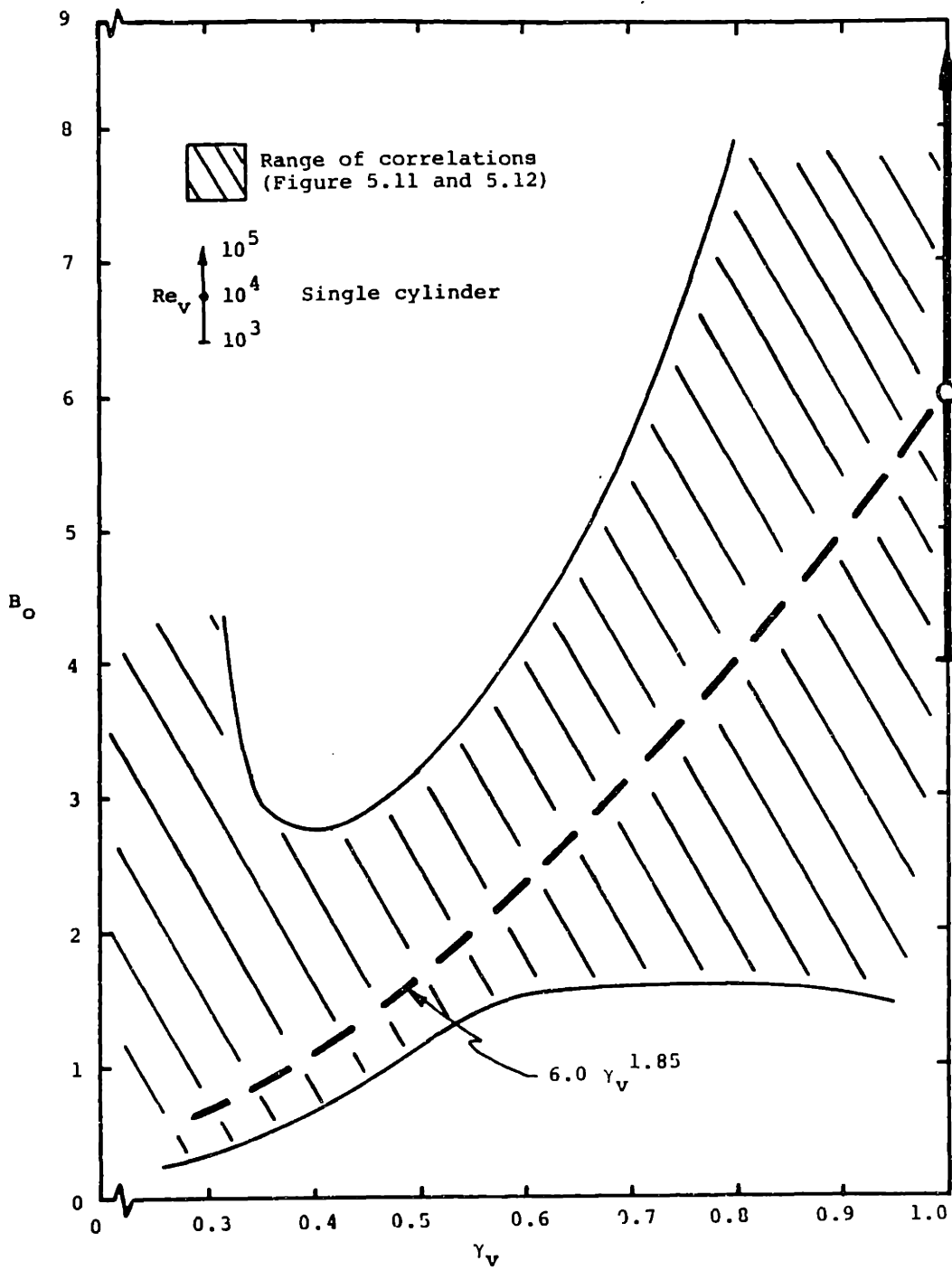


Figure 5.13 Array independent crossflow correlation.

5.5 Inclined Flow Resistance

Data on flow resistance for inclined flows in a rod array are very sparse; consequently explicit correlations for inclined flows do not exist. To overcome this deficiency the limited data are used in conjunction with current parallel and crossflow correlations to develop superposition models. Superposition models basically construct the total flow resistance vector from known correlations for the principal component directions utilizing appropriate compensating velocities and lengths.

5.5.1 Single Cylinder Superposition Model

A well documented example of superposition is the principle of independence for form drag across an inclined cylinder. It has been shown theoretically for laminar flow [W.5], and experimentally for turbulent flow [B.8, H.1], that for inclined cylinders of equal crossflow component velocity, the pressure distribution, separation point, and consequently form drag are equal. This means the total form drag is dependent only on the crossflow velocity component, independent of the parallel flow component; hence the name principle of independence. The total form drag for an inclined cylinder, therefore, can be evaluated from a correlation for pure crossflow when the correct compensating velocity is used. Fig. 5.14 graphically illustrates the principle of independence.

The above observations suggest some additional questions:

- (1) Can the skin friction force also be evaluated by the principle of independence?
- (2) Does the principle of independence also apply to rod arrays? Is

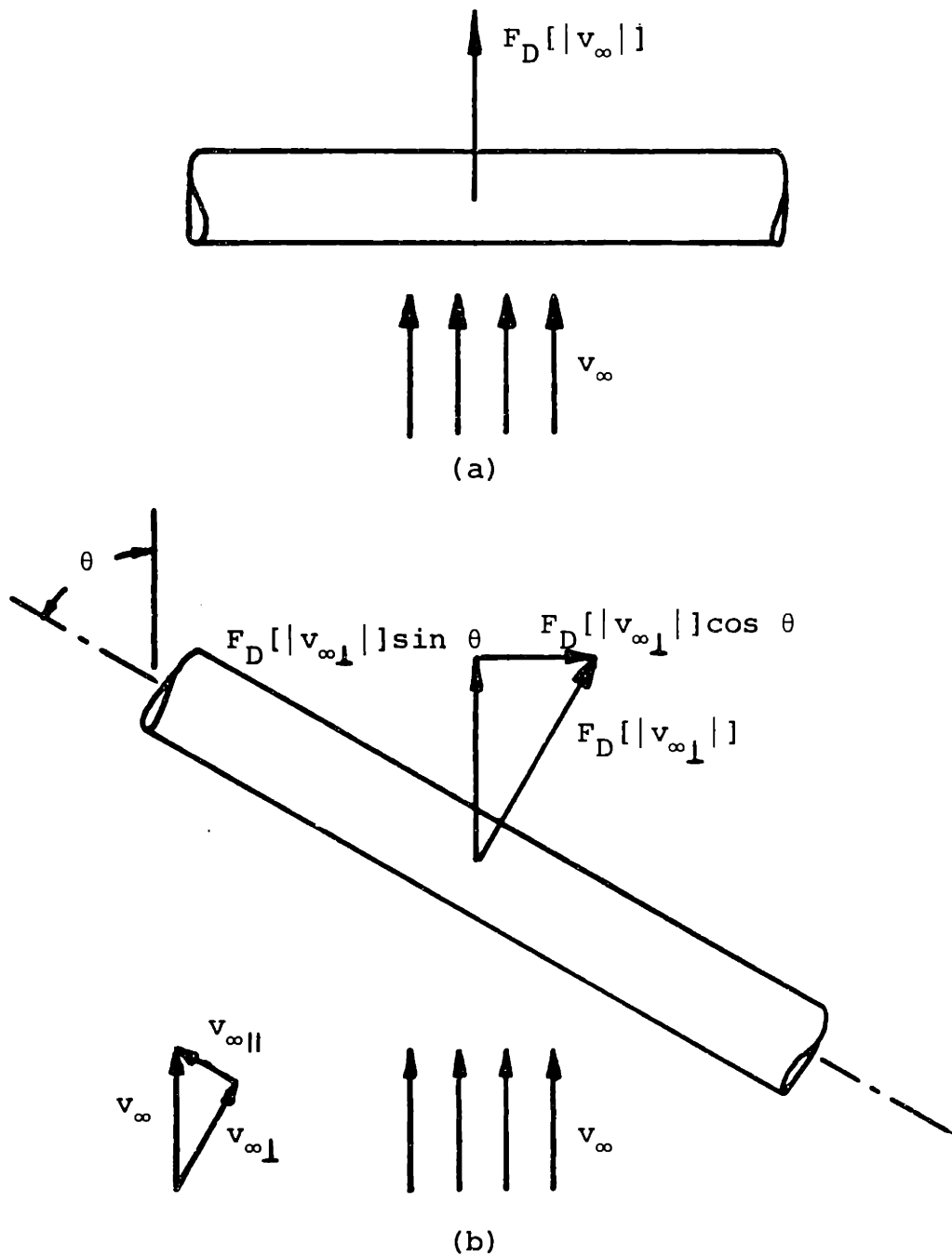


Figure 5.14 Principle of independence for inclined cylinder.

some other superposition principle more appropriate? or is the concept of superposition not applicable for rod arrays?

To answer these questions we present several superposition models developed for rod arrays and compare them with the available experimental data base.

5.5.2 Rod Array Superposition Models

All the superposition models discussed here are based on choosing an appropriate compensating characteristic velocity and retaining the characteristic lengths as defined in the one-dimensional correlations. Individual superposition models for the parallel and crossflow components of Eq. (5.26) will be described, then specific combinations of the individual models will be compared with data.

5.5.2.1 Parallel Flow Component

We define the parallel flow superposition factor, $g_1(\theta)$, as the parallel flow resistance component for a flow at inclination θ , normalized by the resistance for the flow if it were purely parallel

$$g_1(\theta) \triangleq \frac{R_{\parallel}(\theta)}{R_{\parallel}(0^\circ)} = \frac{f_{\theta\parallel}[\underline{u}] \frac{|\underline{u}|}{u_{\parallel}}}{f_{\parallel}[\langle \underline{v} \rangle] \langle v_{\parallel}(0^\circ) \rangle} \quad (5.37)$$

Model ①

This model assumes the principle of independence holds for skin friction in rod arrays, so

$$f_{\theta\parallel}[\underline{u}] = f_{\parallel}[|u_{\parallel}|] \frac{|u_{\parallel}|}{|\underline{u}|} \quad (5.38)$$

where the characteristic velocity \underline{u} is the average velocity $\langle \underline{v} \rangle$, giving

$$g_1(\theta) = \frac{f_{||} [|\langle \underline{v}_{||} \rangle|] |\langle \underline{v}_{||} \rangle| \langle \underline{v}_{||} \rangle}{f_{||} [|\langle \underline{v} \rangle|] |\langle \underline{v} \rangle| \langle \underline{v}_{||} (0^\circ) \rangle} \quad (5.39)$$

Now substituting in Eq. (5.30) for $f_{||}$, noting that $\langle \underline{v}_{||} (0^\circ) \rangle = |\langle \underline{v} \rangle|$ gives the parallel superposition factor

$$g_1(\theta) = \left| \frac{\langle \underline{v}_{||} \rangle}{\langle \underline{v} \rangle} \right|^{2-n} \frac{\langle \underline{v}_{||} \rangle}{|\langle \underline{v}_{||} \rangle|} = (\cos \theta)^{2-n} \quad (5.40)$$

where for the second equality we have restricted θ to the first quadrant ($\langle \underline{v}_{||} \rangle$ is positive). Throughout the remainder of the chapter we will assume θ varies between only 0 and 90 degrees. More general expressions covering all angles can be developed simply by including the normalized directional terms (i.e., $\langle \underline{v}_{||} \rangle / |\langle \underline{v}_{||} \rangle|$).

Models (2) and (3)

A more realistic model does not assume that the form drag principle holds for skin friction, but instead the parallel friction

factor is independent of flow direction $f_{\theta||}[\underline{u}] = f_{||}[|\underline{u}|]$ thus

$$\begin{aligned} g_1(\theta) &= \frac{f_{||} [|\langle \underline{v} \rangle|] |\langle \underline{v} \rangle| \langle \underline{v}_{||} \rangle}{f_{||} [|\langle \underline{v} \rangle|] |\langle \underline{v} \rangle| \langle \underline{v}_{||} (0^\circ) \rangle} = \left| \frac{\langle \underline{v}_{||} \rangle}{\langle \underline{v} \rangle} \right| \frac{\langle \underline{v}_{||} \rangle}{|\langle \underline{v}_{||} \rangle|} \quad (5.41) \\ &= \cos \theta \end{aligned}$$

This model is called the magnitude-component since the magnitude of resistance is directly proportional to the component of velocity.

(Models (2) and (3) are identical with respect to the parallel superposition factor.)

Model (4)

Model (4) proposed by Böttgenbach [B.4] amplifies the parallel flow friction factor of model (2) and (3), to match his experimental data

$$g_1(\theta) = \frac{f_{||} [|\langle \underline{v} \rangle|]}{(\cos 0.9\theta)^2} \frac{|\langle \underline{v} \rangle| \langle v_{||} \rangle}{f_{||} [|\langle \underline{v} \rangle|] |\langle \underline{v} \rangle| \langle v_{||} (0^\circ) \rangle} = \frac{\cos \theta}{(\cos 0.9\theta)^2} \quad (5.42)$$

Model (5)

Finally we introduce two new models. The first is a mechanistic model based on the inclined flow mainstream characteristic velocity $\underline{v}_{(1)}$ instead of $\langle \underline{v} \rangle$. The velocity $\underline{v}_{(1)}$ is modeled simply as a smoothly varying velocity between the two limits-- $\langle v_{||} (0^\circ) \rangle$ for parallel flow and $v_{ms \perp} (90^\circ)$ for crossflow,

$$\underline{v}_{(1)} = \langle v_{||} \rangle \underline{e}_{||} + v_{ms \perp} \underline{e}_{\perp} \quad (5.43)$$

or

$$\begin{aligned} |\underline{v}_{(1)}| &= \sqrt{|\langle \underline{v} \rangle|^2 \cos^2 \theta + |v_{ms \perp}|^2 \sin^2 \theta} \\ &= |\langle \underline{v} \rangle| \sqrt{\cos^2 \theta + \frac{1}{\delta_v^2} \sin^2 \theta} \end{aligned} \quad (5.44)$$

and

$$\tan \theta_{(1)} = \frac{|v_{ms \perp}| \sin \theta}{|\langle \underline{v} \rangle| \cos \theta} = \frac{1}{\delta_v} \tan \theta \quad (5.45)$$

Figure 5.15 shows graphically the construction of $\underline{v}_{(1)}$ from $\langle \underline{v} \rangle$, $v_{ms \perp}$, and θ . A more physical development of $\underline{v}_{(1)}$ is reserved for Chapter 6.

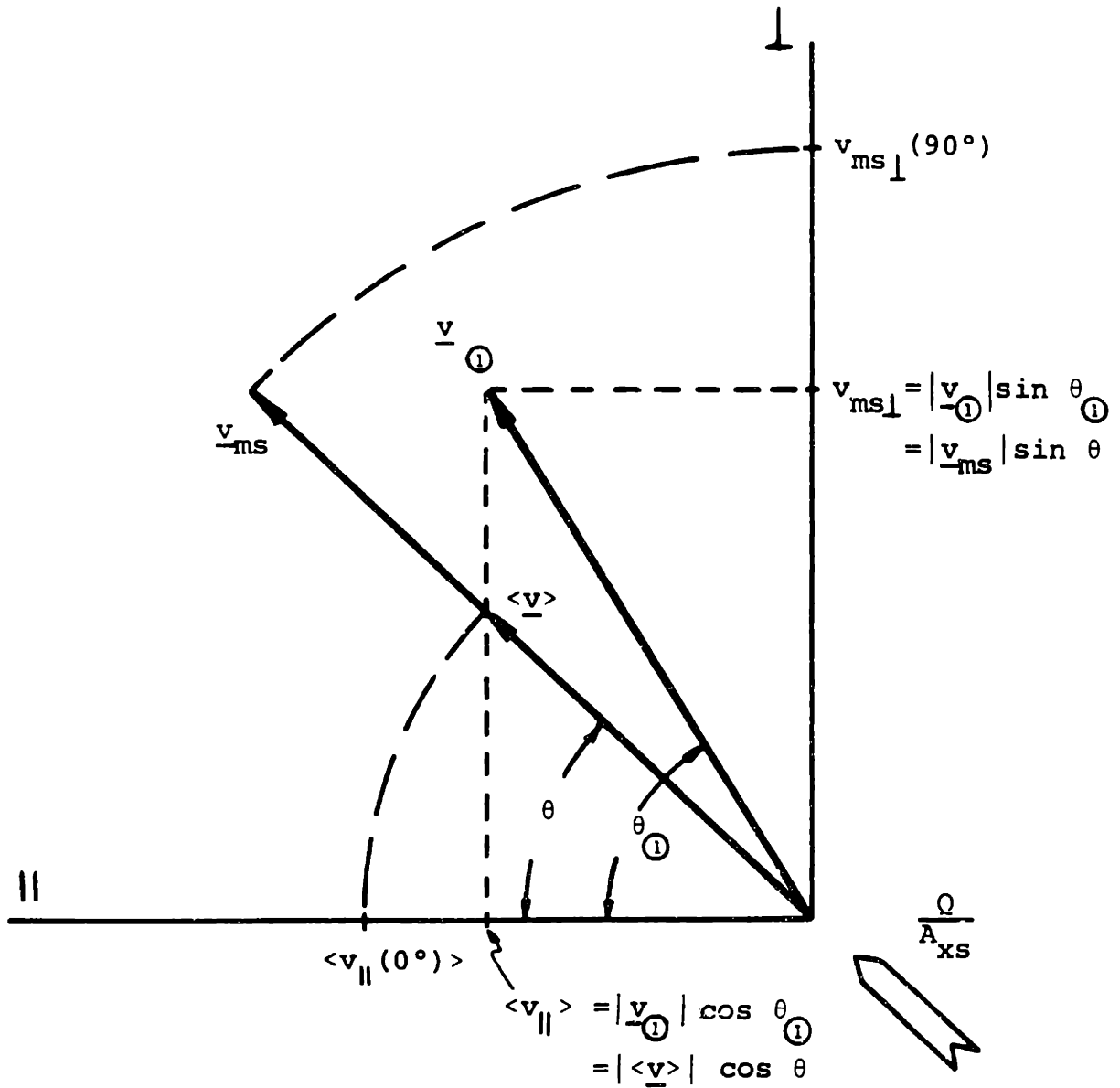


Figure 5.15 Inclined flow mainstream velocity model.

Replacing u by $v_{(1)}$ in Eq. (5.37) and assuming the magnitude-component principle gives

$$\begin{aligned}
 g_1(\theta) &= \frac{f_{||} [|v_{(1)}|] |v_{(1)}| v_{(1)||}}{f_{||} [|\langle v \rangle|] |\langle v \rangle| \langle v_{||} (0^\circ) \rangle} \\
 &= (\cos^2 \theta + \frac{1}{\delta_v^2} \sin^2 \theta)^{\frac{1-n}{2}} \cos \theta
 \end{aligned}
 \tag{5.46}$$

Model (6)

In contrast to model (5) which proposes a more physical characteristic velocity, model (6) is simply a generalized form of the first three models

$$f_{\theta||} [\underline{u}] = f_{||} [\underline{u}] \left| \frac{u_{||}}{\underline{u}} \right|^{n'}
 \tag{5.47}$$

Where $\underline{u} = \langle v \rangle$ and n' is a correlated parameter which may be a function of geometry, inclination and/or Reynolds number. The parallel superposition factor becomes

$$g_1(\theta) = \left| \frac{\langle v_{||} \rangle}{\langle v \rangle} \right|^{n'+1} \frac{\langle v_{||} \rangle}{|\langle v_{||} \rangle|} = (\cos \theta)^{n'+1}
 \tag{5.48}$$

5.5.2.2 Crossflow Component

Analogous to $g_1(\theta)$ we define the crossflow superposition factor $h_1(\theta)$ as

$$h_1(\theta) \triangleq \frac{R_{\perp}(\theta)}{R_{\perp}(90^\circ)} = \frac{b_{\theta\perp}[\underline{u}] \left| \frac{\underline{u}}{|\underline{u}|} \right| u_{\perp}}{b_{\perp} \left[\left| \frac{\underline{v}_{ms}}{|\underline{v}_{ms}|} \right| \right] \left| \frac{\underline{v}_{ms}}{|\underline{v}_{ms}|} \right| v_{ms\perp}(90^\circ)} \quad (5.49)$$

Model ①

As shown in Sec. 5.2.4, b_{\perp} is the combination of both skin friction and form drag. If it is assumed that the form drag is the dominant force and the principle of independence applies for rod arrays, then

$$b_{\theta\perp}[\underline{u}] = b_{\perp} \left[\left| \frac{\underline{u}}{|\underline{u}|} \right| \right] \frac{\left| \frac{\underline{u}}{|\underline{u}|} \right|}{\left| \frac{\underline{u}}{|\underline{u}|} \right|} \quad (5.50)$$

The characteristic velocity is now \underline{v}_{ms} , thus

$$h_1(\theta) = \frac{b_{\perp} \left[\left| \frac{\underline{v}_{ms\perp}}{|\underline{v}_{ms\perp}|} \right| \right] \left| \frac{\underline{v}_{ms\perp}}{|\underline{v}_{ms\perp}|} \right| v_{ms\perp}}{b_{\perp} \left[\left| \frac{\underline{v}_{ms}}{|\underline{v}_{ms}|} \right| \right] \left| \frac{\underline{v}_{ms}}{|\underline{v}_{ms}|} \right| v_{ms\perp}(90^\circ)} \quad (5.51)$$

substituting in Eq. (5.36) for b_{\perp} and noting $v_{ms\perp}(90^\circ) = |\underline{v}_{ms}|$ gives

$$h_1(\theta) = \frac{\left| \frac{\underline{v}_{ms\perp}}{|\underline{v}_{ms\perp}|} \right|^{2-m} \frac{v_{ms\perp}}{|\underline{v}_{ms\perp}|}}{\left| \frac{\underline{v}_{ms}}{|\underline{v}_{ms}|} \right|} = (\sin \theta)^{2-m} \quad (5.52)$$

Again the last equality is true when θ is restricted to the first quadrant.

Model ②

For the case where skin friction is important or the principle of independence is not valid for rod arrays a model based on a constant crossflow coefficient, $b_{\theta\perp} [\underline{u}] = b_{\perp} [|\underline{u}|]$, and characteristic velocity v_{ms} , is postulated

$$h_1(\theta) = \frac{b_{\perp} [|\underline{v}_{ms}|] |\underline{v}_{ms}| v_{ms\perp}}{b_{\perp} [|\underline{v}_{ms}|] |\underline{v}_{ms}| v_{ms\perp} (90^\circ)} = \frac{v_{ms\perp}}{v_{ms}} \frac{v_{ms\perp}}{v_{ms\perp}} = \sin \theta \quad (5.53)$$

Model ③

Todreas and Coëffé [T.2] suggested correcting Model ② based on data interpreted by Idel'chik [I.2].

Their resultant model is

$$h_1(\theta) = \eta'(\theta) \sin \theta \quad (5.54)$$

where

θ	0°	30°	45°	60°	90°
$\eta'(\theta)$	0.25	0.60	0.76	0.94	1.00

Model ④

In contrast, Böttgenbach, based on his data, proposed a different correction factor, $(\sin \theta)^{0.9}$, giving

$$h_1(\theta) = \frac{b_{\perp} [|\underline{v}_{ms}|] (\sin \theta)^{0.9} |\underline{v}_{ms}| v_{ms\perp}}{b_{\perp} [|\underline{v}_{ms}|] |\underline{v}_{ms}| v_{ms\perp} (90^\circ)} = (\sin \theta)^{1.9} \quad (5.55)$$

Model (5)

This new model assumes the principle of independence, but based on the inclined mainstream velocity $v_{\perp 1}$ instead of the crossflow velocity v_{ms}

$$h_1(\theta) = \frac{b_{\perp} [v_{\perp 1}] |v_{\perp 1}| v_{\perp 1}}{b_{\perp} [v_{ms}] |v_{ms}| v_{ms \perp} (90^\circ)} = \left| \frac{v_{\perp 1}}{v_{ms}} \right|^{2-m} \frac{v_{\perp 1}}{|v_{\perp 1}|} \quad (5.56)$$

However for the model of $v_{\perp 1}$ given in Eq. (5.44) we get $v_{\perp 1} = v_{ms \perp}$, or

$$h_1(\theta) = (\sin \theta)^{2-m} \quad (5.51)$$

which is simply model (1).

Model (6)

This last model is simply a generalized form of models (1) through (4)

$$b_{\theta \perp} [u] = b_{\perp} [|u|] \left| \frac{u_{\perp}}{u} \right|^{m'}$$

where $u = v_{ms}$ and m' is a correlated parameter. The crossflow superposition factor becomes

$$h_1(\theta) = \left| \frac{v_{ms \perp}}{v_{ms}} \right|^{m'-1} \frac{v_{ms \perp}}{|v_{ms \perp}|} = (\sin \theta)^{m'-1} \quad (5.58)$$

5.5.2.3 Summary

Table 5.4, Fig. 5.16, and 5.17 summarize and compare the different superposition models. An interesting point is that the correction factors of Todreas-Coëffé (Model (3)) and Böttgenbach (Model (4)) essentially convert the crossflow superposition model (2) back into

TABLE 5.4

Superposition Models

Model	$g_1(\theta)$	$h_1(\theta)$	Constants	Reference
①	$(\cos \theta)^{2-n}$	$(\sin \theta)^{2-m}$	$n = 0.25$ $m = 0.15$	T-H codes: COBRA-TF [C.4] TRAC-PIA [T.3] THERMIT [R.3]
②	$\cos \theta$	$\sin \theta$	-----	Gorchakov et. al. [G.6]
③	$\cos \theta$	$\eta'(\theta)\sin \theta$	$\eta'(\theta)$ given in Equation (5.54)	Todreas-Coëffé [T.2]
④	$\frac{\cos \theta}{(\cos 0.98)^2}$	$(\sin \theta)^{1.9}$	-----	Böttgenbach [B.4]
⑤	$(\cos^2 \theta + \frac{1}{\delta^2} \sin^2 \theta)^{\frac{1-n}{2}} \cos \theta$ $\delta^2 = \frac{v}{v}$	$(\sin \theta)^{2-m}$	$n = 0.25$ $m = 0.15$ $\delta_v = 0.5$	This Study
⑥	$(\cos \theta)^{n'+1}$	$(\sin \theta)^{m'+1}$	$n' = 0$ $m' = 0.4$	This Study

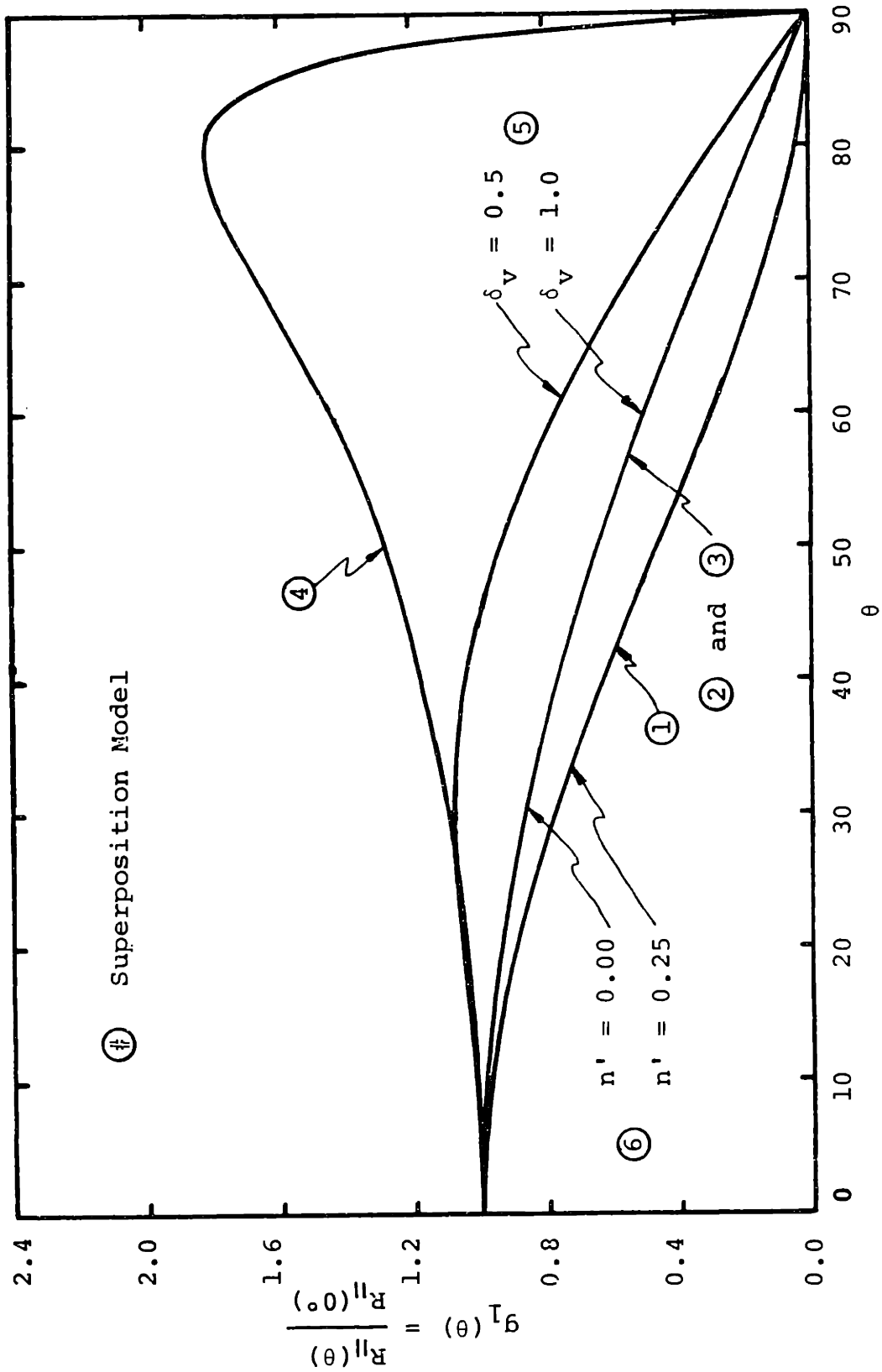


Figure 5.16 Parallel flow superposition models.

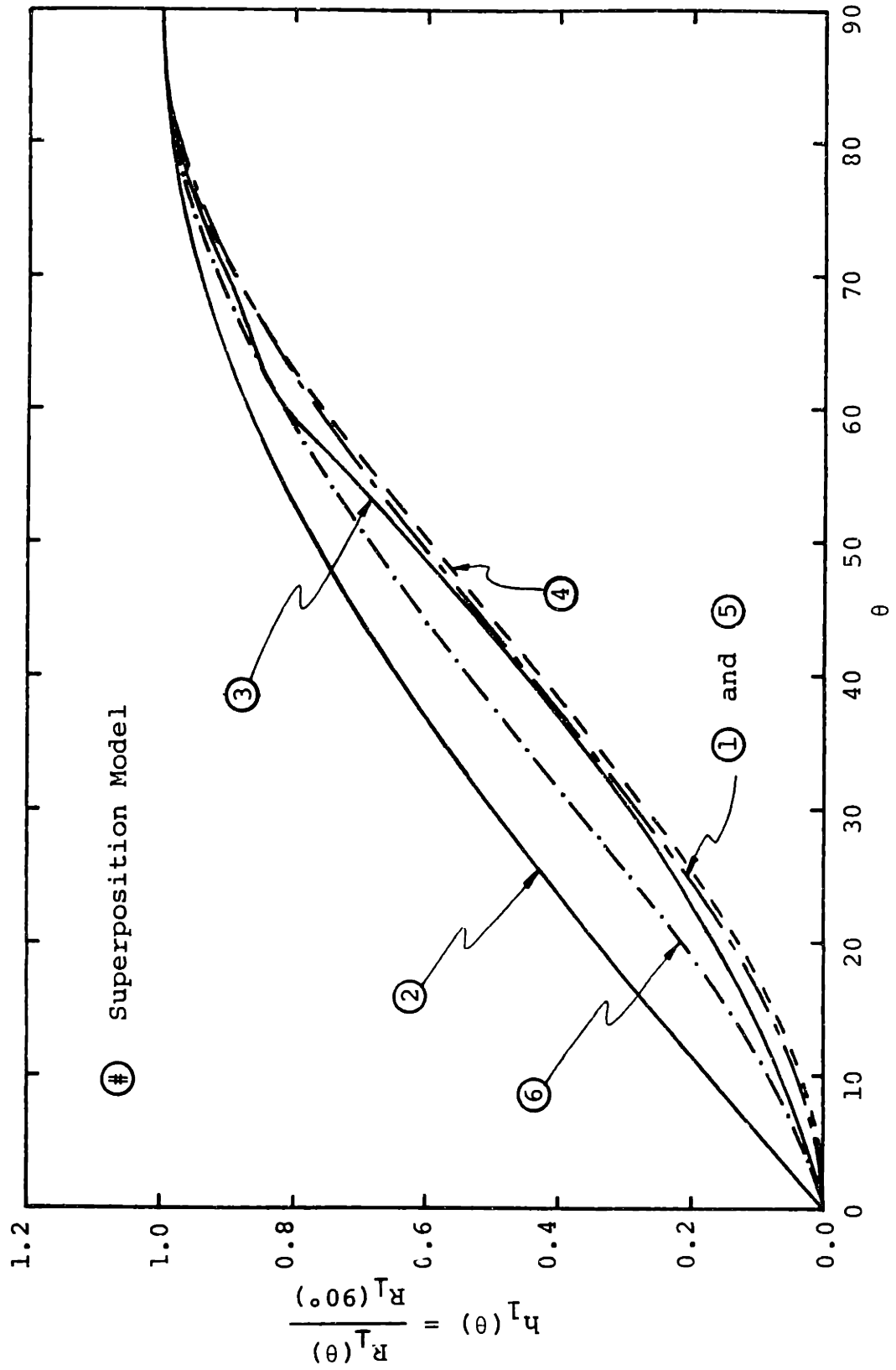


Figure 5.17 Crossflow superposition models.

model ①. There is a larger disparity between parallel superposition models, but as will be seen later, for most turbulent flow conditions this factor has an insignificant effect on the total flow resistance. Also notice that all the reviewed superposition models are a function of flow inclination only. The Reynolds number and geometry dependences are assumed correctly accounted for by the one-dimensional parallel and crossflow correlations.

Ideally, using the appropriate superposition models $g_1(\theta)$ and $h_1(\theta)$, the total flow resistance can be calculated from

$$\langle \underline{R} \rangle = R_{||}(0^\circ) g_1(\theta) \underline{e}_{||} + R_{\perp}(90^\circ) h_1(\theta) \underline{e}_{\perp} \quad (5.59)$$

The remainder of this chapter is concerned with assessing the above superposition models with past and new data.

5.6 Lift/Drag Flow Resistance Components

5.6.1 Coordinate System

Most of the available data for inclined flows is limited to the drag component of resistance (component in the average flow direction). Therefore we introduced a second (x,y) coordinate system where x is the average flow direction (drag force direction) and y is perpendicular to the average flow direction (lift force direction). Mathematically

$$\langle \underline{v} \rangle = v_x \underline{e}_x + v_y \underline{e}_y \quad (5.60)$$

where

$$\begin{aligned} v_x &= |\langle \underline{v} \rangle| \\ v_y &= 0 \end{aligned} \quad (5.61)$$

The resistance vector (Eq. (5.26)) then becomes

$$\langle \underline{R} \rangle = R_x(\theta) \underline{e}_x + R_y(\theta) \underline{e}_y \quad (5.62)$$

where $R_x(\theta) = R_{||}(\theta) \cos \theta + R_{\perp}(\theta) \sin \theta \quad (5.63)$

$$R_y(\theta) = -R_{||}(\theta) \sin \theta + R_{\perp}(\theta) \cos \theta$$

Both vectors and components are shown in Fig. 5.18.

5.6.2 Composite Superposition Models

To assess the superposition models on their merit alone, independent of the absolute magnitude of the total resistance, we normalize the above equations by the crossflow resistance $R_x(90^\circ)$ ($= R_{\perp}(90^\circ)$), giving

$$\frac{1}{R_x(90^\circ)} \langle \underline{R} \rangle = \frac{R_x(\theta)}{R_x(90^\circ)} \underline{e}_x + \frac{R_y(\theta)}{R_x(90^\circ)} \underline{e}_y \quad (5.64)$$

where

$$\frac{R_x(\theta)}{R_x(90^\circ)} = \left(\frac{R_{||}(0^\circ)}{R_{\perp}(90^\circ)} \right) g_1(\theta) \cos \theta + h_1(\theta) \sin \theta \quad (5.65)$$

$$\frac{R_y(\theta)}{R_x(90^\circ)} = \left(\frac{R_{||}(0^\circ)}{R_{\perp}(90^\circ)} \right) g_1(\theta) \sin \theta + h_1(\theta) \cos \theta$$

All inclined flow data can also be put in this form since $R_x(90^\circ)$ was measured in all cases. Notice that to evaluate the above expressions using the individual superposition models the ratio of parallel to crossflow resistance is also needed.

In Fig. 5.19 the parallel/crossflow ratio is evaluated for the generalized models developed in Sections 5.3 and 5.4. For turbulent flow the ratio is approximately 0.02 ± 0.01 which means the crossflow superposition factor $h_1(\theta)$ dominates both components of Eq. (5.64) for

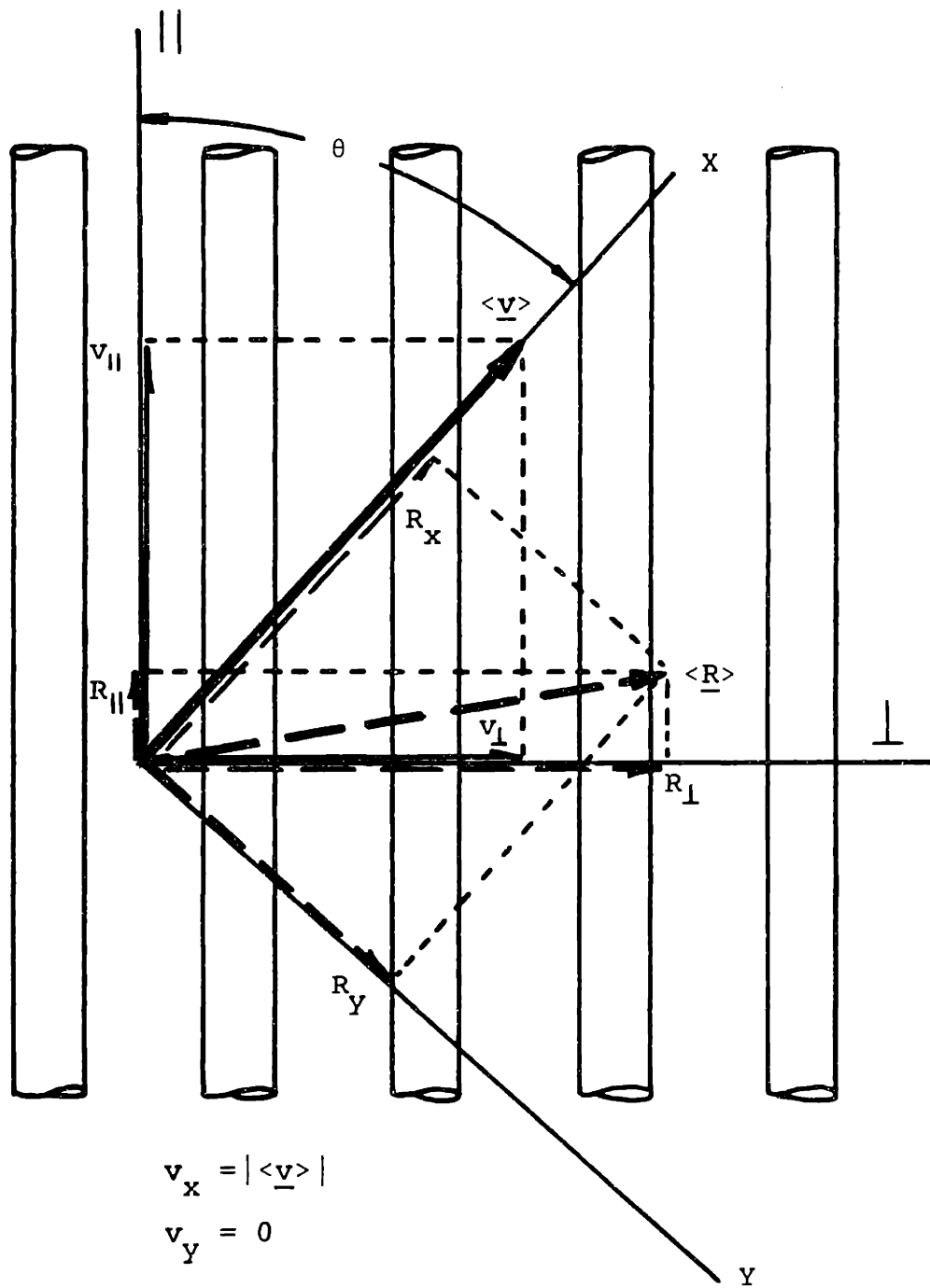


Figure 5.18 (x,y) coordinate system.

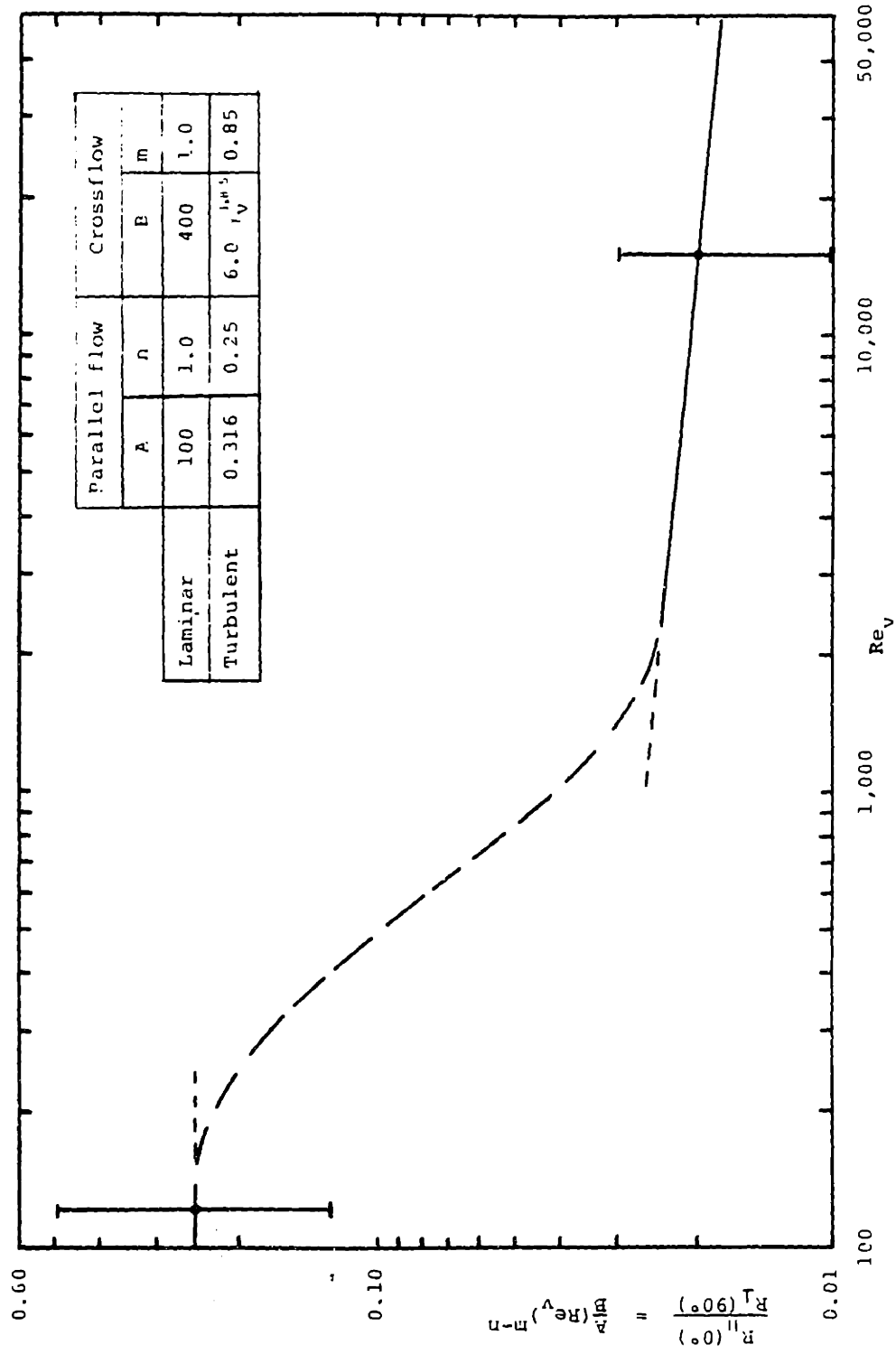


Figure 5.19 Range of parallel/crossflow ratio.

all angles except very close to parallel flow ($\theta < 3^\circ$). Hence the exact numerical value of the parallel/crossflow ratio is insignificant. For all data-model comparisons a value of 0.02 is used.

Theoretically, all combinations of the individual superposition factors $g_1(\theta)$ and $h_1(\theta)$ should be examined, however since $g_1(\theta)$ has a negligible contribution we shall consider only the six basic combinations listed in Table 5.4.

The normalized drag and lift components are plotted in Fig. 5.20 and 5.21. Because $h_1(\theta)$ is the dominant term models ①, ③, ④, and ⑤ are all still grouped together. In comparisons with all the inclined flow data we shall use only models ① and ② since they represent the span of the different models. After assessing the composite superposition models (actually $h_1(\theta)$) the significance of superposition factor $g_1(\theta)$ will be appraised; but first we present the inclined flow resistance data base.

5.7 Published Data Base

Previous to this work four researchers have published data for flow resistance in inclined rod arrays: Kazakevich [K.2], Groehn [G.4], Möller [M.3], and Böttgenbach [B.4]. Several other researchers have also published correlations for the normalized drag component of resistance (i.e., $R_x(\theta)/R_x(90^\circ)$) [I.2, G.1, Z.1].

5.7.1 Kazakevich

The first published data for inclined rod array flow were by Kazakevich in 1952. He measured pressure drops of air flows progressively across one to seven rows of rods for inclinations of 90, 60, 45 and 30 degrees. The pressure drop measured was in the direction

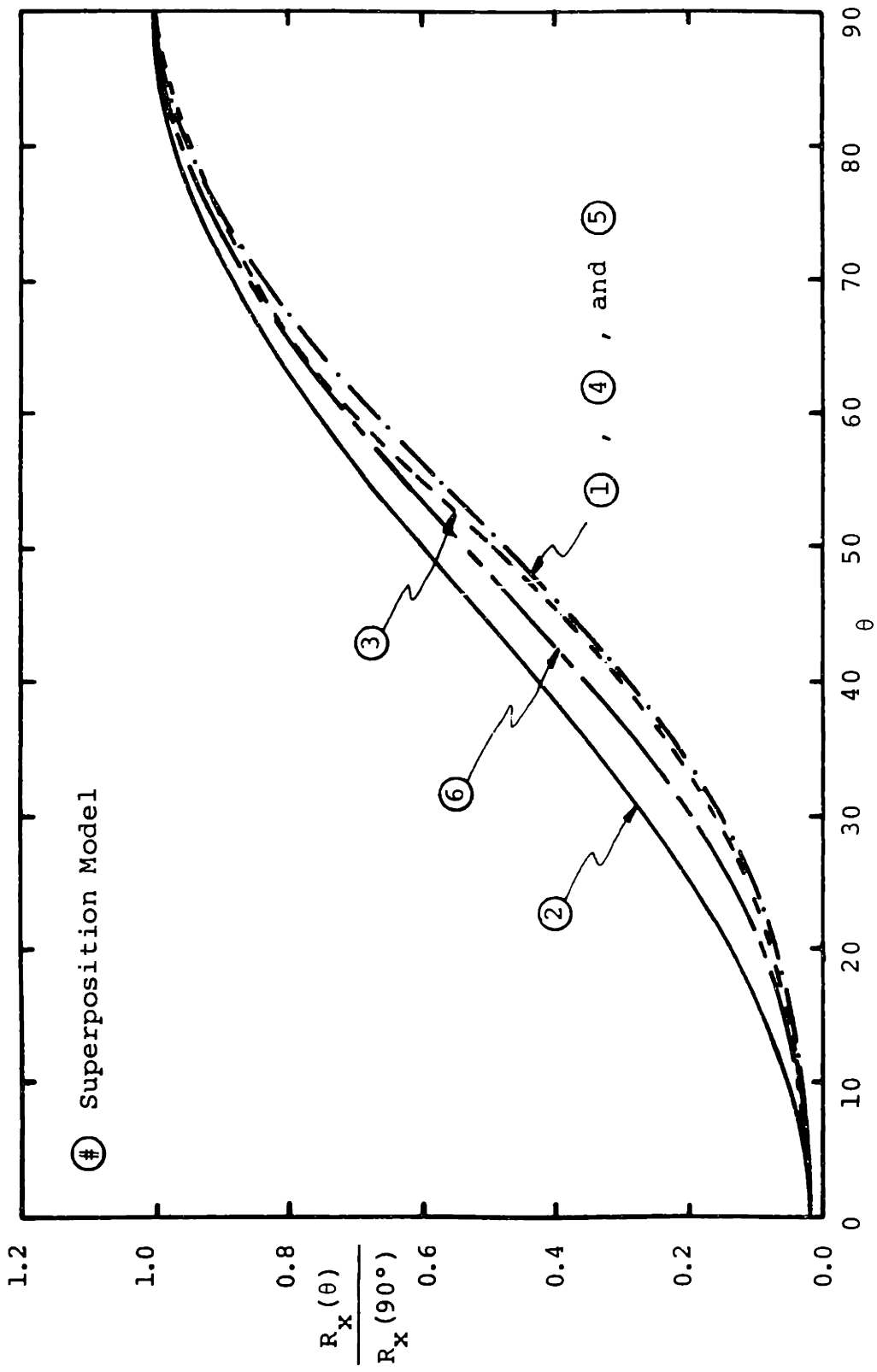


Figure 5.20 Superposition model prediction of drag resistance component.

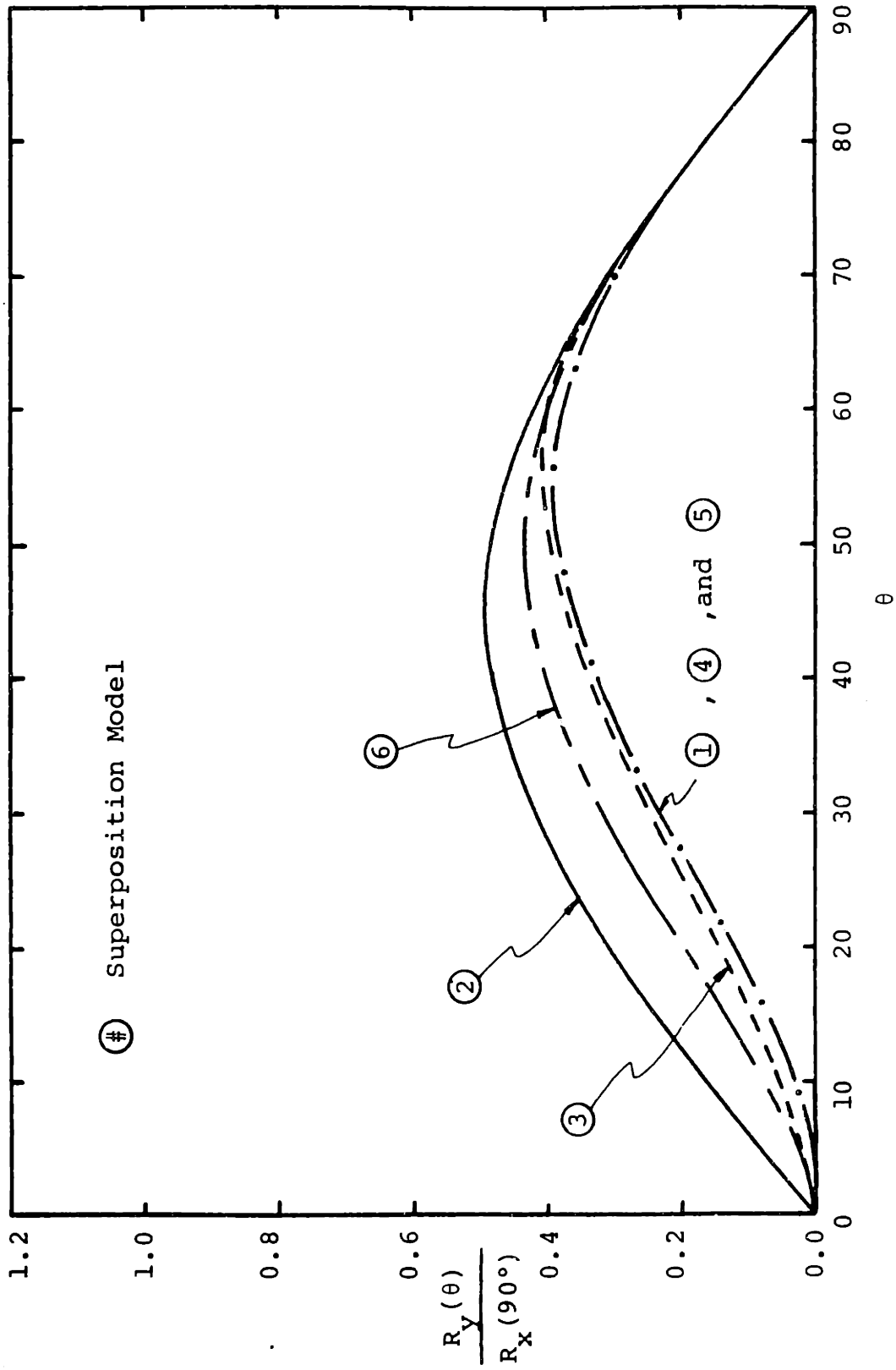


Figure 5.21 Superposition model prediction of lift resistance component.

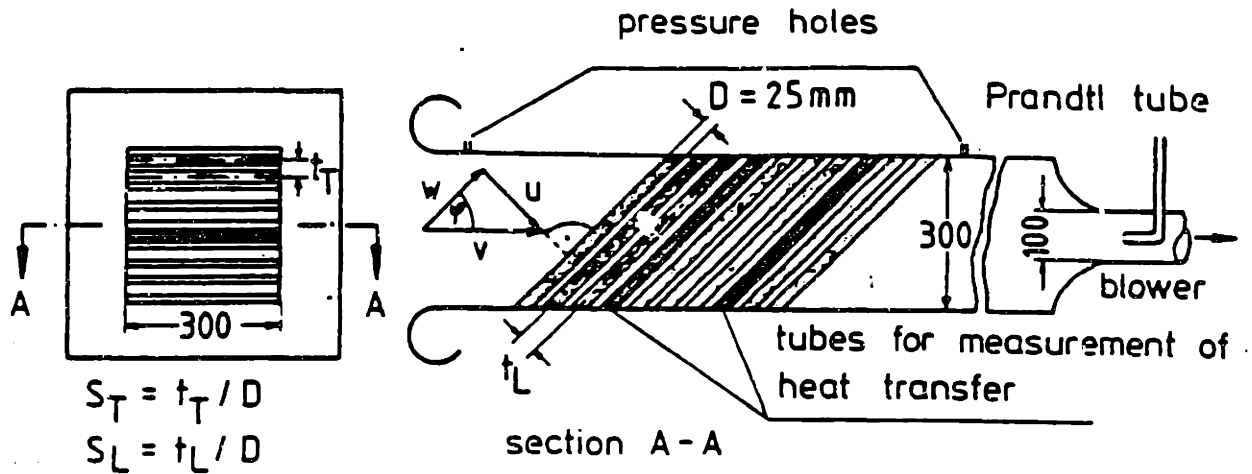
of flow yielding only the drag component of resistance. He measured six in-line and eight staggered rod arrangements for Reynolds numbers, Re_d , from 7,000 to 100,000.

5.7.2 Groehn

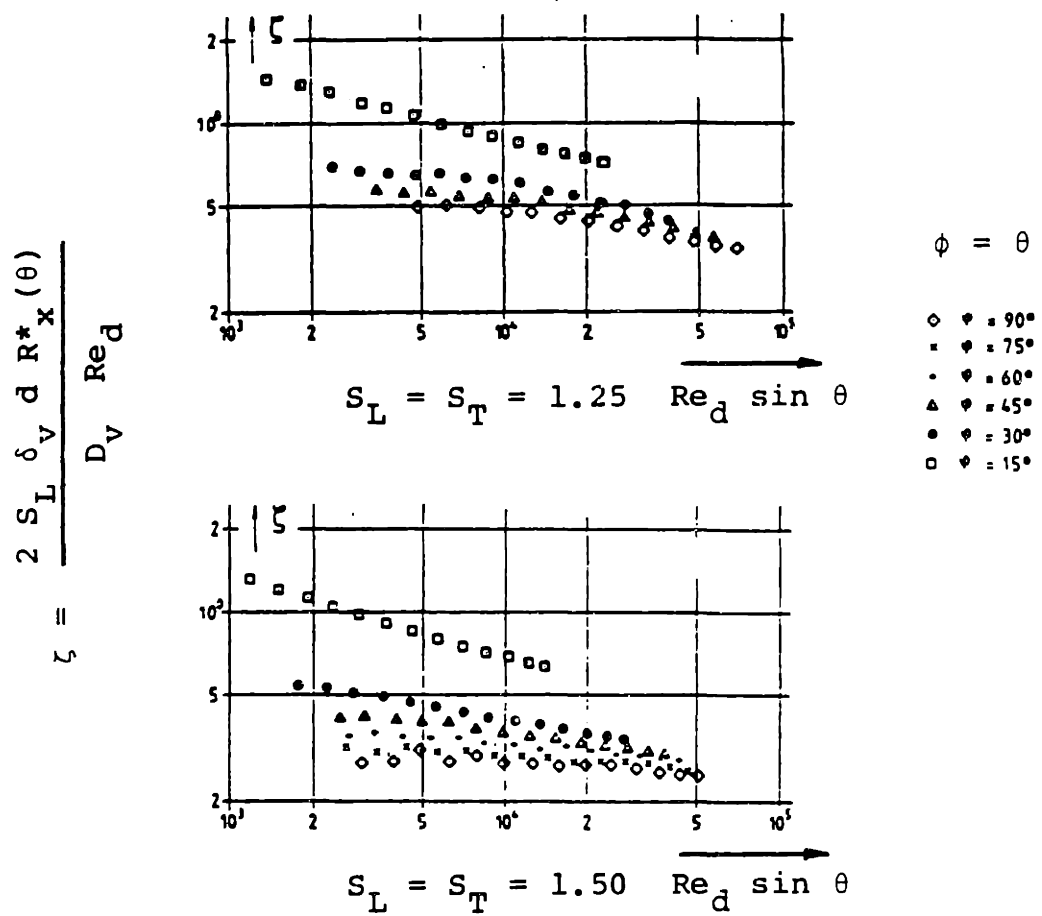
More recently, Groehn made measurements similar to Kazakevich. Groehn, however, measured air flow pressure drops progressively across one to ten rows of rods and for a more extensive range of inclinations: 90, 75, 60, 45, 30, and 15 degrees. His experimental apparatus and a sample of his data are shown in Fig. 5.22. Groehn's goal was to develop a more consistent pressure drop data set while also obtaining heat transfer data for inclined arrays. Like Kazakevich he only measured the drag component of resistance.

5.7.3 Möller

Möller developed a rod arrangement independent, two-dimensional flow resistance correlation using superposition model (1) and specific parallel and crossflow correlation from the literature. He attempted to confirm the model by making both parallel and perpendicular pressure drop measurements in inclined arrays. His rod arrays were of irregular arrangements at inclinations of 90, 60, and 45 degrees. Because of limitations of his air blower system he took only a few data points at a Reynolds number, Re_v , of $\approx 1,100$. The few data points he did obtain are questionable because (1) he attempted to measure the parallel component of resistance directly, which is a very small quantity leading to large experimental errors and (2) his array geometry was not well controlled between different flow inclinations.



(a)



(b)

Figure 5.22 Groehn's (a) experimental setup and (b) sample data [G.1].

5.7.4 Böttgenbach

The most comprehensive inclined flow data taken to date were by Böttgenbach. He measured both components of flow resistance for air in a square array of $P/d = 1.2$. He measured the resistance vector across one to ten rows of rods for inclinations of 90, 75, 60, 45 and 30 degrees. His data were taken in the high Reynolds number, Re_v , range of 55,000 to 550,000. Böttgenbach's test apparatus and data are shown in Fig. 5.23 and 5.24, respectively. The only drawback of Böttgenbach's data is a large scatter due to the localized measuring techniques he employed.

5.7.5 Data Summary

The above data base is summarized in Table 5.5. All researchers also measured the flow resistance for crossflow ($\theta = 90^\circ$) for the same Reynolds numbers range and geometries as their inclined flow measurements. Hence experiment specific normalized data can be obtained from each data set.

5.7.6 Drag Component Correlations

Several empirical correlations for the normalized drag flow resistance component have been published based on the above data and possibly additional unpublished data.

Idel'chik [I.2] proposed a tabular correlation based on the data of Kazakevich [K.2].

θ	30°	45°	60°	90°
$\frac{R_x(\theta)}{R_x(90^\circ)}$	0.15	0.38	0.71	1.0

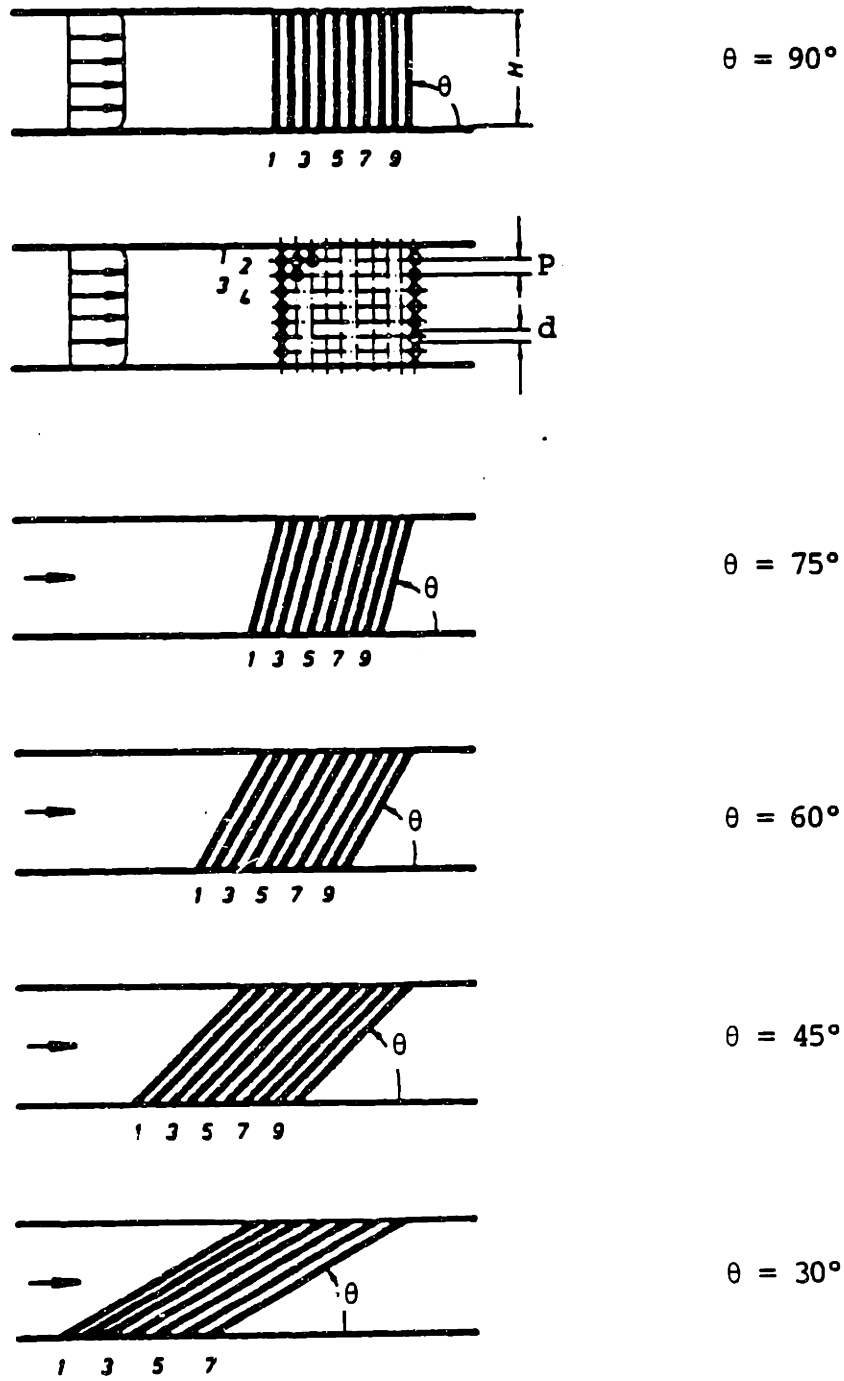


Figure 5.23 Böttgenbach's test apparatus [B.4].

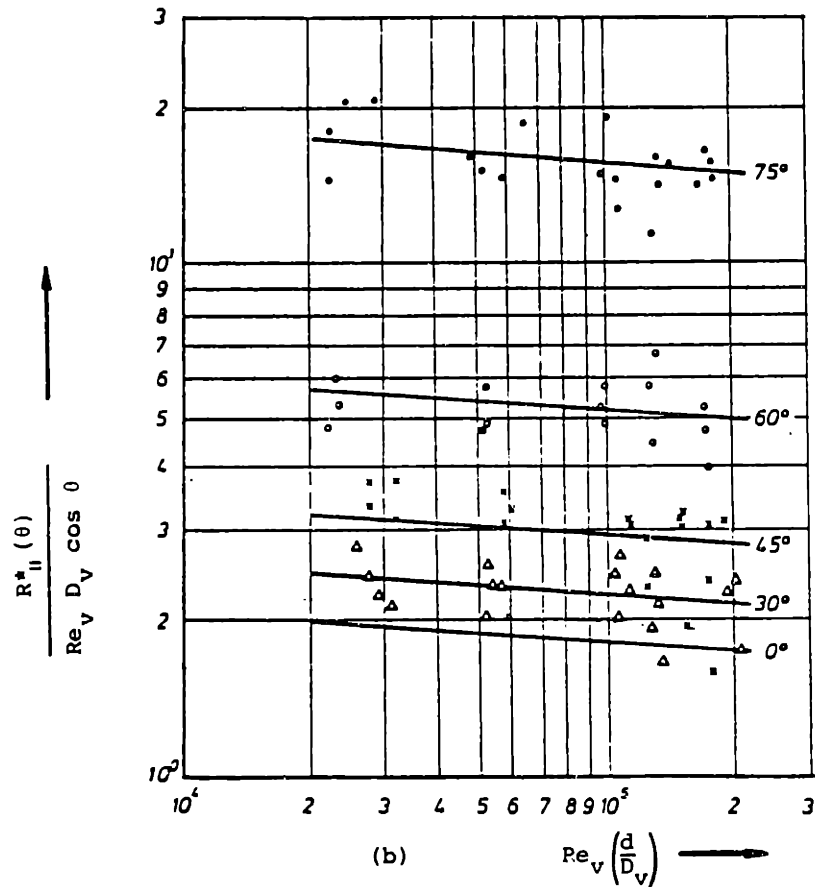
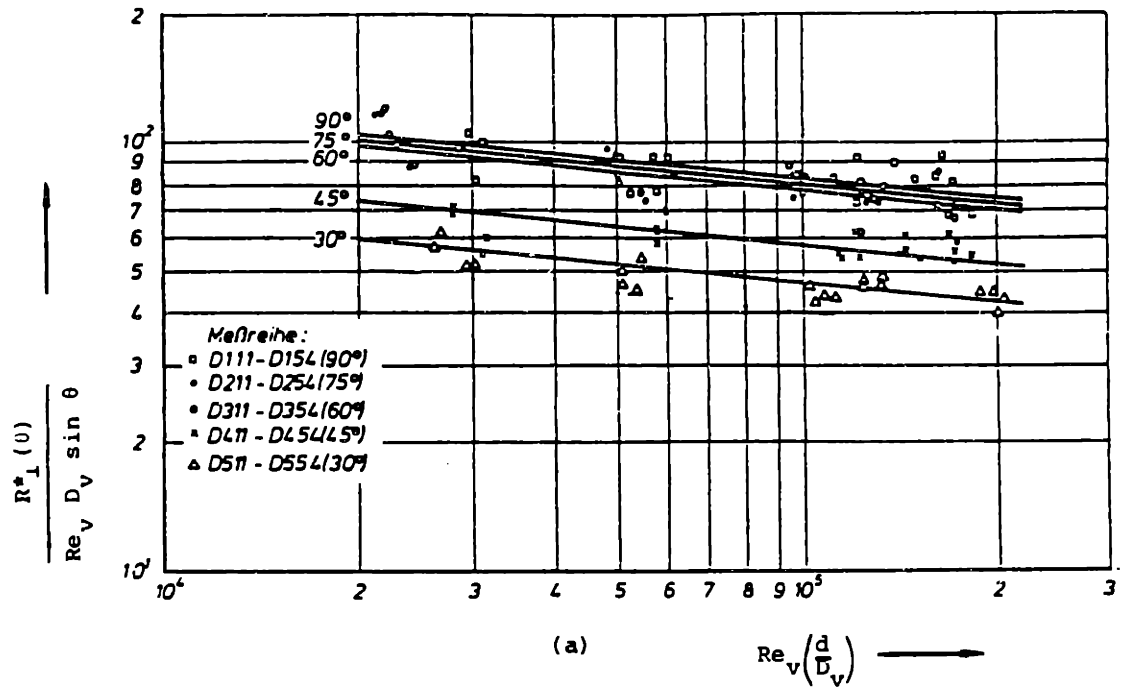


Figure 5.24 Böttgenbach's reduced data (a) crossflow component and (b) parallel flow component [B.4].

TABLE 5.5

Published Inclined Flow Data

Reference	Rod Arrangement	$\frac{S_T}{d}$	$\frac{S_L}{d}$	γ_v	θ (degree)	† rows of rods	$R_x^*(\theta)$	measured $R_y^*(\theta)$	Re_d range $\times 10^{-3}$
Kazekavich [K.2] Fluid: air	in-line	1.26	1.87	0.667	60	6	x		10-95
		1.61	1.87	0.739	60	5	x		7-80
		1.45	1.87	0.710	60	6	x		7-25
		2.90	1.87	0.855	60	6	x		7-25
		1.26	1.71	0.636	45	6	x		10-100
		1.26	1.50	0.584	30	5	x		10-100
	staggered	1.26	1.87	0.667	60	6	x		10-95
		1.61	1.87	0.739	60	6	x		7-80
		1.45	1.87	0.710	60	7	x		7-25
		1.26	1.71	0.636	45	6	x		10-100
		1.26	1.50	0.584	30	5	x		10-100
		2.90	1.87	0.855	60	7	x		7-25
		1.26	3.00	0.792	30	3	x		10-90
1.61	3.74	0.870	60	3	x		7-75		
Groehn [G.1] Fluid: air	in-line	1.50	1.50	0.651	75	10	x		2-100
					60		x		
					45		x		
					30		x		
					15		x		
		1.25	1.25	0.497	45		x		
			30		x				
			15		x				

TABLE 5.5 (continued)

Published Inclined Flow Data

Reference	Rod Arrangement	$\frac{S_T}{d}$	$\frac{S_L}{d}$	γ_v	θ (degree)	rows of rods	$R_x^*(\theta)$	measured $R_y^*(\theta)$	Re range $\times 10^{-3}$
Groehn [G.1] Fluid: air	staggered	1.50	1.30	0.597	60	10	x		2-100
					45		x		
					30		x		
					15		x		
					45		x		
30		x							
15		x							
45		x							
30		x							
15		x							
Moller [M.3] Fluid: air	irregular	-----	-----	0.53	60	-25	x	x	-1.8
				0.56	45	-25	x	x	-1.8
Bottgenbach [B.4]	in-line	1.20	1.20	0.455	75	10	x	x	55-550
					60		x	x	
					45		x	x	
					30		x	x	
					15		x	x	
This Study Fluid: water	in-line	1.50	1.50	0.651	45	-60	x	x	1-27
					30		x	x	
					0		x		

† 90 degree data was taken by all Authors for all geometries.

Groehn [G.1] compared his data to the above correlation of Idel'chik and correlations by Michejew [M.4] and VDI-Wärmeatlas [V.1]. Groehn also proposed a tentative correlation dependent on Reynolds number

$$\frac{R_x(\theta)}{R_x(90^\circ)} = (\sin \theta)^{[a(\text{Re}_d \sin \theta)^{-0.2} + 2]} \quad (5.66)$$

where $a = 3.8$ for $P/d = 1.5$.

Böttgenbach [B.7] in a review paper published before his experimental work recommended a correlation developed by Wiemer [W.4]

$$\frac{R_x(\theta)}{R_x(90^\circ)} = (\sin \theta)^{2.355} \quad (5.67)$$

More recently Zūkauskas and Ulinskas [Z.1] have proposed separate in-line and staggered correlations

$$\frac{R_x(\theta)}{R_x(90^\circ)} = 1.107 e^{-0.301(\theta)^{-2.412}} \sin \theta \quad (5.68)$$

and

$$\frac{R_x(\theta)}{R_x(90^\circ)} = 1.245 e^{-0.478(\theta)^{-1.733}} \sin \theta \quad (5.69)$$

respectively, where θ is in radians.

All these correlations are plotted in Fig. 5.25. They are valid only for angles greater than about 30 degrees. Excluding VDI-Wärmeatlas they all agree rather well, within ± 7 percent.

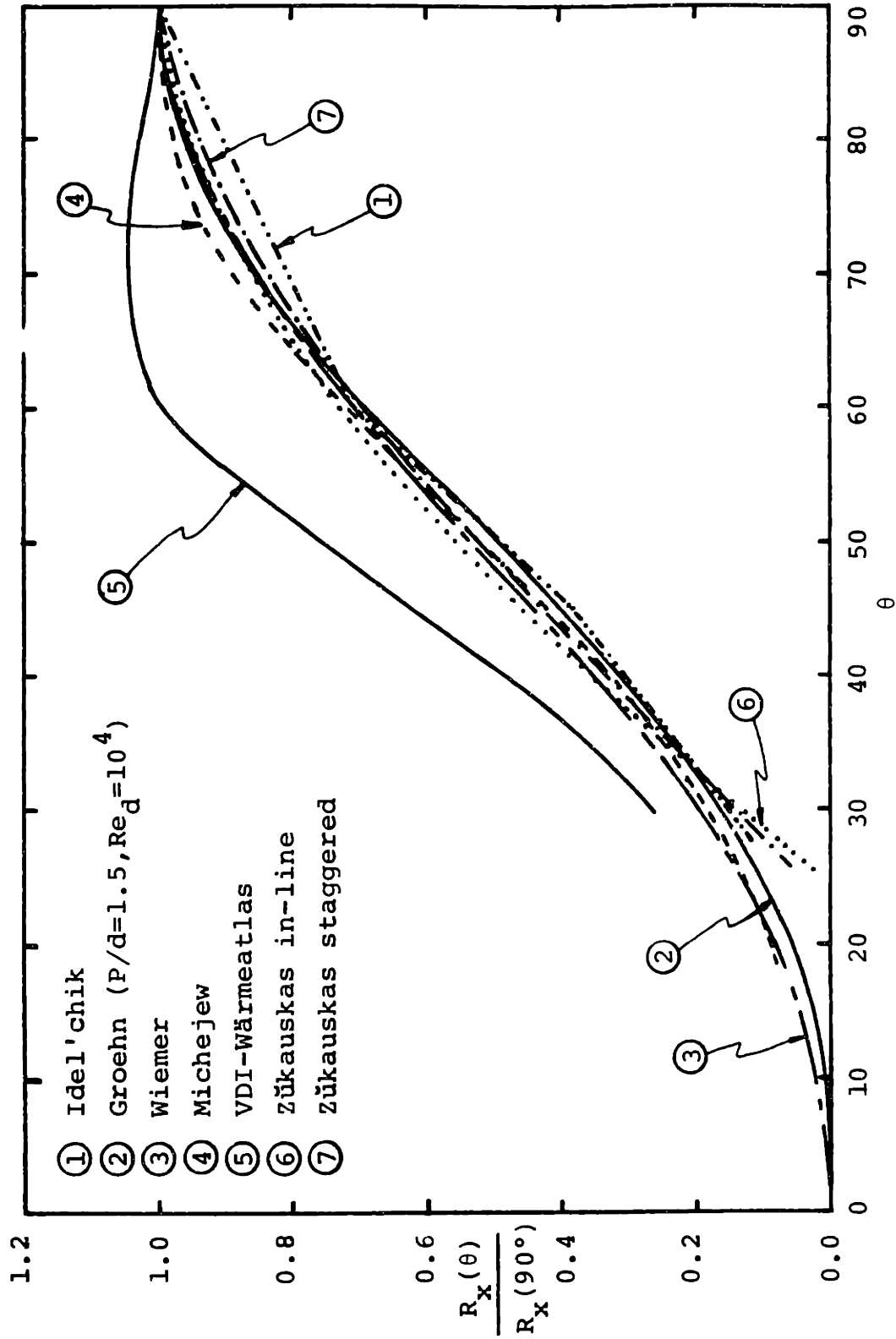


Figure 5.25 Normalized drag flow resistance correlations.

5.8 Experimental Data

The test apparatus described in Chapter 4 was used to take comprehensive flow resistance data in the Reynolds number range of 1,000 to 25,000 for 0, 30, 45, and 90 degree flow inclinations. In contrast to previous experiments, water was used as the working fluid and measurements were taken within a fully-developed flow region. Before flow resistance data could be taken, the test section flow field was studied to find the fully-developed flow region.

5.8.1 Flow Fields

A pitot-static tube (described in Sec. 4.5.5) was used to measure the center line velocity and pressure profiles across the width of the test sections at various elevations. A complete flow profile for the 45 degree test section at $Re_v = 7,450$ is shown in Fig. 5.26, 5.27, and 5.28.

At the test section entrance a linear pressure gradient sets up rapidly, while the velocity, despite the presence of a flow straightener, takes longer to develop a fully developed profile. (A velocity profile at $x/L_x = 0.04$ was not obtained because the support pins obstructed pitot tube motion.) Toward the middle of the test section the velocity profile does become fully developed. Ideally the profile should be flat, however it is not. A dip at the left wall and a peak at the right wall are observed. This can be explained by the postulated flow description given in Sec. 5.1. The flow consists of a mainstream moving to the right of the average flow direction (vertical or x-direction). The pitot tube measures the vertical component of the mainstream flow. As the mainstream flow approaches the right wall it

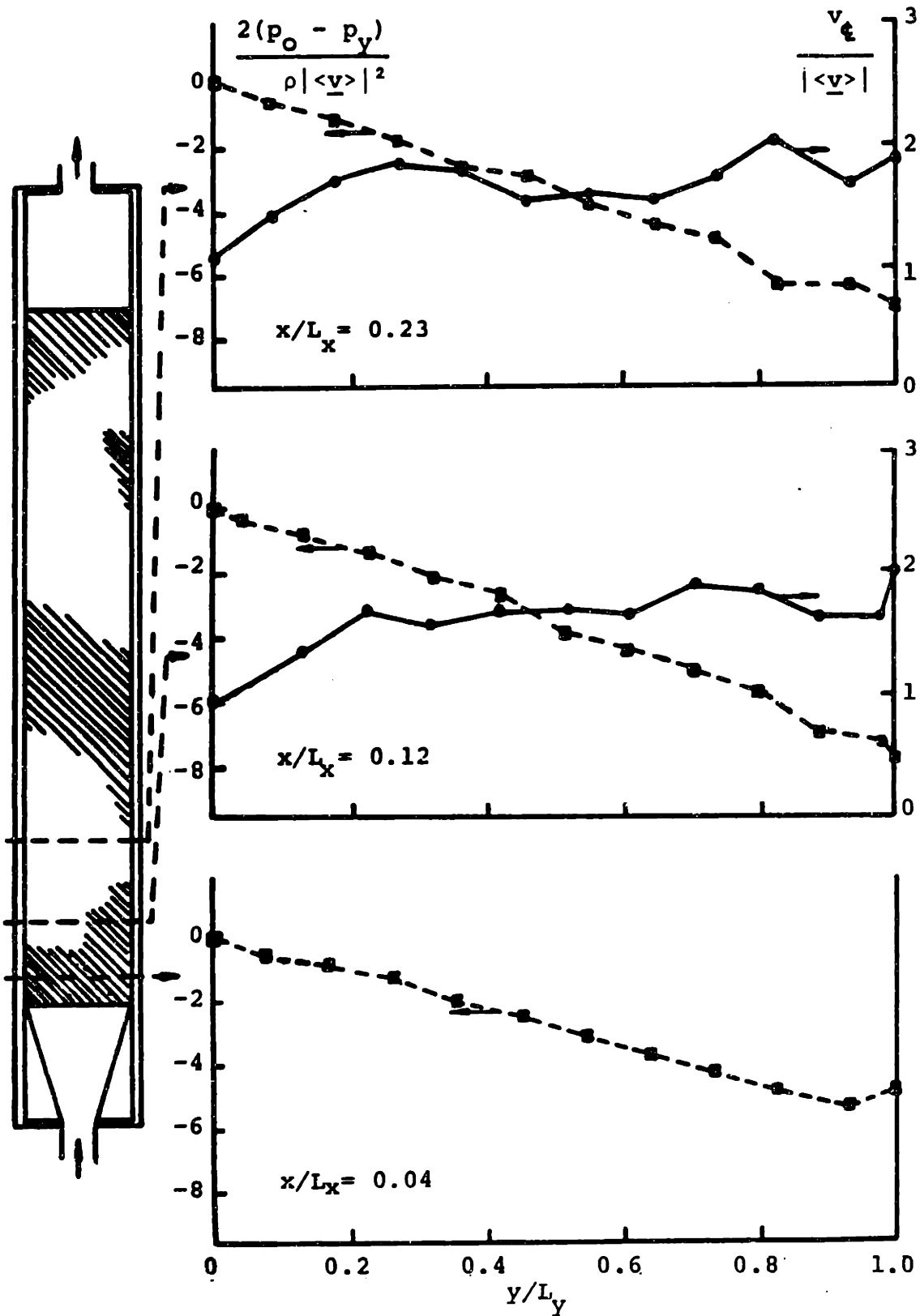


Figure 5.26 45 degree test section flow profile, $Re_v = 7,450$ (bottom).

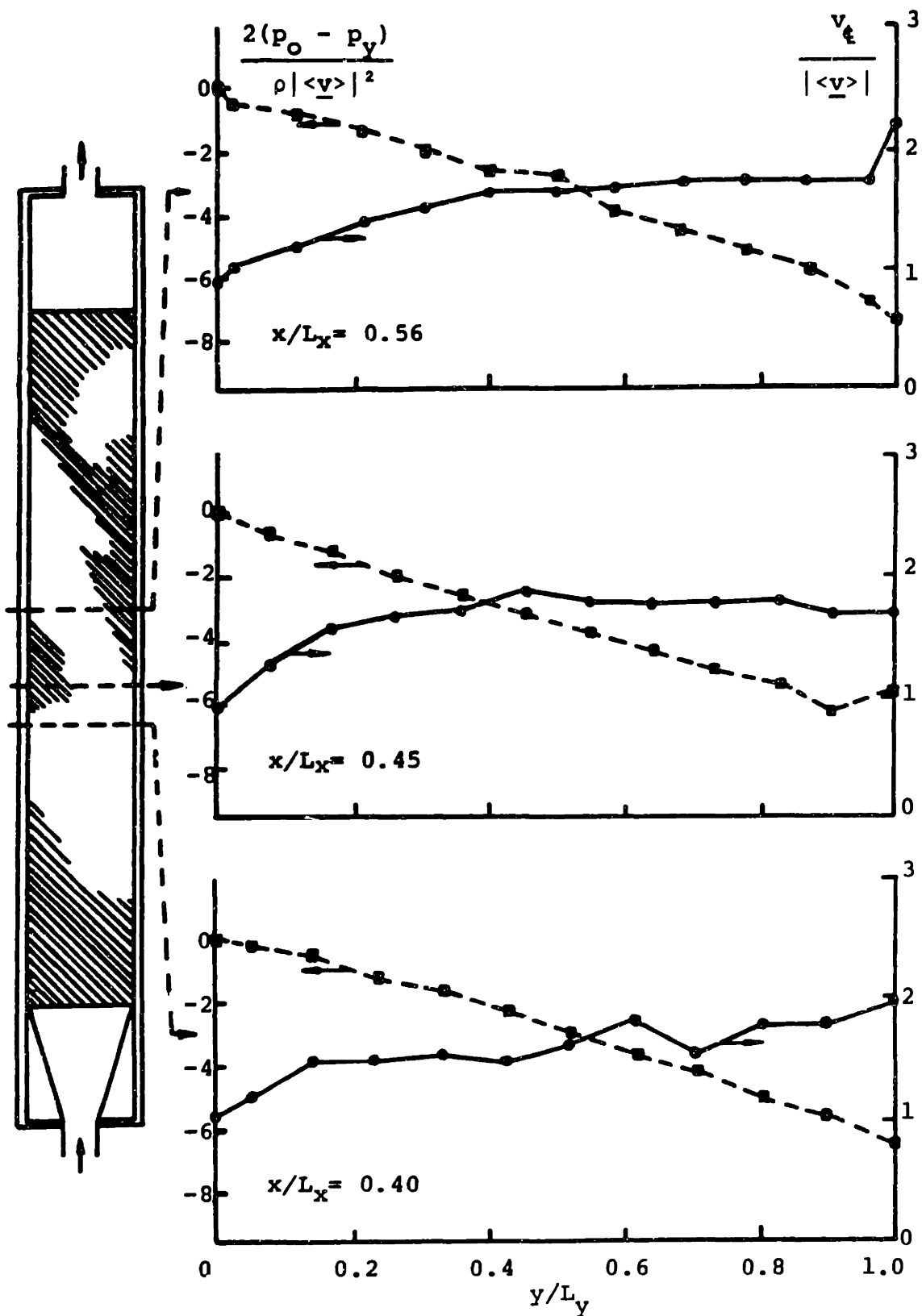


Figure 5.27 45 degree test section flow profile, $Re_v = 7,450$ (middle).

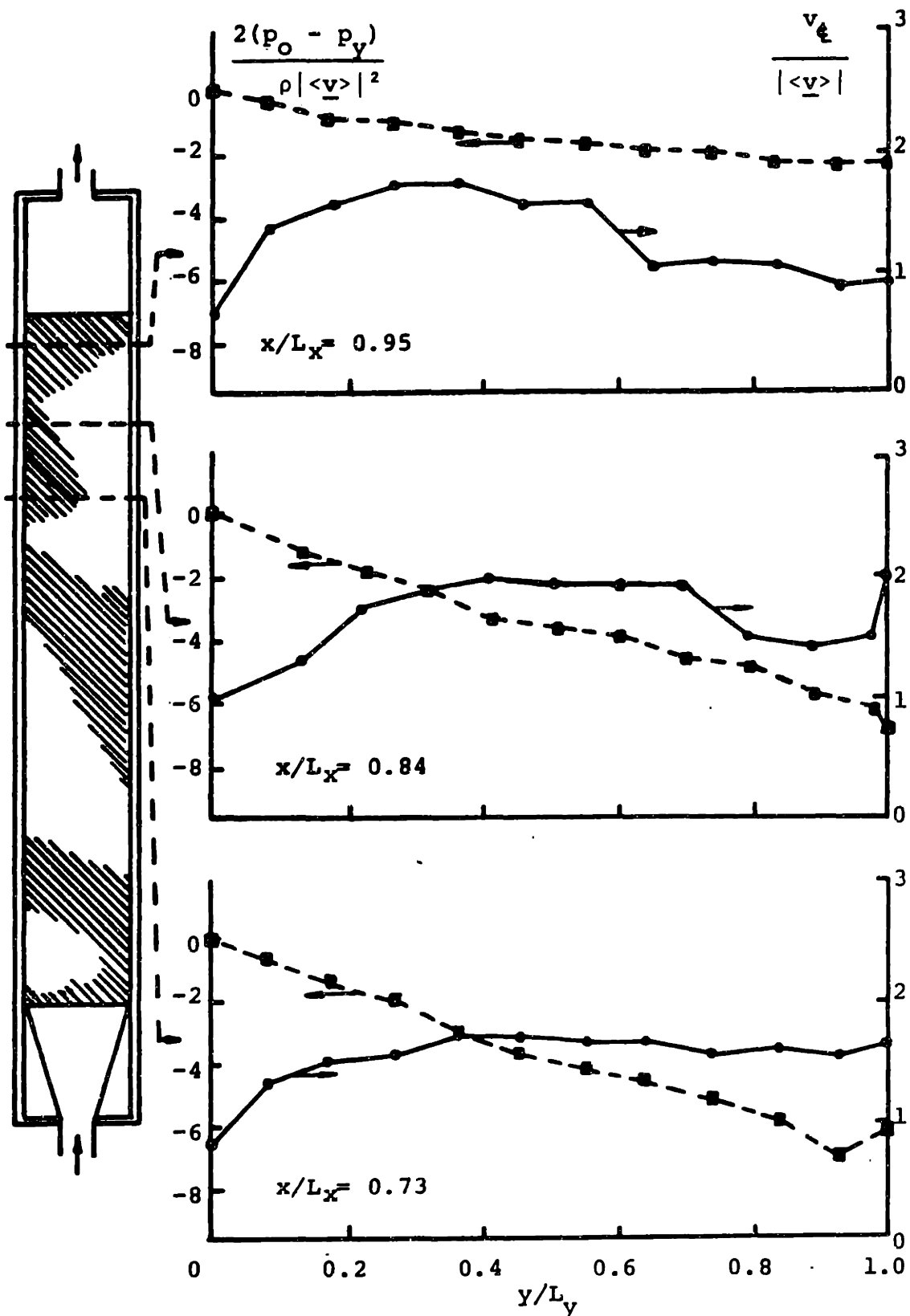


Figure 5.28 45 degree test section flow profile, $Re_v = 7,450$ (top).

diverted along the wall resulting in a higher vertical velocity component; conversely, at the left wall rightward motion of the mainstream leaves a stagnating region which is replenished by the recirculating flow behind the rods. Thus, the presence of walls limits the extent of an ideal flat, fully developed velocity profile. At the exit of the test section the large plenum causes a flattening out of the pressure profile and a corresponding acceleration of the velocity to the left.

The effect of varying the Reynolds number on the resulting profiles was examined at $x/L_x = 0.56$. Figure 5.29 shows normalized velocity and pressure profiles for a Re_v of 2,150 and 7,450. No significant change in the pressure profile is observed. The velocity profiles agree well too, when it is considered that the slower velocity is an order of magnitude smaller measurement (velocity is proportional to $\sqrt{\Delta p}$) and is reaching the lower limit of the instrumentation.

Similar profiles were observed for the 30 degree test section (Fig. 5.30). Velocity profiles were also taken for the parallel and crossflow test sections and were reasonably flat as expected (Fig. 5.31). Pressure variations across these latter two test sections were too small to measure, hence a flat pressure profile was obtained.

5.8.2 Flow Resistance

Solving the conservation of momentum equation, Eq. (3.8) and (3.9), for a

- steady state,
- two-dimensional (x,y),
- fully-developed flow; with

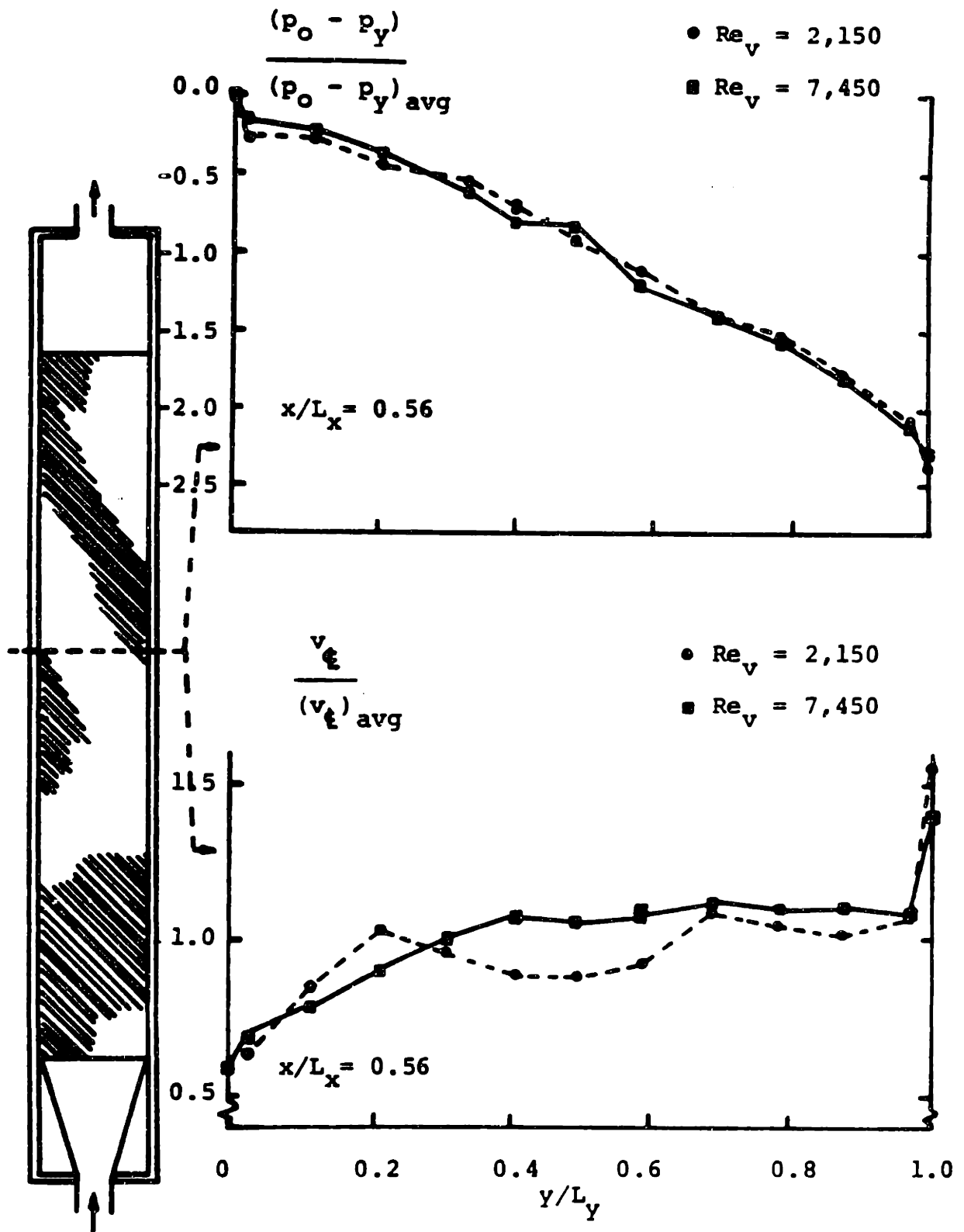


Figure 5.29 Effect of Reynolds number on velocity and pressure profile, 45 degree test section.

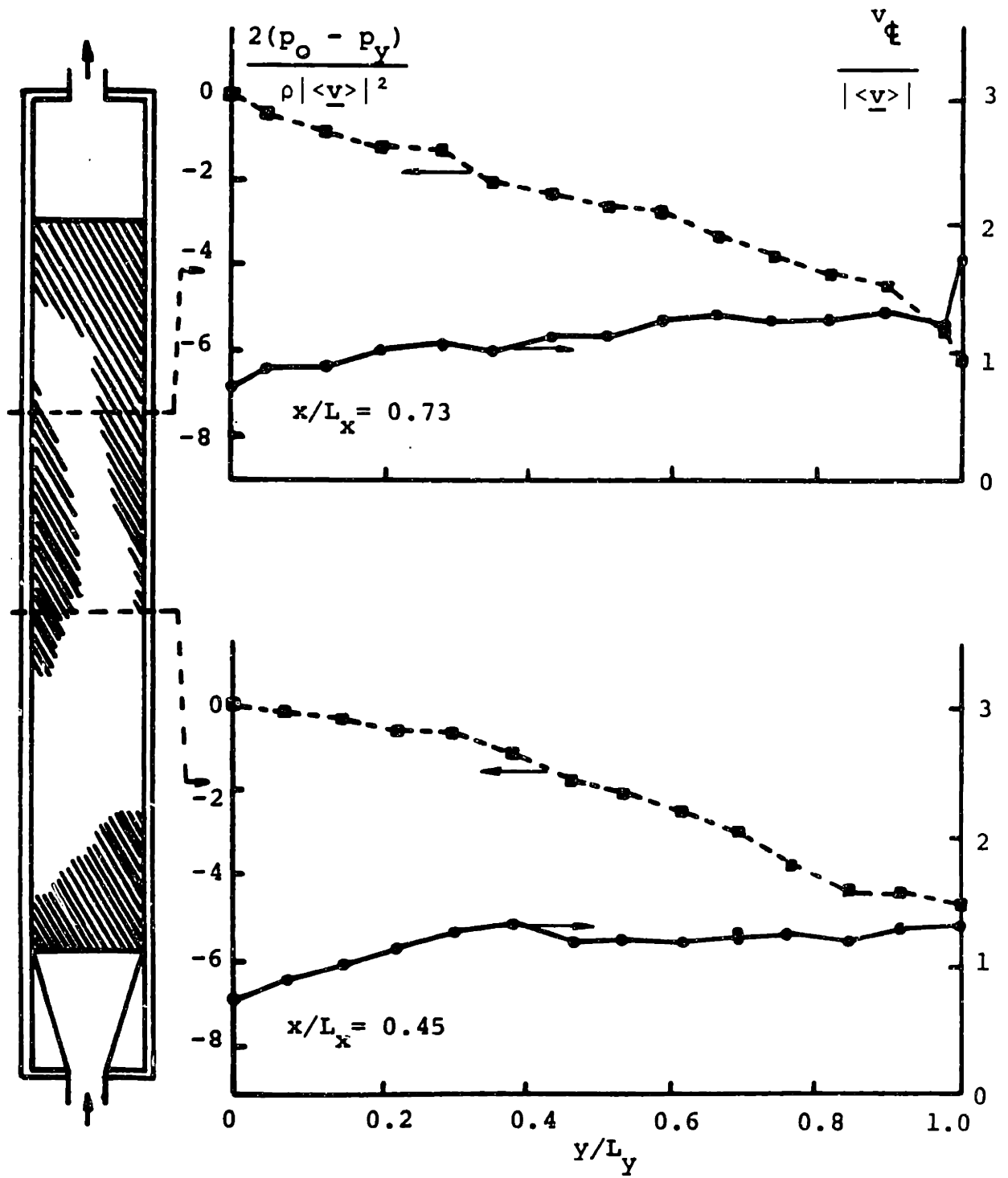


Figure 5.30 30 degree test section flow profile,
 $Re_v = 7,450$.

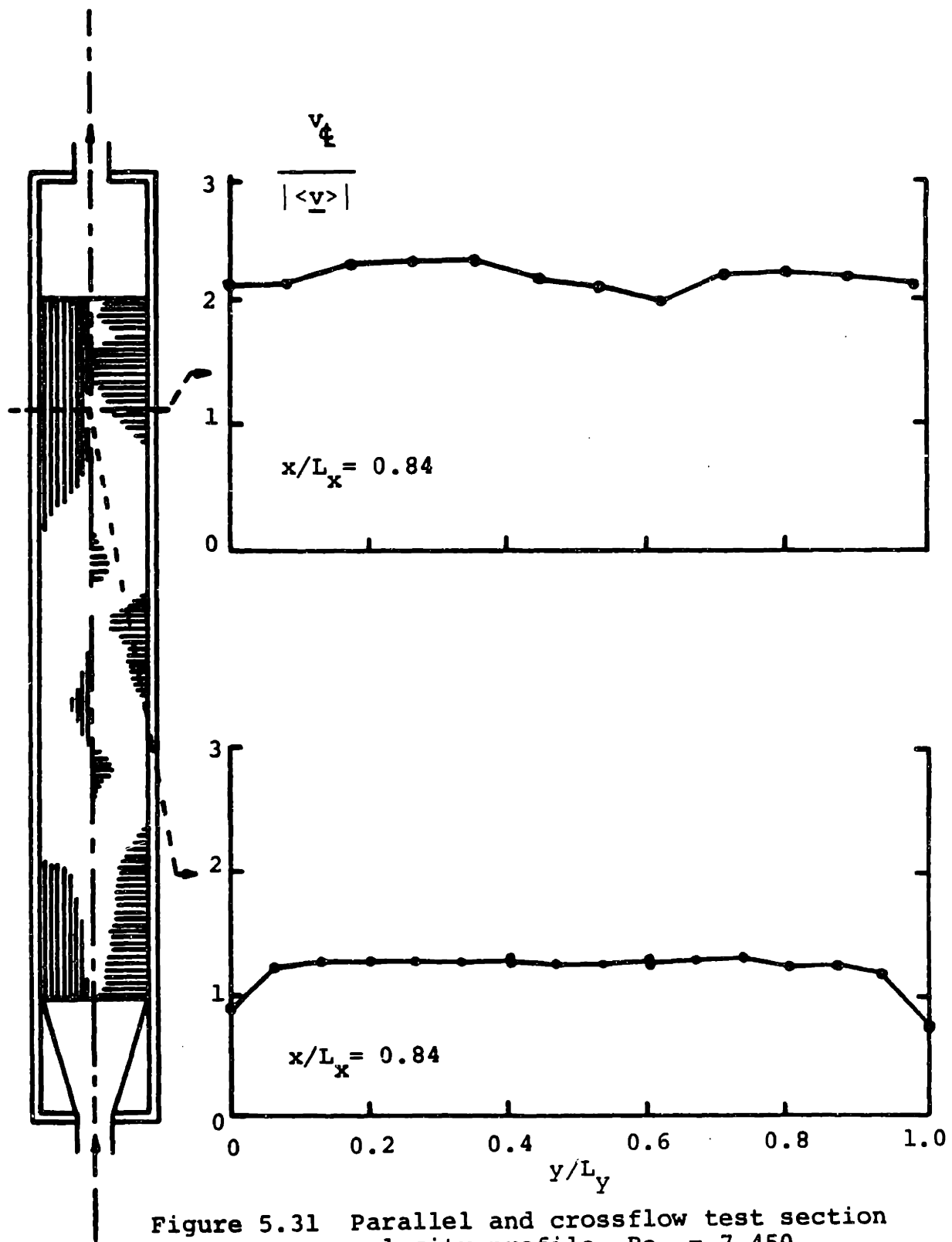


Figure 5.31 Parallel and crossflow test section velocity profile, $Re_v = 7,450$.

- gravity in the negative x-direction, and
- constant porosity;

gives

$$\langle R_x \rangle = - \frac{\partial}{\partial x} \langle \bar{p} \rangle - \rho g \quad (5.70)$$

$$\langle R_y \rangle = - \frac{\partial}{\partial y} \langle \bar{p} \rangle \quad (5.71)$$

the momentum equation for a control volume within the fully-developed region of a test section.

As shown above, the pressure field is linear in the fully-developed region so the partial derivatives can be accurately approximated by measurable, differential quantities, thus

$$R_x = \langle R_x \rangle = \frac{\Delta p_x}{L_x} \quad (5.72)$$

$$R_y = \langle R_y \rangle = \frac{\Delta p_y}{L_y} \quad (5.73)$$

where the gravitation term has been dropped since it is already included in the Δp_x measurement. Finally we may obtain the total resistance vector $\langle \underline{R} \rangle$ by simply measuring the x- and y-component pressure drops within a fully-developed flow region.

Figure 5.32 shows the measured variables and typical locations. The complete tabulation of data is given in Appendix E. Plots of the reduced data are shown in Fig. 5.33 through 5.38. The least square curve fits are shown together in Fig. 5.39 and also listed in Table 5.6.

The large scatter in the reduced parallel flow ($\theta = 0^\circ$) data is because a loop temperature of 60°F (15°C) was assumed for all runs.

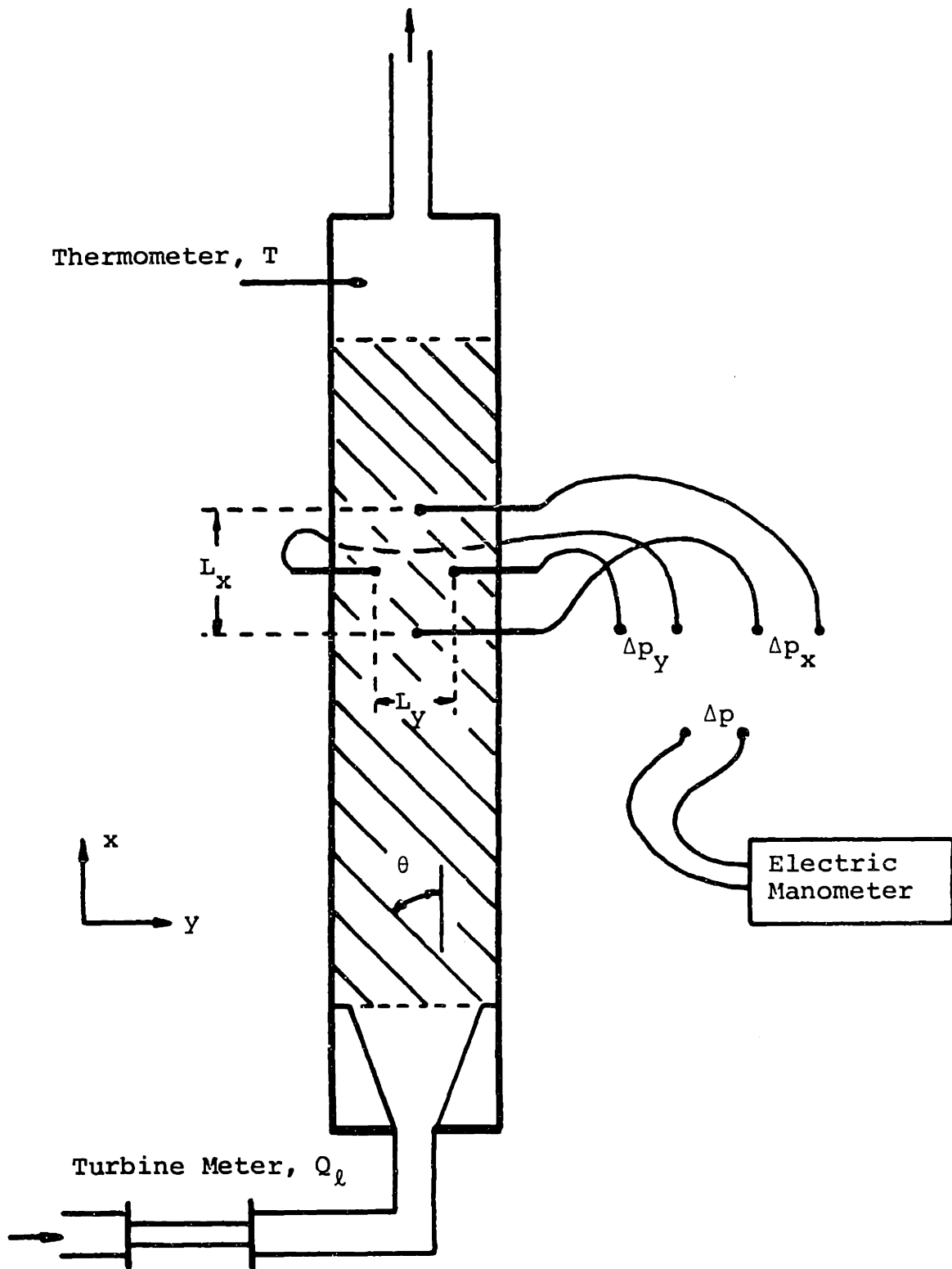


Figure 5.32 Measured variables and locations.

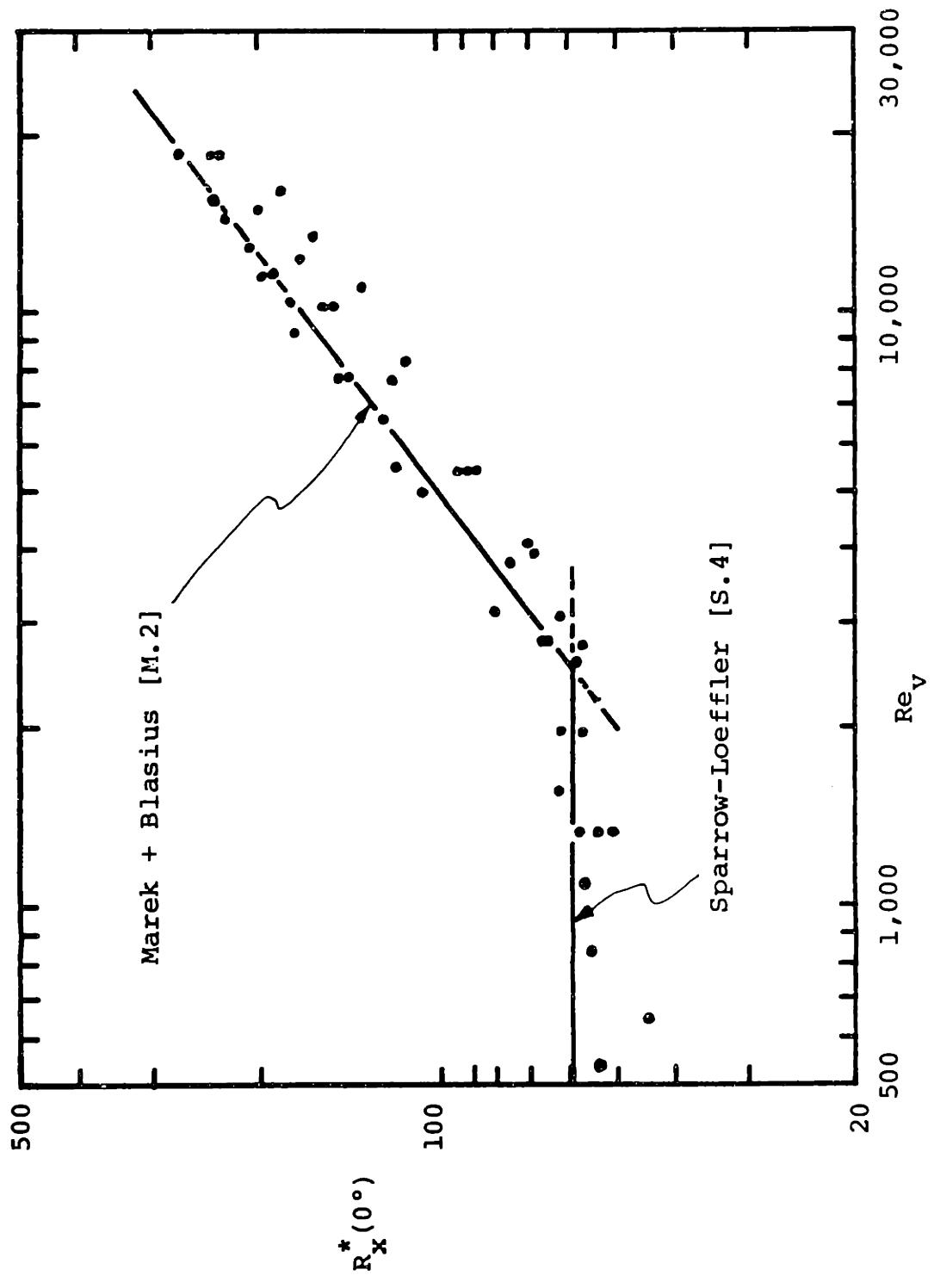


Figure 5.33 Parallel flow resistance, drag component.

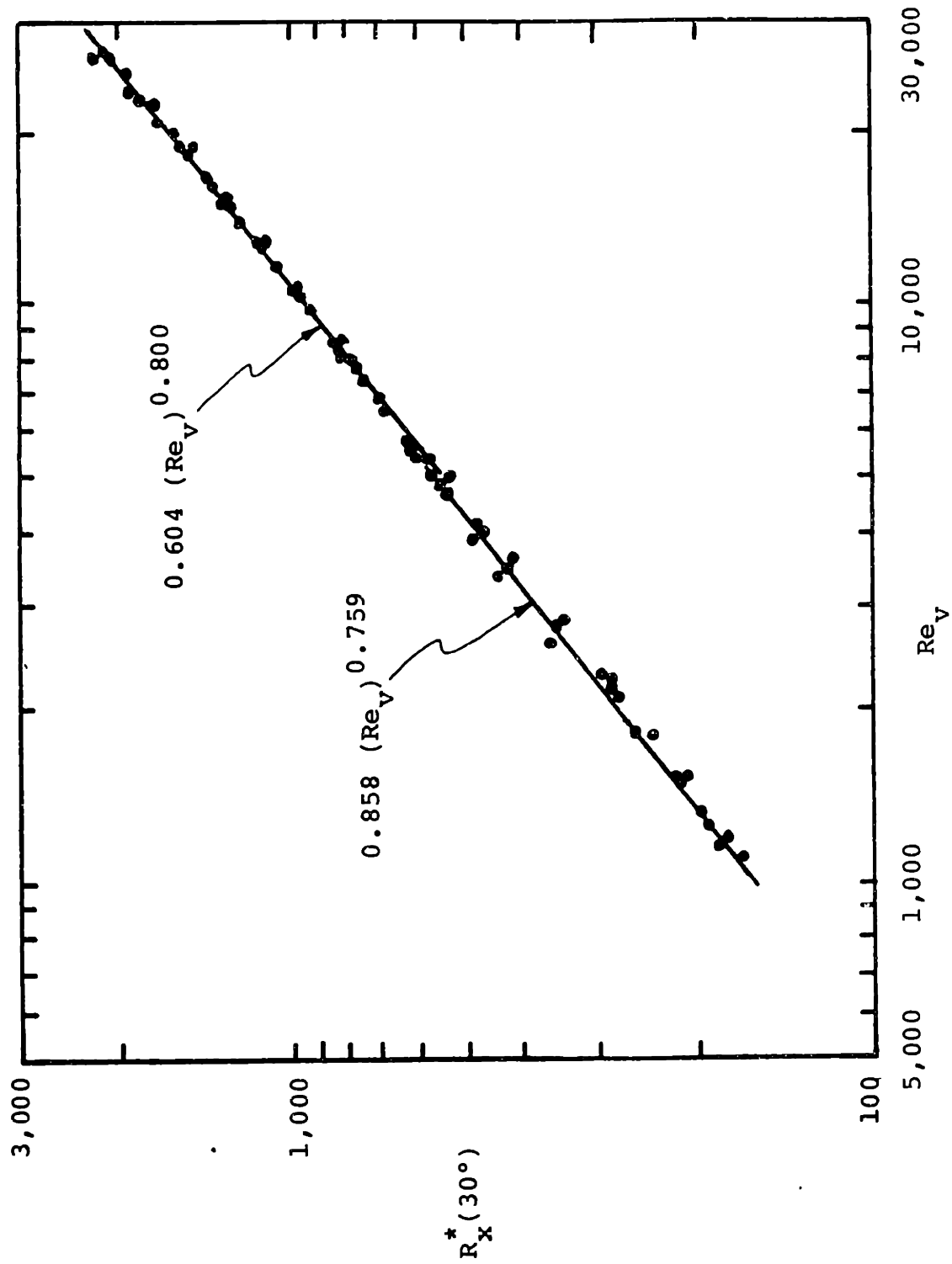


Figure 5.34 30 degree test section flow resistance, drag component.

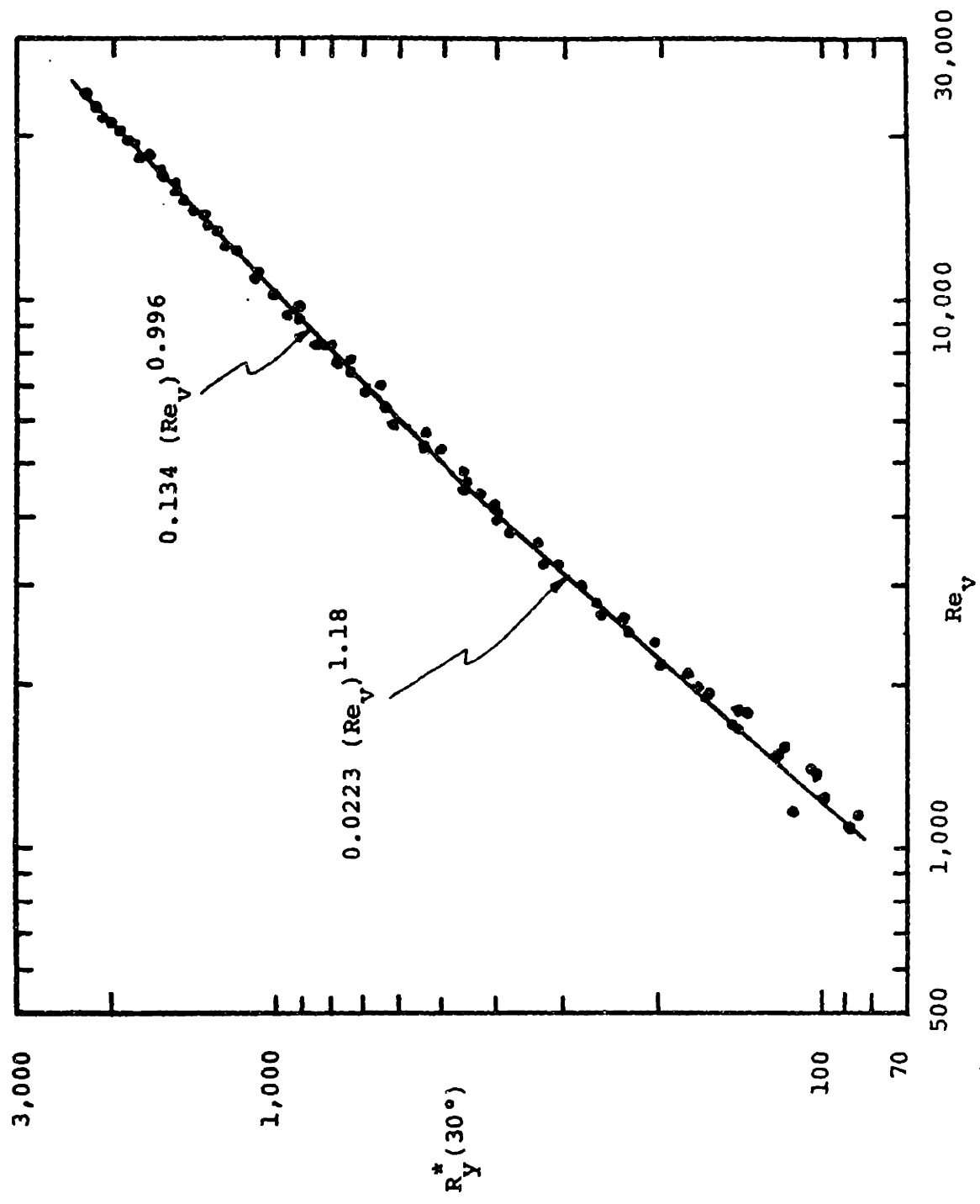


Figure 5.35 30 degree test section flow resistance , lift component.

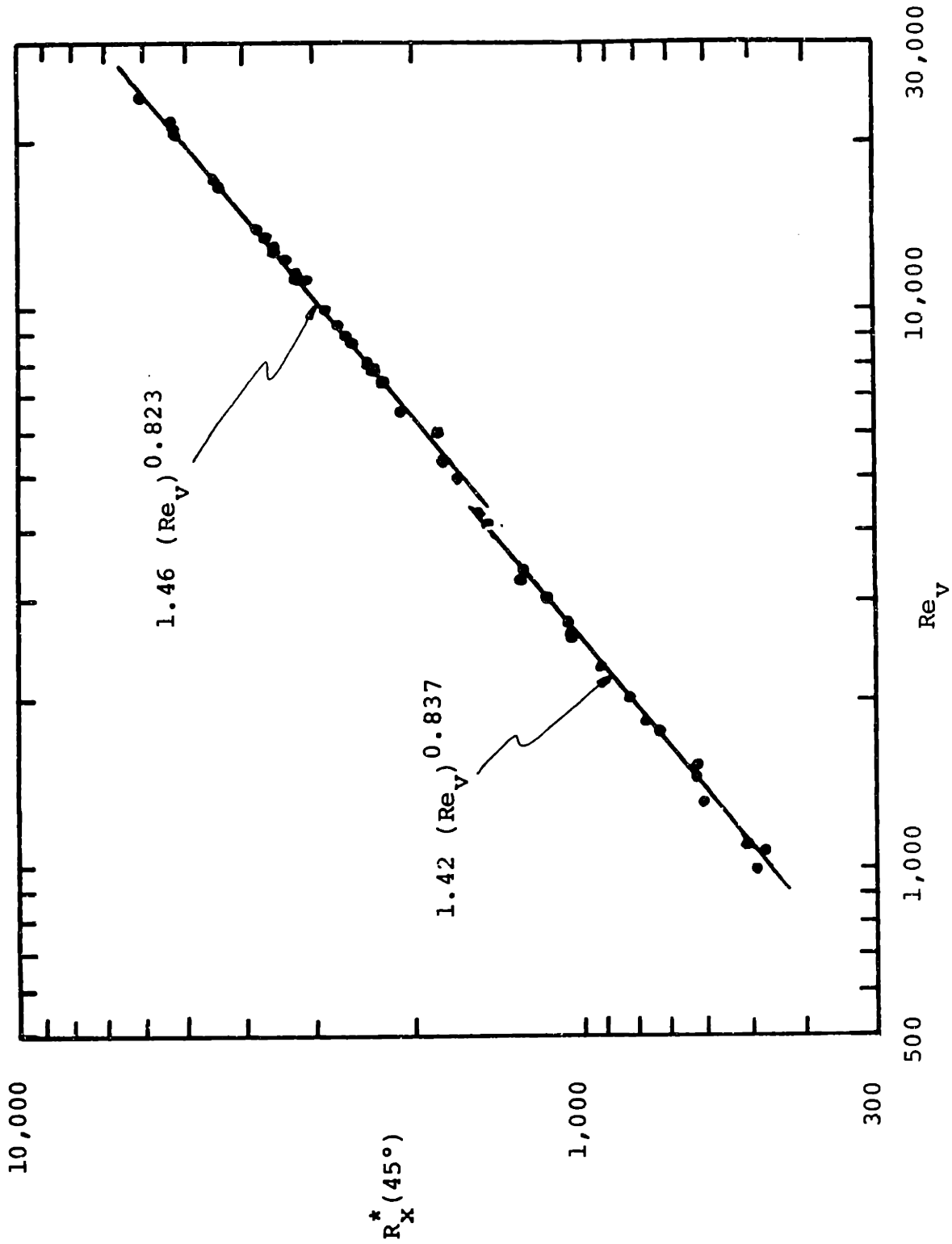


Figure 5.36 45 degree test section flow resistance, drag component.

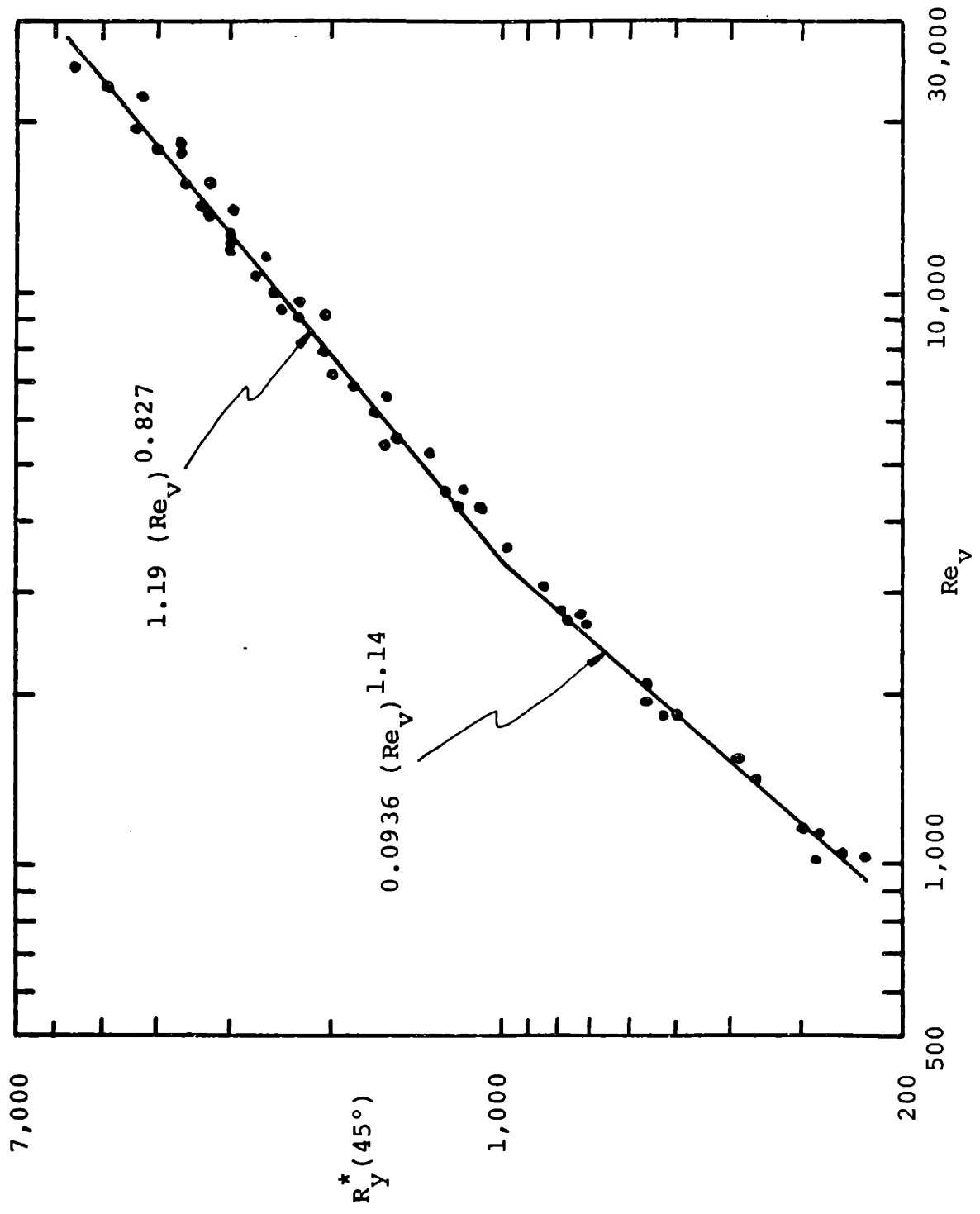


Figure 5.37 45 degree test section flow resistance, lift component.

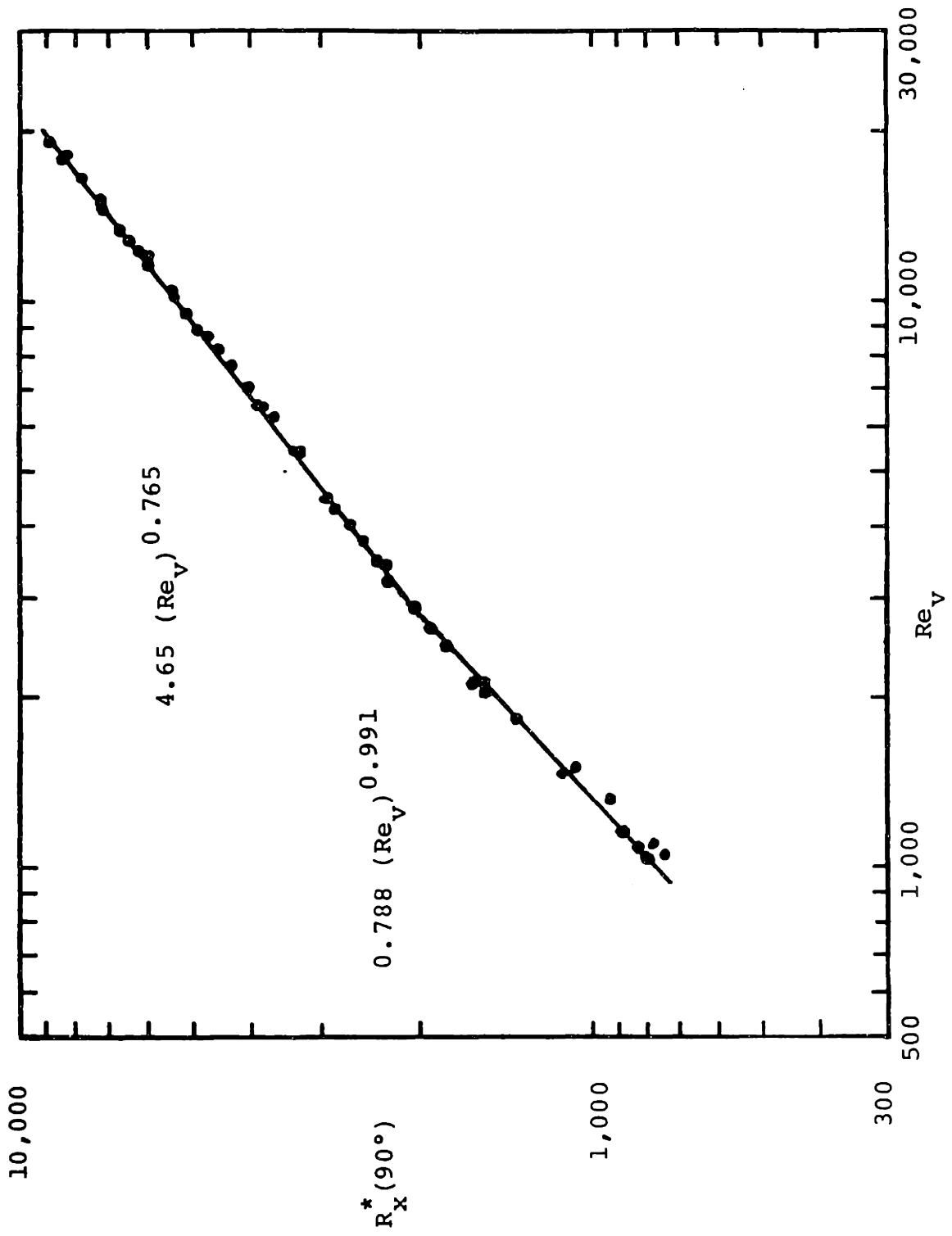


Figure 5.38 Crossflow resistance, drag component.

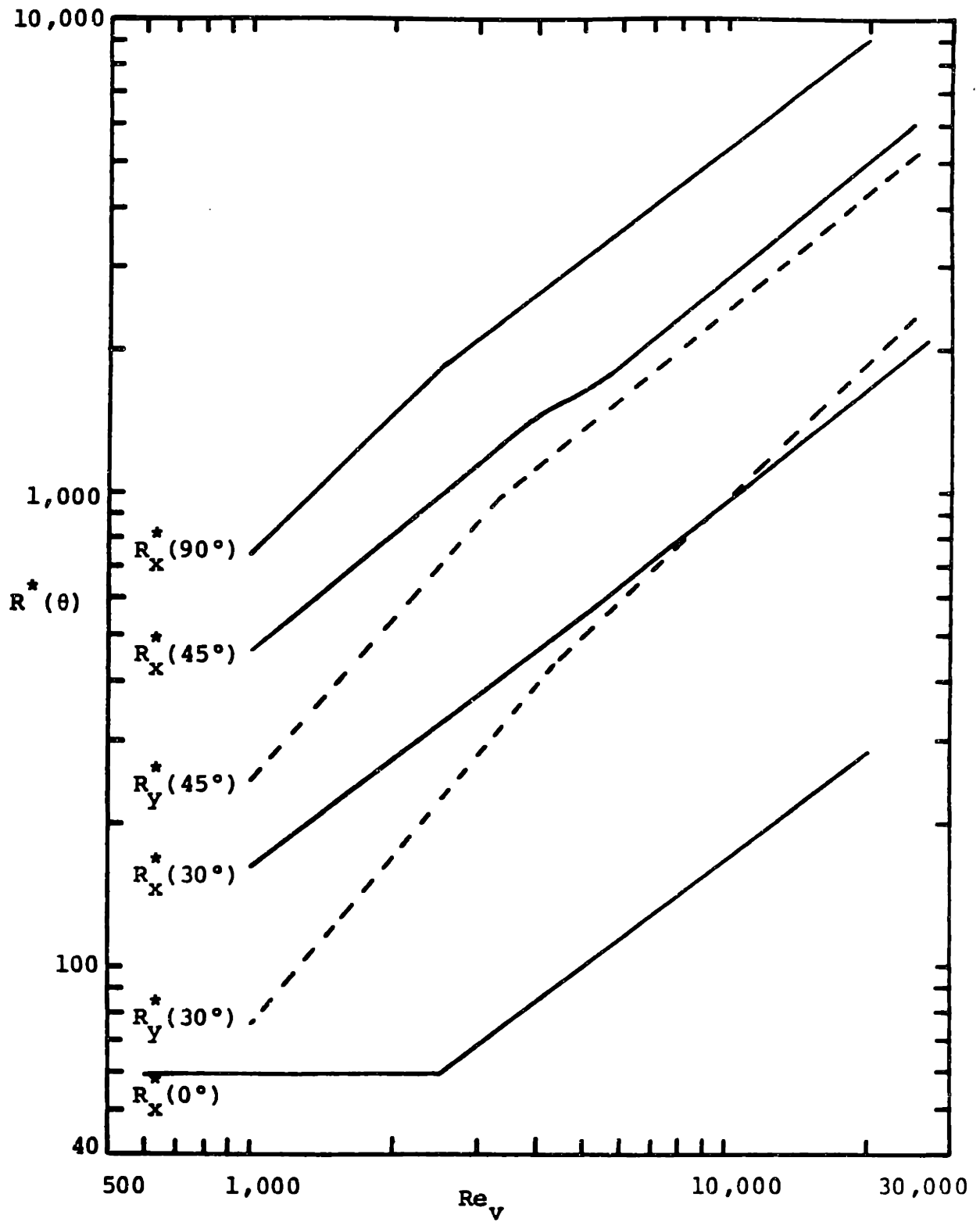


Figure 5.39 Flow resistance curve fits.

TABLE 5.6

Linear Fits for Flow Resistance Data

Flow Resistance	Range
$R_x^*(0^\circ) \stackrel{\Delta}{=} \begin{cases} 60 \text{ (Sparrow and Loeffler)} \\ 0.169 (Re_v)^{0.75} \text{ (Marek + Blasius)} \end{cases}$ $R_y^*(0^\circ) \stackrel{\Delta}{=} 0$	$Re_v < 2,510$ $2,510 < Re_v < 20,000$ <p style="text-align: center;">-----</p>
$R_x^*(30^\circ) = \begin{cases} 0.858 (Re_v)^{0.759} \\ 0.604 (Re_v)^{0.800} \end{cases}$ $R_y^*(30^\circ) = \begin{cases} 0.0223 (Re_v)^{1.18} \\ 0.134 (Re_v)^{0.966} \end{cases}$	$1,000 < Re_v < 5,230$ $5,230 < Re_v < 27,000$ $1,000 < Re_v < 4,360$ $4,360 < Re_v < 25,000$
$R_x^*(45^\circ) = \begin{cases} 1.42 (Re_v)^{0.837} \\ 1.46 (Re_v)^{0.823} \end{cases}$ $R_y^*(45^\circ) = \begin{cases} 0.0936 (Re_v)^{1.14} \\ 1.19 (Re_v)^{0.827} \end{cases}$	$1,000 < Re_v < 4,500$ $4,500 < Re_v < 25,000$ $1,000 < Re_v < 3,370$ $3,370 < Re_v < 25,000$
$R_x^*(90^\circ) = \begin{cases} 0.788 (Re_v)^{0.991} \\ 4.65 (Re_v)^{0.765} \end{cases}$ $R_y^*(90^\circ) \stackrel{\Delta}{=} 0$	$1,000 < Re_v < 2,580$ $2,580 < Re_v < 20,000$ <p style="text-align: center;">-----</p>

Although there is some scatter, the general agreement with current correlations is still quite good. The linear fit of the crossflow data ($\theta = 90^\circ$) is compared with correlations in Fig. 5.9. Again the agreement is good. At higher numbers the data is below the mean, but in light of the accuracy of crossflow correlations in general, the deviation is not unexpected.

5.9 Model, Correlation, and Data Comparison

Now we systematically assess the Reynolds number (Re_d), inclination (θ), porosity (γ_v), and rod arrangement dependence of the data base and compare them with the superposition models and correlations (which are only a function of inclination). Remember when we assess the drag and lift component resistances as predicted by the composite superposition models, Eq. (5.65), we are only appraising the crossflow superposition factor, $h_1(\theta)$.

5.9.1 Correlation and Composite Superposition Model Evaluation

The purpose of normalizing the resistance components by the one-dimensional correlations is to separate the inclination dependence from the geometry and Reynolds dependence. This, of course, assumes that the geometry and Reynolds dependence are completely characterized by the one-dimensional limits, independent of the flow angle, θ . To test this hypothesis, consider first the geometry dependence of the drag/lift flow resistance components for a fixed Reynolds number ($Re_d = 10^4$).

Figures 5.40 and 5.41 show the data for all geometries plotted versus inclination, θ , and versus porosity, γ_v . Also plotted for

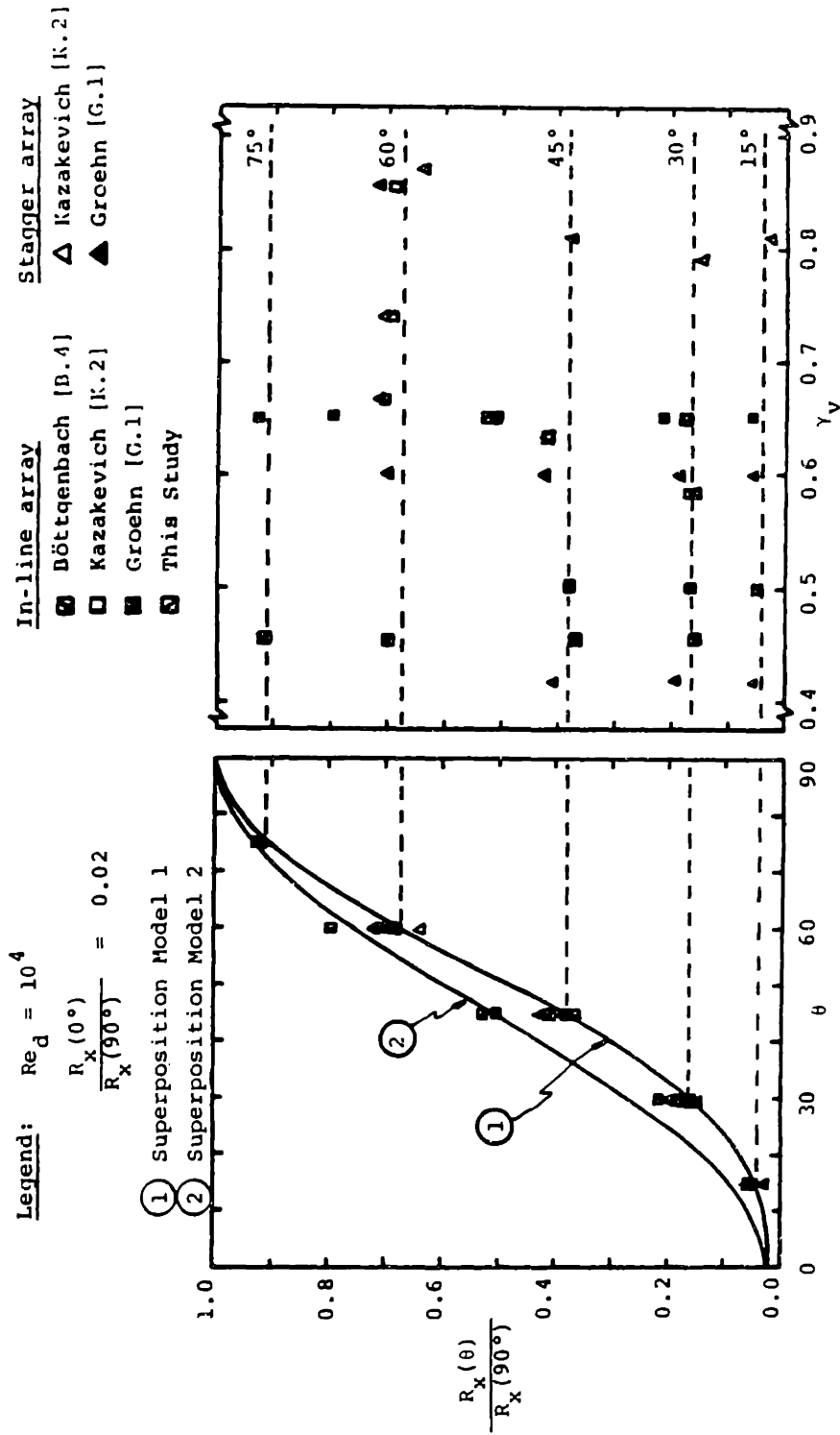


Figure 5.40 Angle and geometry dependence of flow resistance, drag component ($Re_d = 10^4$).

Legend: $Re_d = 10^4$

In-line arrays

Böttgenbach [B.4]
 This Study

Superposition Model 1
 Superposition Model 2

$\frac{R_x(0^\circ)}{R_x(90^\circ)} = 0.02$

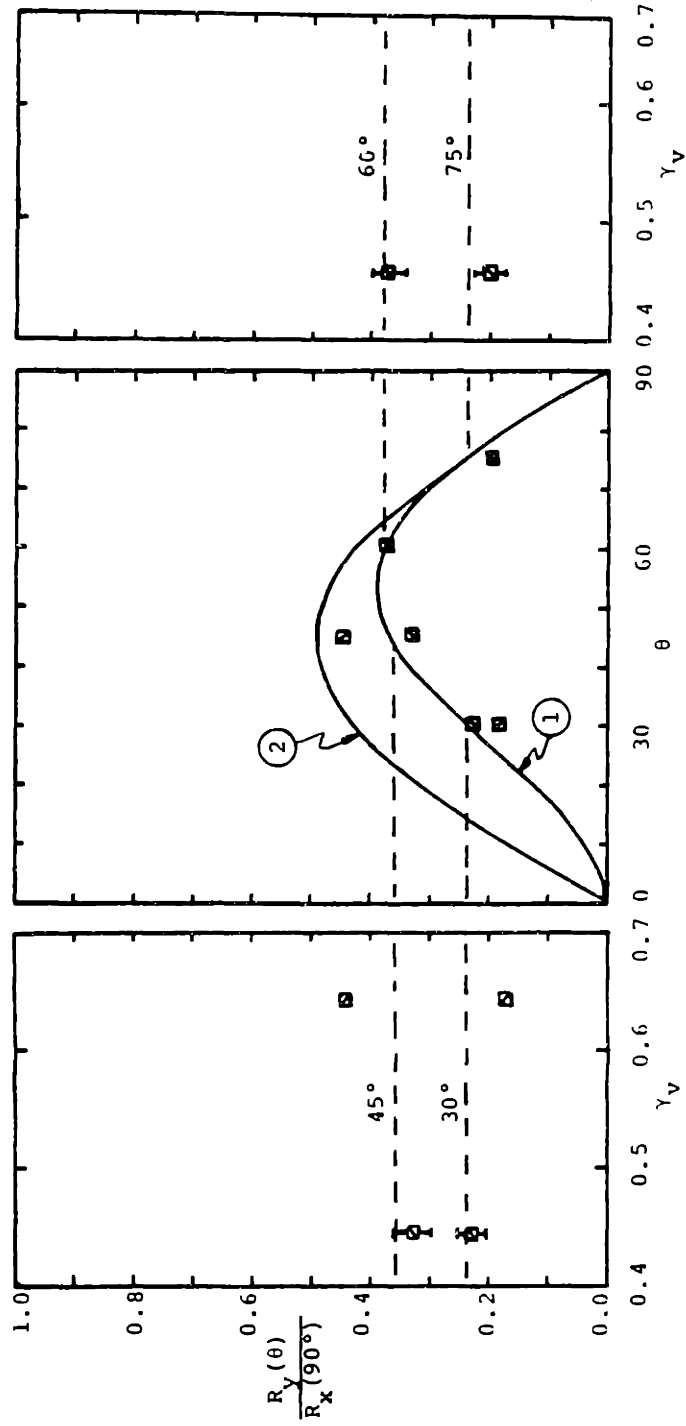


Figure 5.41 Angle and geometry dependence of flow resistance, lift component ($Re_d = 10^4$).

comparison are the two superposition models (1) and (2). Böttgenbach's data is for a higher Reynolds number, but is included here by extrapolating down to $Re_d = 10^4$. Kazakevich's staggered data points ($\gamma_v = 0.792$, $\theta = 30^\circ$) and ($\gamma_v = 0.870$, $\theta = 60^\circ$) which appear low, should be weighted lightly since they are based on only three rows of rods. For total drag resistance no distinct porosity or rod arrangement dependence is apparent. The scatter in the data base is also nicely bracketed by the two superposition models. The few data points for the lift resistance component, on the other hand, suggest Model (1) is more appropriate.

Now we examine the Reynolds number dependence for a fixed, mean porosity. Figures 5.42 and 5.43 show Reynolds dependence of the available data for $\gamma_v \approx 0.65$. Again for reference, superposition models (1) and (2) are also plotted. Examining the curves collectively the only justifiable assumption is that the normalized resistance components are constant independent of Reynolds number. A slight decreasing trend in the drag component and increasing trend in the lift component could be postulated; however in light of the absolute differences between data sets, limited Re_d range of each data set and overall limited quantity of data, correlating this trend for general use is not justifiable. Like the geometry dependence, the Reynolds number variation in normalized drag component is bracketed by the two superposition models (1) and (2). One might argue that the superposition models already account for the above mentioned dependence by the parallel/crossflow ratio term $(A/B)(Re_v)^{m-n}$, which has been assumed constant in the above comparison. Although this dependence is

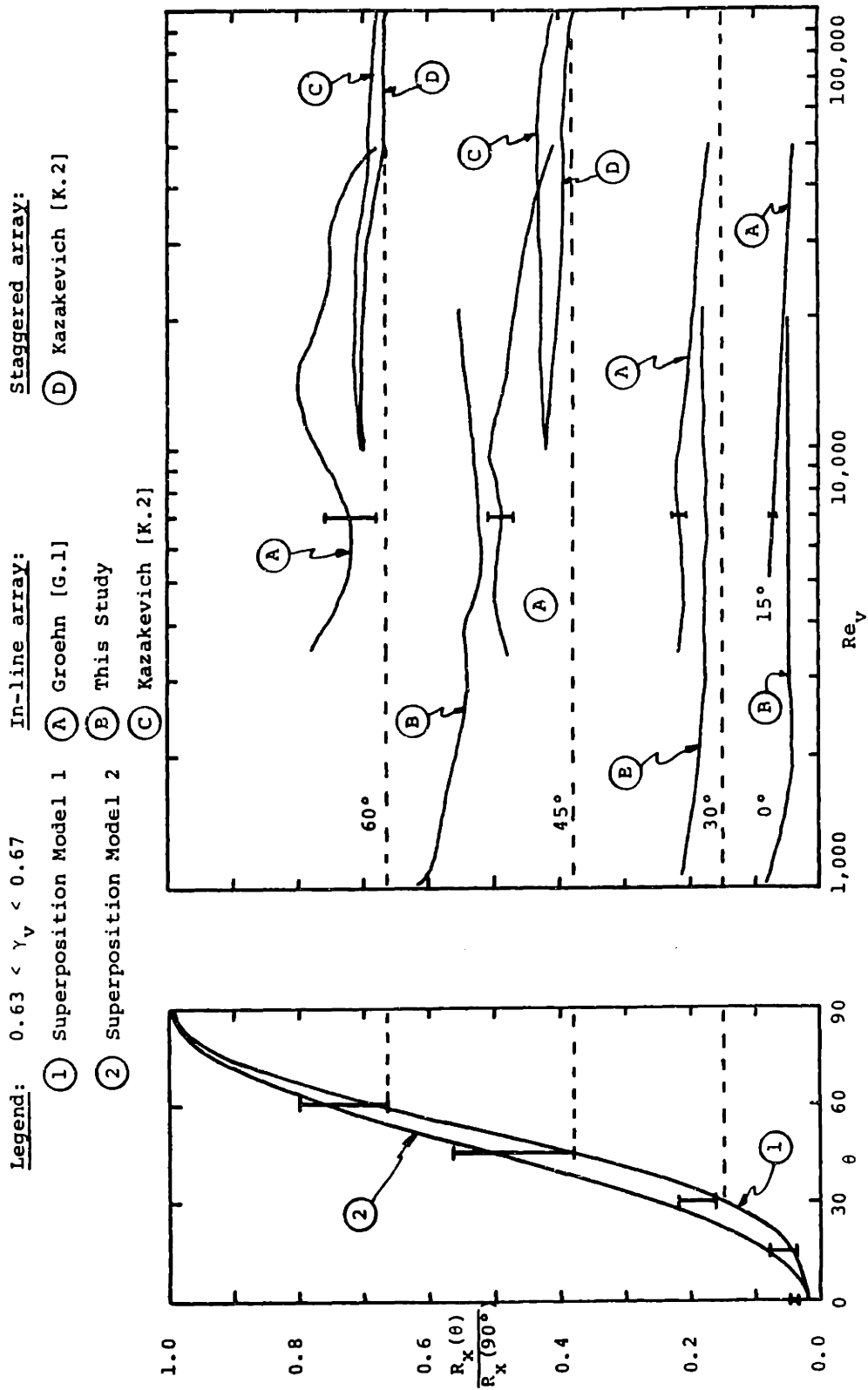


Figure 5.42 Reynolds number dependence of flow resistance, drag component ($\gamma_v = 0.65$).

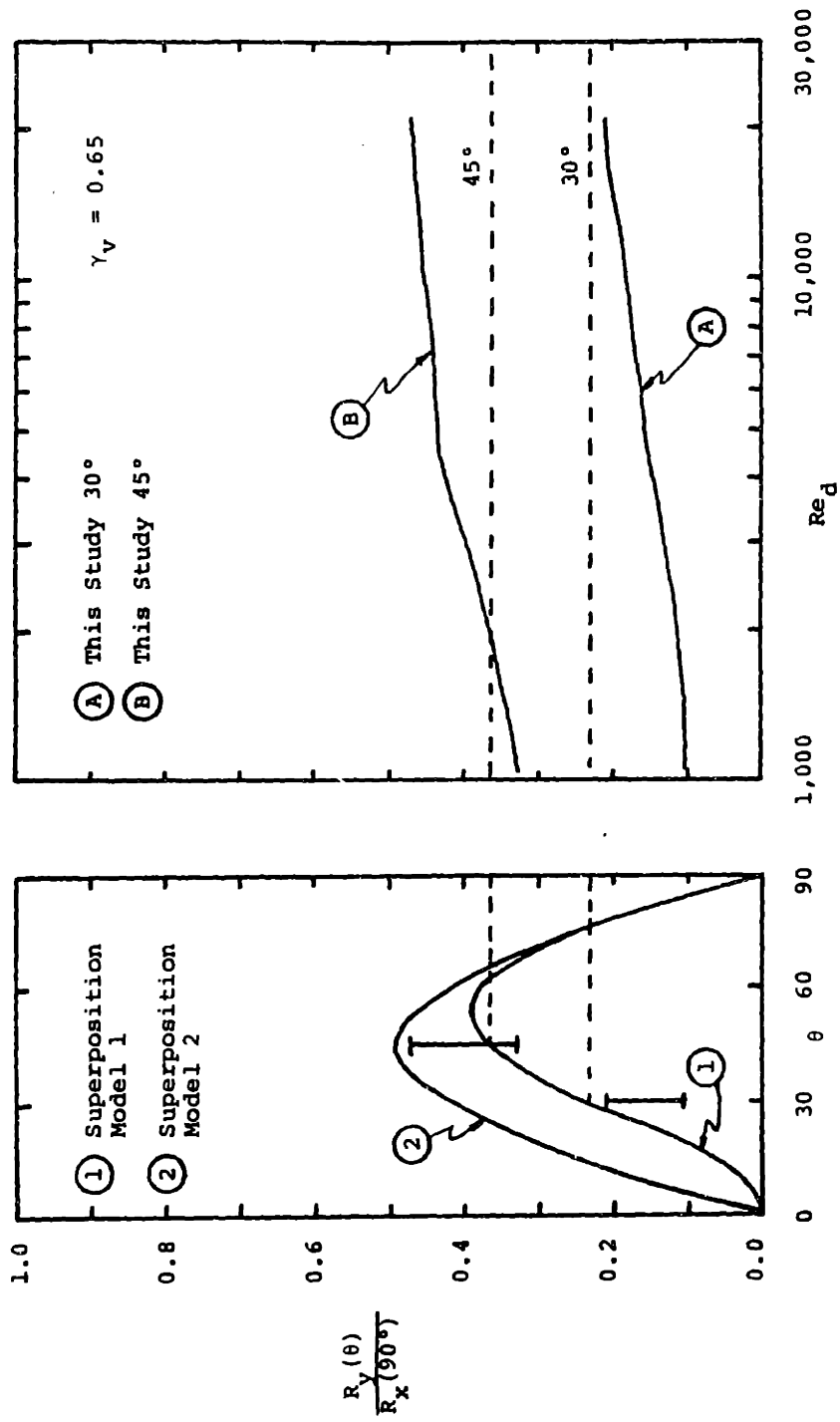


Figure 5.43 Reynolds number dependence of flow resistance, lift component ($\gamma_v \approx 0.65$).

in the right direction, the magnitude is so small that no significant change would be observed (about a one percent change over the entire Re_d range considered.)

The empirical correlations for the normalized drag component are replotted in Fig. 5.44 with superposition models (1), (2) and (6) and the geometry and Reynolds number averaged data. All the correlations also fall between superposition models (1) and (2) and match the mean of the data, however below 30 degrees the correlations either diverge or approach zero resistance. Model (6) nicely predicts the mean of the correlations and data (the exponent m of model (6) was chosen to match the mean of the data base, $m' = 0.4$). Figure 5.45 shows the normalized lift component as predicted by models (1), (2) and (6) along with the averaged data. No empirical correlations for the lift component have been published to date. For the limited data available, superposition model (1) appears good.

5.9.2 Recommendations

From the above comparisons superposition model (6) overall best predicts the average of the data and correlations. Unlike the empirical correlations it reduces to the parallel flow limit and predicts a lift component of resistance.

All the superposition models lie within the error bars of the data. Robinson [E.1] performed a sensitivity study to assess the importance of the range in the data base on overall calculations. He used superposition models (1) and (2) to predict the overall pressure drop and flow distribution of a baffled heat exchanger experiment. He concluded that the choice of superposition model has a much smaller

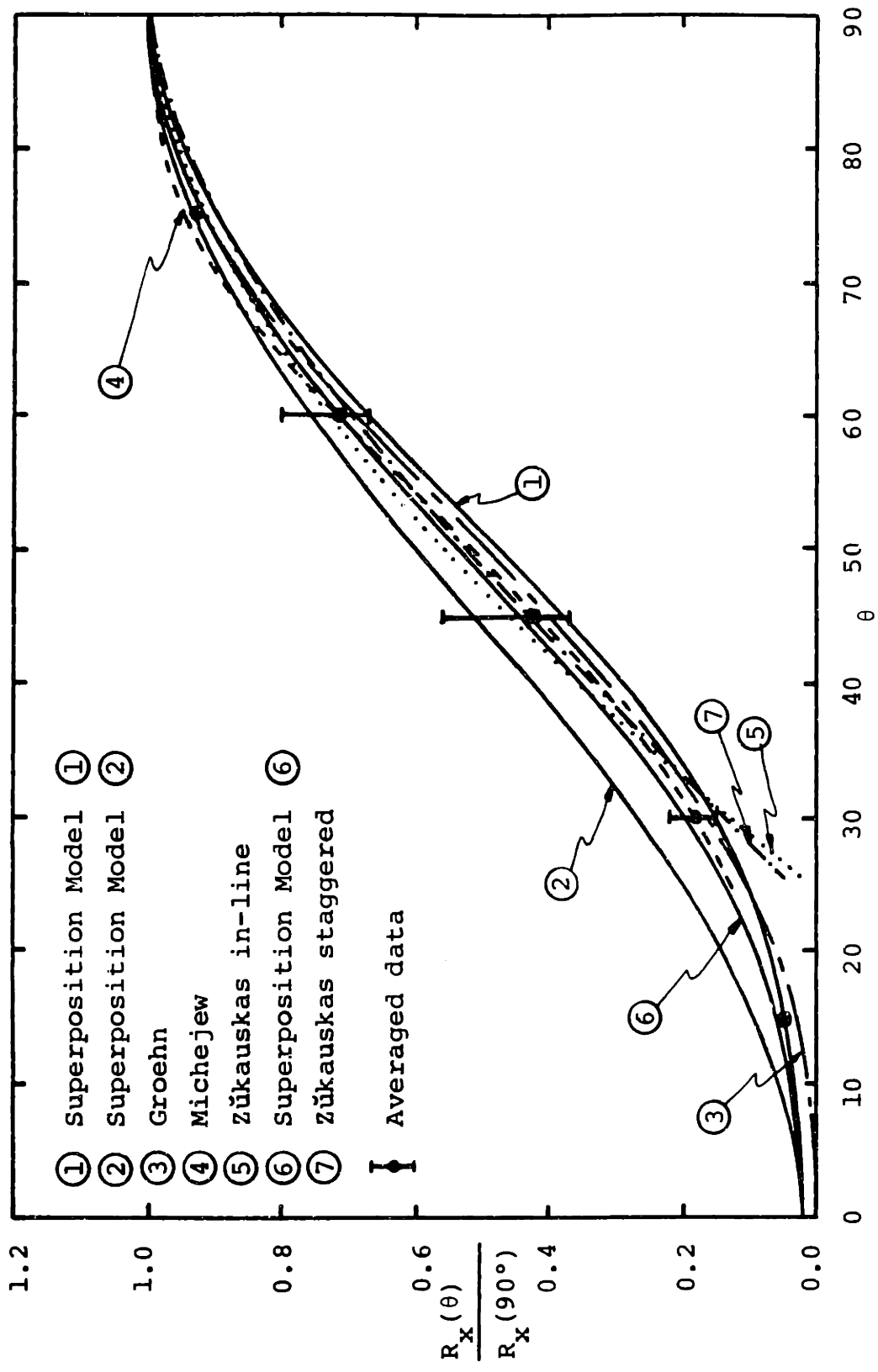


Figure 5.44 Data, correlation, and model comparison, drag component.

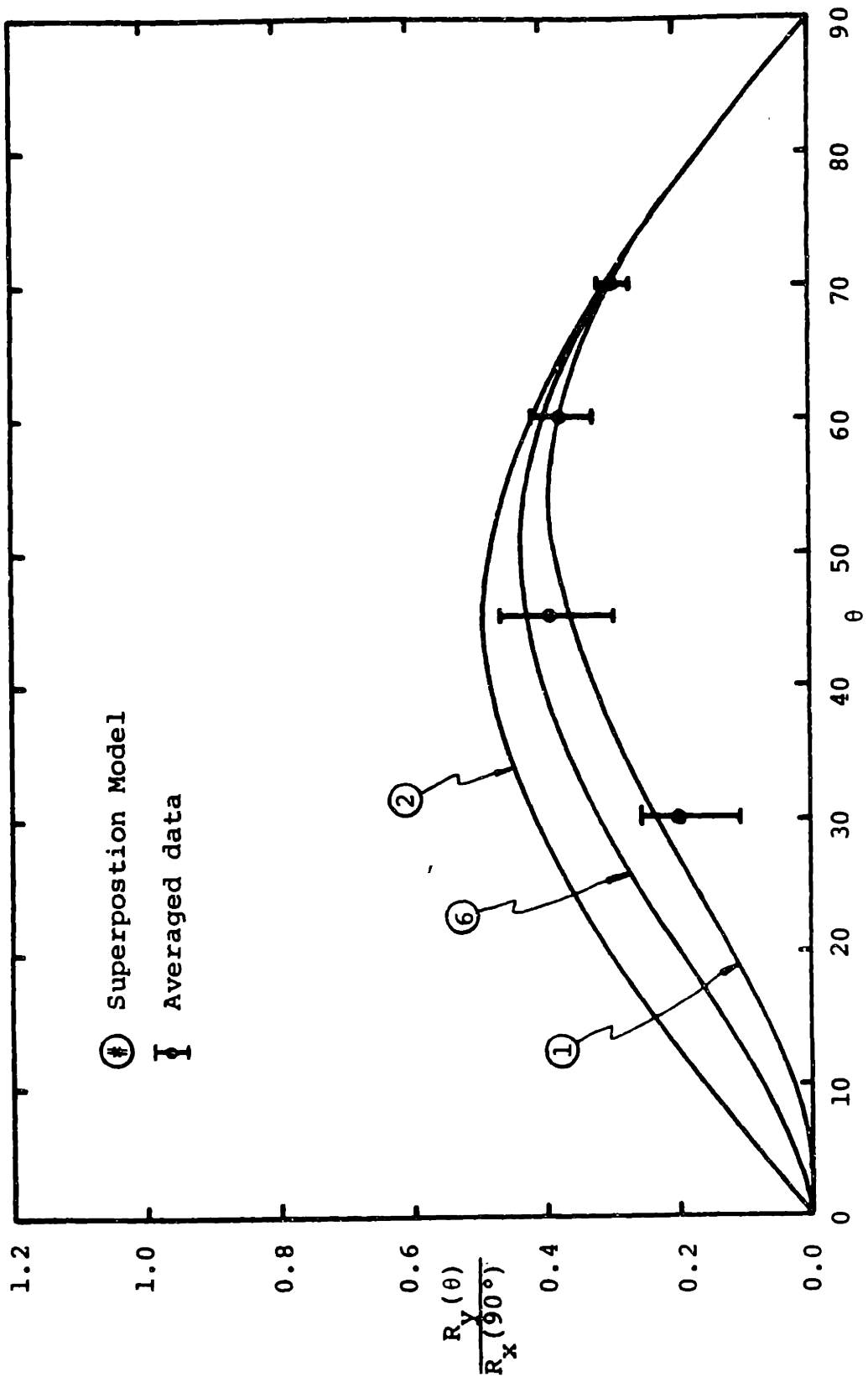


Figure 5.45 Data and model comparison, lift component.

impact on the predictions than the choice of the accompanying one-dimensional correlations ($R_{||}(0^\circ)$ and $R_{\perp}(90^\circ)$). Within the accuracy of the available data for both incline and one-dimensional flows, the geometry-Reynolds number independent superposition models are sufficient for application in computer codes.

In conclusion, for predicting turbulent flow resistance in incline rod arrays, we recommend:

- (1) For general design using superposition model (6) with $m' = 0.4$ and $n' = 0$,

$$\begin{aligned} \langle \underline{R} \rangle = & f_{||} [|\langle \underline{v} \rangle|] \frac{1}{D_v} \frac{\rho |\langle \underline{v} \rangle|}{2} \langle v_{||} \rangle \underline{e}_{||} + \\ & b_{\perp} [|v_{ms\perp}|] \frac{1}{D_v} \frac{\rho |v_{ms}|^{0.6} |v_{ms\perp}|^{0.4}}{2} v_{ms\perp} \underline{e}_{\perp} \end{aligned} \quad (5.74)$$

since it best predicts the data base average over all ranges of inclinations.

- (2) For precise design calculations consulting the actual available data base for the conditions of interest before using the generalized superposition model above.
- (3) For current multidimensional computer code applications using superposition model (1)

$$\begin{aligned} \langle \underline{R} \rangle = & f_{||} [|\langle v_{||} \rangle|] \frac{1}{D_v} \frac{\rho |\langle v_{||} \rangle|}{2} \langle v_{||} \rangle \underline{e}_{||} + \\ & b_{\perp} [|v_{ms\perp}|] \frac{1}{D_v} \frac{\rho |v_{ms\perp}|}{2} v_{ms\perp} \underline{e}_{\perp} \end{aligned} \quad (5.75)$$

since it is easier to implement than model (6). Considering the overall accuracy of thermal-hydraulic codes, the accuracy lost by using model (1) is far outweighed by the simplicity gained in implementing model (1) in the current staggered mesh numerical algorithms. (The simplification arises from each resistance component being only a function of the corresponding velocity component.)

5.10 Individual Superposition Factor Evaluation

The previous section recommended superposition models for turbulent flow, where the only requirement of the parallel superposition factor $g_1(\theta)$ was that it approached one as θ approached zero. For laminar flow the above models have not been validated and clearly need further examination.

In laminar flow the parallel/crossflow ratio of Eq. (5.65) is approximately 0.25, resulting in a significant contribution of $g_1(\theta)$ to the total resistance prediction for flow inclinations as large as 60 degrees. Physically, skin friction is no longer a negligible portion of the total resistance. The correct way to appraise the superposition models for laminar flow is to assess $h_1(\theta)$ and $g_1(\theta)$ independently with data for the parallel and crossflow resistance components evaluated from comprehensive inclined flow data.

We shall illustrate this procedure by using the comprehensive turbulent flow data. This procedure should be repeated with laminar flow data for proper evaluation of the superposition models for laminar flow. To date no laminar flow data for rod arrays have been published.

The data of Möller, Böttgenbach, and this study (Fig. 5.46) are evaluated for the parallel and crossflow components and compared with

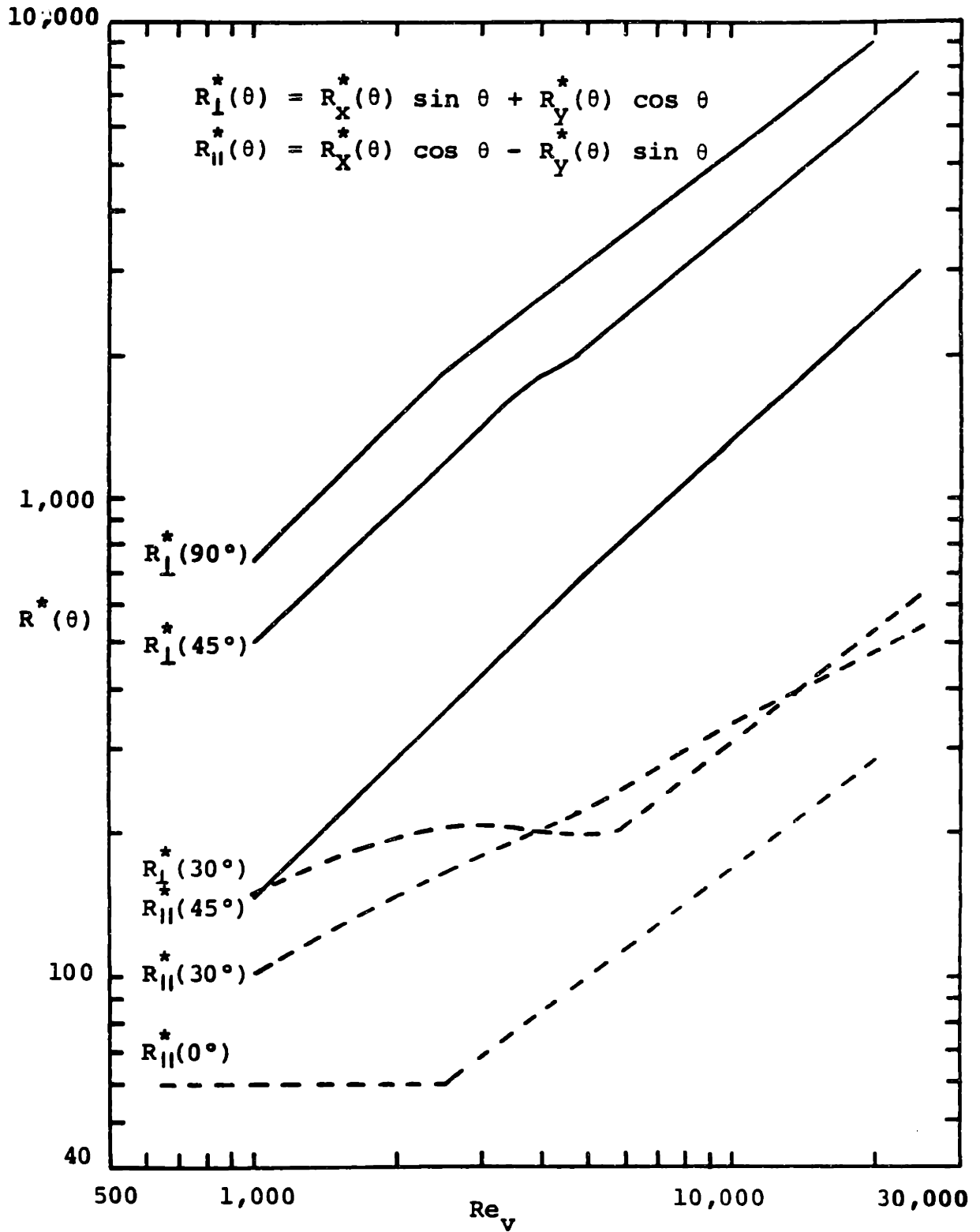


Figure 5.46 Parallel and crossflow resistance components.

the individual superposition models. The superposition factor $h_1(\theta)$ is shown in Fig. 5.47. To no surprise the crossflow component data generally lie between models (1) and (2). This was already shown in the last section with a more complete data base. Notice, however, that at about 45 degrees the resistance data becomes progressively larger as the Reynolds number (or Reynolds number range) decreases. This can be explained physically as an increasingly larger contribution from skin friction which is not correctly modeled by the principle of independence (model (1)).

This hypothesis is further illuminated by looking at the deviation of the drag resistance component from model (1) for low Reynolds numbers (Fig. 5.42); and for arrays of intermediate porosity and flow inclination (Fig. 5.40). At low Reynolds number skin friction becomes a significant portion of the total resistance. Also for intermediate porosities and flow angles the flow exhibits an appreciable amount of weaving motion, not exhibited in crossflow, which would explain a larger skin friction and consequently larger total resistance.

The parallel resistance component comprised totally of skin friction, further confirms the hypothesis of a larger skin friction in incline flows. Figure 5.48 shows the models and data for $g_1(\theta)$. The data is much larger than any of the model predictions, but is also not well correlated. Fundamentally, the lack of correlation is expected because for turbulent flow the parallel resistance component is a very small component of a much larger total resistance, making measurement and correlating of the quantity difficult. In laminar flow $g_1(\theta)$

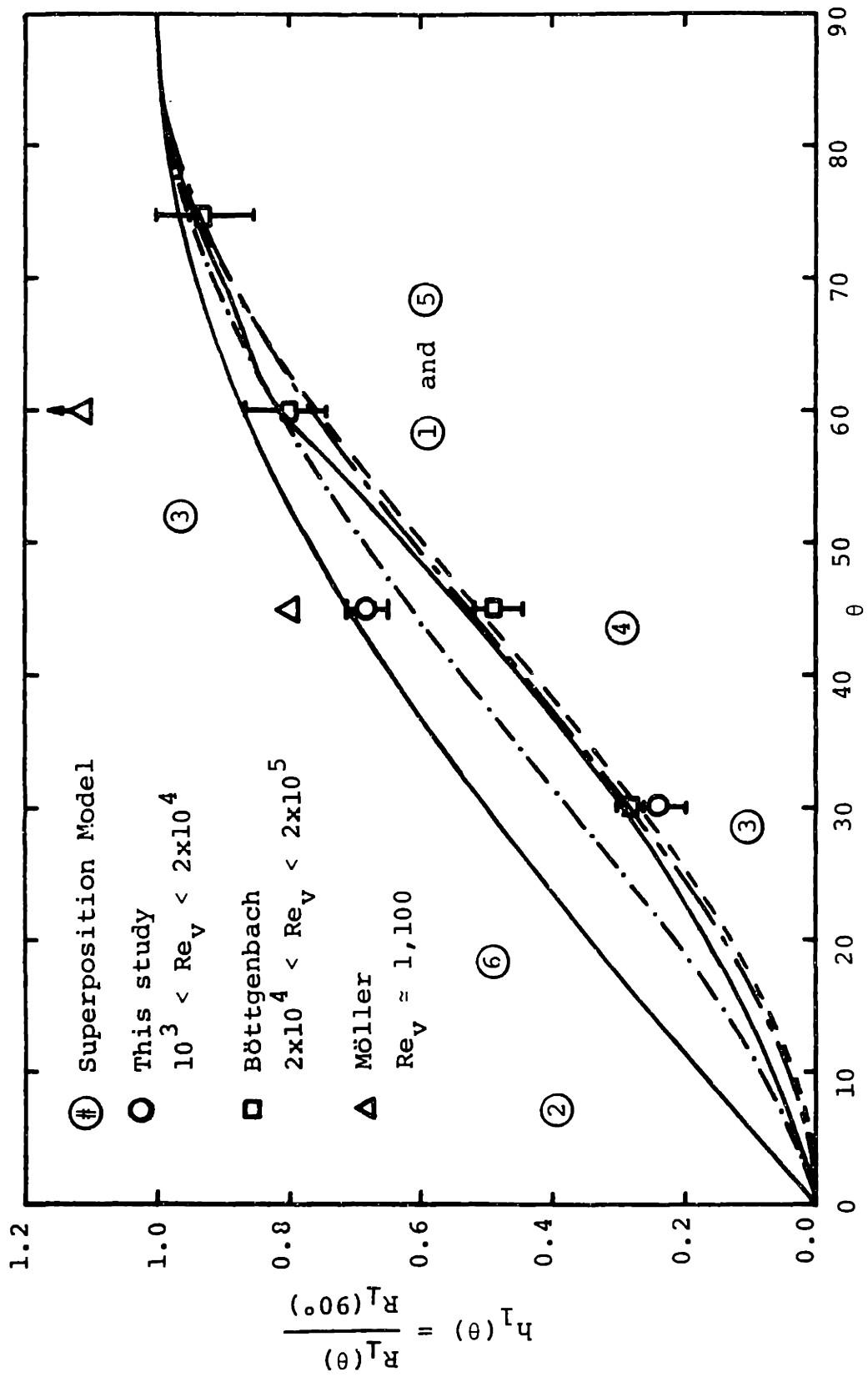


Figure 5.47 Data, crossflow superposition model comparison.

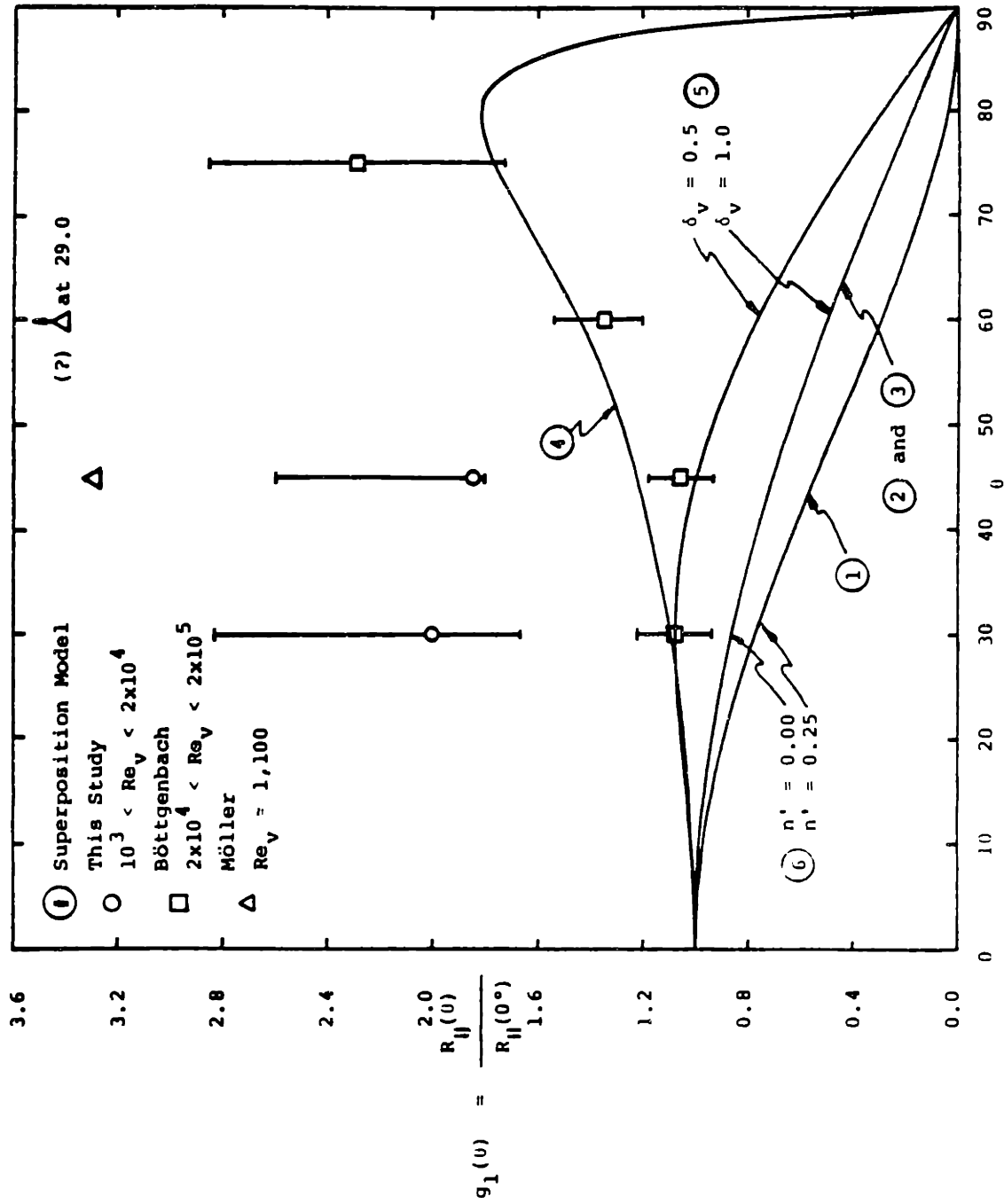


Figure 5.48 Data, parallel flow superposition model comparison.

would have a larger contribution, data would be better correlated, and a better evaluation of the parallel superposition models could be made.

In conclusion, a comprehensive data base of laminar flow resistance in inclined rod arrays is desired. Ideally drag and lift resistance components should be measured in laminar flow for inclinations of 15, 30, 45, and 60 degrees. Within this range of angles $g_1(\theta)$ and $h_1(\theta)$ can both easily be evaluated and hence modeled. Hopefully with this data base a better physical understanding of the separate skin friction and form drag superposition principles can be obtained. Then when the superposition models are applied to the limiting case of turbulent flow they will smoothly reduce to the models recommended in the previous section.

5.11 Summary

In this chapter a comprehensive review and evaluation of correlations, superposition models, and data for single-phase incline turbulent flow resistance in rod arrays was performed. The first complete flow resistance data for incline water flow was taken. This data was taken in a well-defined, fully-developed flow field at Reynolds numbers ranging from 1,000 to 25,000. This data together with Böttgenbach's high Reynolds number air flow data are the first to verify the superposition principle for calculating the lift component of resistance.

In the range of accuracy of the incline flow data base no generalized geometry or Reynolds dependence can be formulated. In addition the current accuracy of crossflow correlations limits the accuracy that can be achieved by using a superposition formulation for

calculating incline flow resistance. In general, superposition model ⑥ best predicts the complete data base. For multidimensional, thermal-hydraulic codes superposition model ① with a circumferentially averaged crossflow correlation is sufficient and the simplest to implement. To date no circumferentially-averaged crossflow correlations have been developed.

An attempt to understand the actual flow field in a rod array, interpret the separate effects of form drag and skin friction, and develop a physically based superposition model (i.e. model ⑤) proved inconclusive for turbulent flow. It was inconclusive primarily because form drag dominated all flow inclinations. These developments, however, may prove useful in laminar flow, where to date, superposition models for rod arrays have not been validated.

CHAPTER 6

TWO-PHASE FLOW MODELING

The two principle constitutive relations for two-phase flow hydrodynamic modeling are the two-phase flow resistance and interfacial momentum exchange force. In this chapter we shall focus on developing models for the interfacial force which governs the relative slip between the phases. The time/volume averaged interfacial momentum exchange force $\langle \underline{M}_i^d \rangle$ is the average of the shear and pressure forces on the interface between gas and liquid, mathematically

$$\langle \underline{M}_i^d \rangle \triangleq \frac{\Delta}{\Delta t} \int \frac{1}{\Delta t} \int \frac{1}{V_f} \int \frac{1}{A_i} [(\{\{\bar{p}_i\}\}^i - p_i) \underline{I} + \underline{\tau}_i] \cdot \underline{n}_i \, dA \, dt \quad (6.1)$$

where the integral of the local pressure is relative to the interfacial surface averaged pressure $\{\{\bar{p}_i\}\}^i$.

Equation (6.1) is a local definition of the interfacial force applicable for all flow situations. However in application the local variables in Eq. (6.1) are unknown, so it is desired to develop an integral correlation for $\langle \underline{M}_i^d \rangle$ dependent only on known average flow variables for the specific fluid topology and geometry of interest.

First a formal development of the modeling correlations shall be presented; then current one-dimensional correlations are reviewed. Next, based on data taken in this study, one-dimensional correlations for parallel and crossflow in rod arrays will be examined. Finally, single and multiple bubble observations in inclined arrays are discussed, and multidimensional formulations for rod arrays proposed.

6.1 Model Formulation

6.1.1 General Formulation

To see the contribution to the interfacial momentum exchange force in terms of momentum of each phase we solve the phasic momentum equations for $\langle \underline{M}_i^d \rangle$

$$\langle \underline{M}_i^d \rangle = \langle \underline{M}_g^d \rangle = - \langle \underline{M}_l^d \rangle \quad (6.2)$$

where the mixture momentum (surface tension forces) $\langle \underline{M}_m \rangle$ is neglected. The phasic momentum equation, Eq. (A.89), when solved for the interfacial force under the constraints:

- constant phasic densities,
- gravity as body force,
- constant volume porosity,
- no phase change, and
- combined viscous and turbulent shear, i.e.,

$$\langle \langle \underline{\tau}_{=k}^e \rangle \rangle \stackrel{\Delta}{=} \langle \langle \underline{\tau}_{=k}^m \rangle \rangle + \langle \langle \underline{\tau}_{=k}^T \rangle \rangle$$

becomes

$$\begin{aligned} \langle \underline{M}_g^d \rangle &= \langle \underline{R}_g \rangle - \langle \alpha \rangle \rho_g \underline{g} + \langle \alpha \rangle \nabla \langle \langle \underline{p}_g^m \rangle \rangle \\ &+ \Delta p_g^i \nabla \langle \alpha \rangle - \nabla \cdot [\langle \alpha \rangle \langle \langle \underline{\tau}_{=g}^e \rangle \rangle] \\ &+ \frac{\partial}{\partial t} [\langle \alpha \rangle \rho_g \langle \langle \underline{v}_{=g}^m \rangle \rangle] + \nabla \cdot [\underline{C}_{gm} \langle \alpha \rangle \rho_g \langle \langle \underline{v}_{=g}^m \rangle \rangle \langle \langle \underline{v}_{=g}^m \rangle \rangle] \end{aligned} \quad (6.3)$$

and

$$\begin{aligned} \langle \underline{M}_l^d \rangle &= \langle \underline{R}_l \rangle - (1 - \langle \alpha \rangle) \rho_l \underline{g} + (1 - \langle \alpha \rangle) \nabla \langle \langle \underline{p}_l^m \rangle \rangle \\ &- \Delta p_l^i \nabla \langle \alpha \rangle - \nabla \cdot [(1 - \langle \alpha \rangle) \langle \langle \underline{\tau}_{=l}^e \rangle \rangle] \\ &+ \frac{\partial}{\partial t} [(1 - \langle \alpha \rangle) \rho_l \langle \langle \underline{v}_{=l}^m \rangle \rangle] + \nabla \cdot [\underline{C}_{lm} (1 - \langle \alpha \rangle) \rho_l \langle \langle \underline{v}_{=l}^m \rangle \rangle \langle \langle \underline{v}_{=l}^m \rangle \rangle] \end{aligned} \quad (6.4)$$

where

$$\langle \alpha \rangle \stackrel{\Delta}{=} \langle \alpha_g \rangle = - \langle \alpha_l \rangle$$

Now starting with the identity

$$\begin{aligned}\langle \underline{M}_i^d \rangle &= (1 - \langle \alpha \rangle) \langle \underline{M}_i^d \rangle + \langle \alpha \rangle \langle \underline{M}_i^d \rangle \\ &= (1 - \langle \alpha \rangle) \langle \underline{M}_g^d \rangle - \langle \alpha \rangle \langle \underline{M}_l^d \rangle\end{aligned}\quad (6.5)$$

and substituting in Eq. (6.3) and (6.4) gives

$$\begin{aligned}\langle \underline{M}_i^d \rangle &= (1 - \langle \alpha \rangle) \langle \underline{R}_g \rangle - \langle \alpha \rangle \langle \underline{R}_l \rangle && \left. \vphantom{\langle \underline{M}_i^d \rangle} \right\} \text{Structural Resistance Force} \\ &- (1 - \langle \alpha \rangle) \langle \alpha \rangle (\rho_g - \rho_l) \underline{g} && \left. \vphantom{\langle \underline{M}_i^d \rangle} \right\} \text{Buoyancy Force} \\ &+ (1 - \langle \alpha \rangle) \langle \alpha \rangle \nabla (\langle \underline{p}_g \rangle - \langle \underline{p}_l \rangle) && \left. \vphantom{\langle \underline{M}_i^d \rangle} \right\} \text{Mechanical Disequilibrium} \\ &+ ((1 - \langle \alpha \rangle) \Delta p_g^i + \langle \alpha \rangle \Delta p_l^i) \nabla \langle \alpha \rangle && \left. \vphantom{\langle \underline{M}_i^d \rangle} \right\} \text{Forces} \\ &- \{ (1 - \langle \alpha \rangle) \nabla \cdot [\langle \alpha \rangle \langle \underline{\tau}_g^e \rangle] - && \left. \vphantom{\langle \underline{M}_i^d \rangle} \right\} \text{Viscous and Turbulent Shear} \\ &\quad \langle \alpha \rangle \nabla \cdot [(1 - \langle \alpha \rangle) \langle \underline{\tau}_l^e \rangle] \} && \left. \vphantom{\langle \underline{M}_i^d \rangle} \right\} \text{Forces (i.e., Basset and} \\ & && \left. \vphantom{\langle \underline{M}_i^d \rangle} \right\} \text{lift forces)} \\ &+ (1 - \langle \alpha \rangle) \left\{ \frac{\partial}{\partial t} [\langle \alpha \rangle \rho_g \langle \underline{v}_g \rangle] + && \left. \vphantom{\langle \underline{M}_i^d \rangle} \right\} \text{Spatial and Temporal} \\ &\quad \nabla \cdot [\underline{C}_{gm} \langle \alpha \rangle \rho_g \langle \underline{v}_g \rangle \langle \underline{v}_g \rangle] \} && \left. \vphantom{\langle \underline{M}_i^d \rangle} \right\} \text{acceleration Forces} \\ &- \langle \alpha \rangle \left\{ \frac{\partial}{\partial t} [(1 - \langle \alpha \rangle) \rho_l \langle \underline{v}_l \rangle] + && \left. \vphantom{\langle \underline{M}_i^d \rangle} \right\} \text{(i.e., virtual mass)} \right. \\ &\quad \left. \nabla \cdot [\underline{C}_{lm} (1 - \langle \alpha \rangle) \rho_l \langle \underline{v}_l \rangle \langle \underline{v}_l \rangle] \right\} && (6.6)\end{aligned}$$

The first two terms are the steady state forces and the remaining are transient forces.

In practice, correlations for the individual contributions are modeled separately and then assumed mutually independent so that the total interfacial force can be evaluated by summing the individual models. In steady state the structural resistance and buoyancy forces are modeled together as an interfacial drag force. In transients,

correlations for the Basset and virtual mass forces have been developed [D.1, I.5]. Basset force is the effect of acceleration on viscous drag and boundary layer development. Virtual mass is the force associated with accelerating the surrounding liquid phase when the relative velocity changes. The inclusion of virtual mass is important to obtaining numerical stability in transient two-fluid codes, however its contribution to phase separation is not completely understood. The lift force may be important only in viscous systems, and the mechanical disequilibrium only for rapid depressurization situations.

6.1.2 Drag Force Formulation

In this study we shall be concerned with modeling the steady state drag forces which are the dominant terms for a large range of gas-liquid flows. We shall also restrict our discussion to flows where the gas phase is dispersed in the liquid (i.e., bubbly flow.).

First consider partitioning $\langle M_i^d \rangle$ into individual drag forces $F_{Dj} V_{bj}$, for each closed interface j , where V_{bj} is the closed interface (bubble) volume and F_{Dj} is the drag force per bubble volume.

Then

$$-\langle M_i^d \rangle = \frac{\text{Interfacial Force}}{\text{Fluid Volume}} = \frac{\sum_j^{N_b} F_{Dj} V_{bj}}{V_f} \quad (6.7)$$

where N_b is the number of bubbles in the averaging volume. Now noting that

$$V_g = \sum_j^{N_b} V_{bj} = \langle \alpha \rangle V_f \quad (6.8)$$

Eq. (6.7) becomes

$$-\frac{\langle \underline{M}_i^d \rangle}{\langle \alpha \rangle} = \frac{\sum_j^{N_b} \underline{F}_{Dj} V_{bj}}{\sum_j^{N_b} V_{bj}} \stackrel{\Delta}{=} \underline{F}_D \quad (6.9)$$

The bubble drag per unit bubble volume \underline{F}_D , may be interpreted either as the drag force of an average size bubble in N_b , or if all N_b bubbles are of identical size, the force on one of the bubbles.

Comparing Eq. (6.9) with Eq. (6.6) for steady state flow where only the liquid phase contacts the solid surfaces ($\langle \underline{R}_g \rangle = 0$) gives

$$\begin{aligned} \underline{F}_D &= \underline{F}_R + \underline{F}_G \\ &= \langle \underline{R}_\ell \rangle + (1 - \langle \alpha \rangle)(\rho_g - \rho_\ell) \underline{g} \end{aligned} \quad (6.10)$$

We have now reduced the problem of modeling $\langle \underline{M}_i^d \rangle$ down to modeling the drag force on a typical bubble of given volume V_b in a specified environment.

One-dimensional drag formulas for a bubble have historically been modeled in the form

$$|\underline{F}_D| = C_D \frac{A_{proj}}{V_b} \frac{\rho_\ell |\underline{v}_r|^2}{2} \quad (6.11)$$

where C_D is the scalar drag coefficient, A_{proj} , is the projected area of the bubble, and $|\underline{v}_r|$ is the relative velocity between the bubble and liquid. This formula can be generalized to multidimensional flows for thermal-hydraulic code applications thus

$$\underline{F}_D = \underline{C}_D a_p \frac{\rho_\ell |\underline{v}_r|}{2} \underline{v}_r \quad (6.12)$$

where \underline{C}_D is now a drag coefficient tensor; the relative velocity is defined in terms of volume-averaged velocities

$$\begin{aligned} \frac{v}{r} &\stackrel{\Delta}{=} \langle \langle \underline{\underline{v}}_{\underline{\underline{g}}} \rangle \rangle - \langle \langle \underline{\underline{v}}_{\underline{\underline{l}}} \rangle \rangle \\ &= \langle \underline{\underline{v}}_{\underline{\underline{g}}} \rangle - \langle \underline{\underline{v}}_{\underline{\underline{l}}} \rangle \end{aligned} \quad (6.13)$$

where the second equality applies to a single bubble; and A_{proj}/V_b has been defined for a spherical bubble of equivalent volumetric diameter D_b ,

$$a_p \stackrel{\Delta}{=} \frac{\pi \frac{D_b^2}{4}}{\pi \frac{D_b^3}{6}} = \frac{3}{2} \frac{1}{D_b} \quad (6.14)$$

The drag coefficient ideally is a universal scalar constant applicable for all flow situations. This is true only if the bubble shape (i.e., A_{proj}), local gas, and local liquid velocities are used in the model. In reality, however, only the average velocities and phase volumes are known. To account for the differences between local variables and measurable average variables, the drag coefficient becomes a tensor function dependent on the specific flow environment of interest.

6.2 Flow Environments

Four environmental conditions which effect the bubble drag coefficient C_D , are considered here: the geometry, gravitation field, liquid velocity field, and gas distribution.

The geometry may be a large pool, round tube, or rod array. In a large pool (infinite medium) the boundaries have no influence on the liquid translation and rotation around the bubble. In a round tube or rod array the liquid motion in the neighborhood of the bubble can be inhibited by the zero liquid velocity constraint at the solid boundaries. Consequently in restricted geometries the effective drag

should be greater than that in an infinite medium. However, as will be seen later, this is not always true.

For zero and low liquid flows the dominant driving force is bouyancy created by the gravitational field. In these cases the direction of gravity with respect to the flow geometry is critical. For high liquid flows the flow resistance force is the dominant driving force diminishing the importance of gravity. Also for nonzero liquid velocities in some geometries (i.e., inclined rod arrays) the velocity field can change significantly from that of zero liquid flow. Thus the drag coefficients correlated from and applicable for zero flow may not apply for the flowing liquid fields. Last, a system of many bubbles in close proximity will influence each other either increasing or decreasing the average bubble velocity.

It is not practical to study all possible combinations of environmental conditions that occur. Instead a few fundamental cases are addressed, the importance of each weighed, and if possible superimposed to describe more elaborate environments. For example the drag coefficient has been correlated extensively for a single bubble in an infinite medium (with buoyancy as the only driving force.). These basic correlations are then corrected for the presence of multiple bubbles, finite geometry, or flowing liquid.

In correlating drag coefficients several dimensionless groups have successfully incorporated the influence of fluid properties. They are

- The Eötvös number

$$Eo \triangleq \frac{g(\rho_l - \rho_g)D_b^2}{\sigma} \quad (6.15)$$

The dimensionless bubble number where D_b is the equivalent

spherical bubble diameter

$$D_b \triangleq \left(\frac{6V_b}{\pi} \right)^{1/3} \quad (6.16)$$

- The bubble Reynolds number

$$Re_b \triangleq \frac{\rho_l D_b |\underline{v}_r|}{\mu_l} \quad (6.17)$$

and

- The dimensionless viscosity number

$$\hat{M} \triangleq \frac{g \mu_l^4 (\rho_p - \rho_g)}{\rho_l^2 \sigma^3} \quad (6.18)$$

which is sometimes defined as

$$N_\mu \triangleq \hat{M}^{1/4} \quad (6.19)$$

6.3 One-Dimensional Drag Coefficient Models

In this section we review and amend the state of the art of the drag coefficient for one-dimensional bubbly flow; specifically for single and multiple bubbles in an infinite medium, vertical tubes, parallel and crossflow arrays.

In one-dimensional flow the relative velocity \underline{v}_r , and drag force \underline{F}_D , are collinear so Eq. (6.12) can be written

$$C_D = \underline{C}_D = \frac{2 |\underline{F}_D|}{a_p \rho_l |\underline{v}_r|^2} \quad (6.20)$$

where the drag coefficient C_D is a scalar. For zero liquid flow Eq. (6.20) reduces to

$$C_D = \frac{2 |\underline{F}_G|}{a_p \rho_l |\langle \underline{v} \rangle|^2} \quad (6.21)$$

6.3.1 Single Bubble in Infinite Medium

Three basic regimes of a single bubble flowing in an infinite

medium have been identified. They are spherical viscous bubbles, distorted bubbles, and capped bubbles. Sample bubbles for these three regimes are shown in Plate 6.1(a), (b), and (c).

Table 6.1 lists the reviewed models for drag coefficient in an infinite medium, $C_{D\infty}$. Figure 6.1 plots the reviewed models versus bubble Reynolds number for a viscosity number \hat{M} of 10^{-11} (characteristic of gas-liquid systems such as air-water and steam-water). The low $Re_{b\infty}$ monotonically decreasing region is the viscous regime, where the bubbles behave as a solid sphere. The monotonically increasing region is the distorted regime. The high $Re_{b\infty}$ plateau is the capped regime. As shown in the insert of Fig. 6.1 the liquid purity can effect the transition from viscous to distorted bubbles. This is because surfactants in contaminated liquids effect the surface tension forces which determine the bubble volume at which distortion from spherical begins. For very pure liquid systems internal circulation of the gas reduces the bubble drag, dropping the drag coefficient below that for a solid sphere [C.3]. Figure 6.2 shows the regime boundaries as predicted by Ishii [I.3] and Peeble-Garber [P.1] overlaid on the regime map of Clift et al. [C.3]. The distorted regime of Peeble-Garber is small because their model is based on data in pure water systems. In the developments to follow we shall use the infinite medium drag model of Ishii as a base since it is the most comprehensive model to date.

Figure 6.3 shows air bubble rise data taken in standing water in the experimental test duct (The data is tabulated in Appendix F).



(A)



(B)



(C)



(D)



(E)



(F)

PLATE 6.1 (A) SPHERICAL, (B) DISTORTED, AND (C) CAPPED BUBBLES IN INFINITE MEDIUM; (D) DISTORTED AND (E) SLUG BUBBLES IN PARALLEL ARRAY; (F) SLUG BUBBLE IN CROSSFLOW ARRAY.

TABLE 6.1

Drag Coefficient Models for Single Bubble in Infinite Medium

$$C_{D_{\infty}} \triangleq \frac{2|F_D|}{\rho_l \rho_l |\mathbf{v}_{r_{\infty}}|^2}, \quad Re_{b_{\infty}} \triangleq \frac{\rho_l D_b |\mathbf{v}_{r_{\infty}}|}{\mu_l}, \quad \hat{M} \triangleq \frac{g \mu_l^4 (\rho_l - \rho_g)}{\rho_l^2 \sigma^3}$$

Model	Drag Coefficient $C_{D_{\infty}}$	Range
Ishii [I.3]	$\frac{24}{Re_{b_{\infty}}} (1 + 0.1 Re_{b_{\infty}}^{0.75})$ $\frac{2}{3} D_b \sqrt{\frac{g(\rho_l - \rho_g)}{\sigma}}$ $\frac{8}{3}$	$\hat{M}^{1/4} \leq \frac{36\sqrt{2}}{Re_{b_{\infty}}^2} (1 + 0.1 Re_{b_{\infty}}^{0.75})$ <p>elsewhere</p> $D_b \geq 4 \sqrt{\frac{\sigma}{g(\rho_l - \rho_g)}}$
TRAC-PIA [T.3]	240 $24/Re_{b_{\infty}}$ $18.7/Re_{b_{\infty}}$ 0.44	$Re_{b_{\infty}} \leq 0.1$ $0.1 < Re_{b_{\infty}} \leq 2$ $2 < Re_{b_{\infty}} \leq 248$ $248 < Re_{b_{\infty}}$
Stonecypher [S.5]	$26.34 Re_{b_{\infty}} \left\{ \begin{array}{l} -0.889 + 0.03421 \ln(Re_{b_{\infty}}) \\ + 0.00144 (\ln(Re_{b_{\infty}}))^2 \end{array} \right\}$	viscous bubbles

TABLE 6.1 (Continued)

Drag Coefficient Models for Single Bubble in Infinite Medium

Model	Drag Coefficient $C_{D\infty}$	Range
Peeble and Garber [P.1]	$24/Re_{b\infty}$ $18.7/Re_{b\infty}^{0.68}$ $0.0275 \hat{M} Re_{b\infty}^4$ $0.82 \hat{M}^{0.25} Re_{b\infty}$	$Re_{b\infty} \leq 2$ $2 < Re_{b\infty} \leq 4.02 \hat{M}^{-0.214}$ $4.02 \hat{M}^{-0.214} < Re_{b\infty} \leq 3.10 \hat{M}^{-0.25}$ $3.10 \hat{M}^{-0.25} < Re_{b\infty}$
Wallis [W.6]	$6.30/Re_{b\infty}^{0.385}$	viscous bubbles
Haas and Brauer [H.3]	$14.9/Re_{b\infty}^{0.78}$	viscous bubbles $Re_{b\infty} > 2$
Grace et. al [G.3]	$C_{D\infty} = (C_{D\infty})_{cont.} / (1 + \Gamma)^2$ where $(C_{D\infty})_{cont.} = ftn[Re_b, \hat{M}]$ $\Gamma = ftn[D_b, \mu_g/\mu_l]$	distorted bubbles contaminated water: $\Gamma = 0$ pure water: $\Gamma = 2$
Clift et. al. [C.3]	$\frac{8}{3}$	capped bubbles

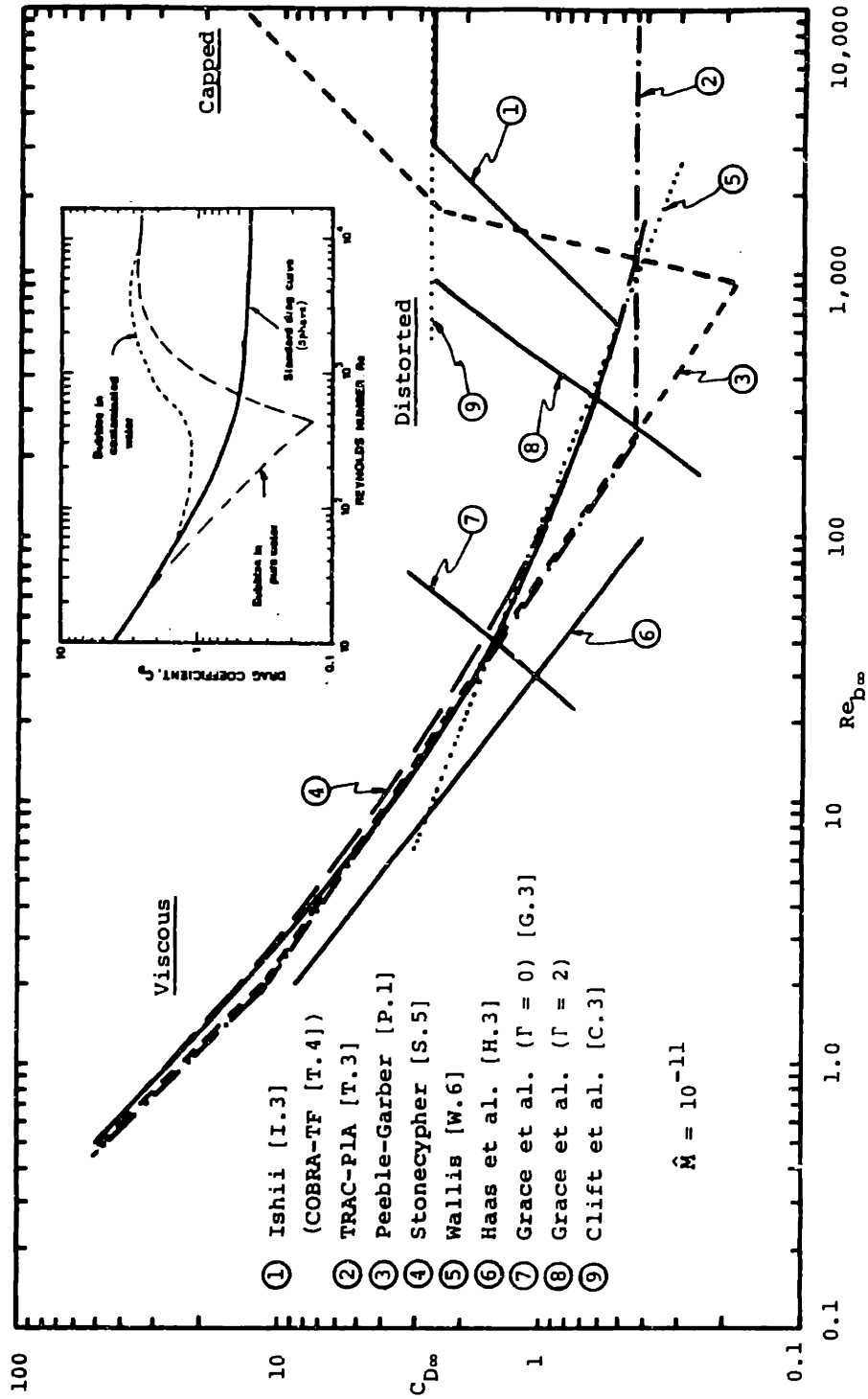


Figure 6.1 Single bubble drag coefficient in an infinite medium. (Insert from Ref. [C.3]).

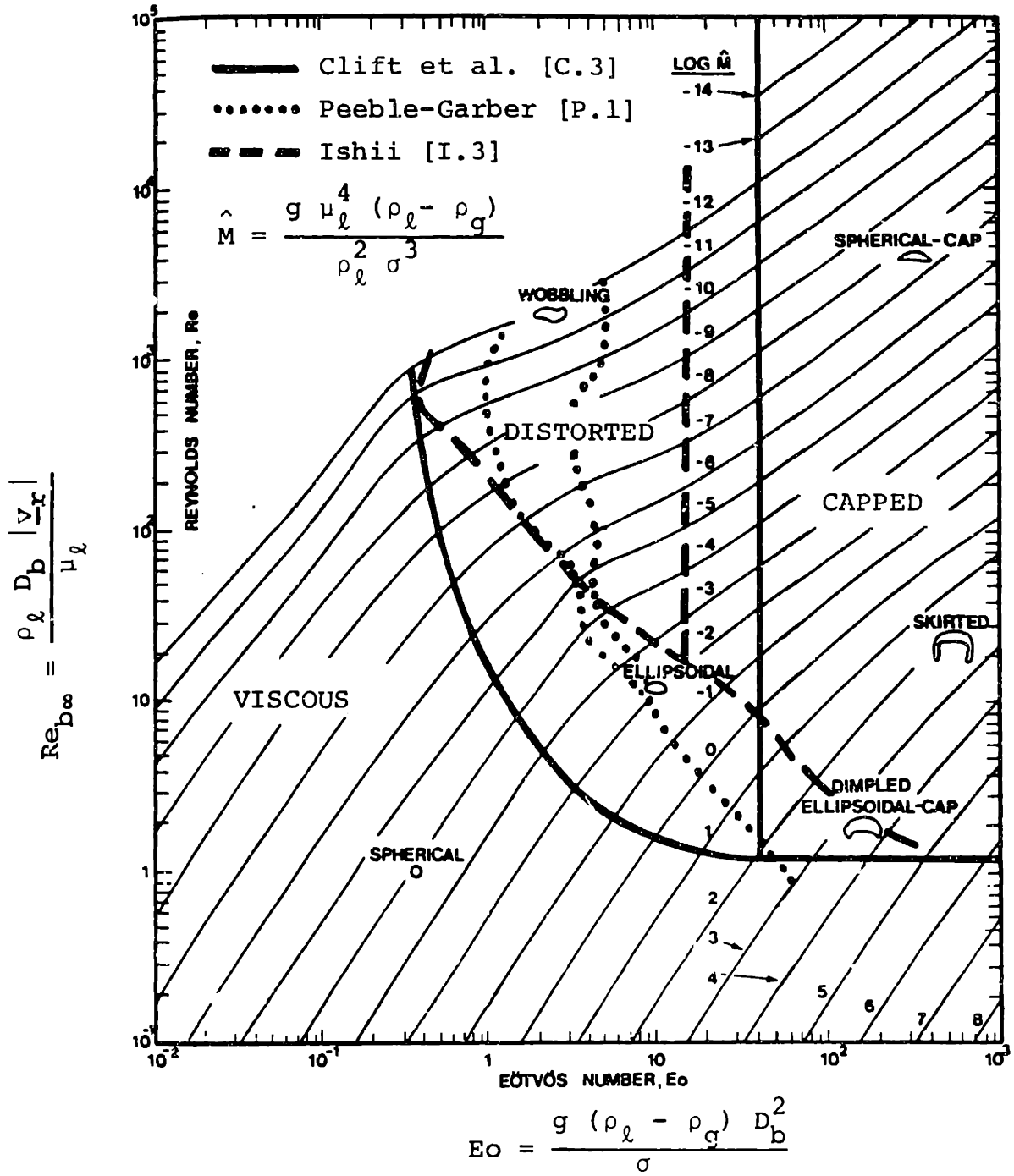


Figure 6.2 Bubble shape regimes for buoyancy flow in infinite medium (adapted from Ref. [C.3]).

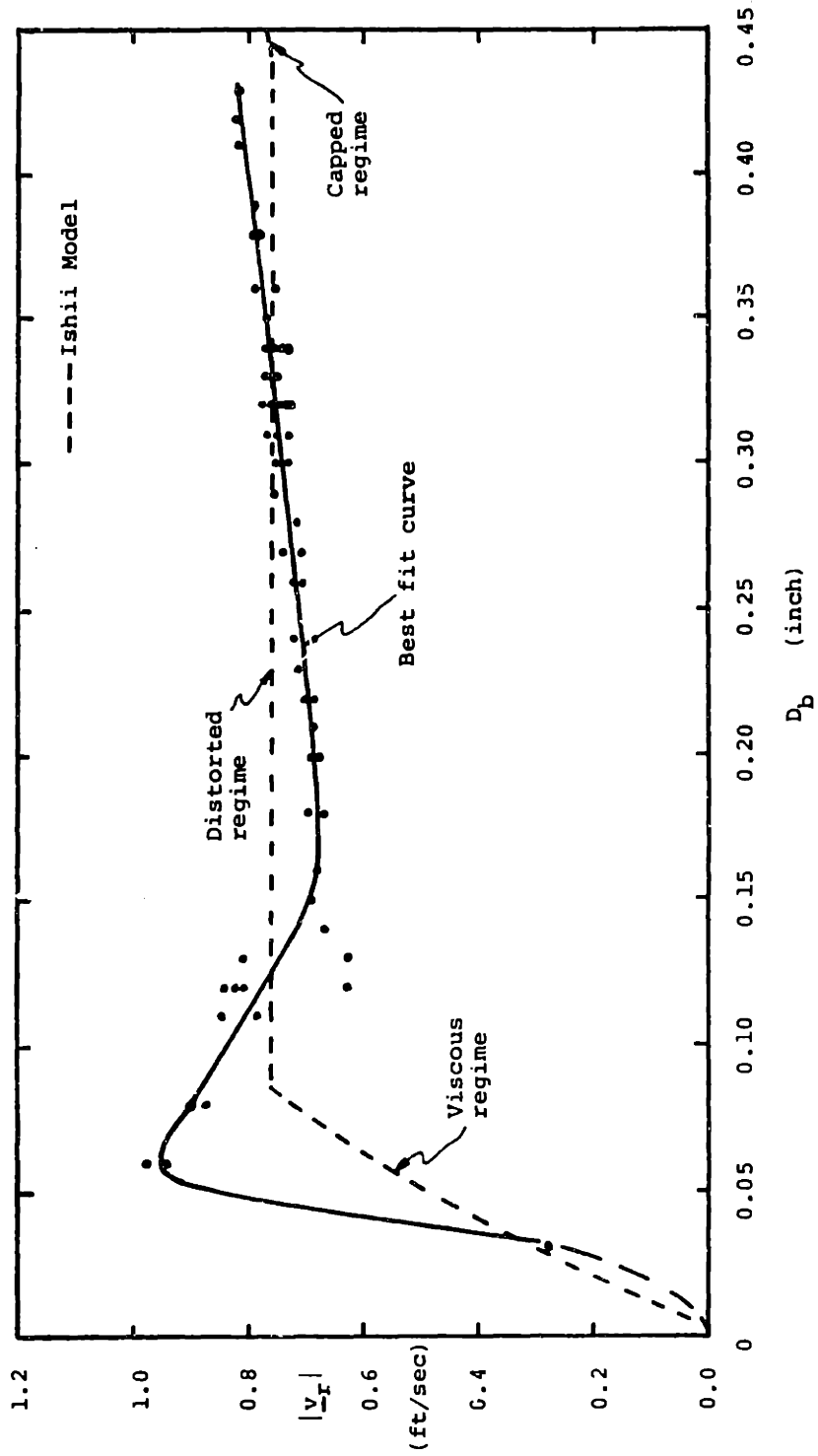


Figure 6.3 Bubble rise velocity in test duct.

Good agreement between this data and previous work is shown in Fig 6.4, reproduced from Clift et al. [C.3]. Also plotted in Fig. 6.3 is the model of Ishii. His model predicts the average trends well, however it does not account for the peak in rise velocity at $D_b = 0.06$ inch (0.15 cm) caused by the relatively pure water system.

6.3.2 Multiple Bubbles in Infinite Medium

Ishii [1.3] has developed a bubble drag coefficient model for multiple bubbles in an infinite medium. Additional bubbles in the neighborhood of a single bubble will alter the single bubble drag coefficient by adding resistance to deformation of the surrounding medium and by adding direct interaction between bubble wakes. A detailed derivation of Ishii's model is given in Appendix G.

In the viscous regimes Ishii hypothesizes that similarity between single bubble and multiple bubble drag can be drawn when the liquid viscosity is replaced by the mixture viscosity, μ_m . The justification for using mixture viscosity similarity is: as a bubble moves through a dispersed two-phase medium it causes translation and rotation of the medium in the neighborhood of the bubble. The addition of discrete bubbles in the liquid makes the surrounding medium appear more rigid increasing the resistance to motion. This increased resistance is accounted for by the higher viscosity of the mixture relative to that for the liquid alone. The increased drag results in a slower rise velocity than for single bubbles. The resultant drag coefficient is

$$C_{D,\infty}^V [Re_{b,\infty}] = \frac{24}{Re_{b,\infty}} \left(\frac{\mu_m}{\mu_l} \right) \left(1 + 0.1 \left(Re_{b,\infty} \frac{\mu_l}{\mu_m} \right)^{0.75} \right) \quad (6.22)$$

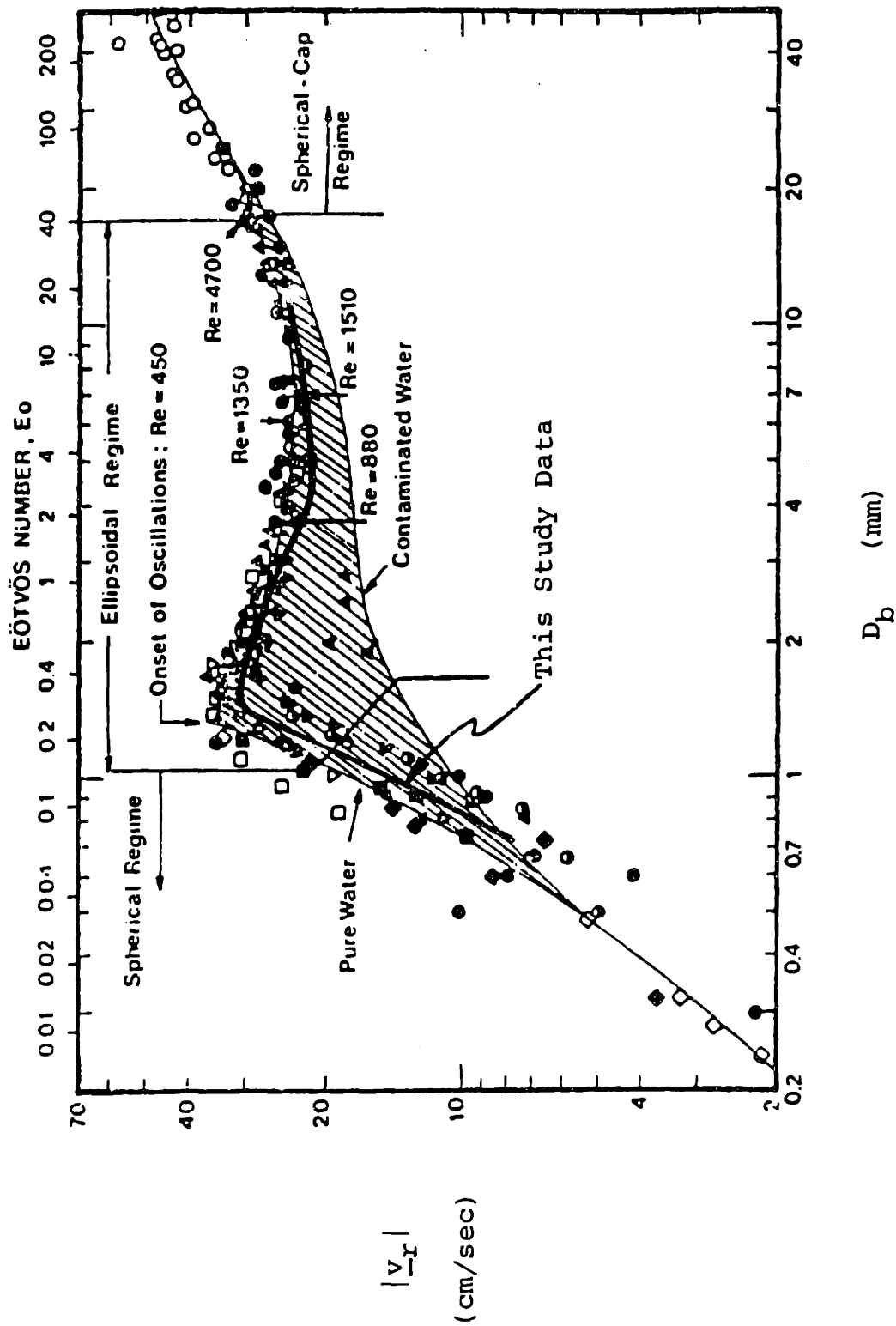


Figure 6.4 Comparison of bubble rise velocity in infinite medium of this study with previous work [C.3].

where the superscript V denotes viscous regimes, the prime denotes multiple bubbles, and for bubbly flow the viscosity ratio is

$$\frac{\mu_m}{\mu_l} = \frac{1}{1 - \langle \alpha \rangle} \quad (6.23)$$

In the distorted regime the single bubble drag is independent of relative velocity and viscosity. Assuming that the same is true for multiple bubbles and maintaining continuity of drag (and relative velocity) at the viscous-distorted transition point gives

$$C_{D', \infty}^D [Re_{b', \infty}] = \frac{2}{3} D_b \sqrt{\frac{g(\rho_l - \rho_g)}{\sigma}} \frac{C_{D', \infty}^V [Re_{b', \infty}^{VD}]}{C_{D\infty}^V [Re_{b\infty}^{VD}]} \quad (6.24)$$

The transition point drag coefficient ratio can be evaluated from the viscous regime correlations at the transition Reynolds number $Re_{b\infty}^{VD}$. Ishii approximates $Re_{b\infty}^{VD}$ by the Reynolds number at the viscous-Newton transition, $Re_{b\infty}^{VN} = 1,006$ (The Newton regime is where the solid sphere drag coefficient reaches an asymptote of 0.45). Using approximations to reduce the formula to an explicit expression gives

$$\frac{C_{D', \infty}^V [Re_{b', \infty}^{VD}]}{C_{D\infty}^V [Re_{b\infty}^{VD}]} \approx \frac{C_{D', \infty}^V [Re_{b', \infty}^{VN}]}{C_{D\infty}^V [Re_{b\infty}^{VN}]} \approx \left(\frac{1.0 + 17.86 f'[\alpha]^{6/7}}{18.86 f'[\alpha]} \right)^2 \quad (6.25)$$

where

$$f'[\alpha] = (1 - \langle \alpha \rangle)^{1.5} \quad (6.26)$$

By solving for $Re_{b', \infty}^{VD}$ directly and using approximations only to reduce to an explicit expression gives the more general formula

$$\frac{C_{D,\infty}^V [Re_{b,\infty}^{VD}]}{C_{D,\infty}^V [Re_{b,\infty}^{VD}]} = \left[\frac{1 + \frac{0.460}{\sqrt{N_\mu}} f'[\alpha]^{6/7}}{f'[\alpha] \left(1 + \frac{0.460}{\sqrt{N_\mu}}\right)} \right]^2 \quad (6.27)$$

Equation (6.24) with Eq. (6.25) or (6.27) gives multiple bubble drag coefficient in the distorted regime.

In the capped regime multiple bubbles interact with the wakes of neighboring bubbles creating a churning, hence this regime is more appropriately called churn-turbulent. Ishii assumes the average motion is governed by the drag of the largest bubble formed (i.e., capped bubble) where the characteristic velocity is the drift velocity, $|\underline{v}_{gj}| = (1 - \langle \alpha \rangle) |\underline{v}_r|$. Thus the churn-turbulent drag coefficient is

$$C_{D,\infty}^C [Re_{b,\infty}^C] = \frac{8}{3} (1 - \langle \alpha \rangle)^2 \quad (6.28)$$

Notice that in this regime the drag is reduced by the bubbles following in the wake of leading bubbles.

The multiple bubble infinite medium model is summarized in Table 6.2 and shown graphically relative to the single bubble model in Fig. 6.5. Ishii has shown good agreement with experimental data for a wide range of flow conditions [1.3].

6.3.3 Single Bubble in Finite Geometry

The presence of a solid boundary in the neighborhood of a single bubble will change the uniform liquid velocity condition remote from the bubble to a no slip condition near the bubble. Physically, the finite geometry restricts the translation and rotation of the surrounding liquid around the moving bubble. The restriction increases the bubble

TABLE 6.2

Multiple Bubble Drag Coefficient

$$|F_{D',\infty}| = C_{D',\infty} a \rho_L \frac{|v_{r',\infty}|^2}{2}$$

Drag Coefficient		Range
$C_{D',\infty}^V = \frac{24}{(1 - \langle\alpha\rangle) Re_{b',\infty}} \{1 + 0.1[(1 - \langle\alpha\rangle) Re_{b',\infty}]^{0.75}\}$		$D_b \leq D_b^{VD}$
$C_{D',\infty}^D = \frac{2}{3} D_b \sqrt{\frac{g(\rho_L - \rho_g)}{\sigma}}$ $\left\{ \frac{1 + \frac{0.460}{\sqrt{N_\mu}} (1 - \langle\alpha\rangle)^{9/7}}{(1 - \langle\alpha\rangle)^{3/2} (1.0 + \frac{0.460}{\sqrt{N_\mu}})} \right\}^2$		$D_b^{VD} \leq D_b < D_b^{DC}$
$C_{D',\infty}^C = \frac{8}{3} (1 - \langle\alpha\rangle)^2$		$D_b^{DC} \leq D_b$
<p>where: $D_b^{VD} \approx 5.42 N_\mu^{1/3} \sqrt{\frac{\sigma}{g(\rho_L - \rho_g)}}$</p> $D_b^{DC} = 4 \sqrt{\frac{\sigma}{g(\rho_L - \rho_g)}} (1 - \langle\alpha\rangle)^5 \left\{ \frac{1 + \frac{0.460}{\sqrt{N_\mu}}}{1 + \frac{0.460}{\sqrt{N_\mu}} (1 - \langle\alpha\rangle)^{9/7}} \right\}^2$		

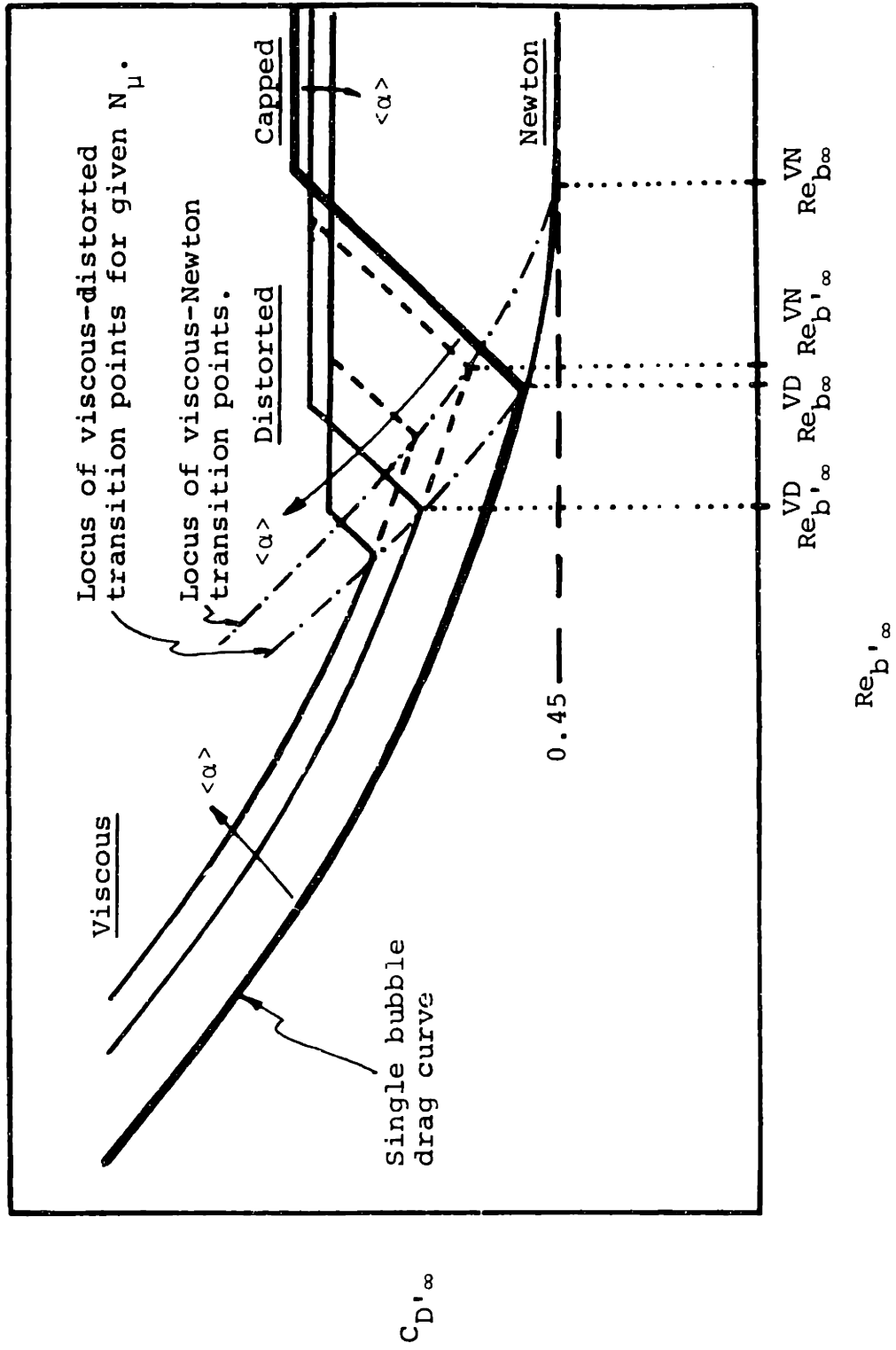


Figure 6.5 Multiple bubble drag coefficient for infinite medium.

drag and consequently decreases the bubble velocity relative to an infinite medium.

The finite geometry drag coefficient C_{Dw} , defined by

$$|\underline{F}_{-Dw}| = C_{Dw}[Re_{bw}] a_p \frac{\rho_l |\underline{v}_{-rw}|^2}{2} \quad (6.29)$$

can be expressed in terms of the infinite medium drag coefficient

$C_{D\infty}$

$$|\underline{F}_{-D\infty}| = C_{D\infty}[Re_{b\infty}] a_p \frac{\rho_l |\underline{v}_{-r\infty}|^2}{2} \quad (6.30)$$

by dividing Eq. (6.29) by Eq. (6.30); hence

$$C_{Dw}[Re_{bw}] = C_{D\infty}[Re_{b\infty}] \left| \frac{\underline{v}_{-r\infty}}{\underline{v}_{-rw}} \right| \left| \frac{\underline{v}_{-r\infty}}{\underline{v}_{-rw}} \right|^2 \left| \frac{\underline{F}_{-Dw}}{\underline{F}_{-D\infty}} \right| \quad (6.31)$$

Models for C_{Dw} can be developed by substituting in correlations for $|\underline{v}_{-rw}/\underline{v}_{-r\infty}|$ developed from buoyancy driven data $|\underline{F}_{Dw}| = |\underline{F}_{D\infty}| = |\underline{F}_G|$, and hypothesizing that the resultant drag coefficient holds for nonzero liquid flow conditions where $|\underline{F}_{Dw}| \neq |\underline{F}_G|$. Extensive data and correlations are available for rise velocities in round tubes [C.3]. However minimal data has been taken in other geometries [G.7].

6.3.3.1 Round Tubes

In general the relative velocity ratio for vertical round tubes $|\underline{v}_{ro}/\underline{v}_{r\infty}|$, is correlated against the dimension ratio D_b/L_c where the characteristic length L_c is the tube diameter D , and a second parameter, i.e., Re_b . For $Re_b > 200$ the Reynolds dependence is negligible [C.3]. For gas bubbles of $Re_b < 200$ the bubble diameters are so small that the wall effect for the geometries of interest here, will be negligible. Hence we shall consider only the

dimension ratio dependence

$$\left| \frac{v_{r0}}{v_{r\infty}} \right| = \text{ftn} \left[\frac{D_b}{D} \right] \quad (6.32)$$

Correlations for the velocity ratio for $D_b < 0.6 D$ in the viscous, distorted, and capped regimes are listed in Table 6.3.

For bubble diameters greater than $0.6 D$ the tube walls not only restrict the liquid motion but also deform the bubble shape significantly. The condition

$$\frac{D_b}{D} > 0.6 \quad (6.33)$$

is arbitrarily chosen as the transition point from viscous, distorted, or capped regime to the slug regime. In the slug regime the bubble rise velocity becomes independent of the bubble diameter and only dependent on the tube diameter. In the slug regime it is therefore more convenient to use a correlation for $|v_r|$ directly.

Figure 6.6 shows the correlated slug velocities in terms of Froude number

$$\text{Fr} \triangleq |v_r| \sqrt{\frac{\rho_l}{gD(\rho_l - \rho_g)}} \quad (6.34)$$

as a function of the tube diameter D , and fluid properties. The corresponding slug regime drag coefficient C_D^S , can be written

$$C_D^S = \frac{4}{3} \frac{D_b}{D} \frac{1}{\text{Fr}^2} \quad (6.35)$$

It is useful to solve for $|v_{r0}/v_{r\infty}|$ in the slug regime, $D_b/D > 0.6$, for comparison with data. Normalizing Eq. (6.35) the infinite medium capped bubble drag coefficient (Table 6.1) gives

TABLE 6.3

Round Tube Relative Velocity Ratio

Model	$\left \frac{v_{-r_0}}{v_{-r_\infty}} \right $ for $\frac{D_b}{D} < 0.6$	Range
Edgar [W.7]	$\left[1 + 1.6 \left(\frac{D_b}{D} \right) \right]^{-1}$	Viscous regime (bubble behaves as fluid sphere, $\mu_g \ll \mu_l$)
Ladenburg [W.7]	$\left[1 + 2.4 \left(\frac{D_b}{D} \right) \right]^{-1}$	Viscous regime (bubble behave as solid sphere)
Wallis [W.7]	$\left[1 - \frac{1}{0.9} \frac{D_b}{D} \right]$	viscous regime (linear approxi- mation of Edgar and Ladenburg)
Clift et al. [C.2]	$\left[1 - \left(\frac{D_b}{D} \right)^2 \right]^{1.5}$	distorted regime
Collins [W.7]	1.0 for $\frac{D_b}{D} \leq 0.125$ $1.13 e^{-(D_b/D)}$ for $0.125 < \frac{D_b}{D} \leq 0.6$	Capped regime

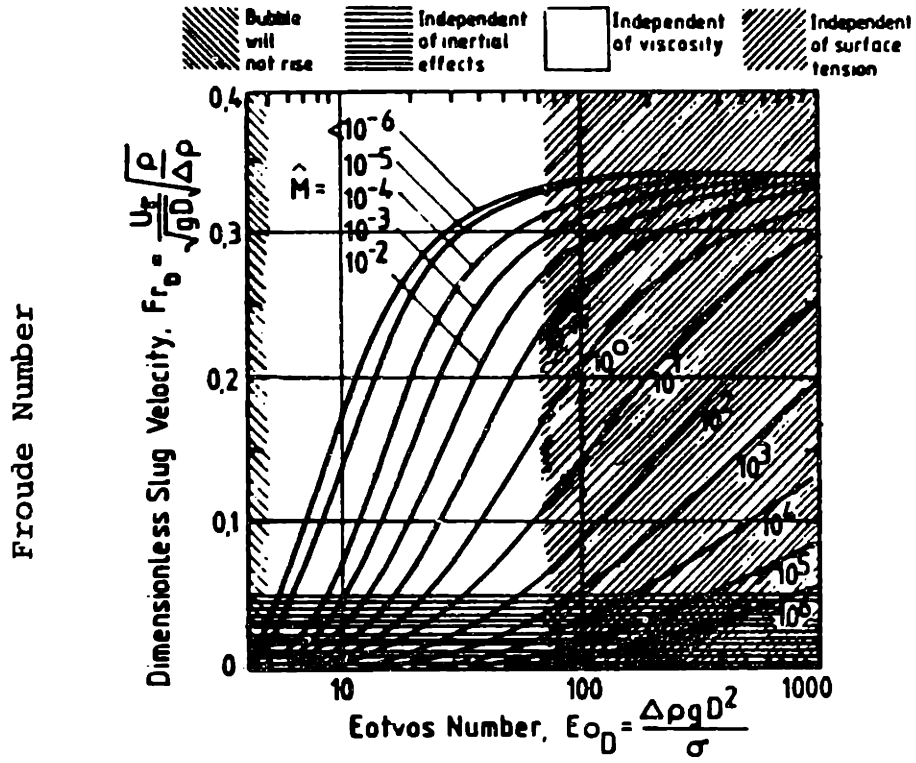


Figure 6.6 Slug velocity in round tube [C.3].

$$\left| \frac{v_{-r0}^S}{v_{-r\infty}^C} \right| = \sqrt{\frac{C_{D\infty}^C}{C_D^S}} = \sqrt{2} Fr \left(\frac{D_b}{D} \right)^{-1/2} \quad (6.36)$$

$$= 0.495 \left(\frac{D_b}{D} \right)^{-1/2} \text{ for } Eo_D \geq 70$$

Using the distorted bubble drag coefficient in an infinite medium (Table 6.1, Ishii model) gives

$$\left| \frac{v_{-r0}^S}{v_{-r\infty}^D} \right| = \frac{\sqrt{2}}{2} Fr Eo_D^{0.25} \quad (6.37)$$

where Eo_D is defined in terms of the tube diameter D , instead of D_b . In the viscous regime Wallis [W.7] proposes

$$\left| \frac{v_{-r0}^S}{v_{-r\infty}^V} \right| = 0.12 \left(\frac{D_b}{D} \right)^{-2} \quad (6.38)$$

The velocity ratio correlations are plotted in Fig. 6.7 for $\hat{M} < 10^{-6}$. Ideally these correlations could be extended to other geometries providing the correct characteristic length L_c , is used in place of the tube diameter D .

6.3.3.2 Parallel Array

Single bubble rise velocity data were taken for the parallel test section to examine the effect of rods on the bubble velocity. The data (tabulated in Appendix F) is plotted in Fig. 6.8. The best fit curve of the infinite medium data is also shown for comparison. Clearly the parallel rods do increase the drag (decrease the bubble velocity) for small bubble diameters. For larger bubbles, however, the drag in a rod array is decreased relative to a bubble of the same diameter in an infinite medium.

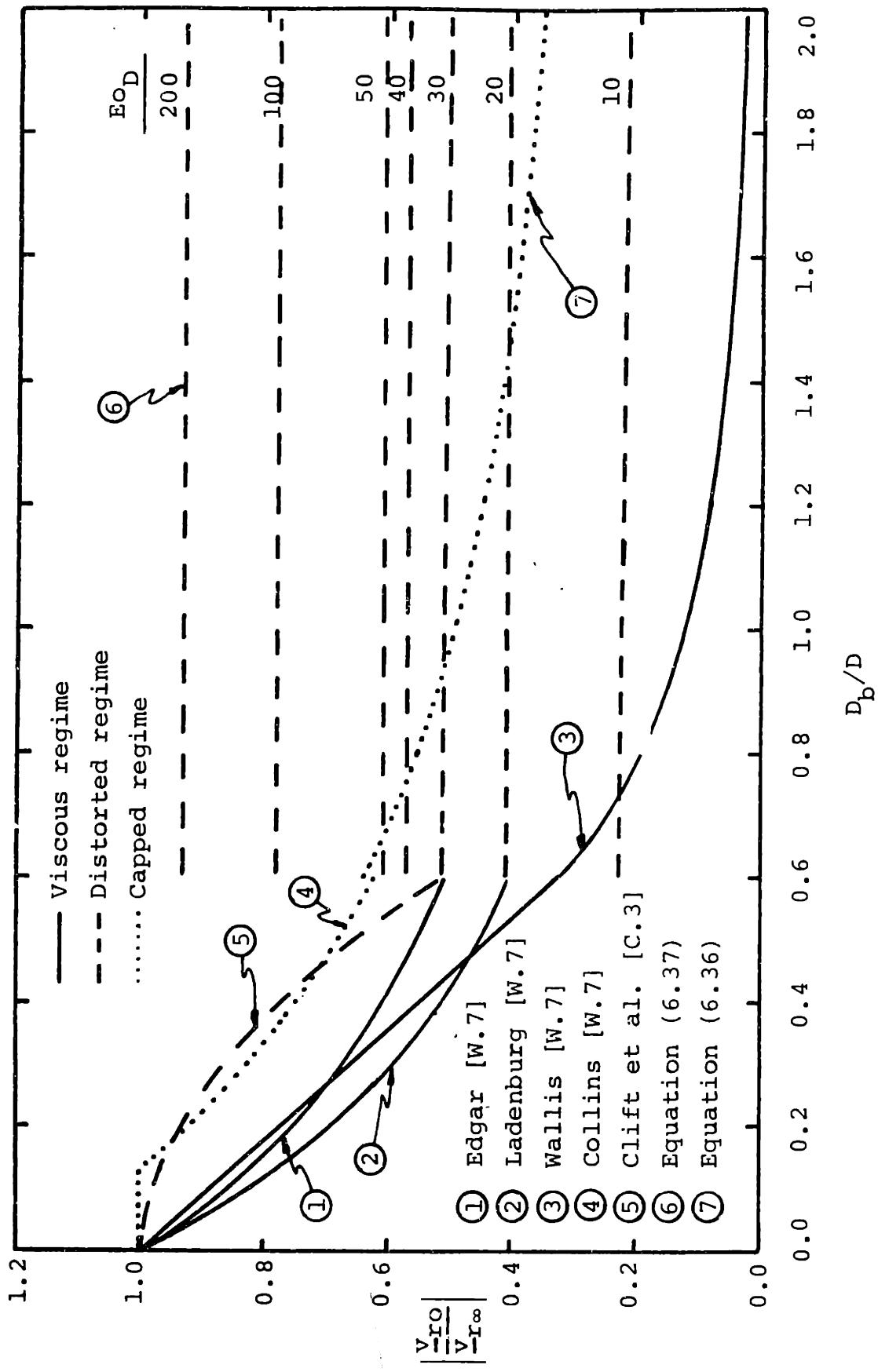


Figure 6.7 Effect of round tube on bubble rise velocity.

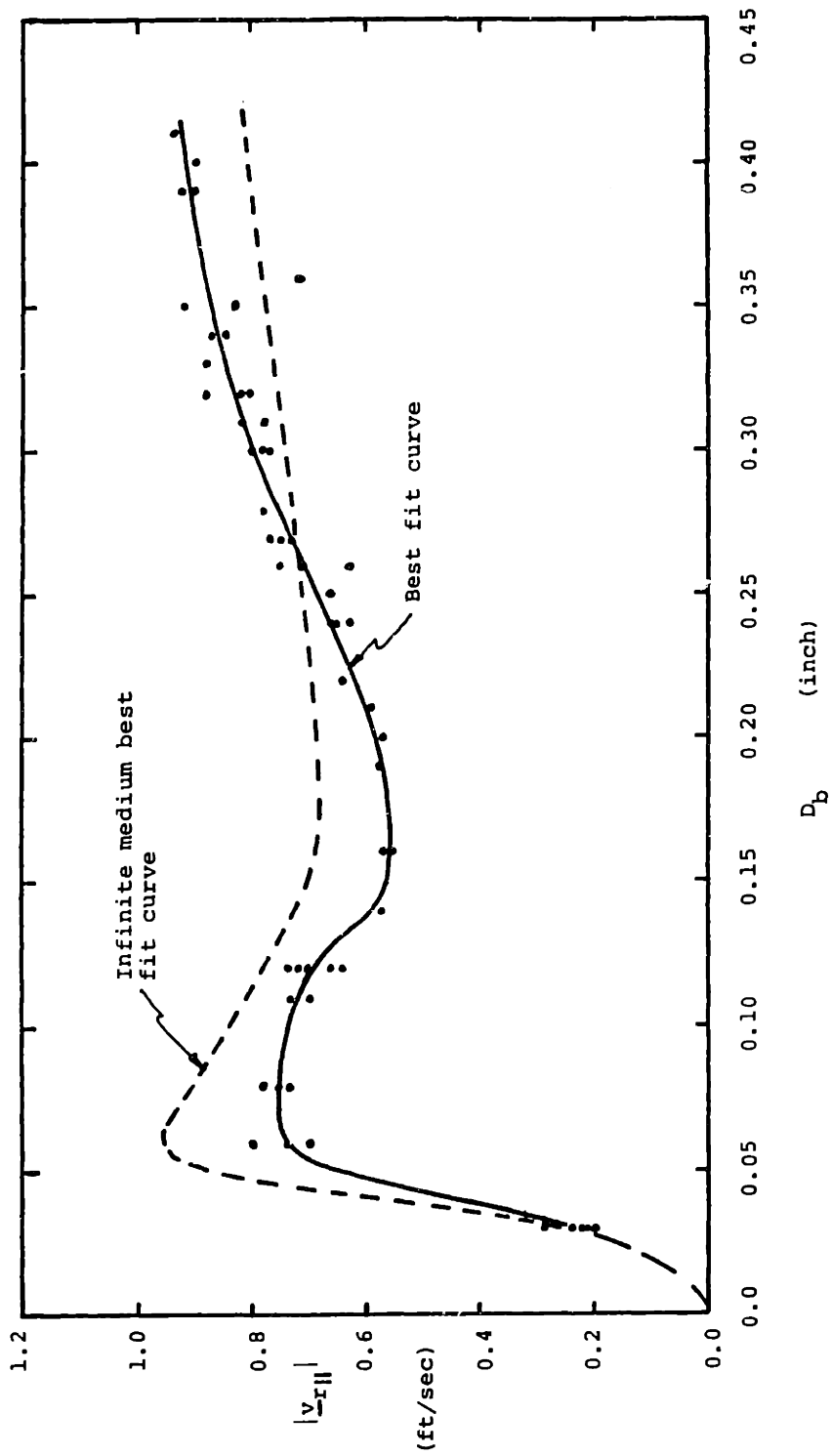


Figure 6.8 Bubble rise velocity in parallel test section.

Comparison of the relative velocity ratio with round tube correlations is shown in Fig. 6.9 where the volumetric hydraulic diameter $D_v = 0.466$ inch (1.18 cm), is used as the characteristic length (See Fig. 6.10(a)). The data does follow the correlations in the viscous regime, transfers to the distorted-capped correlations at the transition bubble diameter D_b^{VD} (as predicted by Ishii's model, See Appendix G), then at $D_b/D_v > 0.35$ the data diverges from all round tube correlations. This unexplained increased velocity for large slug bubbles in parallel rod arrays has been also observed by Griffith [G.7]. A complete understanding of the marked increase in slug bubble velocity in rod arrays relative to equal volume bubbles in round tubes or infinite medium is still unresolved. A plausible description of the distorted bubble departure point at $D_b/D_v = 0.35$, is the point where the bubble diameter reaches 0.6 of the inscribed diameter of the rod array D_{insc} , (See Fig. 6.10(b) for definition). Using the rod array dimensions shows this correspondance i.e.,

$$\frac{D_b^{DS}}{D_v} = \frac{0.6 D_{insc}}{D_v} = \frac{(0.6)(0.280 \text{ inch})}{0.466 \text{ inch}} = 0.36 \quad (6.39)$$

Further study is required before a full understanding of slug bubbles in parallel rod arrays is reached.

For calculations performed later in this chapter the following approximate analytical expression is used to model the parallel array relative velocity ratio

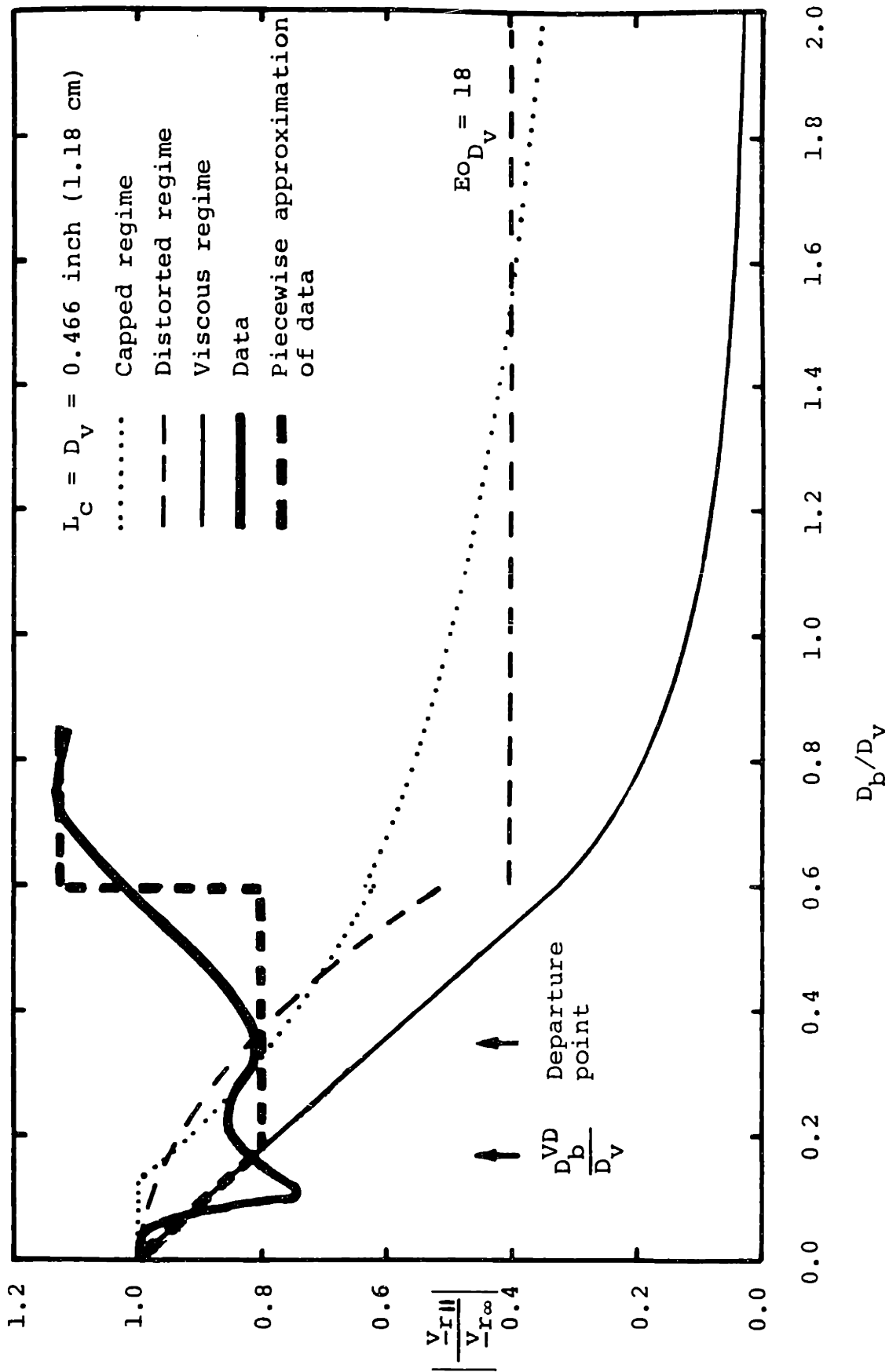
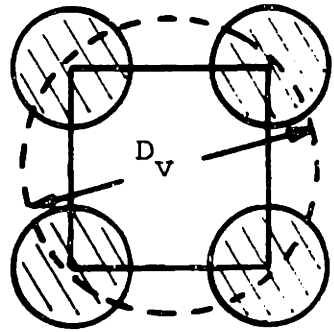


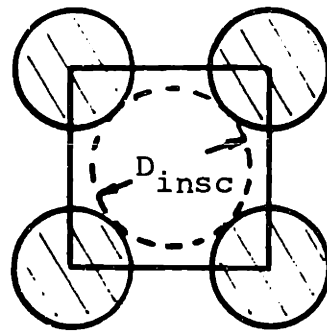
Figure 6.9 Effect of parallel rod array on bubble rise velocity.



$$D_v = \left(\frac{\gamma_v}{1 - \gamma_v} \right) d$$

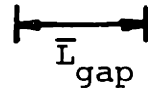
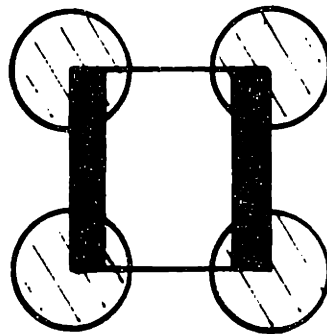
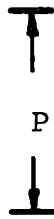
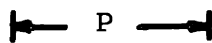
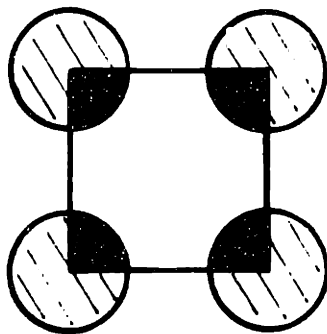
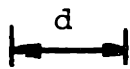
$$\gamma_v = 1 - \frac{\pi \left(\frac{d}{P} \right)^2}{4}$$

(a)



$$D_{insec} = \sqrt{2} P - d$$

(b)



$$\bar{L}_{gap} = P - \gamma_v d$$

(c)

Figure 6.10 Definition of characteristic length for square rod array (a) volumetric hydraulic diameter, (b) inscribe diameter, and (c) average gap width.

$$\left| \frac{v_{-r}}{v_{-r_\infty}} \right| = \begin{cases} 1 - \frac{1}{0.9} \left(\frac{D_b}{D_v} \right) & 0 < D_b < D_b^{VD} \\ 1 - \frac{1}{0.9} \left(\frac{D_b^{VD}}{D_v} \right) & D_b^{VD} < D_b < 0.6 D_v \\ 1.12 & 0.6 D_v < D_b \end{cases} \quad (6.40)$$

This piecewise approximation of the data is shown in Fig. 6.9.

6.3.3.3 Crossflow Array

Bubble rise velocity data were taken in the crossflow test section. The resulting data (tabulated in Appendix F) are plotted with the infinite medium best fit curve in Fig 6.11. The bubble drag in the crossflow array is consistently greater than the drag for a bubble in an infinite medium (or parallel array). However when the relative velocity ratio is evaluated and compared with round tube correlations (Fig.6.12) where now the chosen characteristic length L_c , is the average gap width \bar{L}_{gap} (See Fig. 6.10(c)), we again see a divergence for large (slug) bubbles. With \bar{L}_{gap} as the characteristic length the viscous regime trend and transition point are reasonably modeled with the round tube correlations. Also $D_b/\bar{L}_{gap} \approx 0.6$ can be postulated as the distorted-slug transition point, but again the slug velocity is much larger than that for an equal volume bubble in a round tube.

For calculations performed later the following approximation of the measured crossflow array relative velocity ratio is used

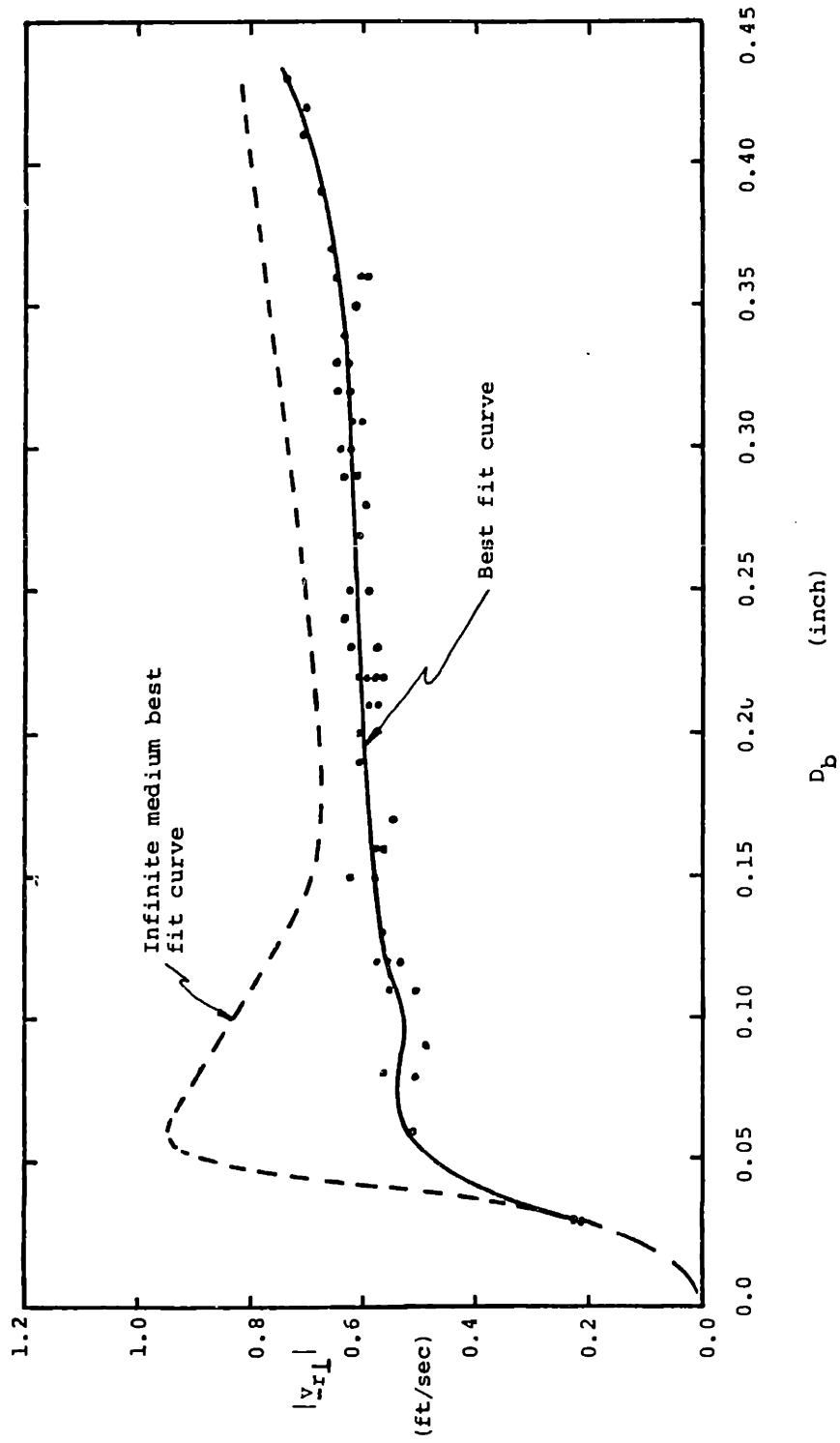


Figure 6.11 Bubble rise velocity in crossflow test section.

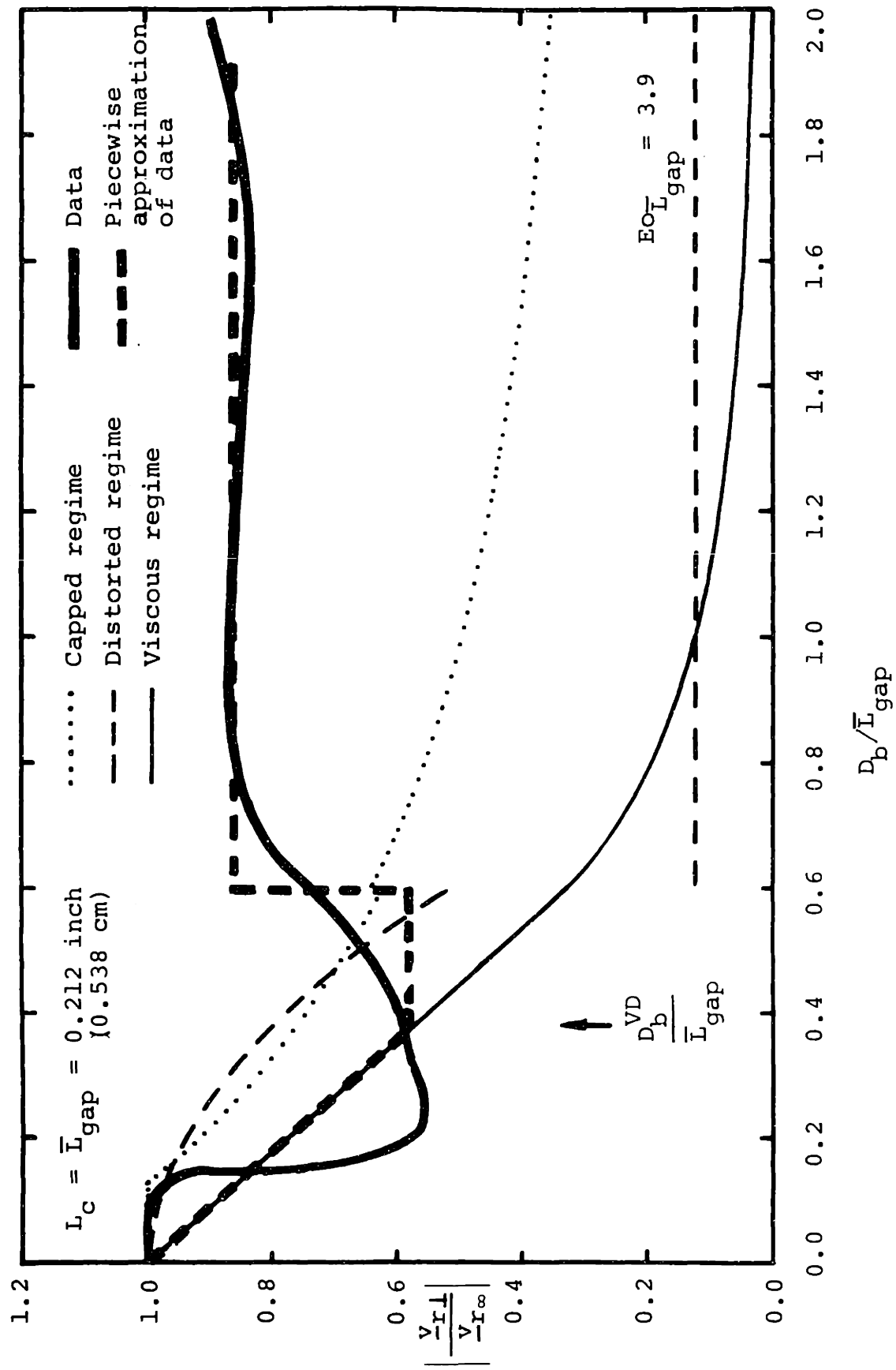


Figure 6.12 Effect of crossflow rod array on bubble rise velocity.

$$\left| \frac{v}{v_{\infty}} \right| = \begin{cases} 1 - \frac{1}{0.9} \frac{D_b}{\bar{L}_{gap}} & 0 < D_b \leq D_b^{VD} \\ 1 - \frac{1}{0.9} \frac{D_b^{VD}}{\bar{L}_{gap}} & D_b^{VD} < D_b \leq 0.6 \bar{L}_{gap} \\ 0.85 & 0.6 \bar{L}_{gap} < D_b \end{cases} \quad (6.41)$$

This piecewise approximation of the data is shown in Fig. 6.12.

6.3.4 Multiple Bubbles in Finite Geometry

We mention here that the two bubble drag environmental effects--multiple bubbles and finite geometry--have been to date only studied independently. The effect of multiple bubbles in a confined geometry has not been explicitly addressed. A model easily could be developed by superimposing the two contributions on a single bubble drag model, however the mutual independence of the two contributions is still unsubstantiated. This area needs further attention.

6.3.5 Liquid Flow

The experimental basis for all the bubble drag models developed above has been buoyancy driven experiments in standing liquid. It has always been hypothesized that the drag coefficient models developed for zero flow also apply for flowing liquid systems because the relative velocity between the liquid and gas and the total drag force correctly account for the liquid motion and additional pressure forces. This assumption is valid for an infinite medium. For vertical one-dimensional flow geometries it is a reasonable assumption because the liquid velocity field changes only slightly and the direction of the total drag force is the same as the buoyancy force. However as will be

seen in the next section this assumption does not hold for multidimensional geometries.

6.4 Inclined Array Flow Observations

The dynamics of bubbles in standing and flowing liquid within a 45 degree inclined array were studied to develop insight into modeling the interfacial drag force in multidimensional geometries.

6.4.1 Single Bubble in Inclined Array

Single bubble trajectories ϕ_b , and velocities $|\langle \underline{v}_g \rangle|$, were measured for standing liquid and two liquid velocities in the 45 degree test section described in Chapter 4. Figure 6.13 defines the measured variables.

6.4.1.1 Zero Liquid Flow

For zero liquid flow, the bubble velocity for 45 degree inclined rods is in close agreement with the bubble velocity for crossflow at all bubble diameters measured (See Fig. 6.14). The bubble trajectory, however, deviates from the direction of the buoyancy driving force (vertical) by as much as 10 degrees and is very dependent on the bubble size (See Fig. 6.15). Very small viscous bubbles are insignificantly effected by the rods and rise vertically as expected. As the bubble diameter becomes bigger than the rod gap spacing, $P-d = 0.125$ inch (0.318 cm), the bubbles tend toward the direction of the rod axis. However as the bubble diameter becomes larger than the average gap width, $\bar{L}_{gap} = P-\gamma_d$ (0.212 inch, 0.529 cm) they tend toward the crossflow direction.

These trends can be explained by conceptualizing the bubble motion as two discrete steps: an undeformed bubble step between rows of rods (space step) and a deformed bubble step through the rod gaps. The direction of motion in each step is toward the path of least

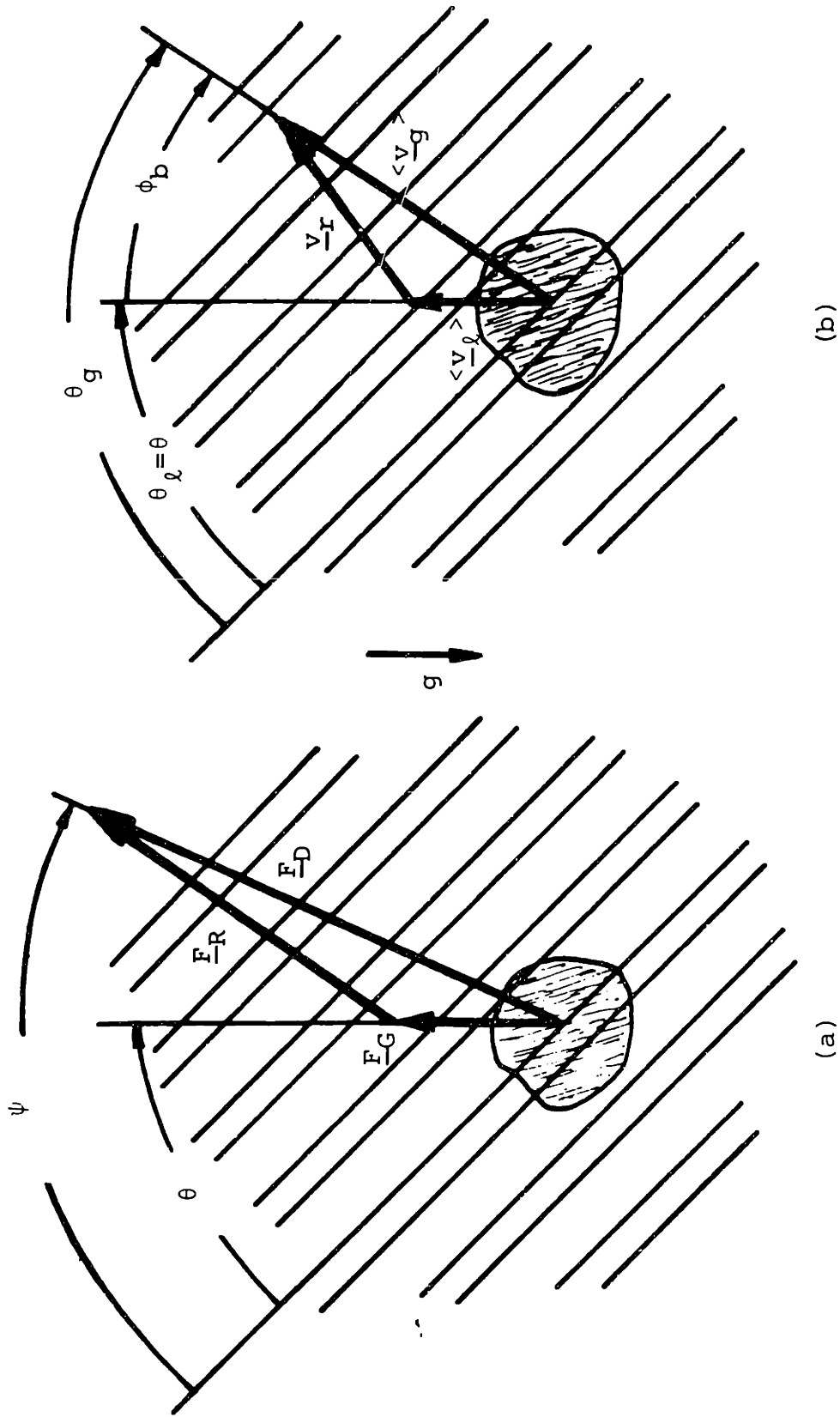


Figure 6.13 Bubble (a) force and (b) velocity vector definitions.

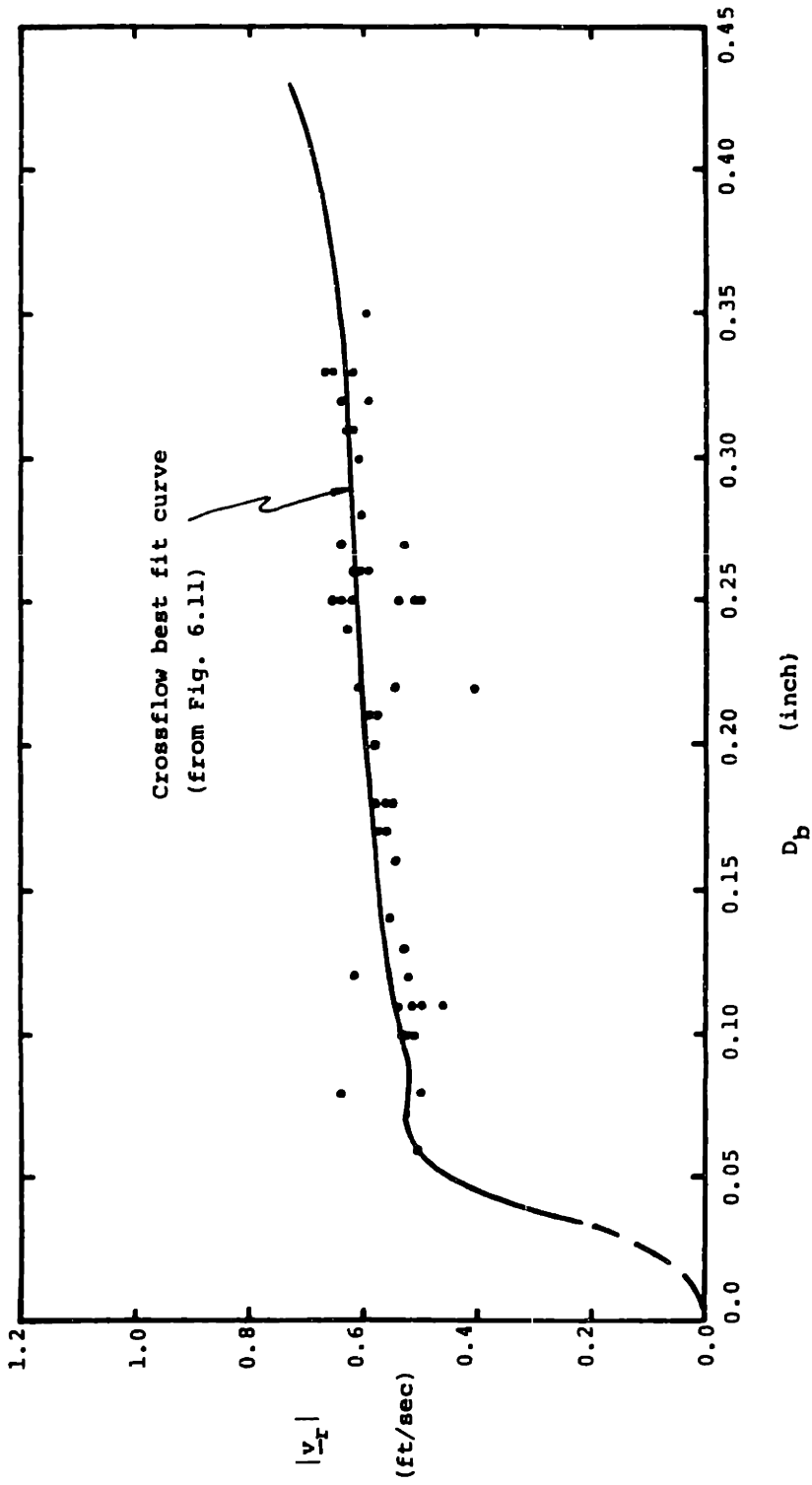


Figure 6.14 Bubble rise velocity in 45 degree test section for zero liquid flow.

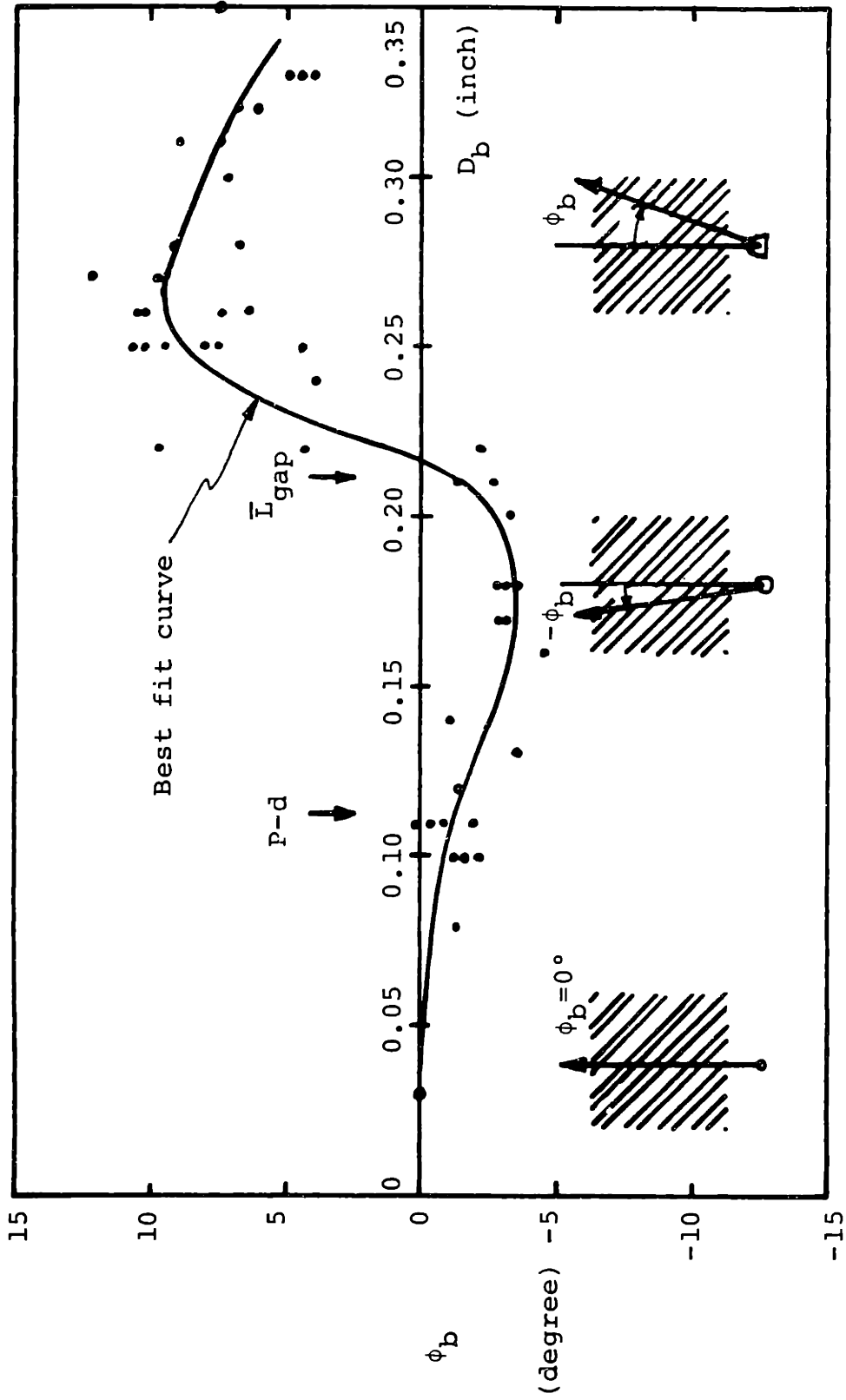


Figure 6.15 Bubble trajectory in 45 degree test section for zero liquid flow.

resistance. In the gap step the path of least resistance is toward crossflow (shortest path out of the gap); in the space step the path of least resistance is toward the rod axis (avoiding the gap). The smaller size bubbles have a large undeformed step and on an average traverse toward the rod axis. The larger size bubbles have a large region where they are deformed, consequently have a large, deformed gap step, and traverse on an average toward crossflow. Figure 6.16 illustrates the two steps for a small and large bubble. (Tracks of actual bubble trajectories for zero liquid flow can be seen in Plate 6.2(a).)

6.4.1.2 Liquid Flow

Single bubble trajectory data were obtained for large bubbles at two average liquid velocities: 0.36 ft/sec (0.11 m/sec) and 0.56 ft/sec (0.17 m/sec). For 0.28 inch (0.71 cm) diameter bubbles the bubble velocity was also measured. This data is shown in Fig. 6.17, 6.18, and 6.19 respectively, and tabulated in Appendix F.

Shear forces in the flowing liquid (i.e., critical Weber number criteria) limited the maximum observable bubble diameter. The trajectories for bubbles smaller than about the average gap width were not recorded because the bubbles did not follow a visually observable path. Very small single bubbles also could not be followed visually. To study the motion of very small and intermediate size bubbles a rapid stream of bubbles were released and photographed.

6.4.2 Stream of Bubbles in Inclined Array

To observe photographically the trajectories of small diameter bubbles in an inclined array with flowing liquid, a steady stream of bubbles was released from a small horizontal orifice inserted in the 45 degree test section. (The photographic technique is described in Sec.

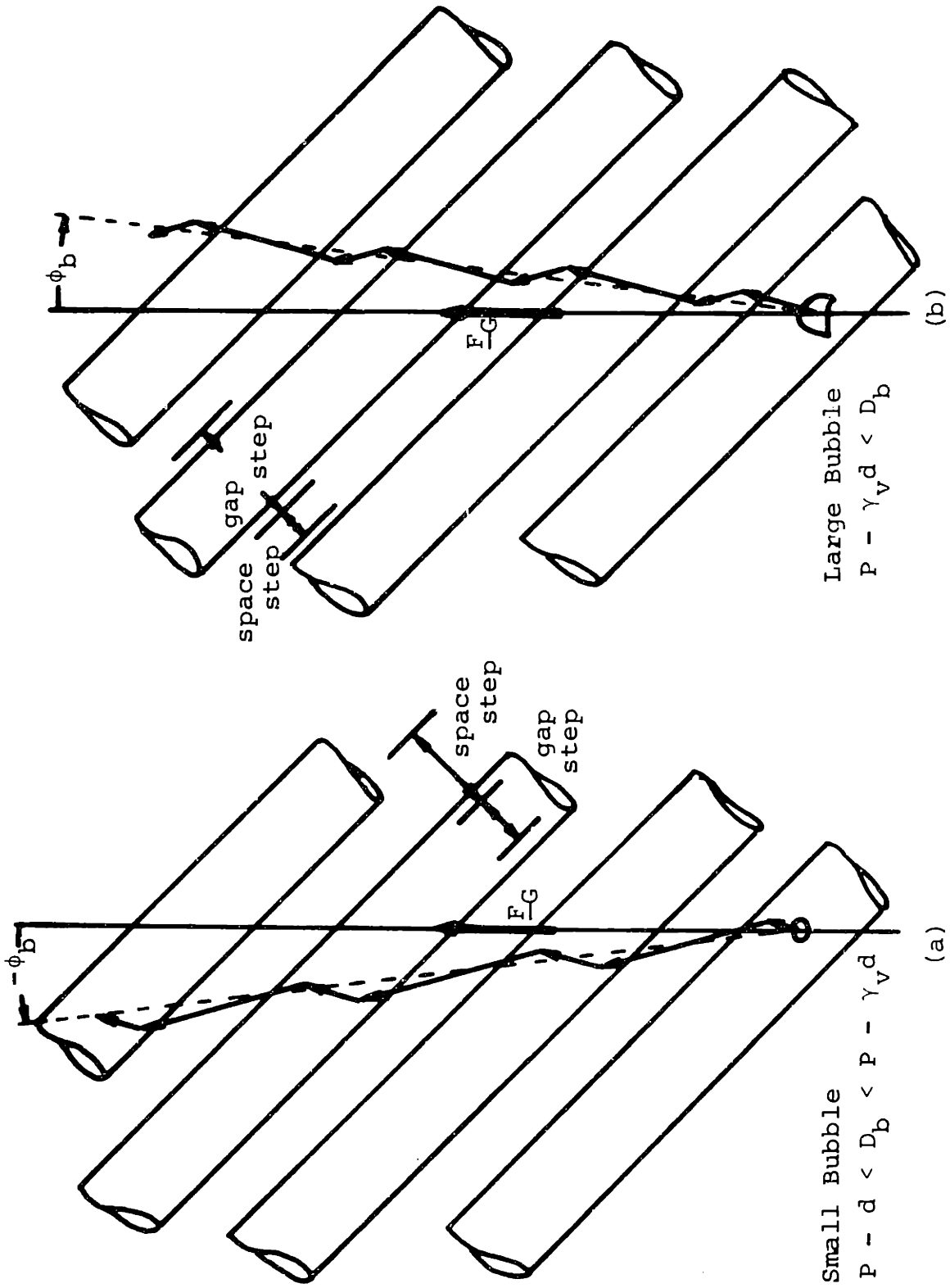


Figure 6.16 Two step description of bubble trajectory in inclined rod array of standing liquid.

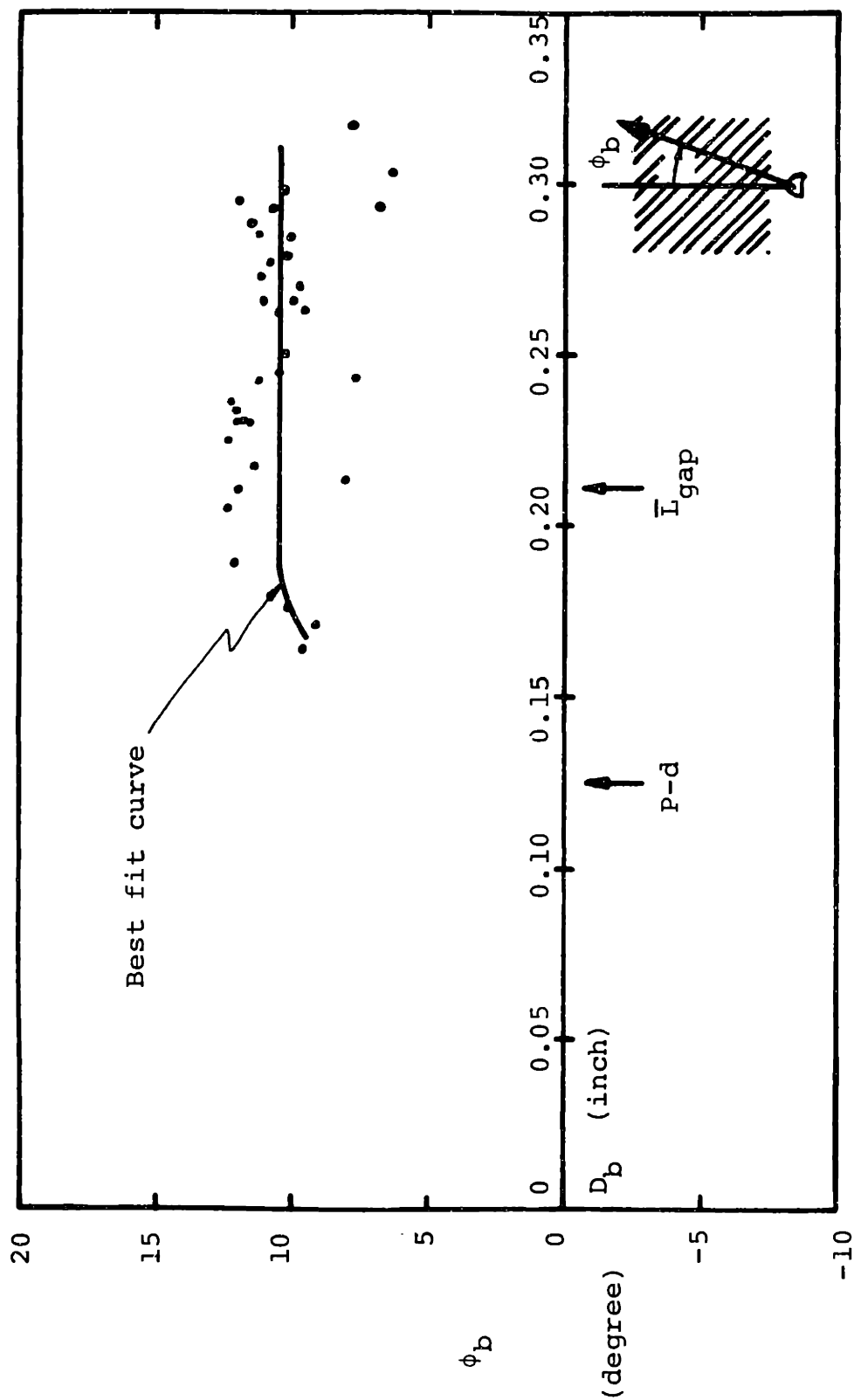


Figure 6.17 Bubble trajectory in 45 degree test section for 0.36 ft/sec (0.11 m/sec) liquid velocity.

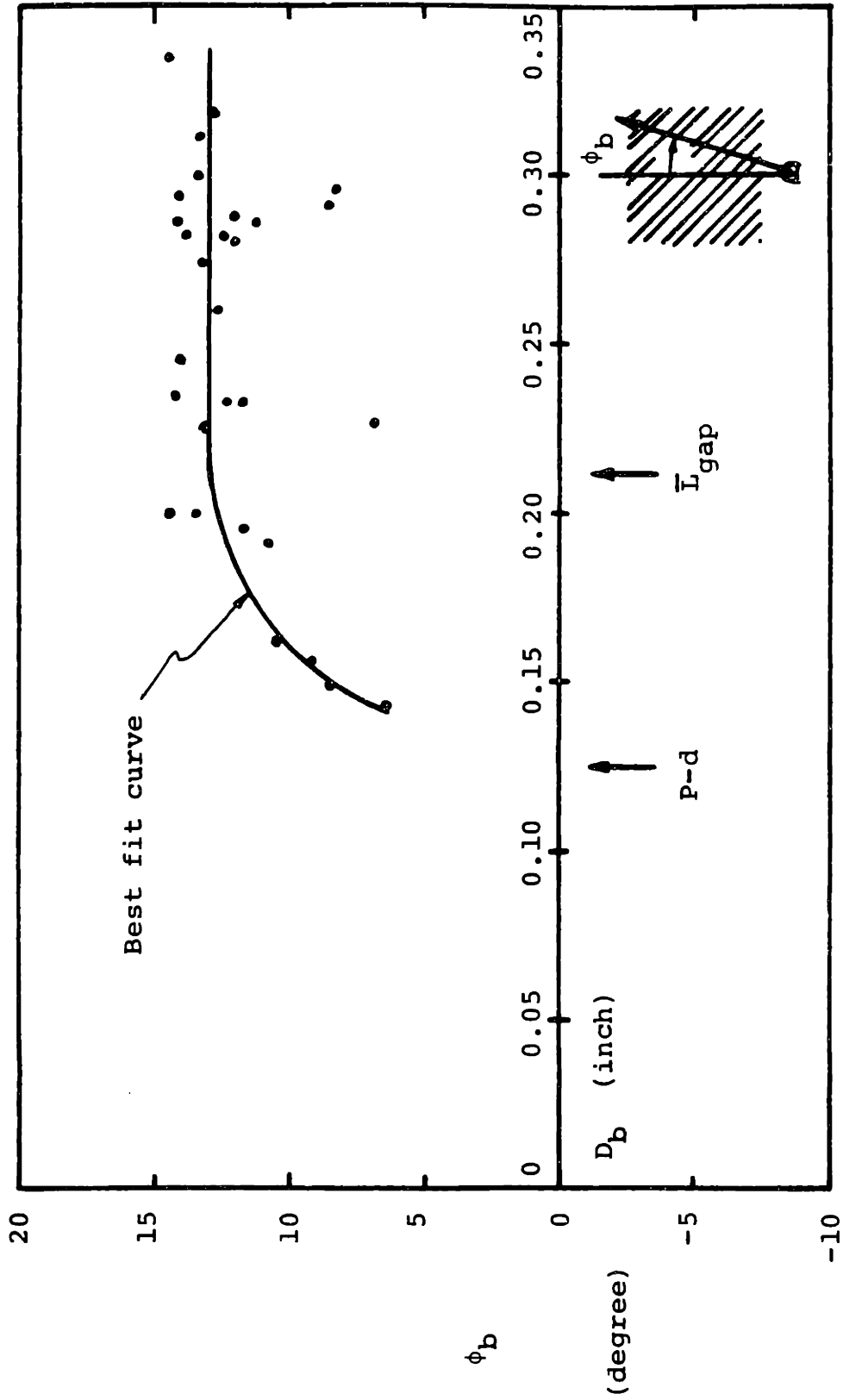


Figure 6.18 Bubble trajectory in 45 degree test section for 0.56 ft/sec (0.17 m/sec) liquid velocity.

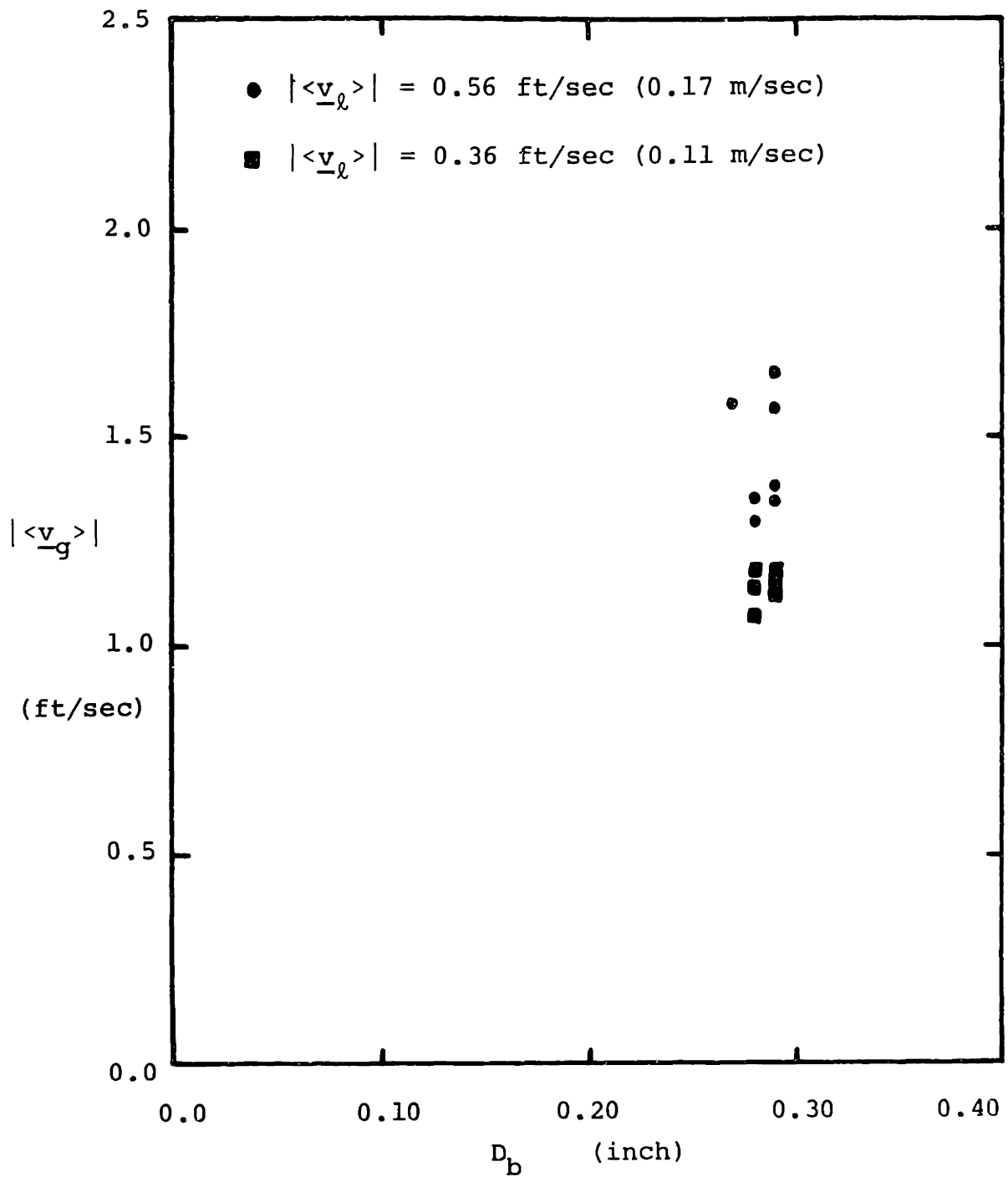


Figure 6.19 Bubble velocity in 45 degree test section for two liquid flow rates.

4.5.7.) Plate 6.2 shows a still and time exposed photography of a stream of bubbles at three liquid flow rates: $|\langle \underline{v}_\ell \rangle| =$ zero, 0.43, and 0.73 ft/sec (zero, 0.13, and 0.22 m/sec). The white streaks in the time exposed photographs mark the path of illuminated bubbles. The very dark slanted lines are the 45 degree inclined rods. At the bottom the horizontal orifice can also be seen. Two discrete trajectories are clearly visible, one along the rod axis and one inclined, across the rods. The resulting fan distribution of bubbles indicates that the two paths occur randomly.

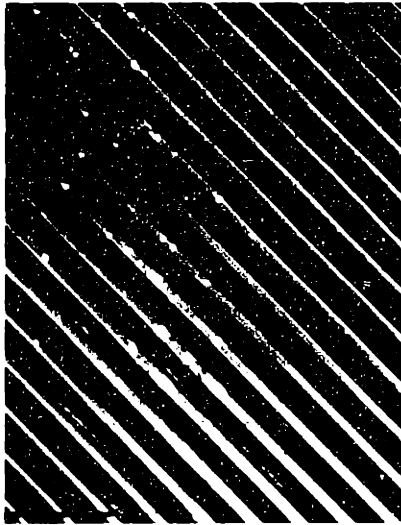
Plate 6.3(a) shows a smaller diameter stream of bubbles at $|\langle \underline{v}_\ell \rangle| = 0.43$ ft/sec (created by reducing the air flow rate). Small bubbles when released in the mainstream (between rods) migrate behind the rods and flow up along the rod axis. In contrast, intermediate size bubbles as shown in Plate 6.2, interchange directions of flow randomly, and large bubbles as shown in the data of Fig. 6.17 and 6.18 travel continuously across the rods.

Plate 6.3(b) shows a close-up view of small bubbles moving behind the rods in a helical motion. This can be explained by the single-phase flow observations (Sec. 5.1) of vortices behind inclined rods spiraling up along the rod axis. A model describing the two-step behavior observed here will be presented in Sec. 6.5.4.

6.4.3 Two-Phase Flow in Inclined Array

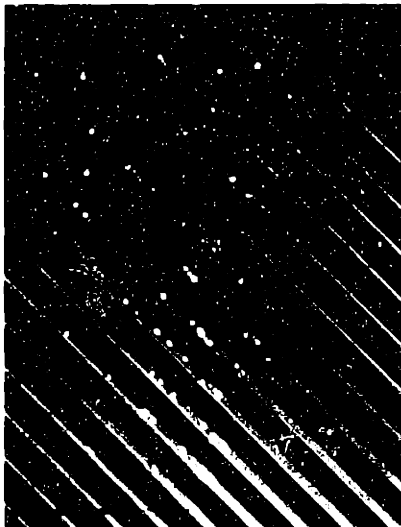
6.4.3.1 Previous Work

To date only two multidimensional two-phase flow experiments have been published. Baush and Lahey [B.10] performed a high void fraction ($\langle \alpha \rangle = 0.39 - 0.80$) flow experiment in a vertical array one row deep and 24 rows wide. The two-phase flow was introduced at the bottom and



$|\langle v_{\xi} \rangle| = 0,0 \text{ FT/SEC}$
 $= 0,0 \text{ M/SEC}$

(A)



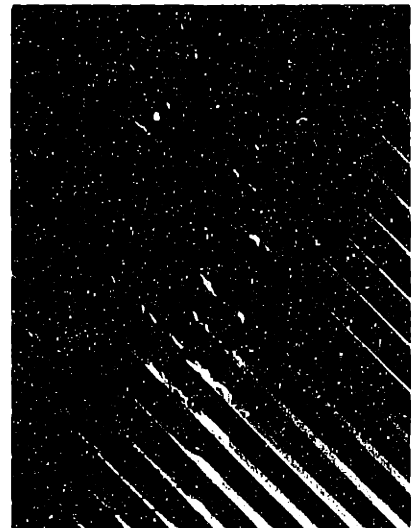
$|\langle v_{\xi} \rangle| = 0,43 \text{ FT/SEC}$
 $= 0,13 \text{ M/SEC}$

(B)



$|\langle v_{\xi} \rangle| = 0,73 \text{ FT/SEC}$
 $= 0,22 \text{ M/SEC}$

(C)



STILL

TIME EXPOSURE

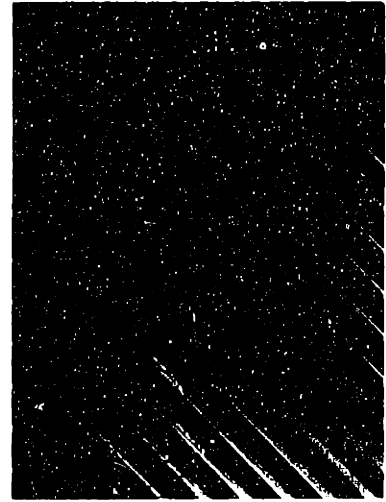
PLATE 6.2 BUBBLE TRAJECTORIES FOR A STREAM OF BUBBLES IN 45 DEGREE TEST SECTION WITH
(A) $Re_v = 00$, (B) $Re_v = 1,600$, AND (C) $Re_v = 2,750$.



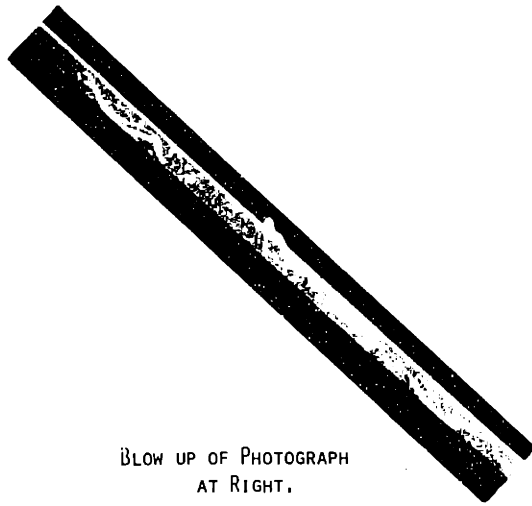
STILL

$$|\langle v_t \rangle| = 0.43 \text{ FT/SEC} \\ = 0.13 \text{ M/SEC}$$

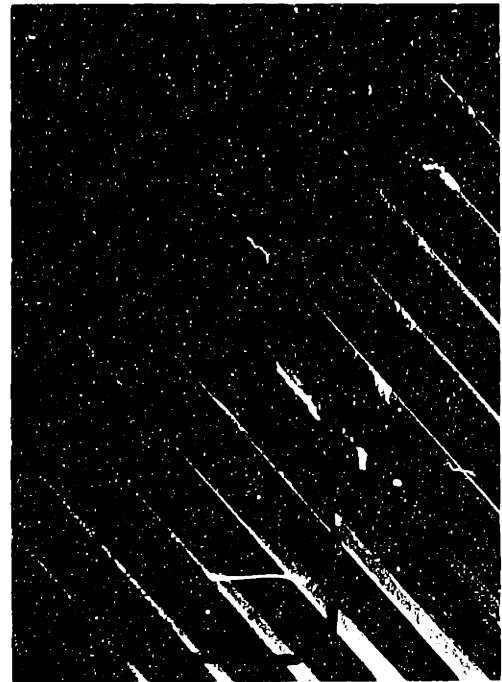
(A)



TIME EXPOSURE



BLOW UP OF PHOTOGRAPH
AT RIGHT.



(B)

PLATE 6.3 BUBBLE TRAJECTORIES FOR A STREAM OF BUBBLES IN 45 DEGREE TEST SECTION (A) FOR SMALL BUBBLES AT $Re_v = 1,600$, (B) CLOSE-UP OF SPIRAL MOTION AT $Re_v = 5,150$.

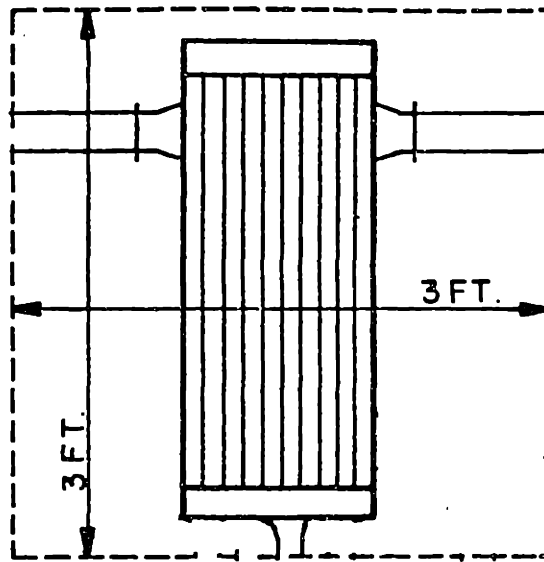
discharged with a range of flow splits at the top left and right sides (See Fig. 6.20(a)). Aside from obtaining benchmarking void and liquid velocity distributions, their main observation was that the inclusion of the rod array reduced the phase separation observed in the test duct without the array.

Osakabe and Adachi [O.1] measured two-phase pressure drops in zero, 15, and 30 degree test sections of similar design to the ones of this study, except their test sections were inclined to retain the rod axis vertical (See Fig. 6.20(b)). Osakabe and Adachi took pressure measurements for zero net liquid flow in the separated flow regime shown in Fig. 6.20(b).

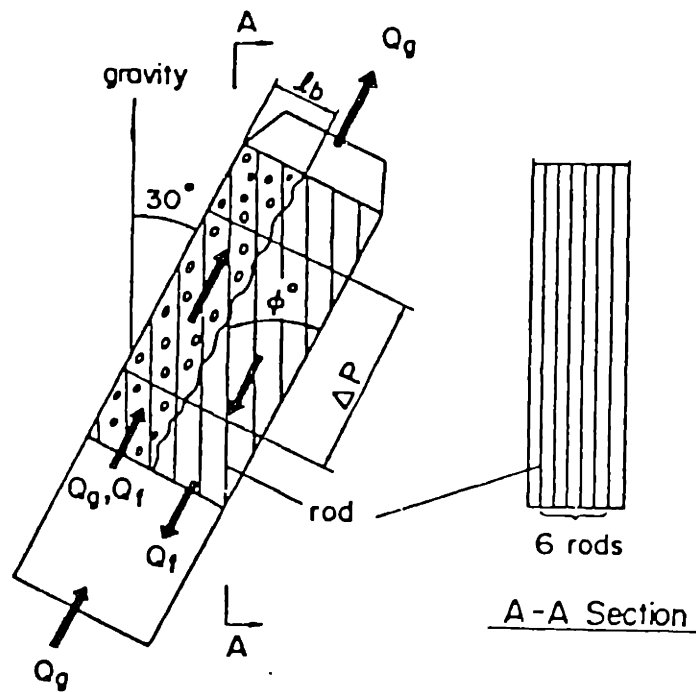
6.4.3.2 Bubbly Flow Observations in Inclined Array

A photographic study of flow regimes in the 45 degree test section was made for a range of gas and liquid flow rates. A map of the flow conditions photographed is shown in Fig. 6.21. Plates 6.4 and 6.5 show the flow development through the test section for two liquid flow rates. These photographs verify that the bubble distribution observed in the exit plenum is equivalent to that observed in the developed regime within the test section. Plates 6.7, 6.8, and 6.9 are photographs of the exit plenum for a range of inlet gas flow rates.

The key observation from this photographic study is that the influence of bubble size on bubble trajectory observed for individual bubbles also can be seen in global bubbly flow situations. At low liquid flows a wide distribution of bubble sizes is generated and the large bubbles migrate to the right wall across the rods, while small bubbles migrate along the rod axis, to the left wall (See Plates 6.4, 6.6(b), 6.7(b), and 6.8(b)). At high liquid flows after the development



(a)



(b)

Figure 6.20 Test section designs of (a) Baush and Lahey [B.10] and (b) Osakabe and Adachi [O.1].

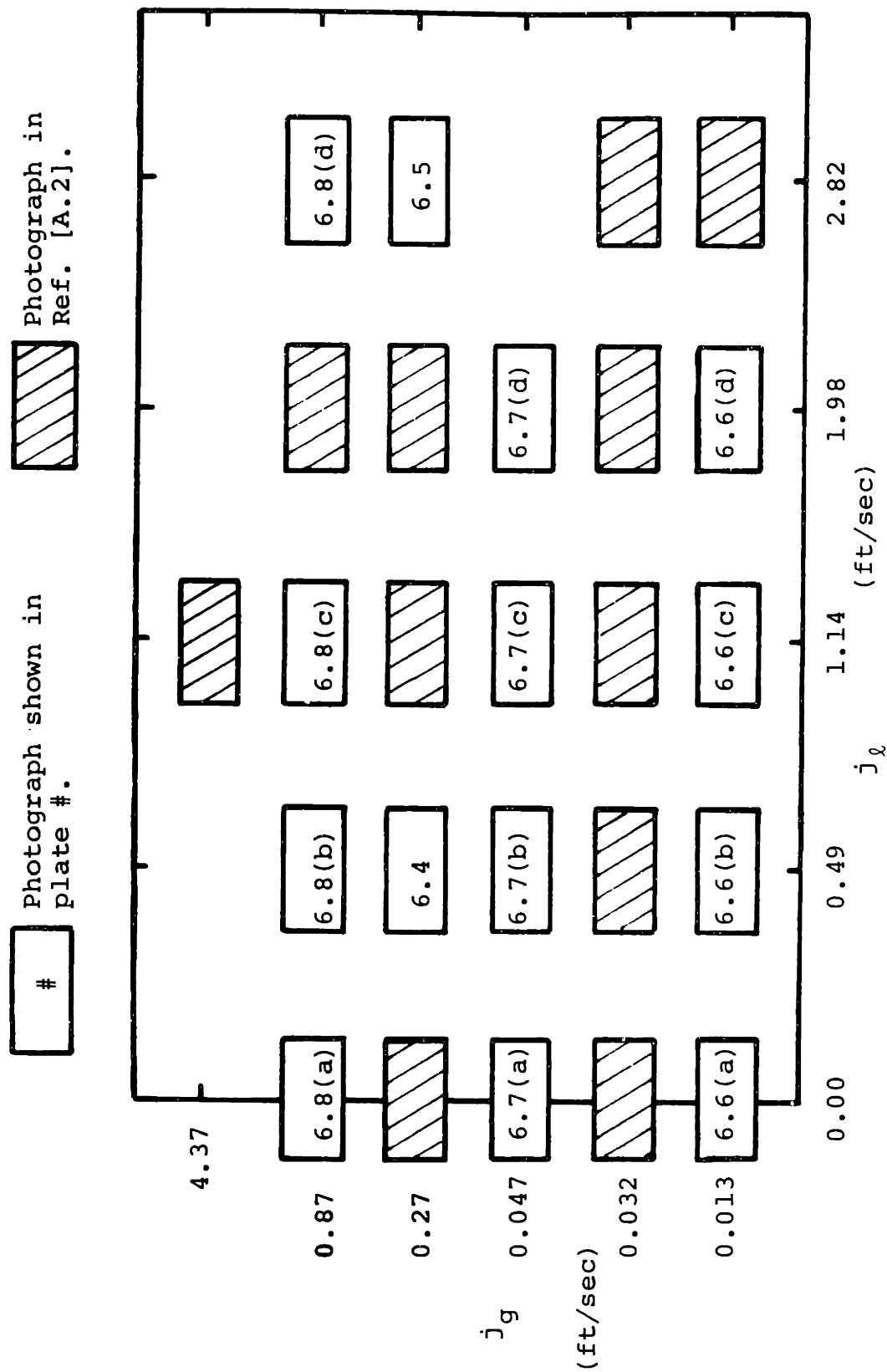
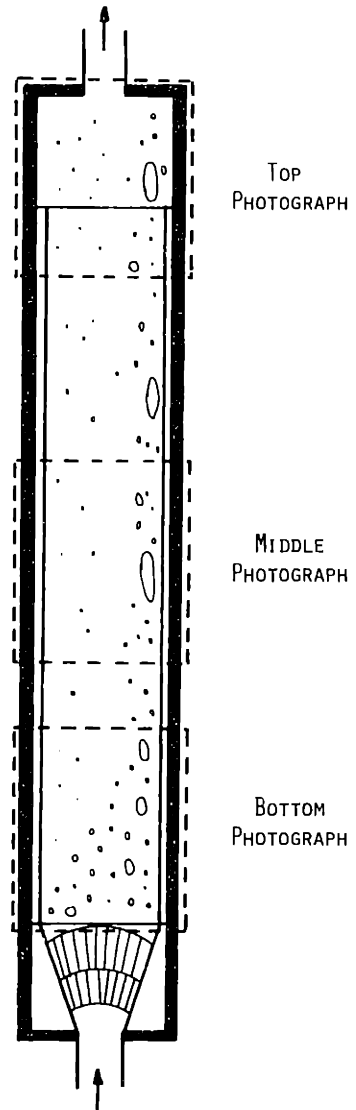
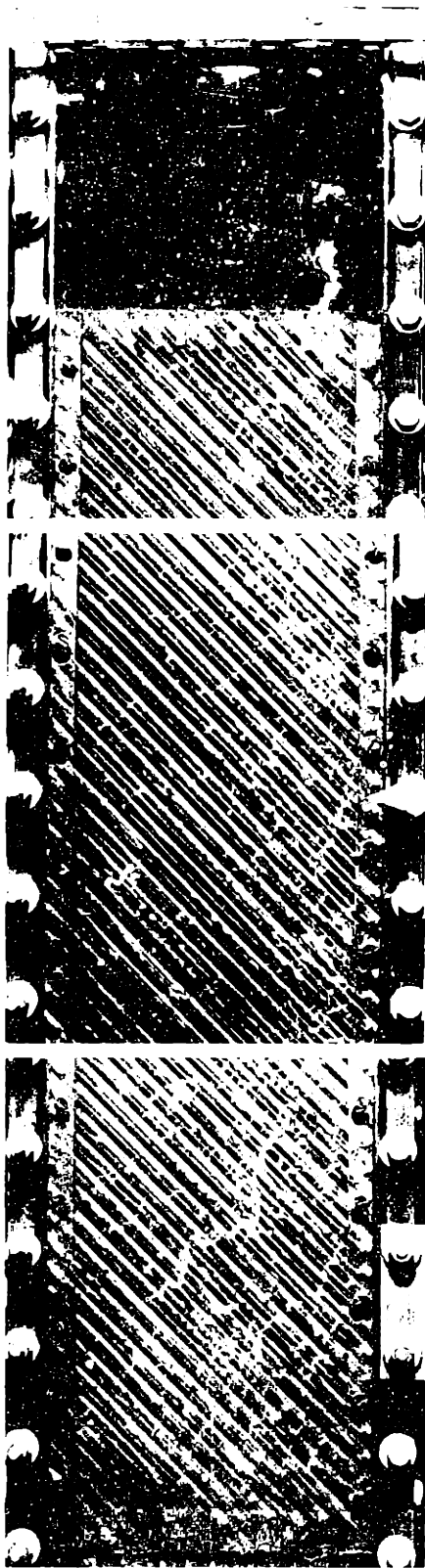
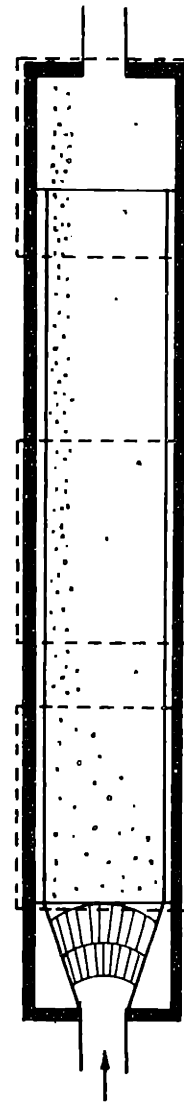
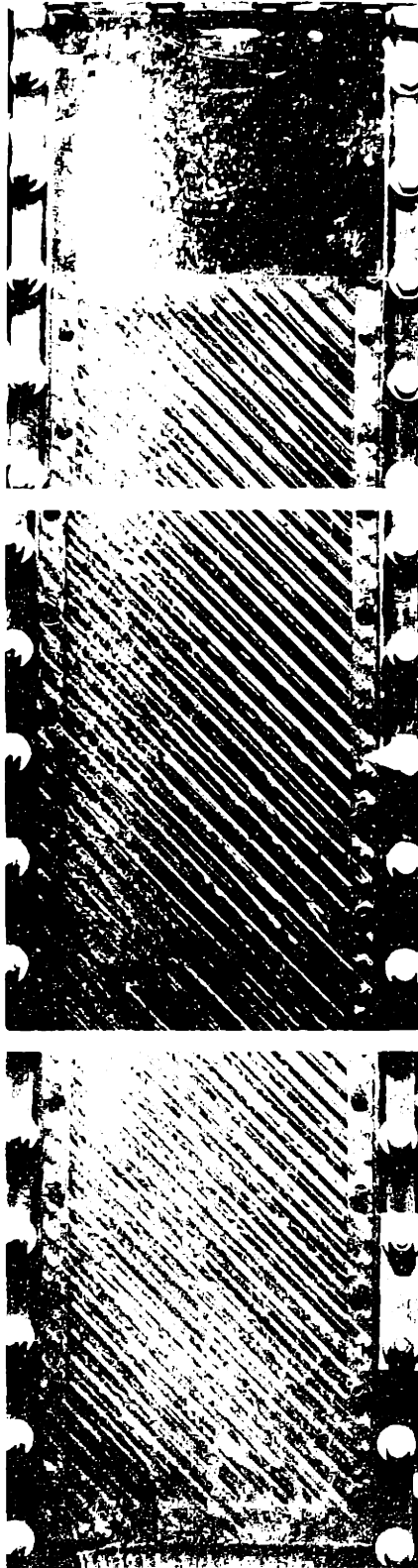


Figure 6.21 Map of flow conditions photographed.



$$\begin{aligned}
 j_l &= 0.49 \text{ FT/SEC} \\
 &= 0.15 \text{ M/SEC} \\
 j_g &= 0.27 \text{ FT/SEC} \\
 &= 0.083 \text{ M/SEC} \\
 \beta &= 0.36
 \end{aligned}$$

PLATE 6.4 FLOW PATTERN IN 45 DEGREE TEST SECTION FOR LOW LIQUID FLOW RATE.



TOP
PHOTOGRAPH

MIDDLE
PHOTOGRAPH

BOTTOM
PHOTOGRAPH

$$j_l = 2.82 \text{ FT/SEC}$$

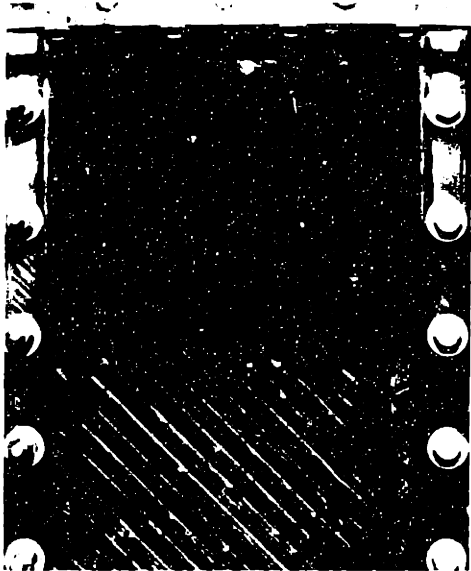
$$0.86 \text{ M/SEC}$$

$$j_g = 0.27 \text{ FT/SEC}$$

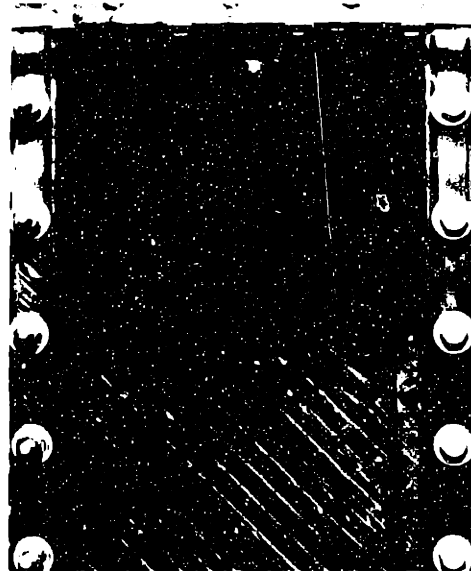
$$0.083 \text{ M/SEC}$$

$$\beta = 0.087$$

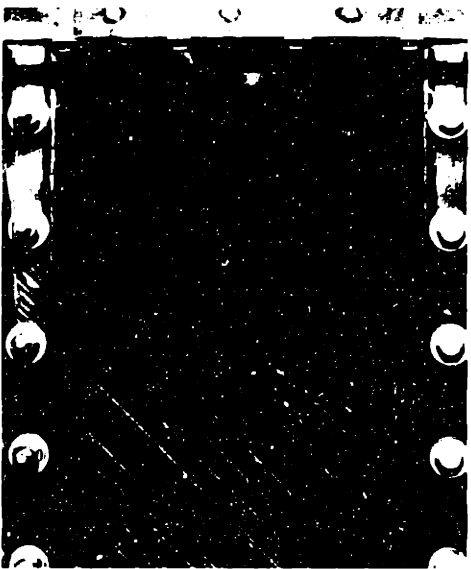
PLATE 6.5 FLOW PATTERN IN 45 DEGREE TEST SECTION FOR HIGH LIQUID FLOW RATE.



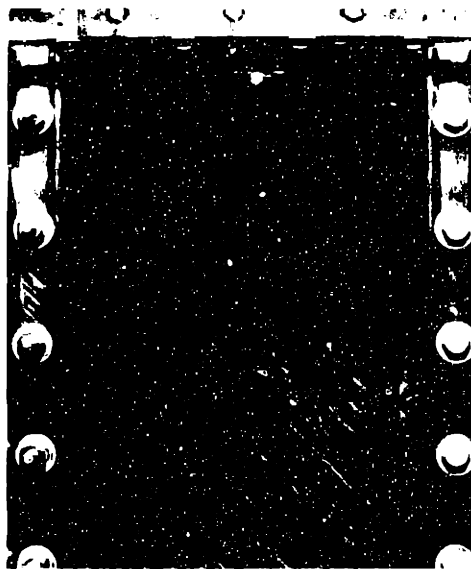
(A) $J_i = 0.0 \text{ FT/SEC}$
 $= 0.0 \text{ M/SEC}$
 $\beta = 1.0$



(B) $J_i = 0.49 \text{ FT/SEC}$
 $= 0.15 \text{ M/SEC}$
 $\beta = 0.026$



(C) $J_i = 1.14 \text{ FT/SEC}$
 $= 0.35 \text{ M/SEC}$
 $\beta = 0.011$



(D) $J_i = 1.98 \text{ FT/SEC}$
 $= 0.60 \text{ M/SEC}$
 $\beta = 0.0065$

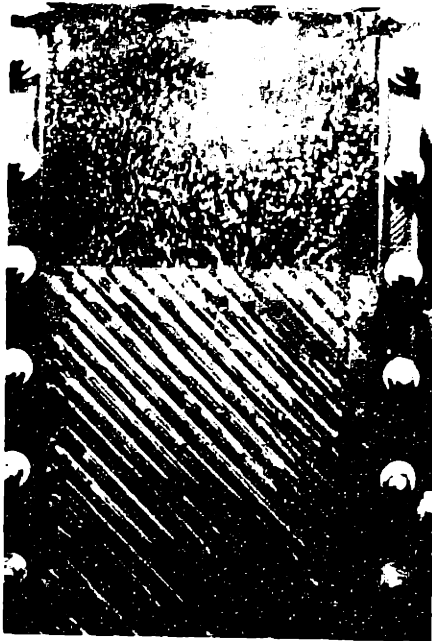
PLATE 6.6 FLOW DISTRIBUTION AT EXIT PLENUM OF 45 DEGREE TEST SECTION FOR $J_g = 0.013 \text{ FT/SEC}$ (0.0038 M/SEC).



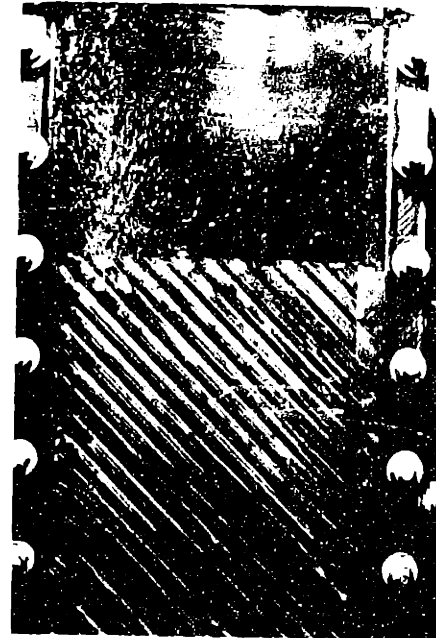
(A) $J_k = 0,0$ FT/SEC
 $= 0,0$ M/SEC
 $\beta = 1,0$



(B) $J_k = 0,49$ FT/SEC
 $= 0,15$ M/SEC
 $\beta = 0,088$

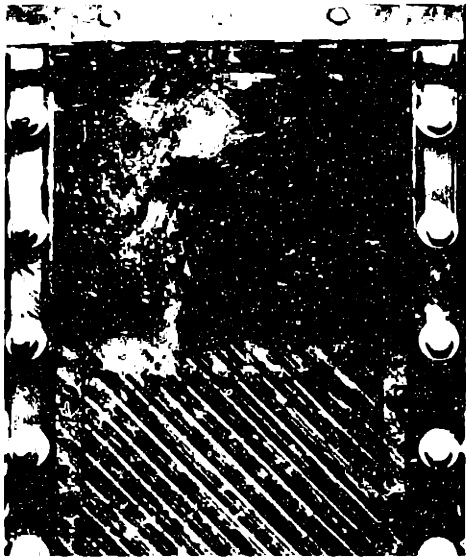


(C) $J_k = 1,14$ FT/SEC
 $= 0,35$ M/SEC
 $\beta = 0,040$

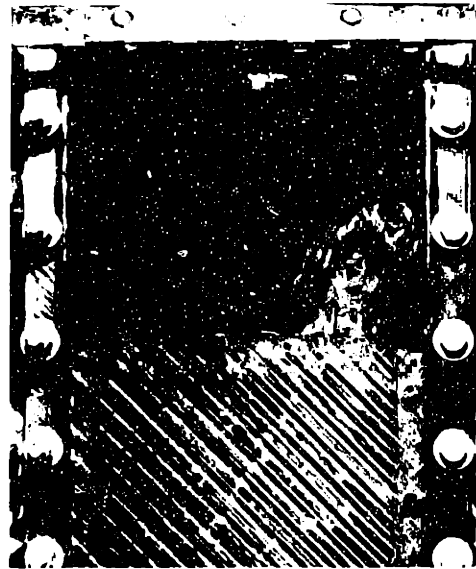


(D) $J_k = 1,98$ FT/SEC
 $= 0,60$ M/SEC
 $\beta = 0,023$

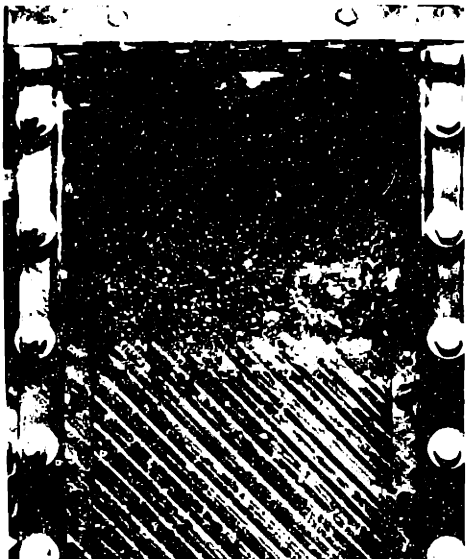
PLATE 6.7 FLOW DISTRIBUTION AT EXIT PLENUM OF 45 DEGREE TEST SECTION FOR $J_g = 0,047$ FT/SEC (0,014 M/SEC).



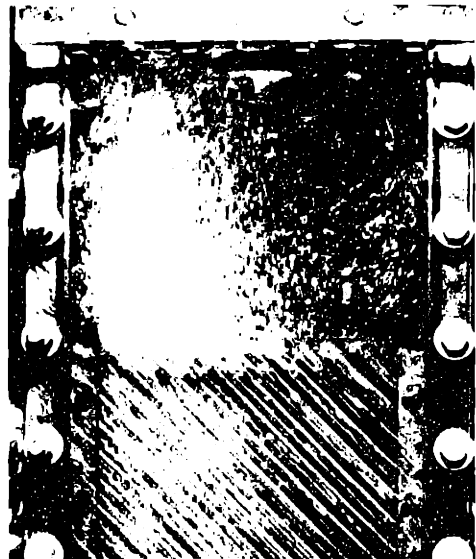
(A) $J_2 = 0.0 \text{ FT/SEC}$
 $= 0.0 \text{ M/SEC}$
 $\beta = 1.0$



(B) $J_2 = 0.49 \text{ FT/SEC}$
 $= 0.15 \text{ M/SEC}$
 $\beta = 0.64$



(C) $J_2 = 1.14 \text{ FT/SEC}$
 $= 0.35 \text{ M/SEC}$
 $\beta = 0.43$



(D) $J_2 = 2.82 \text{ FT/SEC}$
 $= 0.86 \text{ M/SEC}$
 $\beta = 0.24$

PLATE 6.8 FLOW DISTRIBUTION AT EXIT PLENUM OF 45 DEGREE TEST SECTION FOR
 $J_g = 0.87 \text{ FT/SEC (0.27 M/SEC)}$.

region, only small bubbles persist. Small bubbles move along the rod axis and up the left side, consequently the exit void accumulates at the left wall (See Plates 6.5, 6.6(d), 6.7(d), and 6.8(d)). If the left wall were not present then the bubbles would continue along the rod axis.

At zero net liquid flow for small gas flowrates the bubbles distribute according to size as expected from the individual bubble observations (See Plate 6.6(a)). However at high gas flow rates a channel of recirculating liquid is created along the right wall causing the distribution of bubbles to be compressed toward the left wall. (See Plates 6.7(a) and 6.8(a)). This regime was also observed by Osakabe and Adachi when the rod array is also inclined (Fig. 6.20(b)).

The ability of drag interfacial force models to mathematically predict the flow observations described above will be explored in the next section.

6.5 Multidimensional Drag Coefficient

6.5.1 Current Code Models

Two-fluid thermal-hydraulic codes currently model the interfacial force $\langle \underline{M}_i^d \rangle$ by only the steady state drag force,

$$\langle \underline{M}_i^d \rangle = \langle \alpha \rangle \underline{F}_D = \langle \alpha \rangle \underline{C}_D a_p \frac{\rho_l |\underline{v}_r|}{2} \underline{v}_r \quad (6.42)$$

where

$$\underline{v}_r = \langle \underline{v} \rangle - \langle \underline{v}_l \rangle \quad (6.43)$$

(A few advanced codes have included models for the virtual mass (spatial and temporal acceleration) forces principally to add numerical stability to the solution algorithm.) The drag coefficient \underline{C}_D is

modeled several ways:

- (1) by a correlation for a single bubble in an infinite medium,
i.e.,

$$\underline{C}_D = C_D = C_{D\infty} \quad (\text{Sec. 6.3.1})$$

- (2) by a correlation for multiple bubbles in an infinite medium,
i.e.,

$$\underline{C}_D = C_D = C_{D'\infty} \quad (\text{Sec. 6.3.2})$$

- (3) by a large number yielding homogeneous flow, i.e.,

$$\underline{C}_D = C_D = 10^8$$

- (4) by an empirical correlation of average void fraction $\langle \alpha \rangle$,
[R.3, L.3, K.3] generally based on one-dimensional round tube
data.

The following discussion of drag models will be presented in two dimensions. A three-dimensional formulation can be reduced to two by making assumptions analogous to those used for single-phase flow resistance (Sec. 5.22). In theory the drag force is

$$\underline{F}_D = F_{Dx} \underline{e}_x + F_{Dy} \underline{e}_y \quad (6.44)$$

$$\underline{F}_D = C_D a_p \frac{\rho_\ell |\underline{v}_r|}{2} v_{rx} \underline{e}_x + C_D a_p \frac{\rho_\ell |\underline{v}_r|}{2} v_{ry} \underline{e}_y \quad (6.45)$$

where C_D is one of the above models and (x,y) is an arbitrary coordinate system. Equation (6.45) is reference frame invariant, independent of the coordinate system chosen. This formulation assumes the drag coefficient correlated for zero average liquid flow ($\langle \underline{v}_\ell \rangle = 0$) is valid for nonzero flows ($\langle \underline{v}_\ell \rangle > 0$). In application, all the codes reviewed [R.3, S.1, T.3, C.4] use a staggered numerical mesh which provides only one velocity component at a given spatial cell (or

surface). Hence to eliminate the computational time required to interpolate the other velocity components in order to evaluate the total relative velocity vector, the codes approximate Eq. (6.45) by

$$\underline{F}_D = C_D a_p \frac{\rho_l |v_{rx}|}{2} v_{rx} \underline{e}_x + C_D a_p \frac{\rho_l |v_{ry}|}{2} v_{ry} \underline{e}_y \quad (6.46)$$

$$\underline{F}_D = \left(C_D \frac{|v_{rx}|}{|v_r|} \right) a_p \frac{\rho_l |v_r|}{2} v_{rx} \underline{e}_x + \left(C_D \frac{|v_{ry}|}{|v_r|} \right) a_p \frac{\rho_l |v_r|}{2} v_{ry} \underline{e}_y \quad (6.47)$$

This form is not reference frame invariant since the magnitude of the effective drag coefficients in parentheses is coordinate system dependent. However the (x,y) coordinate system of Eq. (6.47) was arbitrarily chosen creating an unjustified directional dependence of \underline{F}_D .

Even when this discrepancy between theory and application is eliminated (by implementing Eq. (6.45) in the codes) the current interfacial drag models still do not predict the observations described in Sec. 6.4.3. Simulations of the 45 degree test section for two liquid flow rates were performed with a modified version of THERMIT-2 [K.3] (The modifications are summarized in Appendix H). Comparison of the predicted void distribution, Fig. 6.22(a) and (b), with observed void distributions, Plates 6.4 and 6.5, respectively, show a discrepancy at high flow rates. The isotropic interfacial model predicts the right phase separation for low flows when the bubble size distribution is large, but does not for high flows when the bubble size distribution is small. Obviously the presence of inclined rods can create gross changes in phase separation which are not incorporated in the present interfacial models.

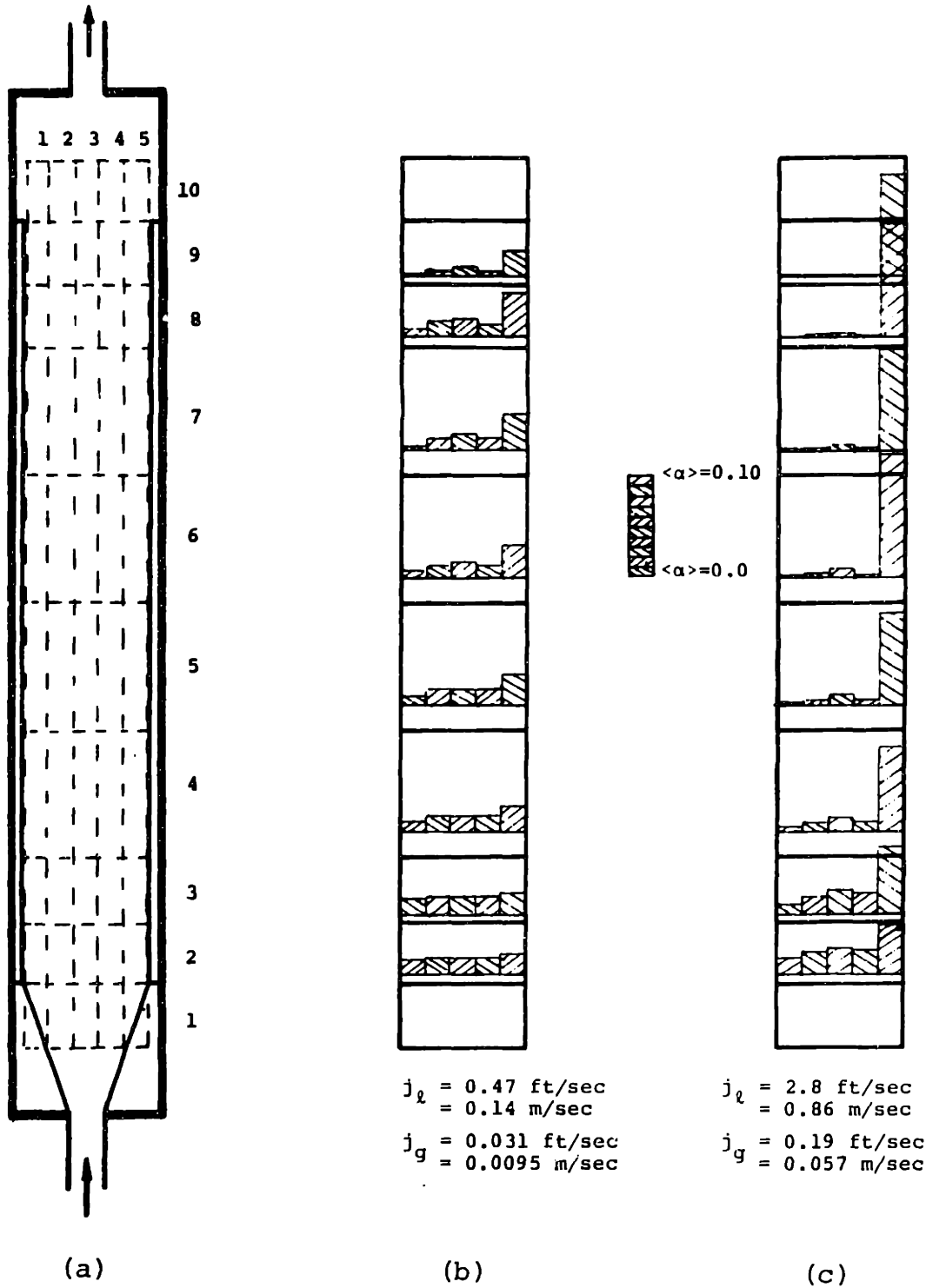


Figure 6.22 Void distribution predictions of 45 degree test section with THERMIT-2 (a) coordinate mesh, (b) low, and (c) high liquid flow rate.

In the remainder of this section we shall explore new interfacial drag formulations which incorporate the physical presence of the rod array.

6.5.2 Isotropic Model

The experiment/prediction comparison of the last section showed that an isotropic drag model predicts the right direction of phase separation for large bubbles. A more precise appraisal can be made by comparing single bubble trajectories for large bubbles with predictions of an isotropic model.

Consider an isotropic model where the scalar drag coefficient is that for crossflow $C_{D\perp}$ (Sec. 6.3.3), then

$$\underline{F}_D = C_{D\perp} a_p \frac{\rho_l |\underline{v}_r|}{2} \underline{v}_r \quad (6.48)$$

where \underline{v}_r is defined in Eq. (6.43). Figure 6.23 shows that the isotropic model grossly underpredicts the measured bubble trajectory (A sample calculation is given in Appendix I). More importantly, with an isotropic model the maximum possible bubble trajectory is bounded by the direction of the total drag force, $\psi - \theta$, since \underline{v}_r and \underline{F}_D are collinear and $\langle \underline{v}_\ell \rangle$ is vertical (See insert in Fig. 6.23). Thus it is impossible to predict the observed large bubble trajectory with a simple isotropic model.

6.5.3 Superposition Model

The next logical step is to introduce a tensor drag coefficient by formulating a superposition model analogous to those developed for single-phase flow resistance (See Chapter 5),

$$\underline{F}_D = F_{D||} \underline{e}_{||} + F_{D\perp} \underline{e}_{\perp} \quad (6.49)$$

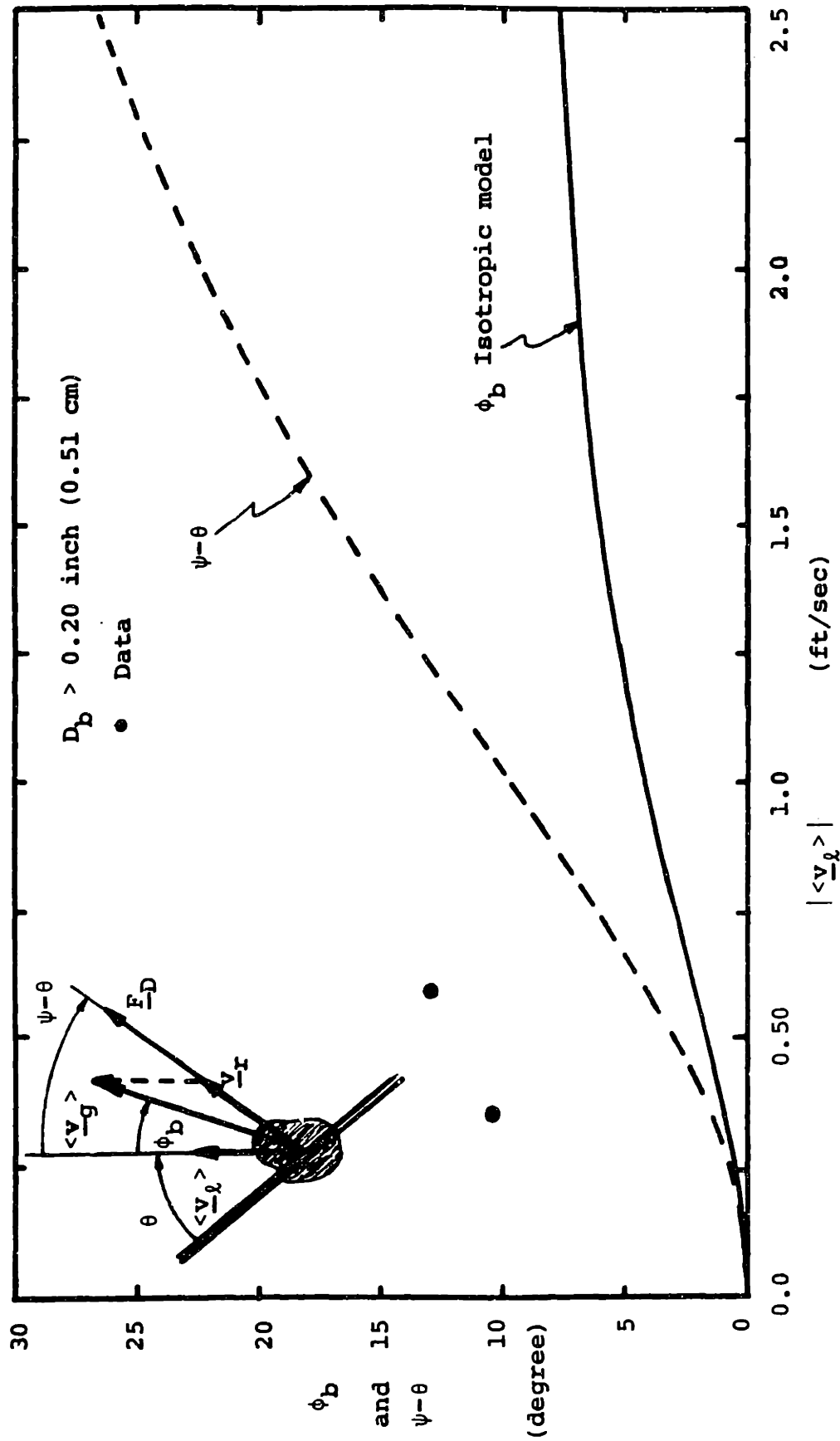


Figure 6.23 Bubble trajectory prediction with isotropic model for large bubbles.

$$\underline{F}_D = C_{D||} a_p \frac{\rho_l |\underline{v}_r|}{2} v_{r||} \underline{e}_{||} + C_{D\perp} a_p \frac{\rho_l |\underline{v}_r|}{2} v_{r\perp} \underline{e}_{\perp} \quad (6.50)$$

In Eq. (6.50) $C_{D||}$ and $C_{D\perp}$ are the drag coefficients for the two principle directions, parallel and crossflow, developed from data in Sec. 6.3.3. The drag coefficient for parallel flow is less than that for crossflow

$$C_{D||} < C_{D\perp} \quad (6.51)$$

This can be seen in Fig. 6.24 by the larger rise velocity for parallel flow. With an anisotropic (tensor) drag coefficient, \underline{F}_D and \underline{v}_r are no longer required to be collinear vectors. However the consequence of Eq. (6.51) is to make the parallel flow direction more preferential, resulting in the bubble trajectory ϕ_b being closer to the parallel direction than the direction drag force i.e.,

$$\phi_b < \psi - \theta \quad (6.52)$$

(Variable definitions are given in Fig. 6.25) For the case of zero liquid flow, Eq. (6.52) can be easily derived. The ratio of the drag force components for zero liquid flow is

$$\begin{aligned} \tan \psi &= \frac{F_{D\perp}}{F_{D||}} = \frac{C_{D\perp} \langle \underline{v}_g \perp \rangle}{C_{D||} \langle \underline{v}_g \parallel \rangle} \\ &= \frac{C_{D\perp}}{C_{D||}} \tan \theta_g \end{aligned} \quad (6.53)$$

but the restriction of $C_{D||} < C_{D\perp}$ requires

$$\theta_g < \psi \quad (6.54)$$

Using the identity $\theta_g = \phi_b + \theta$, Eq. (6.54) becomes Eq. (6.52). Like the isotropic model, the superposition model also restricts the bubble

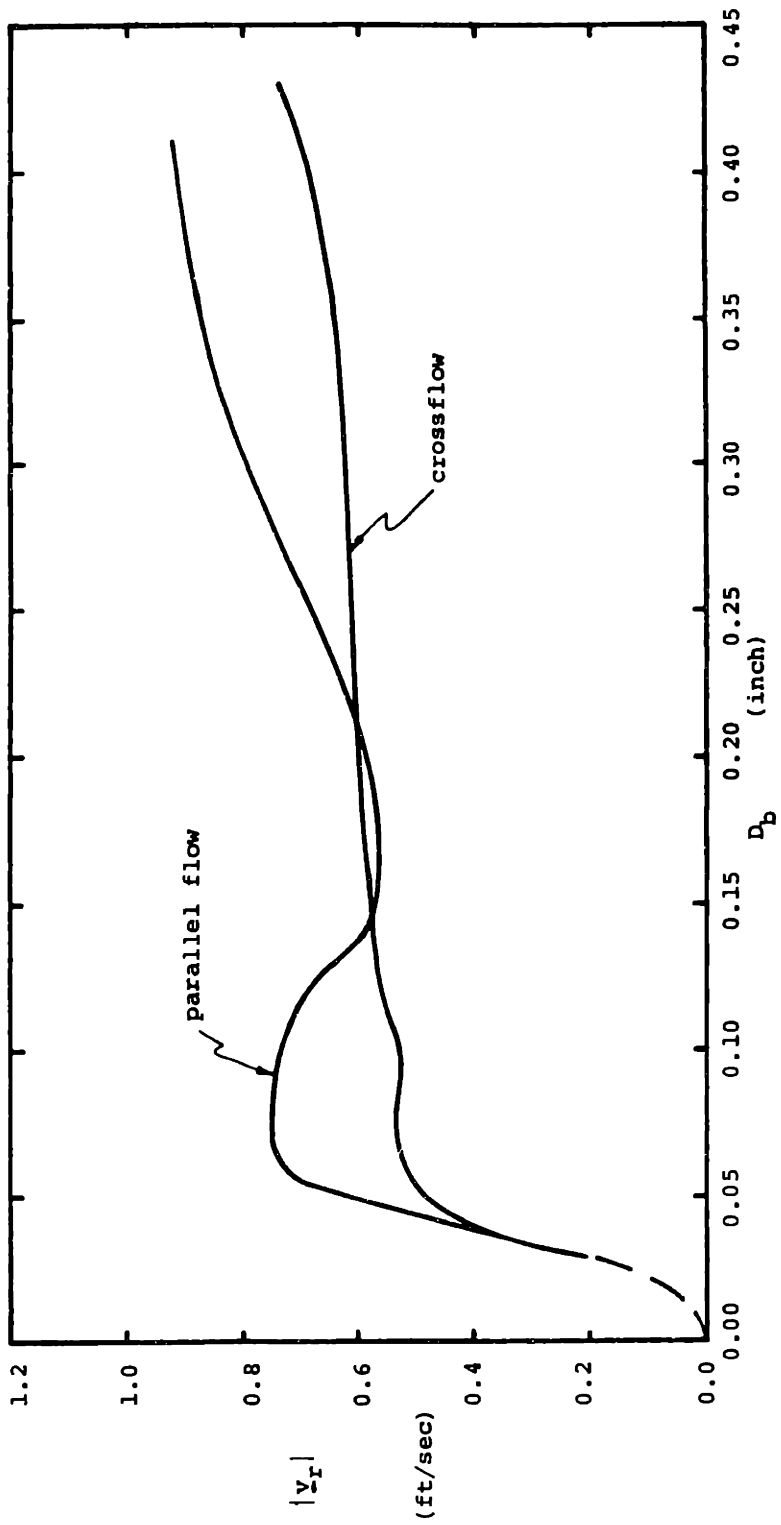


Figure 6.24 Bubble rise velocity in parallel and crossflow test sections.

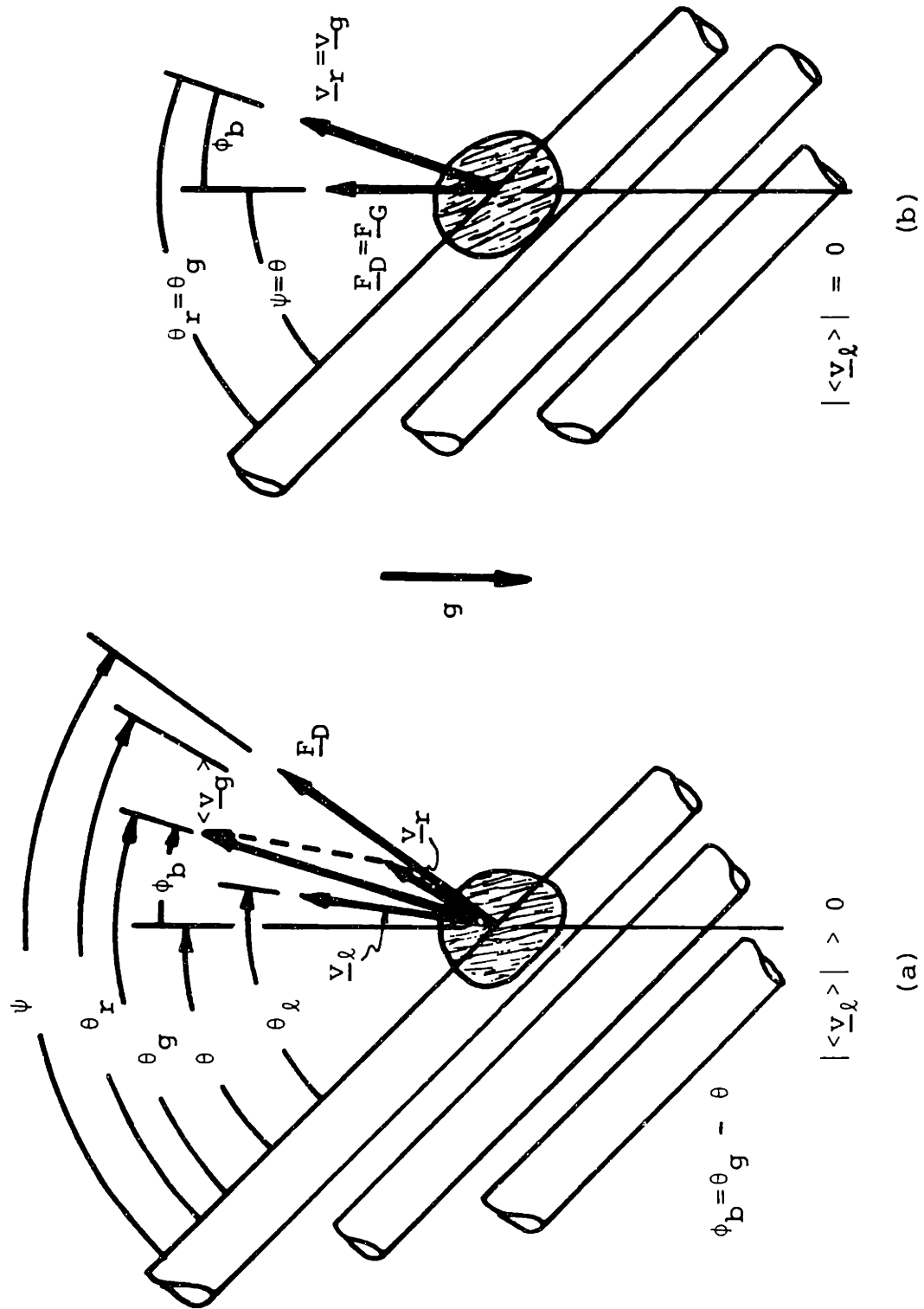


Figure 6.25 Bubble coordinate variable definitions (a) general and (b) for zero liquid flow.

trajectory angle less than the total drag force angle although the converse is observed experimentally.

The superposition model also fails to correctly predict the magnitude of drag (bubble rise velocity). The drag is accurately predicted by crossflow drag (as seen in the rise velocities of Fig. 6.14). The superposition model, however, predicts that the magnitude of drag is

$$\left| \underline{C}_D \right| = \frac{2 \left| \underline{F}_D \right|}{a_p \rho_l \left| \underline{v}_r \right|^2} = \sqrt{(C_{D||} \cos \theta_r)^2 + (C_{D\perp} \sin \theta_r)^2} \quad (6.55)$$

which is less than $C_{D\perp}$ for all $\theta_r < 90^\circ$ since $C_{D||} < C_{D\perp}$.

In light of the deficiencies of the above two models, in the next section we introduce a new formulation which captures the observed physics of two-phase flow in inclined arrays.

6.5.4 Two-Region Model

6.5.4.1 Liquid Velocity Model

The time-exposure photographs of a stream of bubbles (Plates 6.2 and 6.3) show two discrete trajectories of bubbles, one inclined across the rods and one parallel to the rod axis. This observation plus the concept of a mainstream and recirculating drag region observed in single-phase crossflow and inclined flow (Sec. 5.1) suggest partitioning the average liquid velocity for inclined flow into two regions. Region ① is the mainstream region of irrotational flow which weaves between the rods. Region ② is the recirculating drag region behind the rods which spirals along the rod axis (See Fig. 6.26). To mathematically

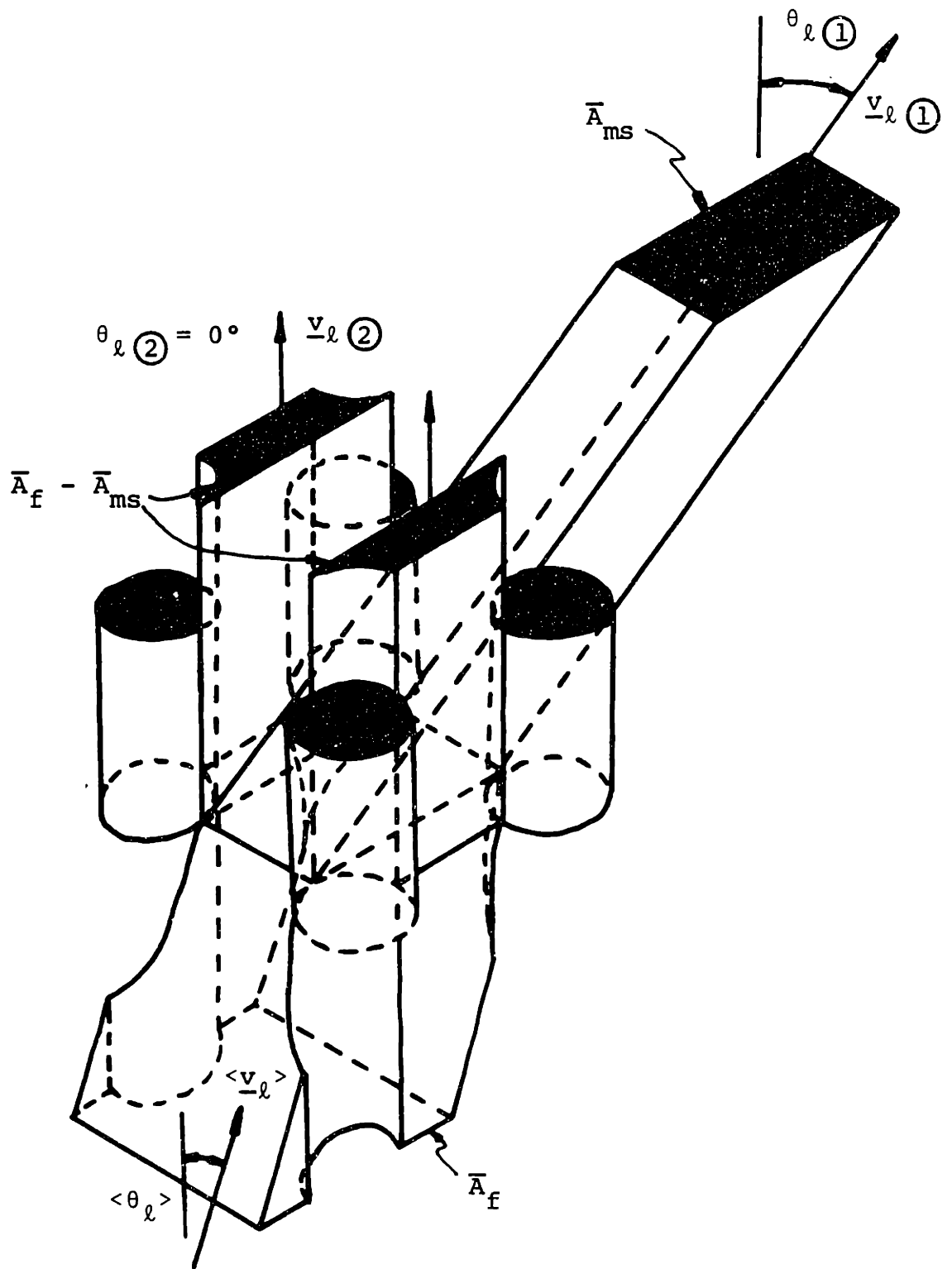


Figure 6.26 Two-region velocity model.

describe these two regions we relate the two region velocities $\underline{v}_\ell \textcircled{1}$ and $\underline{v}_\ell \textcircled{2}$, to the average velocity $\langle \underline{v}_\ell \rangle$, and the crossflow mainstream porosity

$$\delta_v \triangleq \bar{A}_{ms} / \bar{A}_f = V_{ms} / V_f \quad (6.56)$$

(See Appendix D) by using continuity and assuming that:

- The mainstream flow volume V_{ms} , defined for crossflow is constant and applicable for inclined flows,
- The recirculating region velocity $\underline{v}_\ell \textcircled{2}$, follows the rod axis, i.e.,

$$\theta_\ell \textcircled{2} = 0^\circ \quad (6.57)$$

and,

- The net velocity of the recirculating region is the component of the mainstream velocity in the parallel direction, i.e.,

$$|\underline{v}_\ell \textcircled{2}| = |\underline{v}_\ell \textcircled{1}| \cos \theta_\ell \textcircled{1} \quad (6.58)$$

Physically, this last assumption places no slip constraint on the parallel component of velocity of both regions, but allows slip in the crossflow direction because region $\textcircled{2}$ is constrained by the rods.

Continuity of mass in the parallel direction yields

$$\bar{A}_f |\langle \underline{v}_\ell \rangle| \cos \langle \theta_\ell \rangle = \bar{A}_{ms} |\underline{v}_\ell \textcircled{1}| \cos \theta_\ell \textcircled{1} + (\bar{A}_f - \bar{A}_{ms}) |\underline{v}_\ell \textcircled{2}| \quad (6.59)$$

and in the crossflow direction, yields

$$\bar{A}_f |\langle \underline{v}_\ell \rangle| \sin \langle \theta_\ell \rangle = \bar{A}_{ms} |\underline{v}_\ell \textcircled{1}| \sin \theta_\ell \textcircled{1} \quad (6.60)$$

Solving Eq. (6.58), (6.59) and (6.60) for $\theta_\ell \textcircled{1}$ and $|\underline{v}_\ell \textcircled{1}|$ gives

$$\tan \theta_\ell \textcircled{1} = \frac{1}{\delta_v} \tan \langle \theta_\ell \rangle \quad (6.61)$$

and

$$|\underline{v}_\ell \textcircled{1}| = |\langle \underline{v}_\ell \rangle| \frac{\cos \langle \theta_\ell \rangle}{\cos \theta_\ell \textcircled{1}} \quad (6.62)$$

where the definition $\delta_v = \bar{A}_{ms} / \bar{A}_f$ has been used. Consequently the velocity of region $\textcircled{2}$ becomes

$$\theta_\ell \textcircled{2} = 0^\circ \quad (6.63)$$

$$|\underline{v}_\ell \textcircled{2}| = |\langle \underline{v}_\ell \rangle| \cos \langle \theta_\ell \rangle \quad (6.64)$$

A graphic construction of $\underline{v}_\ell \textcircled{1}$ and $\underline{v}_\ell \textcircled{2}$ is shown in Fig. 6.27.

6.5.4.2 Drag Force Formulation

Now consider individual drag formulations for each region

$$\underline{F}_D = C_{D \textcircled{1}} a_p \frac{\rho_\ell |\underline{v}_r \textcircled{1}|}{2} \underline{v}_r \textcircled{1} \quad (6.65)$$

and

$$\underline{F}_D = C_{D \textcircled{2}} a_p \frac{\rho_\ell |\underline{v}_r \textcircled{2}|}{2} \underline{v}_r \textcircled{2} \quad (6.66)$$

where

$$\underline{v}_r \textcircled{1} = \underline{v}_g \textcircled{1} - \underline{v}_\ell \textcircled{1} \quad (6.67)$$

and

$$\underline{v}_r \textcircled{2} = \underline{v}_g \textcircled{2} - \underline{v}_\ell \textcircled{2} \quad (6.68)$$

The two formulas are linked to the average bubble (gas) velocity by

$$\langle \underline{v}_g \rangle = (1 - \lambda) \underline{v}_g \textcircled{1} + \lambda \underline{v}_g \textcircled{2} \quad (6.69)$$

where the function λ is defined as the probability that a bubble of given diameter is in a recirculating region (region $\textcircled{2}$). All that remains are models for $C_{D \textcircled{2}}$ and λ .

6.5.4.3 Mainstream Drag Coefficient

For zero liquid flow, bubbles rise between the rods similar to in

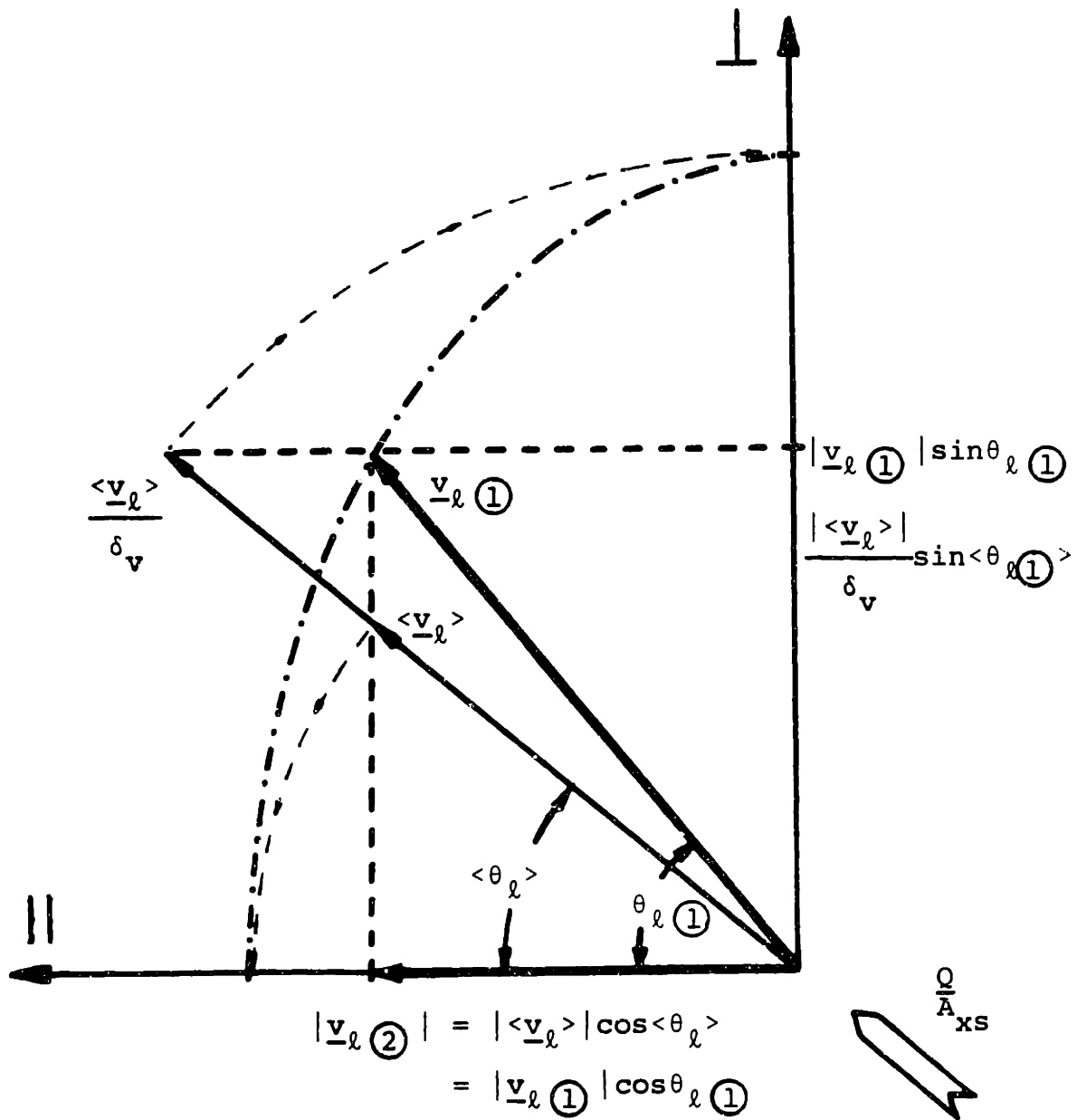


Figure 6.27 Construction of mainstream and recirculation region velocities.

the mainstream region. Hence we postulate a correlation for $\underline{C}_D \textcircled{1}$ which can be evaluated from the zero liquid flow inclined array data. Remembering that the magnitude of drag is relatively constant we split $\underline{C}_D \textcircled{1}$ into a scalar magnitude and directional tensor \underline{J}

$$\underline{C}_D \textcircled{1} = |\underline{C}_D \textcircled{1}| \begin{bmatrix} J_{||} & 0 \\ 0 & J_{\perp} \end{bmatrix} \quad (6.70)$$

where

$$|\underline{C}_D \textcircled{1}| \triangleq \frac{2|\underline{F}_D|}{a_p \rho_l |\underline{v}_r \textcircled{1}|^2} \quad (6.71)$$

The components of \underline{J} can be evaluated in terms of measurable quantities by substituting Eq. (6.70) into Eq. (6.65)

$$\begin{aligned} \underline{F}_D &= |\underline{F}_D| \cos \psi \underline{e}_{||} + |\underline{F}_D| \sin \psi \underline{e}_{\perp} \\ &= |\underline{C}_D \textcircled{1}| J_{||} \frac{a_p \rho_l |\underline{v}_r \textcircled{1}|^2}{2} \cos \theta_r \textcircled{1} \underline{e}_{||} \\ &\quad + |\underline{C}_D \textcircled{1}| J_{\perp} \frac{a_p \rho_l |\underline{v}_r \textcircled{1}|^2}{2} \sin \theta_r \textcircled{1} \underline{e}_{\perp} \end{aligned} \quad (6.72)$$

and then using Eq. (6.71) to get

$$J_{||} = \frac{\cos \psi}{\cos \theta_r \textcircled{1}} \quad (6.73)$$

$$J_{\perp} = \frac{\sin \psi}{\sin \theta_r \textcircled{1}} \quad (6.74)$$

The mainstream drag coefficient then can be correlated thus

$$|\underline{C}_D \textcircled{1}| = \text{ftn}[C_{D||}, C_{D\perp}, \theta_r \textcircled{1}] \quad (6.75)$$

$$\theta_r \textcircled{1} = \text{ftn}[\psi, D_b/\sqrt{L}_{\text{gap}}] \quad (6.76)$$

where the bubble diameter is referenced to the average gap width. Since the only available inclined array bubble data to date is the $\theta = 0, 45,$ and 90 degree data of this study, we present here only a preliminary model to demonstrate the validity of the two-region model. The preliminary model assumes $|C_{D(1)}|$ is that of crossflow, $C_{D\perp}$, except in the limit of parallel flow

$$|C_{D(1)}| = \begin{cases} C_{D\parallel} & \text{for } 0^\circ \leq \psi < -5^\circ \\ C_{D\perp} & \text{for } -5^\circ \leq \psi \leq 90^\circ \end{cases} \quad (6.77)$$

and assumes the relative velocity deflection from \underline{F}_D is small so that

$$\theta_{r(1)} \approx \psi \quad (6.78)$$

The zero liquid flow measured deflection, $\phi_b = \theta_{r(1)} - \psi$, for the 45 degree test section (Fig. 6.15) has a maximum value of -10° , which most likely is the maximum for all angles θ , since in the limits of zero and 90 degrees, $\phi_b = 0$. The transition angle of -5 degrees in Eq. (6.77) is arbitrarily chosen, but is required to maintain continuity in the parallel flow limit.

6.5.4.4 Recirculating Region Drag Coefficient

The recirculating region drag coefficient $C_{D(2)}$ cannot be measured from zero liquid flow data since region (2) does not exist for zero flow. Drag measurements with flow also prove very difficult because of the high speed and small size of the recirculating region bubbles. However a good estimate of $C_{D(2)}$ is that for homogeneous flow (no slip) since only small viscous bubbles have been observed in the recirculating region and the interfacial drag for these bubbles is large. Also contributing to the homogeneous flow assumption are the vortices which

restrict the bubble motion along the rod axis, parallel to v_L (1).

Hence a preliminary model for the region (2) drag coefficient is

$$C_{D(2)} = \begin{cases} C_{D||} & \text{for } 0^\circ \leq \psi < -5^\circ \\ 10^8 & \text{for } -5^\circ \leq \psi \leq 90^\circ \end{cases} \quad (6.79)$$

where in the limit of parallel flow $C_{D(2)}$ reduces to $C_{D||}$.

6.5.4.5 Weighting Function λ

All that remains to complete the two-region model is a correlation for the weighting function λ --the probability of the bubble to be in the recirculating region, i.e.,

$$\lambda = \text{ftn}[D_b/\bar{L}_{\text{gap}}, \langle \alpha \rangle] \quad (6.80)$$

Again a complete model for λ cannot be developed with the limited data to date. The two-region model, however, can be validated for the two limiting cases:

- (1) Large bubbles where the bubbles remain in the mainstream region, $\lambda = 0$, and
- (2) Small bubbles where the bubbles remain in the drag region, $\lambda = 1$.

Then a preliminary model for λ is

$$\lambda = \begin{cases} 1 & \text{for } 0 < D_b < d/2 \\ 0 & \text{for } d/2 \leq D_b \end{cases} \quad (6.81)$$

The transition bubble diameter of half the rod diameter, $d/2$, is chosen because that is the width of the recirculating region vortices. A bubble larger than this width cannot easily stay in the region (2).

The complete model is summarized in Table 6.4. This model is valid for nonzero liquid flows only.

TABLE 6.4

Two-Region Model

$\underline{F}_D = \underline{C}_D \textcircled{1} a_p \frac{\rho_l \underline{v}_r \textcircled{1} }{2} \underline{v}_r \textcircled{1}$ $\underline{F}_D = \underline{C}_D \textcircled{2} a_p \frac{\rho_l \underline{v}_r \textcircled{2} }{2} \underline{v}_r \textcircled{2}$
$\underline{v}_r \textcircled{1} = \underline{v}_g \textcircled{1} - \underline{v}_l \textcircled{1}$ $\underline{v}_r \textcircled{2} = \underline{v}_g \textcircled{2} - \underline{v}_l \textcircled{2}$
$a_p = \frac{3}{2} \frac{1}{D_b}$ $\langle \underline{v}_g \rangle = (1 - \lambda) \underline{v}_g \textcircled{1} - \lambda \underline{v}_g \textcircled{2}$
$\underline{C}_D \textcircled{1} = \begin{cases} C_{D } & \text{for } 0^\circ \leq \psi < -5^\circ \\ C_{D\perp} & \text{for } -5^\circ \leq \psi \leq 90^\circ \end{cases}$ $\underline{C}_D \textcircled{2} = \begin{cases} C_{D } & \text{for } 0^\circ \leq \psi < -5^\circ \\ 10^8 & \text{for } -5^\circ \leq \psi \leq 90^\circ \end{cases}$
$\lambda = \begin{cases} 1 & \text{for } 0 \leq D_b < d/2 \\ 0 & \text{for } d/2 \leq D_b \end{cases}$

6.5.4.6 Model Validation

The single bubble data taken within the 45 degree test section (Sec. 6.4.1) and the observed small bubble trajectory along the rod axis (Sec. 6.4.2) are used here to validate the two-region model. The velocity and trajectory of a single bubble were calculated with the two-region model and for comparison with the isotropic model (See Appendix I). In these calculations the resistance force $\underline{F}_R = \langle \underline{R}_\ell \rangle$, was evaluated from the single-phase flow resistance fits of Chapter 5. This is an excellent assumption because a single bubble has a negligible effect on the total flow resistance force.

Figure 6.28 shows a comparison of the predicted bubble trajectories with data for a range of bubble diameters. The two-region model clearly captures the severe difference between large and small diameter bubbles not possible with the isotropic model. The data/model comparison is shown again for large diameter bubbles in Fig. 6.29. The direction of the total drag force is also plotted. Notice that the introduction of the mainstream velocity \underline{v}_ℓ (1), in a direction to the right of the average velocity $\langle \underline{v}_\ell \rangle$, correctly explains the large bubble trajectories.

The 0.28 inch (0.71 cm) diameter bubble velocity data are compared with model predictions in Fig. 6.30. For large bubbles the discrepancy between models is not as severe as with trajectories, however the two-region model more closely predicts the available data. More important, for small diameter bubbles the isotropic model is really not applicable because the drag coefficient used is based on bubbles moving across rods in the mainstream region where as we observed the bubbles in

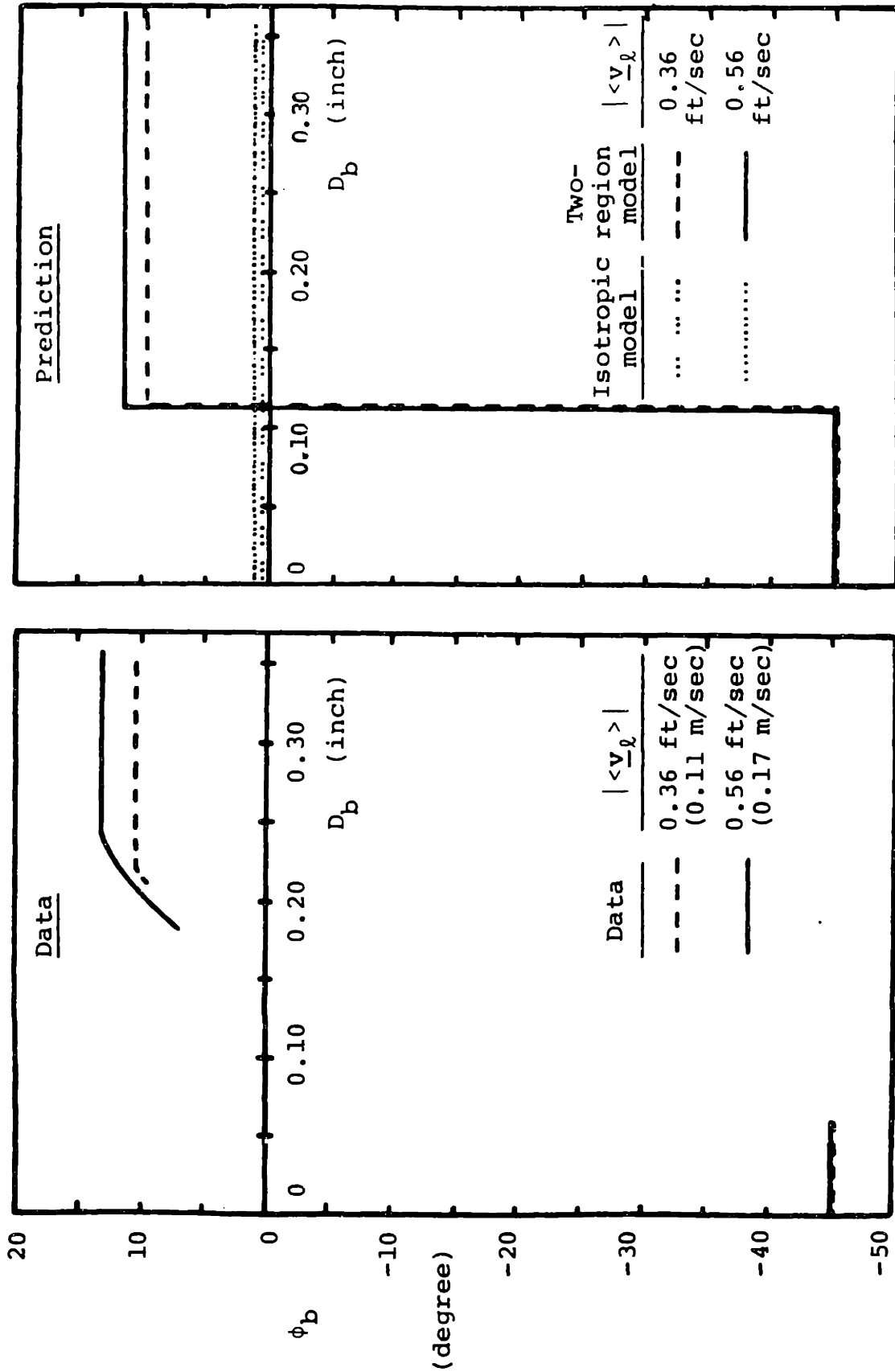


Figure 6.28 Model/data comparison of single bubble trajectory in 45 degree test section.

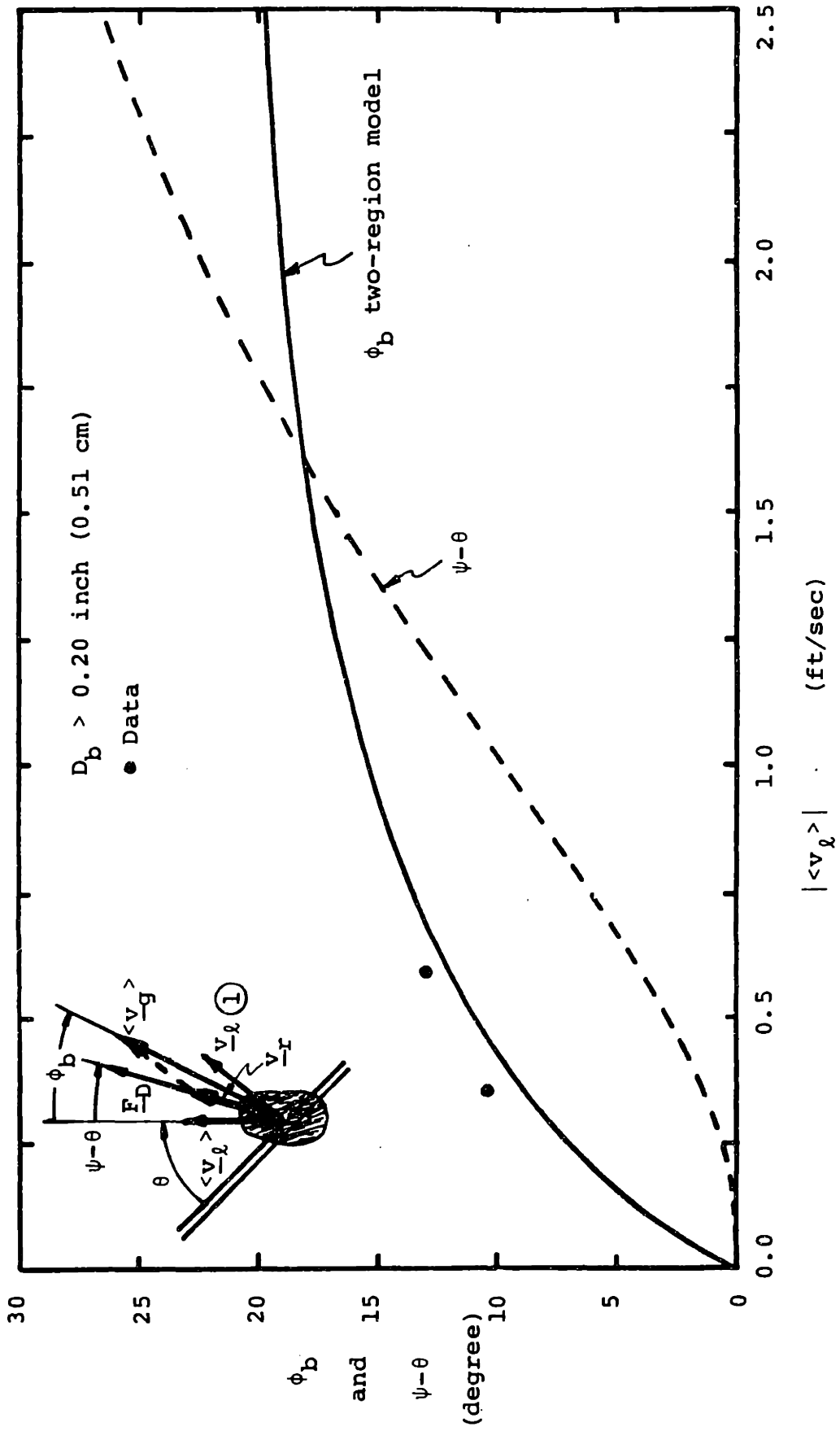


Figure 6.29 Bubble trajectory prediction with two-region model for large bubbles.

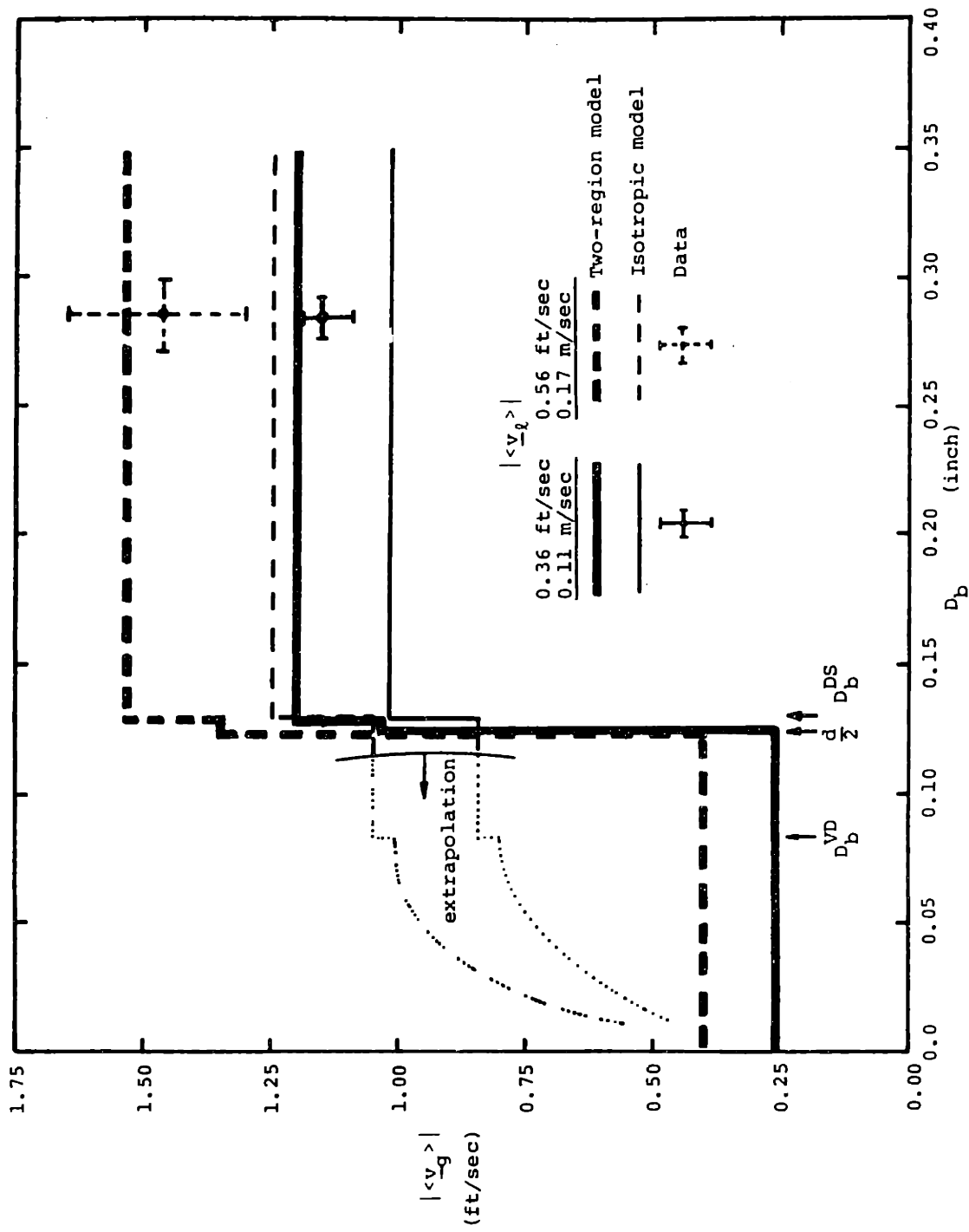


Figure 6.30 Model/data comparison of bubble velocity in 45 degree test section.

a recirculating, vortex flow moving along the rod axis. Bubbles flowing in this recirculating region clearly will have a different drag.

This initial comparison demonstrates the potential of the two-region model to predict single bubble motion within inclined arrays. The extrapolation and extension of this physically based model to multiple bubble systems where bubble interactions will also influence the flow and void distribution is yet to be explored.

6.5.5 Summary

Table 6.5 summarizes the three multidimensional interfacial drag models. With a scalar drag coefficient the isotropic model shows no preferential direction for phase separation. The gas phase slips relative to the liquid phase only in the direction of the driving force independent of the orientation of the rod array.

The superposition model introduces a preferential direction of phase separation by the arbitrary tensor formulation. Although this tensor formulation matches the one-dimensional limits, the additional physics of inclined array flow are not correctly incorporated.

The two-region model, shown in tensor form in Table 6.5, is a judicious construction of a multidimensional drag coefficient. It incorporates a relation between the local, effective liquid velocity and the average liquid velocity, on which the drag formulation is based.

Introducing physical insight into the construction of the multidimensional drag formulation enables inclined array phase separation to be correctly and comprehensively predicted.

TABLE 6.5

Multidimensional Interfacial Drag Models

$$\begin{aligned} \underline{F}_D &\triangleq C_{D\perp} a_p \frac{\rho_l |\underline{v}_r|}{2} \underline{v}_r \\ \underline{v}_r &\triangleq \langle \underline{v}_g \rangle - \langle \underline{v}_l \rangle \\ \langle \underline{v}_l \rangle &\triangleq \langle v_{l\parallel} \rangle \underline{e}_{\parallel} + \langle v_{l\perp} \rangle \underline{e}_{\perp} \\ \langle \underline{v}_g \rangle &\triangleq \langle v_{g\parallel} \rangle \underline{e}_{\parallel} + \langle v_{g\perp} \rangle \underline{e}_{\perp} \end{aligned}$$

Model	Drag Coefficient tensor, \underline{C}_D
Isotropic	$C_{D\perp}$
Superposition	$C_{D\perp} \begin{bmatrix} C_{D\parallel}/C_{D\perp} & 0 \\ 0 & 1 \end{bmatrix}$
Two-Region (for $\psi > -5^\circ$)	$\frac{C_{D\perp}}{(1-\lambda)^2} \left\{ \frac{(\langle v_{g\parallel} \rangle - \langle v_{l\parallel} \rangle)^2 + (\langle v_{g\perp} \rangle - \frac{(1-\lambda)}{\delta_v} \langle v_{l\perp} \rangle)^2}{(\langle v_{g\parallel} \rangle - \langle v_{l\parallel} \rangle)^2 + (\langle v_{g\perp} \rangle - \langle v_{l\perp} \rangle)^2} \right\}^{1/2}$ $\cdot \begin{bmatrix} 1 & 0 \\ 0 & \frac{\langle v_{g\perp} \rangle - \frac{(1-\lambda)}{\delta_v} \langle v_{l\perp} \rangle}{\langle v_{g\perp} \rangle - \langle v_{l\perp} \rangle} \end{bmatrix}$

6.6 Summary and Conclusion

Interfacial force models for bubbly flow currently used in multidimensional codes are generally derived from the drag force for bubbles flowing in a standing liquid pool or round tube. The effect of solid structures in the neighborhood of the bubbles is not incorporated. The major contribution of the solid boundaries is to change the liquid velocity field--distribution and direction--from that on which the drag force correlation is based. For round tubes corrections for the changed velocity profile have been developed, however for flows in rod arrays and other geometries the drag formulas for an infinite medium have been assumed sufficient.

This study explored the influence of a rod array on the single bubble drag and global bubble flow distribution. Observations for bubbly flow in inclined rod arrays showed a pronounced bubble size and flow field effect on the phase separation which is not predictable with current interfacial drag formulas. A two-region velocity model was developed to incorporate the heterogeneous liquid velocity distribution present in inclined rod arrays.

Many elements of a comprehensive multidimensional interfacial model still remain unexplored. The major conclusions to be drawn from this exploratory study are the following.

- For the basic bubble drag formulas currently used in two-fluid codes to be employed correctly, bubble distribution and local velocity distribution models for the geometry of interest are also required. These distribution

models are required to relate the average variables of the codes to the local variable actually governing the bubble interfacial forces.

- Although local distribution models are difficult to formulate they cannot be neglected in multidimensional geometries as seen by the phase separation observations of this study.
- In light of the lack of fundamental experimental data in basic multidimensional geometries, interim global correlations based on prototype experiments also should be developed. Then instead of relying on unsubstantiated interfacial drag models based on one-dimensional data, void distributions can be predicted from actual observed flow distributions.

A start at developing a fundamental knowledge of bubbly flow in rod arrays was performed in this work. Some observations are:

- In inclined rod array flows, bubbles much smaller than the rod diameter migrate into the recirculating vortices and move along the rod axis. In contrast large deformed bubbles move across the rods.
- Large deformed bubbles in parallel and crossflow arrays have an increased bubble velocity unexplainable by wall effect models developed for round tubes.
- The standing liquid bubble velocity for inclined arrays, is well approximated by the crossflow array bubble velocity. In inclined arrays the bubble trajectory is also altered by the inclined rods and dependent on the bubble size.

Some key unanswered questions should be addressed in future studies:

- In multiple bubble flows is the wall effect observed for single bubbles still pronounced or washed out by the interaction between bubbles?
- Can bubble size distribution which is the key to any mechanistic inclined array model be predicted well in application? Or is a more empirical global model the only type within reach?
- What is the impact on design and operational performance of the flow separation observed in this study?

CHAPTER 7

SUMMARY, CONCLUSIONS, AND FUTURE WORK

Thermal-hydraulic analysis is currently an inexact science, it relies heavily on empiricism. External constitutive relations depending on the environmental surroundings are used extensively, because of the lack of universal intrinsic constitutive relations. Multidimensional thermal-hydraulic codes, historically, have been developed in a format of first developing a numerical algorithm and then addressing the problem of describing the resultant constitutive variables with available correlations. This premise has lead towards multidimensional constitutive formulations constructed solely on superposition of available one-dimensional principal coordinate correlations.

A more rational approach is to formulate multidimensional correlations on a basis of physical observations and then tailor these formulations to accommodate the constraining requirements of numerical codes. This study focused on the constitutive correlations for the hydrodynamics of multidimensional single- and two-phase flow in rod arrays. An experimental investigation was conducted to examine, develop, and validate multidimensional correlations for single-phase flow resistance and two-phase interfacial momentum exchange.

In single-phase flow the former method of superimposing one-dimensional correlations faired well when compared with multidimensional data. This is because in turbulent flow the crossflow component dominates the total resistance force. A closer examination of the individual resistance components reveals that the negligible parallel component is grossly underpredicted. In laminar flow where

neither principal component dominates, the superposition method most likely will not be a sufficient formulation. A formulation based on the magnitude of the total resistance force and its direction with respect to the driving vector (i.e., average velocity) is probably a more suitable approach.

In two-phase modeling of the interfacial drag force the insufficiency of simple superposition methods was demonstrated. New flow distribution phenomena not characteristic of one-dimensional rod array flows was inexplicable with simple superposition methods. Hence a new formulation (the two-region model) incorporating the physically observed phenomena, was developed. This formulation was then arranged in a form compatible with numerical codes.

Full refinement and validation of the two-region model is still required. However the importance of the observed phenomena incorporated in this model cannot be understated. The key feature is that bubbles significantly smaller than the array rod diameter move parallel to the rods. In steam-water heat transfer components at typical operating conditions the bubble size is generally much smaller than the rod diameter. Estimations of bubble diameters at 1000 psi (7 MPa) by bubble nucleation, Taylor stability, and critical Weber number criteria, all predicted bubble diameters much less than the typical rod (tube) diameters, 0.25 - 0.50 inch (0.64 - 1.27 cm). Hence in commercial components operating in the bubbly flow regime it would be expected to see the void migrate along the rod axis until a solid boundary is reached, a phenomena not predicted by current computer codes.

The overall conclusion of this study is that models for physical phenomena should not be restricted by the current numerical

computational tools available. Instead the computational tools should be tailored more toward incorporating the physical phenomena as observed, and consequently providing better predictive capabilities.

In following up this study, suggested tasks for future research are:

- Taking single-phase inclined flow resistance data for laminar flow and assessing the superposition formulations in this range.
- Developing an array arrangement independent single-phase crossflow resistance correlation for general application in a porous media of rod arrays.
- Expanding and extending the single bubble trajectory and velocity data for 45 and 30 degree test sections, respectively, to improve and further validate the two-region model.
- Improving the single bubble trajectory photographic measuring technique.
- Exploring the combined influence of liquid flow field and multiple bubbles in inclined arrays.
- Constructing a prototype experiment to explore the impact of the observed bubbly flow phase separation in commercial components.
- Performing a similar review, assessment, evaluation, of the other principle constitutive variables in multidimensional two-fluid thermal-hydraulic codes, i.e., two-phase flow resistance, fluid-solid heat exchange, interfacial heat exchange, and interfacial momentum exchange for other flow regimes.

APPENDIX A

DERIVATION OF THE TIME/VOLUME-AVERAGED MASS AND MOMENTUM CONSERVATION EQUATIONS

The derivation presented here is adapted primarily from the work of Ishii [I.1] and Bouré and Delhaye [B.5]. First the general form of two mathematical theorems is stated, then the local instantaneous conservation equations are derived. Next the local equations are time and volume averaged. Finally some variations of the time/volume-averaged equations are shown.

A.1 Mathematical Theorems

The two theorems stated below will be used repeatedly in various forms in the derivations.

A.1.1 Leibnitz's Rule

For a geometric volume $V(t)$ of closed area $A(t)$ as shown in Fig. A.1(a), Leibnitz's Rule transforms the time rate of change of a volume integral into the sum of a volume and surface integral

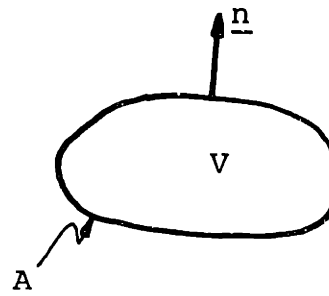
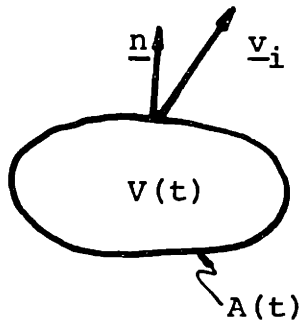
$$\frac{d}{dt} \int_{V(t)} f(\underline{r}, t) dV = \int_{V(t)} \frac{\partial f(\underline{r}, t)}{\partial t} dV + \int_{A(t)} f(\underline{r}, t) \underline{v}_i \cdot \underline{n} dA \quad (\text{A.1})$$

where $f(\underline{r}, t)$ is a function of space and time and \underline{v}_i and \underline{n} are the control volume boundary velocity and outward normal, respectively.

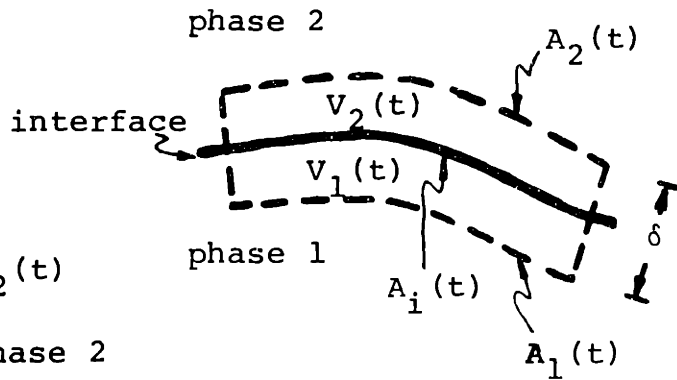
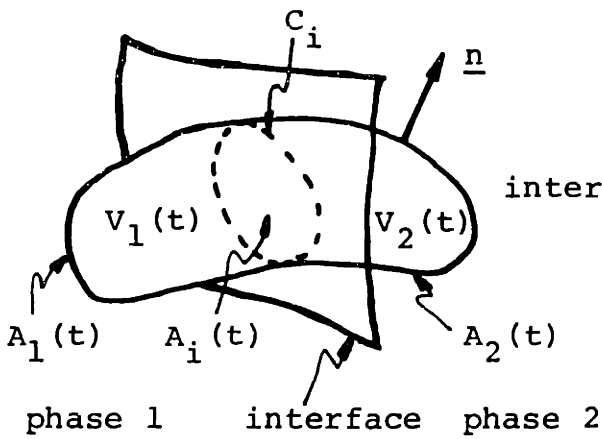
A.1.2 Gauss' Theorem

Gauss' Theorem transforms a volume integral over a material or geometric control volume V , into a surface integral over the closed surface A , by the relation

$$\int_V \nabla \cdot f dV = \oint_A f \cdot \underline{n} dA \quad (\text{A.2})$$



(a) Moving geometric volume. (b) Moving or stationary geometric or material volume.



$$V = V_1(t) + V_2(t)$$

$$A = A_1(t) + A_2(t)$$

(c) Stationary geometric volume. (d) Stationary geometric interface volume.

Figure A.1 Control volume definitions.

where \underline{n} is the outward normal as shown in Fig. A.1(b), and f may be either a vector or tensor variable.

A.2 Local Instantaneous Conservation Equations

A.2.1 Local Instantaneous Mass Equation

Consider a stationary geometric control volume V which is subdivided into two phase volume $V_1(t)$ and $V_2(t)$ by an interface as shown in Fig. A.1(c). An integral mass balance on V requires that the time rate of change of the mass in V plus the efflux of mass through the closed surface A equals zero

$$\frac{d}{dt} \int_V \rho \, dV + \oint_A \rho \, \underline{v} \cdot \underline{n} \, dA = 0 \quad (\text{A.3})$$

where \underline{n} is the outward normal. Partitioning this balance into integrals for each phase gives

$$\frac{d}{dt} \left[\int_{V_1(t)} \rho_1 \, dV + \int_{V_2(t)} \rho_2 \, dV \right] + \int_{A_1(t)} \rho_1 \, \underline{v}_1 \cdot \underline{n}_1 \, dA + \int_{A_2(t)} \rho_2 \, \underline{v}_2 \cdot \underline{n}_2 \, dA = 0 \quad (\text{A.4})$$

Using Leibnitz's Rule on the volume integrals gives

$$\begin{aligned} & \int_{V_1(t)} \frac{\partial \rho_1}{\partial t} \, dV + \int_{A_1(t)} \rho_1 \, \underline{v}_1 \cdot \underline{n}_1 \, dA + \int_{A_i(t)} \rho_1 \, \underline{v}_i \cdot \underline{n}_1 \, dA + \int_{A_1(t)} \rho_1 \, \underline{v}_1 \cdot \underline{n}_1 \, dA \\ & + \int_{V_2(t)} \frac{\partial \rho_2}{\partial t} \, dV + \int_{A_2(t)} \rho_2 \, \underline{v}_2 \cdot \underline{n}_2 \, dA + \int_{A_i(t)} \rho_2 \, \underline{v}_i \cdot \underline{n}_2 \, dA + \int_{A_2(t)} \rho_2 \, \underline{v}_2 \cdot \underline{n}_2 \, dA = 0 \end{aligned} \quad (\text{A.5})$$

where the area integrals have been partitioned into the moving area A_i and the stationary areas $A_1(t)$ and $A_2(t)$. For the stationary surfaces $\underline{v}_i \cdot \underline{n}$ is zero so

$$\sum_k \left[\int_{V_k(t)} \frac{\partial \rho_k}{\partial t} \, dV + \int_{A_k(t)} \rho_k \, \underline{v}_k \cdot \underline{n}_k \, dA + \int_{A_i(t)} \rho_k \, \underline{v}_i \cdot \underline{n}_k \, dA \right] = 0 \quad (\text{A.6})$$

where k is summed over the two phases. Now writing Gauss' Theorem for volume $V_k(t)$ and again partitioning the areas into A_k and A_i gives

$$\int_{A_k(t)} \rho_{k \rightarrow k} \mathbf{v}_{k \rightarrow k} \cdot \mathbf{n}_{\rightarrow k} dA = \int_{V_k(t)} \nabla \cdot \rho_{k \rightarrow k} \mathbf{v}_{k \rightarrow k} dV - \int_{A_i(t)} \rho_{k \rightarrow k} \mathbf{v}_{k \rightarrow k} \cdot \mathbf{n}_{\rightarrow k} dA \quad (\text{A.7})$$

Substituting into Eq. (A.6) gives

$$\sum_k \left[\int_{V_k(t)} \left(\frac{\partial \rho_k}{\partial t} + \nabla \cdot \rho_{k \rightarrow k} \mathbf{v}_{k \rightarrow k} \right) dV - \int_{A_i(t)} \rho_k (\mathbf{v}_{k \rightarrow k} - \mathbf{v}_{i \rightarrow i}) \cdot \mathbf{n}_{\rightarrow k} dA \right] = 0 \quad (\text{A.8})$$

Now consider that control volume V is in phase k only, then $A_i(t)$ is zero and Eq. (A.8) reduces to

$$\int_V \left(\frac{\partial \rho_k}{\partial t} + \nabla \cdot \rho_{k \rightarrow k} \mathbf{v}_{k \rightarrow k} \right) dV = 0 \quad (\text{A.9})$$

however this equation is valid for any V_k in phase k so by the axiom of continuum

$$\frac{\partial \rho_k}{\partial t} + \nabla \cdot \rho_{k \rightarrow k} \mathbf{v}_{k \rightarrow k} = 0 \quad (\text{A.10})$$

must also be valid. Eq. (A.10) is the local instantaneous mass conservation equation.

A.2.2 Mass Jump Condition

Consider a stationary control volume surrounding the interface region between the two phases as shown in Fig. A.1(d). If we take the limit as the control volume thickness δ , goes to zero, but the interface area remains finite, then the integrals in Eq. (A.8) will vanish leaving

$$\sum_k \int_{A_i(t)} \rho_k (\mathbf{v}_{k \rightarrow k} - \mathbf{v}_{i \rightarrow i}) \cdot \mathbf{n}_{\rightarrow k} dA = 0 \quad (\text{A.11})$$

Again this equation is valid for all A_i so using the axiom of

continuum gives the mass jump condition

$$\sum_k \rho_k (\underline{v}_k - \underline{v}_i) \cdot \underline{n}_k = 0 \quad (\text{A.12})$$

Physically, the mass jump condition approximates a sharp but continuous transition in density through the interface region by a discontinuous jump between phasic densities at a discrete interface boundary.

A.2.3 Local Instantaneous Momentum Equation

An integral momentum balance on the control volume V of Fig. A.1(c) requires that the time rate of change of momentum in V , plus the efflux of momentum through the closed surface A , equals the sum of the external body and surface forces on V

$$\frac{d}{dt} \int_V \rho \underline{v} dV + \int_A \rho \underline{v} (\underline{v} \cdot \underline{n}) dA = \int_V \rho \underline{F}_B dV + \int_A \underline{n} \cdot \underline{T} dA \quad (\text{A.13})$$

where \underline{T} is the total stress tensor and \underline{F}_B are the body forces.

Partitioning into integrals for each phase

$$\begin{aligned} & \frac{d}{dt} \int_{V_1(t)} \rho_1 \underline{v}_1 dV + \frac{d}{dt} \int_{V_2(t)} \rho_2 \underline{v}_2 dV + \int_{A_1(t)} \rho_1 \underline{v}_1 (\underline{v}_1 \cdot \underline{n}_1) dA \\ & + \int_{A_2(t)} \rho_2 \underline{v}_2 (\underline{v}_2 \cdot \underline{n}_2) dA = \int_{V_1(t)} \rho_1 \underline{F}_B dV + \int_{V_2(t)} \rho_2 \underline{F}_B dV \\ & + \int_{A_1(t)} \underline{n}_1 \cdot \underline{T}_1 dA + \int_{A_2(t)} \underline{n}_2 \cdot \underline{T}_2 dA + \int_{C_i} \sigma \underline{n} \cdot \underline{H} dC \end{aligned} \quad (\text{A.14})$$

The last term denotes the surface tension forces of the interface along the boundary curve C_i , \underline{H} being the transformation tensor between coordinates. (A more precise treatment of surface forces is given by Ishii [I.1] and Aris [A.1]). Applying Leibnitz's Rule and noting that the boundary areas A_1 and A_2 are stationary gives

$$\sum_k \left[\int_{V_k(t)} \frac{\partial}{\partial t} (\rho_{\underline{k-k}} \underline{v}_{\underline{k-k}}) dV + \int_{A_i(t)} \rho_{\underline{k-k}} \underline{v}_{\underline{k-k}} (\underline{v}_i \cdot \underline{n}_{\underline{k}}) dA + \int_{A_k(t)} \rho_{\underline{k-k}} \underline{v}_{\underline{k-k}} (\underline{v}_{\underline{k}} \cdot \underline{n}_{\underline{k}}) dA \right] \\ = \sum_k \left[\int_{V_k(t)} \rho_{\underline{k-B}} \underline{F} dV + \int_{A_k(t)} \underline{n}_{\underline{k}} \cdot \underline{T}_{\underline{k}} dA + \int_{C_i} \sigma \underline{n} \cdot \underline{H} dC \right] \quad (\text{A.15})$$

Using Gauss' Theorem to eliminate the $A_k(t)$ integrals in favor of volume and interfacial area integrals gives

$$\sum_k \left[\int_{V_k(t)} \left(\frac{\partial}{\partial t} (\rho_{\underline{k-k}} \underline{v}_{\underline{k-k}}) + \nabla \cdot \rho_{\underline{k-k}} \underline{v}_{\underline{k-k}} \underline{v}_{\underline{k-k}} - \rho_{\underline{k-B}} \underline{F} - \nabla \cdot \underline{T}_{\underline{k}} \right) dV \right. \\ \left. - \int_{A_i(t)} \left(\rho_{\underline{k-k}} \underline{v}_{\underline{k-k}} (\underline{v}_{\underline{k}} - \underline{v}_i) \cdot \underline{n}_{\underline{k}} - \underline{n}_{\underline{k}} \cdot \underline{T}_{\underline{k}} + 2H_{21} \sigma \underline{n}_1 \right) dA \right] = 0 \quad (\text{A.16})$$

where H_{21} is the radius of curvature of the interface.

Now consider an arbitrary control volume V entirely within phase k , then Eq. (A.15) reduces to

$$\int_V \left(\frac{\partial}{\partial t} (\rho_{\underline{k-k}} \underline{v}_{\underline{k-k}}) + \nabla \cdot \rho_{\underline{k-k}} \underline{v}_{\underline{k-k}} \underline{v}_{\underline{k-k}} - \rho_{\underline{k-B}} \underline{F} - \nabla \cdot \underline{T}_{\underline{k}} \right) dV = 0 \quad (\text{A.17})$$

and applying the axiom of continuum gives

$$\frac{\partial}{\partial t} (\rho_{\underline{k-k}} \underline{v}_{\underline{k-k}}) + \nabla \cdot \rho_{\underline{k-k}} \underline{v}_{\underline{k-k}} \underline{v}_{\underline{k-k}} - \rho_{\underline{k-B}} \underline{F} - \nabla \cdot \underline{T}_{\underline{k}} = 0 \quad (\text{A.18})$$

which is the local instantaneous momentum conservation equation.

A.2.4 Momentum Jump Condition

Using a development analogous to that for the mass jump condition of Sec. A.2.2 gives, from Eq. (A.15), the integral interface momentum balance

$$\sum_k \int_{A_i(t)} \left(\rho_{\underline{k-k}} \underline{v}_{\underline{k-k}} (\underline{v}_{\underline{k}} - \underline{v}_i) \cdot \underline{n}_{\underline{k}} - \underline{n}_{\underline{k}} \cdot \underline{T}_{\underline{k}} + 2H_{21} \sigma \underline{n}_1 \right) dA = 0 \quad (\text{A.19})$$

or

$$\sum_k \left(\rho_{\underline{k-k}} \underline{v}_{\underline{k-k}} (\underline{v}_{\underline{k}} - \underline{v}_i) \cdot \underline{n}_{\underline{k}} - \underline{n}_{\underline{k}} \cdot \underline{T}_{\underline{k}} \right) = 2H_{21} \sigma \underline{n}_1 \quad (\text{A.20})$$

A.2.5 Summary

$$\frac{\partial \rho_k}{\partial t} + \nabla \cdot \rho_k \underline{v}_k = 0 \quad (\text{A.10})$$

$$\frac{\partial}{\partial t} (\rho_k \underline{v}_k) + \nabla \cdot \rho_k \underline{v}_k \underline{v}_k - \rho_k \underline{F}_B - \nabla \cdot \underline{T}_k = 0 \quad (\text{A.18})$$

$$\sum_k \rho_k (\underline{v}_k - \underline{v}_i) \cdot \underline{n}_k = 0 \quad (\text{A.12})$$

$$\sum_k (\rho_k \underline{v}_k (\underline{v}_k - \underline{v}_i) \cdot \underline{n}_k - \underline{n}_k \cdot \underline{T}_k) = 2H_{21} \sigma \underline{n}_1 \quad (\text{A.20})$$

A.3 Local Time-Averaged Conservation Equations

The local instantaneous conservation equations are time-averaged to transform a set of equations which are alternately applicable at a point to a set which are continuously valid at the same point. This is done by defining new state variables which have the complicated two-phase and turbulent fluctuations smoothed out.

A.3.1 Time-Averaging Definitions and Theorems

Consider a phase density function χ_k defined by

$$\chi_k = \begin{cases} 1 & \text{for the point occupied by phase } k \\ 0 & \text{otherwise} \end{cases}$$

Then the averaging time interval Δt is comprised of piecewise time intervals in each phase and the total time interval in phase k is defined as

$$\Delta t_k \stackrel{\Delta}{=} \int_{\Delta t} \chi_k dt \quad (\text{A.22})$$

Now we define the weighted time-average of function f_k by weighting variable w as

$$\overline{f}_k^w \stackrel{\Delta}{=} \frac{\int_{\Delta t} f_k w dt}{\int_{\Delta t} w dt} \quad (\text{A.23})$$

We also define the specific weighted averages

$$\bar{f}_k \triangleq \frac{\Delta}{\bar{f}_k} \bar{X}_k = \frac{\int_{\Delta t} f_k X_k dt}{\int_{\Delta t} X_k dt} = \frac{\overline{f_k X_k}}{\overline{X_k}} \quad (\text{A.24})$$

$$\bar{f}_k \triangleq \frac{\Delta}{\bar{f}_k} \bar{X}_k \bar{\rho}_k = \frac{\int_{\Delta t} f_k \rho_k X_k dt}{\int_{\Delta t} \rho_k X_k dt} = \frac{\overline{f_k \rho_k}}{\overline{\rho_k}} \quad (\text{A.25})$$

and

$$\alpha_k \triangleq \frac{\Delta}{\bar{X}_k} = \frac{1}{\Delta t} \int_{\Delta t} X_k dt = \frac{\Delta t_k}{\Delta t} \quad (\text{A.26})$$

Finally we rewrite the mathematical theorems for the limiting case of a piecewise line integral. Leibnitz's Rule becomes

$$\int_{\Delta t_k} \frac{\partial f_k}{\partial t} dt = \frac{\partial}{\partial t} \int_{\Delta t_k} f_k dt - \sum_j \frac{1}{|\underline{v}_{-i} \cdot \underline{n}_k|} f_{k-i} \underline{n}_k \quad (\text{A.27})$$

and Gauss' Theorem becomes

$$\int_{\Delta t_k} \nabla \cdot f_k dt = \nabla \cdot \int_{\Delta t} f_k dt + \sum_j \frac{1}{|\underline{v}_{-i} \cdot \underline{n}_k|} \underline{n}_k \cdot f_k \quad (\text{A.28})$$

where j denotes the discontinuities in Δt as shown in Fig. A.2.

A.3.2 Time-Averaged Mass Equation

We start with the local instantaneous k -phase equation, Eq. (A.10), and integrate it over the relevant time interval Δt_k

$$\int_{\Delta t_k} \frac{\partial \rho_k}{\partial t} dt + \int_{\Delta t_k} \nabla \cdot \rho_k \underline{v}_{k-k} dt = 0 \quad (\text{A.29})$$

Then using Leibnitz's Rule and Gauss' Theorem to interchange the integration and differentiation, yields

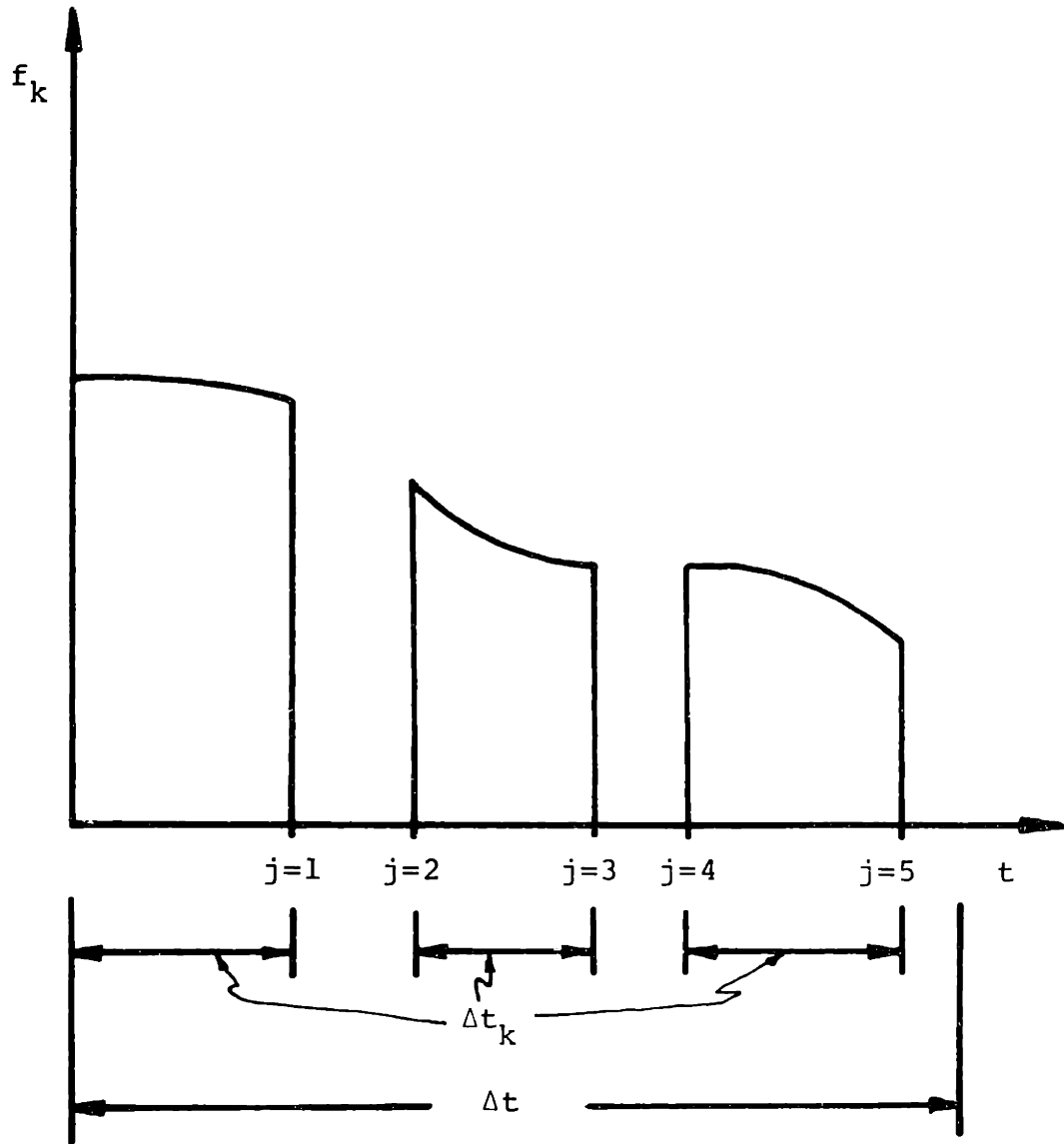


Figure A.2 Time interval definition.

$$\begin{aligned} \frac{\partial}{\partial t} \int_{\Delta t_k} \rho_k dt - \sum_j \frac{1}{|\underline{v}_i \cdot \underline{n}_k|} \rho_k \underline{v}_i \cdot \underline{n}_k + \nabla \cdot \int_{\Delta t_k} \rho_k \underline{v}_k dt \\ + \sum_j \frac{1}{|\underline{v}_i \cdot \underline{n}_k|} \rho_k \underline{v}_k \cdot \underline{n}_k = 0 \end{aligned} \quad (\text{A.30})$$

Next multiplying by $\Delta t_k / (\Delta t_k \cdot \Delta t)$ gives

$$\begin{aligned} \frac{\partial}{\partial t} \left[\frac{\Delta t_k}{\Delta t} \frac{1}{\Delta t_k} \int_{\Delta t_k} \rho_k dt \right] + \nabla \cdot \left[\frac{\Delta t_k}{\Delta t} \frac{1}{\Delta t_k} \int_{\Delta t_k} \rho_k \underline{v}_k dt \right] \\ + \sum_j \frac{1}{|\underline{v}_i \cdot \underline{n}_k| \Delta t} \rho_k (\underline{v}_k - \underline{v}_i) \cdot \underline{n}_k = 0 \end{aligned} \quad (\text{A.31})$$

Finally using the definitions of Sec. A.3.1 and the definition of the interfacial mass source

$$\Gamma_k \triangleq - \sum_j \frac{\rho_k (\underline{v}_k - \underline{v}_i) \cdot \underline{n}_k}{\ell_j} \quad (\text{A.32})$$

where

$$\ell_j \triangleq \Delta t |\underline{v}_i \cdot \underline{n}_k|_j \quad (\text{A.33})$$

is the line coordinate length (surface area concentration) of discontinuity j ; Eq. (A.31) reduces to the time-averaged mass equation

$$\frac{\partial}{\partial t} (\alpha_k \bar{\rho}_k) + \nabla \cdot (\alpha_k \bar{\rho}_k \bar{\underline{v}}_k) = \Gamma_k \quad (\text{A.34})$$

A.3.3 Time-Averaged Mass Jump Condition

Dividing the local jump condition Eq. (A.12) by the local line coordinate length and summing over all discontinuities, j , in time interval Δt gives

$$\sum_k \sum_j \frac{\rho_k (\underline{v}_k - \underline{v}_i) \cdot \underline{n}_k}{\ell_k} = 0 \quad (\text{A.35})$$

Substituting in Eq. (A.32) gives the time-averaged jump condition

$$\sum_k \Gamma_k = 0 \quad (\text{A.36})$$

A.3.4 Time-Averaged Momentum Equation

Following the same steps as performed with the mass equation we first integrate Eq. (A.18) over the time interval Δt_k

$$\int_{\Delta t_k} \frac{\partial}{\partial t} (\rho_{k \rightarrow k} \underline{v}_k) dt + \int_{\Delta t_k} \nabla \cdot \rho_{k \rightarrow k} \underline{v}_k \underline{v}_k dt - \int_{\Delta t_k} \rho_{k \rightarrow B} \underline{F} dt - \int_{\Delta t_k} \nabla \cdot \underline{T}_{\equiv k} dt = 0 \quad (\text{A.37})$$

Then applying the line integral forms of Leibnitz's Rule and Gauss' Theorem gives

$$\begin{aligned} & \frac{\partial}{\partial t} \int_{\Delta t_k} \rho_{k \rightarrow k} \underline{v}_k dt - \sum_j \frac{1}{|\underline{v}_j \cdot \underline{n}_k|} \rho_{k \rightarrow k} \underline{v}_k \cdot \underline{n}_k + \nabla \cdot \int_{\Delta t_k} \rho_{k \rightarrow k} \underline{v}_k \underline{v}_k dt \\ & + \sum_j \frac{1}{|\underline{v}_j \cdot \underline{n}_k|} \rho_{k \rightarrow k} \underline{v}_k \underline{v}_k \cdot \underline{n}_k - \int_{\Delta t_k} \rho_{k \rightarrow B} \underline{F} dt - \nabla \cdot \int_{\Delta t_k} \underline{T}_{\equiv k} dt \\ & - \sum_j \frac{1}{|\underline{v}_j \cdot \underline{n}_k|} \underline{n}_k \cdot \underline{T}_{\equiv k} = 0 \end{aligned} \quad (\text{A.38})$$

Multiplying by $\Delta t_k / (\Delta t_k \cdot \Delta t)$ and substituting in the definitions of Sec. A.3.1 gives

$$\begin{aligned} & \frac{\partial}{\partial t} (\alpha_k \bar{\rho}_{k \rightarrow k} \bar{\underline{v}}_k) + \nabla \cdot (\alpha_k \overline{\rho_{k \rightarrow k} \underline{v}_k \underline{v}_k}) - \alpha_k \bar{\rho}_{k \rightarrow B} \bar{\underline{F}} \\ & - \nabla \cdot (\alpha_k \bar{\underline{T}}_{\equiv k}) + \sum_j \frac{1}{\ell_j} [\rho_{k \rightarrow k} (\underline{v}_k - \underline{v}_j) \cdot \underline{n}_k - \underline{n}_k \cdot \underline{T}_{\equiv k}] = 0 \end{aligned} \quad (\text{A.39})$$

Next we break the second term up into variables which already appear in the other terms, and a covariance term.

The quantity $\overline{\rho_{k \rightarrow k} \underline{v}_k \underline{v}_k}$ is divided into a mean and fluctuating component by using the definition of the velocity fluctuation \underline{v}_k'

$$\underline{v}_k = \bar{\underline{v}}_k + \underline{v}_k' \quad (\text{A.40})$$

Substituting in gives

$$\overline{\rho_{k \rightarrow k} \underline{v} \underline{v}} = \overline{\rho_{k \rightarrow k} \underline{v} \underline{v}} + 2 \overline{\rho_{k \rightarrow k} \underline{v} \underline{v}'} + \overline{\rho_{k \rightarrow k} \underline{v}' \underline{v}'} \quad (\text{A.41})$$

Noting that \underline{v}_k is constant to further time averaging and $\overline{\rho_{k \rightarrow k} \underline{v}' \underline{v}'}$ is zero, yields

$$\overline{\rho_{k \rightarrow k} \underline{v} \underline{v}} = \overline{\rho_{k \rightarrow k} \underline{v} \underline{v}} + \overline{\rho_{k \rightarrow k} \underline{v}' \underline{v}'} \quad (\text{A.42})$$

Finally defining

$$\underline{T}_k^T \triangleq - \overline{\rho_{k \rightarrow k} \underline{v}' \underline{v}'} \quad (\text{A.43})$$

$$\underline{M}_k \triangleq - \sum_j \frac{1}{\ell_j} [\rho_{k \rightarrow k} (\underline{v}_k - \underline{v}_i) \cdot \underline{n}_k - \underline{n}_k \cdot \underline{T}_k^T] \quad (\text{A.44})$$

and substituting Eq. (A.42) through (A.44) into Eq. (A.39) gives the time-averaged momentum equation

$$\begin{aligned} \frac{\partial}{\partial t} (\alpha_k \overline{\rho_{k \rightarrow k} \underline{v}}) + \nabla \cdot (\alpha_k \overline{\rho_{k \rightarrow k} \underline{v} \underline{v}}) - \alpha_k \overline{\rho_{k \rightarrow B} \underline{F}} \\ - \nabla \cdot (\alpha_k (\underline{T}_k^T + \underline{T}_k)) = \underline{M}_k \end{aligned} \quad (\text{A.45})$$

A.3.5 Time-Averaged Momentum Jump Condition

Taking the local momentum jump condition Eq. (A.20), dividing by the local line coordinate length, and summing over all discontinuities gives

$$\sum_k \sum_j \frac{1}{\ell_j} [\rho_{k \rightarrow k} (\underline{v}_k - \underline{v}_i) \cdot \underline{n}_k - \underline{n}_k \cdot \underline{T}_k^T] = \sum_j \frac{1}{\ell_j} 2H_{21} \sigma \underline{n}_1 \quad (\text{A.46})$$

Defining the mixture momentum source \underline{M}_m , as

$$\underline{M}_m \triangleq \sum_j \frac{1}{\ell_j} 2H_{21} \sigma \underline{n}_1 \quad (\text{A.47})$$

and using Eq. (A.44) gives the time-averaged momentum jump condition

$$\sum_k \underline{M}_k = \underline{M}_m \quad (\text{A.48})$$

A.3.6 Summary

We have now transformed instantaneous conservation equations which were valid only in the piecewise time interval Δt_k , into continuously valid, time-averaged equations by introducing new time-averaged state variables, a topological variable α_k , and several new constitutive variables. In summary

$$\frac{\partial}{\partial t} (\alpha_k \bar{\rho}_k) + \nabla \cdot (\alpha_k \bar{\rho}_k \underline{\tilde{v}}_k) = \Gamma_k \quad (\text{A.34})$$

$$\frac{\partial}{\partial t} (\alpha_k \bar{\rho}_k \underline{\tilde{v}}_k) + \nabla \cdot (\alpha_k \bar{\rho}_k \underline{\tilde{v}}_k \underline{\tilde{v}}_k) - \alpha_k \bar{\rho}_k \underline{\tilde{F}}_{k-B} \quad (\text{A.45})$$

$$- \nabla \cdot (\alpha_k \underline{\tilde{T}}_k + \underline{\tilde{T}}_k) = \underline{M}_k$$

$$\sum_k \Gamma_k = 0 \quad (\text{A.36})$$

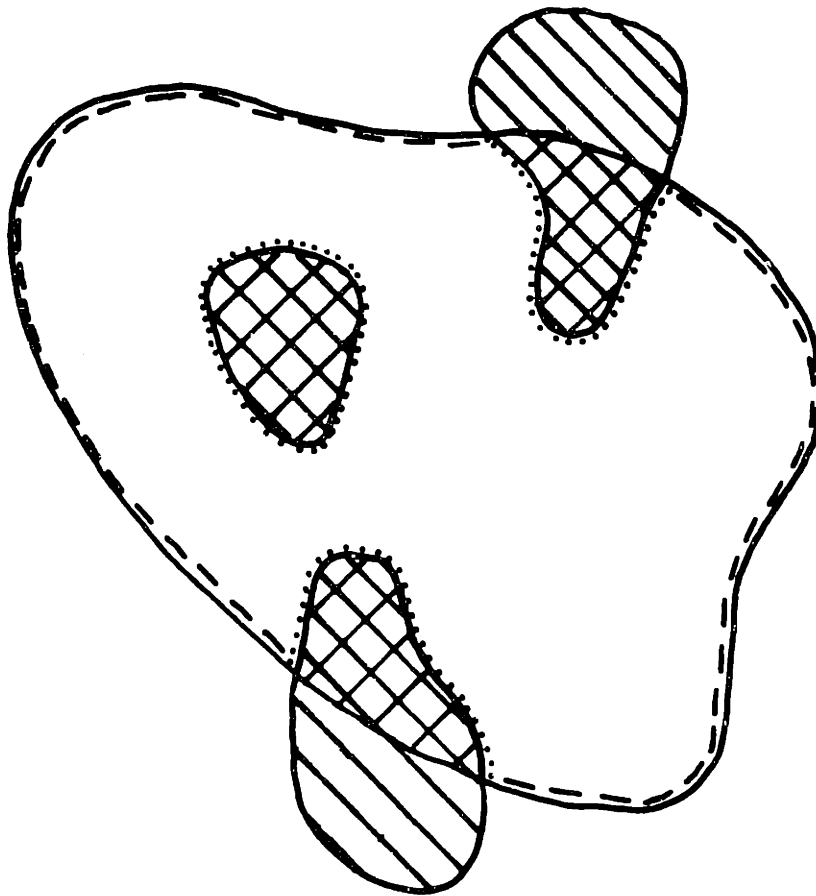
$$\sum_k \underline{M}_k = \underline{M}_m \quad (\text{A.48})$$

and the closure condition is

$$\sum_k \alpha_k = 1 \quad (\text{A.49})$$

A.4 Time/Volume-Averaged Conservation Equations

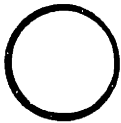
The local, time-averaged equations are now averaged over a fixed geometric volume, V . The volume shall consist of a fluid volume V_f , made up of two phases, and a nondeformable solid volume V_s , as shown in Fig. A.3. The inclusion of solids in the control volume will allow the resulting spatially averaged equations to be applied in porous medium situations.



Nondeformable
Solid



Solid Volume
 V_s



Fluid Volume V_f
(Both phases coexist
in V_f over time.)

----- Fluid-Fluid
Area A_{ff}

..... Fluid-Solid
Area A_{fs}

$$V = V_f + V_s$$

$$A = A_{ff} + A_{fs}$$

Figure A.3 Stationary spatial averaging control volume.

A.4.1 Volume-Averaging Definitions and Theorems

We define the weighted fluid volume average of function f_k by variable w , as

$$\langle f_k \rangle_w \triangleq \frac{\int_{V_f} f_k w \, dV}{\int_{V_f} w \, dV} \quad (\text{A.50})$$

We also define the specific weighted averages

$$\langle\langle f_k \rangle\rangle \triangleq \langle f_k \rangle_{\alpha_k} = \frac{\int_{V_f} \alpha_k f_k \, dV}{\int_{V_f} \alpha_k \, dV} = \frac{\langle \alpha_k f_k \rangle}{\langle \alpha_k \rangle} \quad (\text{A.51})$$

$$\{f_k\} \triangleq \langle f_k \rangle_{\alpha_k \rho_k} = \frac{\int_{V_f} \alpha_k \bar{\rho}_k f_k \, dV}{\int_{V_f} \alpha_k \bar{\rho}_k \, dV} = \frac{\langle\langle \bar{\rho}_k f_k \rangle\rangle}{\langle\langle \bar{\rho}_k \rangle\rangle} \quad (\text{A.52})$$

The volume porosity is defined as

$$\gamma_v \triangleq \frac{\int_{V_f} dV}{\int_V dV} = \frac{V_f}{V} \quad (\text{A.53})$$

Surface averages analogous to the volume averages, are defined:

$$\{f_k\}_w^j \triangleq \frac{\int_{A_j} w f_k \cdot \underline{n}_k \, dA}{\int_{A_j} w \cdot \underline{n}_k \, dA} \quad (\text{A.54})$$

$$\{\{f_k\}\}^j \triangleq \{f_k\}_{\alpha_k}^j = \frac{\int_{A_j} \alpha_k f_k \cdot \underline{n}_k \, dA}{\int_{A_j} \alpha_k \cdot \underline{n}_k \, dA} = \frac{\{\alpha_k f_k\}^j}{\{\alpha_k\}^j} \quad (\text{A.55})$$

$$\left\{ \left\{ f_k \right\} \right\}^j \triangleq \left\{ f_k \right\}_{\alpha_k \rho_k}^j = \frac{\int_{A_j} \alpha_k \rho_k f_k \cdot \underline{n}_k dA}{\int_{A_j} \alpha_k \rho_k \cdot \underline{n}_k dA} = \frac{\left\{ \left\{ \rho_k f_k \right\} \right\}^j}{\left\{ \left\{ \rho_k \right\} \right\}^j} \quad (\text{A.56})$$

where the superscript j denotes the area of integration (i.e., $j=ff$ for fluid-fluid or $j=fs$ for fluid-solid). The surface porosity is defined by

$$\gamma_A^j \triangleq \frac{\int_{A_j} dA}{\int_A dA} = \frac{A_j}{A} \quad (\text{A.57})$$

Leibnitz's Rule for a stationary fluid volume V_f , becomes

$$\frac{\partial}{\partial t} \int_{V_f} f_k dV = \int_{V_f} \frac{\partial f_k}{\partial t} dV \quad (\text{A.58})$$

Gauss' Theorem when partitioned into the fluid-fluid and fluid-solid boundary areas, A_{ff} and A_{fs} respectively, becomes

$$\int_{V_f} \nabla \cdot f_k dV = \nabla \cdot \int_{V_f} f_k dV + \int_{A_{fs}} \underline{n}_k \cdot f_k dA \quad (\text{A.59})$$

A.4.2 Time/Volume-Averaged Mass Equation

The local, time-averaged mass equation for phase k , Eq. (A.34), is integrated over the fluid volume. The time averaging makes the equation valid throughout the entire fluid volume

$$\int_{V_f} \frac{\partial}{\partial t} (\alpha_k \bar{\rho}_k) dV + \int_{V_f} \nabla \cdot (\alpha_k \bar{\rho}_k \bar{\underline{v}}_k) dV = \int_{V_f} \Gamma_k dV \quad (\text{A.60})$$

The time averaging makes each phasic equation valid over the entire fluid volume for all time. Now using the mathematical theorems, Eq. (A.58) and Eq. (A.59), Eq. (A.60) becomes

$$\begin{aligned} \frac{\partial}{\partial t} \int_{V_f} \alpha_k \bar{\rho}_k dV + \nabla \cdot \int_{V_f} \alpha_k \bar{\rho}_k \tilde{\mathbf{v}}_k dV + \int_{A_{fs}} \alpha_k \bar{\rho}_k \tilde{\mathbf{v}}_k \cdot \mathbf{n}_k dV \\ = \int_{V_f} \Gamma_k dV \end{aligned} \quad (\text{A.61})$$

Noting that the phase velocity $\tilde{\mathbf{v}}_k$ across the solid boundary A_{fs} is zero and multiplying by the constant $V_f/(V_f \cdot V)$, gives

$$\frac{\partial}{\partial t} \left[\frac{V_f}{V} \frac{1}{V_f} \int_{V_f} \alpha_k \bar{\rho}_k dV \right] + \nabla \cdot \left[\frac{V_f}{V} \frac{1}{V_f} \int_{V_f} \alpha_k \bar{\rho}_k \tilde{\mathbf{v}}_k dV \right] = \frac{V_f}{V} \frac{1}{V_f} \int_{V_f} \Gamma_k dV \quad (\text{A.62})$$

Finally implementing the definitions of the previous section gives the time/volume-averaged mass equation

$$\frac{\partial}{\partial t} [\gamma_v \langle \alpha_k \rangle \langle \langle \bar{\rho}_k \rangle \rangle] + \nabla \cdot [\gamma_v \langle \alpha_k \rangle \langle \langle \bar{\rho}_k \rangle \rangle \langle \tilde{\mathbf{v}}_k \rangle] = \gamma_v \langle \Gamma_k \rangle \quad (\text{A.63})$$

A.4.3 Time/Volume-Averaged Mass Jump Condition

Integrating Eq. (A.36) over the fluid volume simply gives

$$\sum_k \langle \Gamma_k \rangle = 0 \quad (\text{A.64})$$

A.4.4 Time/Volume-Averaged Momentum Equation

Following the same procedure as for the mass equation, the time-averaged momentum equation Eq. (A.45) is integrated over V_f

$$\begin{aligned} \int_{V_f} \frac{\partial}{\partial t} (\alpha_k \bar{\rho}_k \tilde{\mathbf{v}}_k) dV + \int_{V_f} \nabla \cdot (\alpha_k \bar{\rho}_k \tilde{\mathbf{v}}_k \tilde{\mathbf{v}}_k) dV - \int_{V_f} \alpha_k \bar{\rho}_k \tilde{\mathbf{F}}_k dV \\ - \int_{V_f} \nabla \cdot (\alpha_k (\bar{\mathbf{T}}_k + \mathbf{T}_k^T)) dV = \int_{V_f} \underline{\underline{M}}_k dV \end{aligned} \quad (\text{A.65})$$

Then using the mathematical theorems and multiplying by $V_f/(V_f \cdot V)$,

yields

$$\begin{aligned}
& \frac{\partial}{\partial t} \left[\frac{V_f}{V} \frac{1}{V_f} \int_{V_f} \alpha_k \bar{\rho}_k \bar{v}_k \bar{v}_k dV \right] + \nabla \cdot \left[\frac{V_f}{V} \frac{1}{V_f} \int_{V_f} \alpha_k \bar{\rho}_k \bar{v}_k \bar{v}_k dV \right] \\
& \frac{V_f}{V} \frac{1}{V_f} \int_{A_{fs}} \alpha_k \bar{\rho}_k \bar{v}_k \bar{v}_k \cdot \underline{n}_k dA - \frac{V_f}{V} \frac{1}{V_f} \int_{V_f} \alpha_k \bar{\rho}_k \bar{F}_{k-B} dV \\
& - \nabla \cdot \left[\frac{V_f}{V} \frac{1}{V_f} \int_{V_f} (\alpha_k (\bar{T}_{k=k} + \underline{T}_{k=k}^T)) dV \right] - \frac{V_f}{V} \frac{1}{V_f} \int_{A_{fs}} (\alpha_k \bar{T}_{k=k} \cdot \underline{n}_k + \underline{T}_{k=k}^T \cdot \underline{n}_k) dA \\
& \quad \cdot \\
& \quad = \frac{V_f}{V} \frac{1}{V_f} \int_{V_f} \underline{M}_k dV \tag{A.66}
\end{aligned}$$

However the terms $\bar{v}_k \cdot \underline{n}_k$ and $\underline{T}_{k=k}^T \cdot \underline{n}_k$ are zero on the fluid-solid boundaries. Now we define the momentum covariance coefficient tensor \underline{C}_{mk} as

$$\underline{C}_{mk} \{ \bar{v}_k \} \{ \bar{v}_k \} = \{ \bar{v}_k \bar{v}_k \} \tag{A.67}$$

and define the volumetric flow resistance $\langle \underline{R}_k \rangle$ by

$$\gamma_v \langle \underline{R}_k \rangle \triangleq - \frac{V_f}{V} \frac{1}{V_f} \int_{A_{fs}} \alpha_k \bar{T}_{k=k} \cdot \underline{n}_k dA = - \frac{A}{V} \gamma_A^{fs} \{ \alpha_k \}^{fs} \{ \{ \bar{T}_{k=k} \} \}^{fs} \tag{A.68}$$

Substituting in the above equations and using the definitions of Sec.

A.4.1 gives the time/volume-averaged momentum equation

$$\begin{aligned}
& \frac{\partial}{\partial t} [\gamma_v \langle \alpha_k \rangle \langle \langle \bar{\rho}_k \rangle \rangle \{ \bar{v}_k \}] + \nabla \cdot [\gamma_v \underline{C}_{km} \langle \alpha_k \rangle \langle \langle \bar{\rho}_k \rangle \rangle \{ \bar{v}_k \} \{ \bar{v}_k \}] \\
& - \gamma_v \langle \alpha \rangle \langle \langle \bar{\rho}_k \rangle \rangle \{ \bar{F}_{k-B} \} - \nabla \cdot [\gamma_v \langle \alpha_k \rangle (\langle \langle \bar{T}_{k=k} \rangle \rangle + \langle \langle \underline{T}_{k=k}^T \rangle \rangle)] \\
& + \gamma_v \langle \underline{R}_k \rangle = \gamma_v \langle \underline{M}_k \rangle \tag{A.69}
\end{aligned}$$

A.4.5 Time/Volume-Averaged Momentum Jump Condition

Integrating Eq. (A.48) over the fluid volume results in

$$\sum_k \langle \underline{M}_k \rangle = \langle \underline{M} \rangle \quad (\text{A.70})$$

A.4.6 Summary

Through a rigorous mathematical development we have obtained a set of time/volume-averaged conservation equations of a form analogous to the local instantaneous equations, except for new definitions of the individual state variables and new constitutive variables:

$$\begin{aligned} \frac{\partial}{\partial t} [\gamma_v \langle \alpha_k \rangle \langle \langle \bar{\rho}_k \rangle \rangle] + \nabla \cdot [\gamma_v \langle \alpha_k \rangle \langle \langle \bar{\rho}_k \rangle \rangle \{ \underline{v}_k \}^{\sim}] \\ = \gamma_v \langle \Gamma_k \rangle \end{aligned} \quad (\text{A.63})$$

$$\begin{aligned} \frac{\partial}{\partial t} [\gamma_v \langle \alpha_k \rangle \langle \langle \bar{\rho}_k \rangle \rangle \{ \underline{v}_k \}^{\sim}] + \nabla \cdot [\gamma_{v=km} \langle \alpha_k \rangle \langle \langle \bar{\rho}_k \rangle \rangle \{ \underline{v}_k \}^{\sim} \{ \underline{v}_k \}^{\sim}] \\ - \gamma_v \langle \alpha_k \rangle \langle \langle \bar{\rho}_k \rangle \rangle \{ \underline{F}_k \}^{\sim} - \nabla \cdot [\gamma_v \langle \alpha_k \rangle (\langle \langle \bar{T}_k \rangle \rangle + \langle \langle \bar{T}_k^T \rangle \rangle)] \\ + \gamma_v \langle \underline{R}_k \rangle = \gamma_v \langle \underline{M}_k \rangle \end{aligned} \quad (\text{A.69})$$

$$\sum_k \langle \Gamma_k \rangle = 0 \quad (\text{A.64})$$

$$\sum_k \langle \underline{M}_k \rangle = \langle \underline{M} \rangle \quad (\text{A.70})$$

$$\sum_k \langle \alpha_k \rangle = 1 \quad (\text{A.71})$$

The involved notation has been maintained to amplify the complicated physical nature of each variable. Although these equations are mathematically exact and convenient to solve numerically, the real important task is to interpret and model the state and constitutive variables correctly. Specifically, the assumptions used in relating

these variables to measurable quantities should be carefully noted.

A.5 Time/Surface-Area-Averaged Conservation Equations

A.5.1 Conversion of Volume to Surface-Averaged Equations

An alternative form of the time/volume averaged equations can be written by using the identity

$$\nabla \cdot \int_{V_f} f_k dV = \int_{A_{ff}} f_k \cdot \underline{n}_k dA = \sum_{j=ff} \int_{A_j} f_k \cdot \underline{n}_k dA \quad (A.72)$$

which comes from comparing two forms of Gauss' Theorem, Eq. (A.2) and Eq. (A.59). Using Eq. (A.72) to eliminate the divergence terms in favor of surface variables gives

$$\frac{\partial}{\partial t} [\gamma_v \langle \alpha_k \rangle \langle \bar{\rho}_k \rangle] + \frac{A}{V} \sum_{j=ff} [\gamma_A^j \{\alpha_k\}^j \{\{\bar{\rho}_k\}\}^j \{\underline{v}_k\}^j] = \gamma_v \langle \Gamma_k \rangle \quad (A.73)$$

$$\begin{aligned} & \frac{\partial}{\partial t} [\gamma_v \langle \alpha_k \rangle \langle \bar{\rho}_k \rangle \{\underline{v}_k\}] + \frac{A}{V} \sum_{j=ff} [\gamma_A^j C_{km}^j \{\alpha_k\}^j \{\{\bar{\rho}_k\}\}^j \{\underline{v}_k\}^j \{\underline{v}_k\}^j] \\ & - \gamma_v \langle \alpha_k \rangle \langle \bar{\rho}_k \rangle \{\underline{F}_B\} - \frac{A}{V} \sum_{j=ff} [\gamma_A^j \{\alpha_k\}^j (\{\{\bar{T}_k\}\}^j + \{\{\underline{T}_k^T\}\}^j)] \\ & + \gamma_v \langle \underline{R}_k \rangle = \gamma_v \langle \underline{M}_k \rangle \end{aligned} \quad (A.74)$$

where

$$C_{km}^j \{\underline{v}_k\}^j \{\underline{v}_k\}^j = \{\underline{v}_k \underline{v}_k\}^j \quad (A.75)$$

The jump conditions, Eq. (A.64) and Eq. (A.70), remain the same and in addition to volume closure Eq. (A.71) we also have surface closure of each surface j ,

$$\sum_k \{\alpha_k\}^j = 1 \quad (A.76)$$

A.5.2 Comments on Surface-Averaged Equations

The surface-averaged equations have been used extensively for

porous medium flows by Sha [S.1, S.2]. Although both forms of the conservation equations are mathematically equivalent, in actual implementation different assumptions are required. In the volume-averaged form linear interpolation is used extensively to discretize and solve the conservation equations. All the variables are clearly defined volume averages. Local surface-averaged variables may be obtained, if desired, from the local topology and volume-averaged quantities.

In the surface-averaged form, the conservation equations can be solved exactly, giving a more detailed flow solution directly, **providing** correct relations between the volume- and surface-averaged variables are input. To relate volume and surface variables, equations describing the entire solid topology for each application are required. These equations must also be integrated into the conservation equation numerical algorithm. Because detailed solid topology equations are not readily available for most porous medium geometries, simple linear extrapolation is employed [S.3]. Using linear extrapolation simply reduces all surface quantities to volume quantities, providing the correct volume-averaged topology is input.

Currently the added detail of surface formulations for porous media cannot be fully realized, because simple porous medium topology models have not been developed. In subchannel applications where the solid topology is well-defined, surface-averaged equations are well suited. The disadvantage of using current surface-averaged formulation are that no additional physical detail is introduced while confusion about the actual physical definitions of the variable is added.

A.6 Partitioning of Constitutive Variables in the
Time/Volume-Averaged Momentum Equation

A.6.1 Total Stress Tensor

The total stress tensor for a fluid \underline{T}_k , can be divided into two parts

$$\underline{T}_k = -p_k \underline{I} + \underline{\tau}_k \quad (\text{A.77})$$

This partitioning comes from the fact that a fluid at rest cannot sustain shear and bulk stresses $\underline{\tau}_k$, so that the total stress tensor becomes a scalar quantity called the thermodynamic pressure p_k . (When the bulk stresses are zero, i.e., incompressible flow, then the average pressure which is the average of the normal stresses, reduces to the thermodynamic pressure).

Substituting Eq. (A.77) into the total stress divergence term of the momentum equation, Eq. (A.69), gives

$$\begin{aligned} \nabla \cdot [\gamma_v \langle \alpha_k \rangle (\langle \underline{T}_k \rangle + \langle \underline{\tau}_k^T \rangle)] = \nabla \cdot [\gamma_v \langle \alpha_k \rangle \langle \underline{p}_k \rangle \underline{I}] \\ + \nabla \cdot [\gamma_v \langle \alpha_k \rangle (\langle \underline{T}_k \rangle + \langle \underline{\tau}_k^T \rangle)] \end{aligned} \quad (\text{A.78})$$

A.6.2 Volumetric Flow Resistance

Using Eq. (A.77), the definition of flow resistance, Eq. (A.68), may be written

$$\gamma_v \langle \underline{R}_k \rangle = -\gamma_v \frac{1}{V_f} \int_{A_{fs}} \alpha_k (-\underline{p}_k \underline{I} + \underline{\tau}_k) \cdot \underline{n}_k dA \quad (\text{A.79})$$

The first term in the integral may be interpreted as the phasic-solid form drag and the second the skin friction.

A.6.3 Interfacial Momentum Exchange

The time/volume-averaged interfacial momentum exchange is defined

as

$$\langle \underline{M}_k \rangle \stackrel{\Delta}{=} - \frac{1}{V_f} \int \sum_j \frac{1}{V_f} [\rho_{k \rightarrow k} (\underline{v}_k - \underline{v}_i) \cdot \underline{n}_k - \underline{T}_k \cdot \underline{n}_k] dV \quad (\text{A.80})$$

Using the commutative property of time/volume averaging operations [B.5, pg. 1-62], Eq. (A.80) can be also written

$$\langle \underline{M}_k \rangle = - \frac{1}{\Delta t} \int \frac{1}{\Delta t} \int \frac{1}{V_f} \int_{A_i} [\rho_{k \rightarrow k} (\underline{v}_k - \underline{v}_i) \cdot \underline{n}_k - \underline{T}_k \cdot \underline{n}_k] dA dt \quad (\text{A.81})$$

We define the momentum exchange due to mass transfer $\langle \underline{M}_k^\Gamma \rangle$ as

$$\langle \underline{M}_k^\Gamma \rangle \stackrel{\Delta}{=} - \frac{1}{\Delta t} \int \frac{1}{\Delta t} \int \frac{1}{V_f} \int_{A_i} \rho_{k \rightarrow k} (\underline{v}_k - \underline{v}_i) \cdot \underline{n}_k dA dt \quad (\text{A.82})$$

Substituting Eq. (A.77) and (A.82) into Eq. (A.81) gives

$$\langle \underline{M}_k \rangle = \langle \underline{M}_k^\Gamma \rangle + \frac{1}{\Delta t} \int \frac{1}{\Delta t} \int \frac{1}{V_f} \int_{A_i} (-p_k \underline{I} + \underline{T}_k) \cdot \underline{n}_k dA dt \quad (\text{A.83})$$

Next we add and subtract $\langle \langle \bar{p}_k \rangle \rangle$ and $\{\{\bar{p}_k\}\}^i$ to p_k and note that the two averaged terms are constant to further averaging

$$\begin{aligned} \langle \underline{M}_k \rangle &= \langle \underline{M}_k^\Gamma \rangle + \frac{1}{\Delta t} \int \frac{1}{\Delta t} \int \frac{1}{V_f} \int_{A_i} [(\{\{\bar{p}_k\}\}^i - p_k) \underline{I} + \underline{T}_k] \cdot \underline{n}_k dA dt \\ &+ \frac{1}{\Delta t} \int \frac{1}{\Delta t} \int \frac{1}{V_f} \int_{A_i} [\langle \langle \bar{p}_k \rangle \rangle - \{\{\bar{p}_k\}\}^i - \langle \langle \bar{p}_k \rangle \rangle] \underline{I} \cdot \underline{n}_k dA dt \end{aligned} \quad (\text{A.84})$$

Finally using the identity from Gauss' Theorem

$$\gamma_v \frac{1}{V_f} \int_{A_{fs}} \underline{I} \cdot \underline{n}_k dA = -\nabla \gamma_v \quad (\text{A.85})$$

the commutative property of time and volume averaging, and the definitions

$$\Delta p_k^i \stackrel{\Delta}{=} \frac{\langle \alpha_k \bar{p}_k \rangle}{\langle \alpha_k \rangle} - \frac{\{\alpha_k \bar{p}_k\}^i}{\{\alpha_k\}^i} = \langle \langle \bar{p}_k \rangle \rangle - \{\{\bar{p}_k\}\}^i \quad (\text{A.86})$$

and

$$\langle \underline{M}_k^d \rangle \stackrel{\Delta}{=} \frac{1}{\Delta t} \int \frac{1}{V_f} \int_{A_i} [(\{\{\bar{p}_k\}\}^i - p_k) \underline{I} + \underline{\tau}_k] \cdot \underline{n}_k dA dt \quad (\text{A.87})$$

gives

$$\gamma_v \langle \underline{M}_k \rangle = \gamma_v \langle \underline{M}_k^\Gamma \rangle + \gamma_v \langle \underline{M}_k^d \rangle - \gamma_v \Delta p_k^i \nabla \langle \alpha_k \rangle + \gamma_v \langle \langle \bar{p}_k \rangle \rangle \nabla \langle \alpha_k \rangle \quad (\text{A.88})$$

The total interfacial momentum exchange has been partitioned into:

$\langle \underline{M}_k^\Gamma \rangle$ --mass transfer momentum exchange; $\langle \underline{M}_k^d \rangle$ --steady state

drag forces plus transient virtual mass and Basset forces;

Δp_k^i --momentum exchange due to pressure variations between the bulk

and interface; and the last term is the force due to changes in void distribution.

A.6.3 Summary

Substituting the two partitioned terms, Eqs. (A.78) and (A.88), into Eq. (A.69) and combining the average pressure terms gives the new time/volume-averaged momentum equation

$$\begin{aligned} \frac{\partial}{\partial t} [\gamma_v \langle \alpha_k \rangle \langle \langle \bar{\rho}_k \rangle \rangle \langle \underline{v}_k \rangle] + \nabla \cdot [\gamma_{v=km} \langle \alpha_k \rangle \langle \langle \bar{\rho}_k \rangle \rangle \langle \underline{v}_k \rangle \langle \underline{v}_k \rangle] \\ - \gamma_v \langle \alpha_k \rangle \langle \langle \bar{\rho}_k \rangle \rangle \langle \underline{F}_B \rangle - \nabla \cdot [\gamma_v \langle \alpha_k \rangle (\langle \langle \bar{\tau}_k \rangle \rangle + \langle \langle \bar{\tau}_k^T \rangle \rangle)] \\ + \langle \alpha_k \rangle \nabla \cdot [\gamma_v \langle \langle \bar{p}_k \rangle \rangle] + \gamma_v \langle \underline{R}_k \rangle = \gamma_v \langle \underline{M}_k^\Gamma \rangle \\ + \gamma_v \langle \underline{M}_k^d \rangle - \gamma_v \Delta p_k^i \nabla \langle \alpha_k \rangle \end{aligned} \quad (\text{A.89})$$

APPENDIX B
TEST ASSEMBLY BLUEPRINTS

Figures B.1 through B.7 detail the dimensions and assembly of the four experimental test sections. Figures B.8 through B.11 show the test duct and flow diffuser/straightener. Figure B.12 shows the round calibration tube.

The dimensions in all the figures are given in inches (1 inch = 2.54 centimeters).

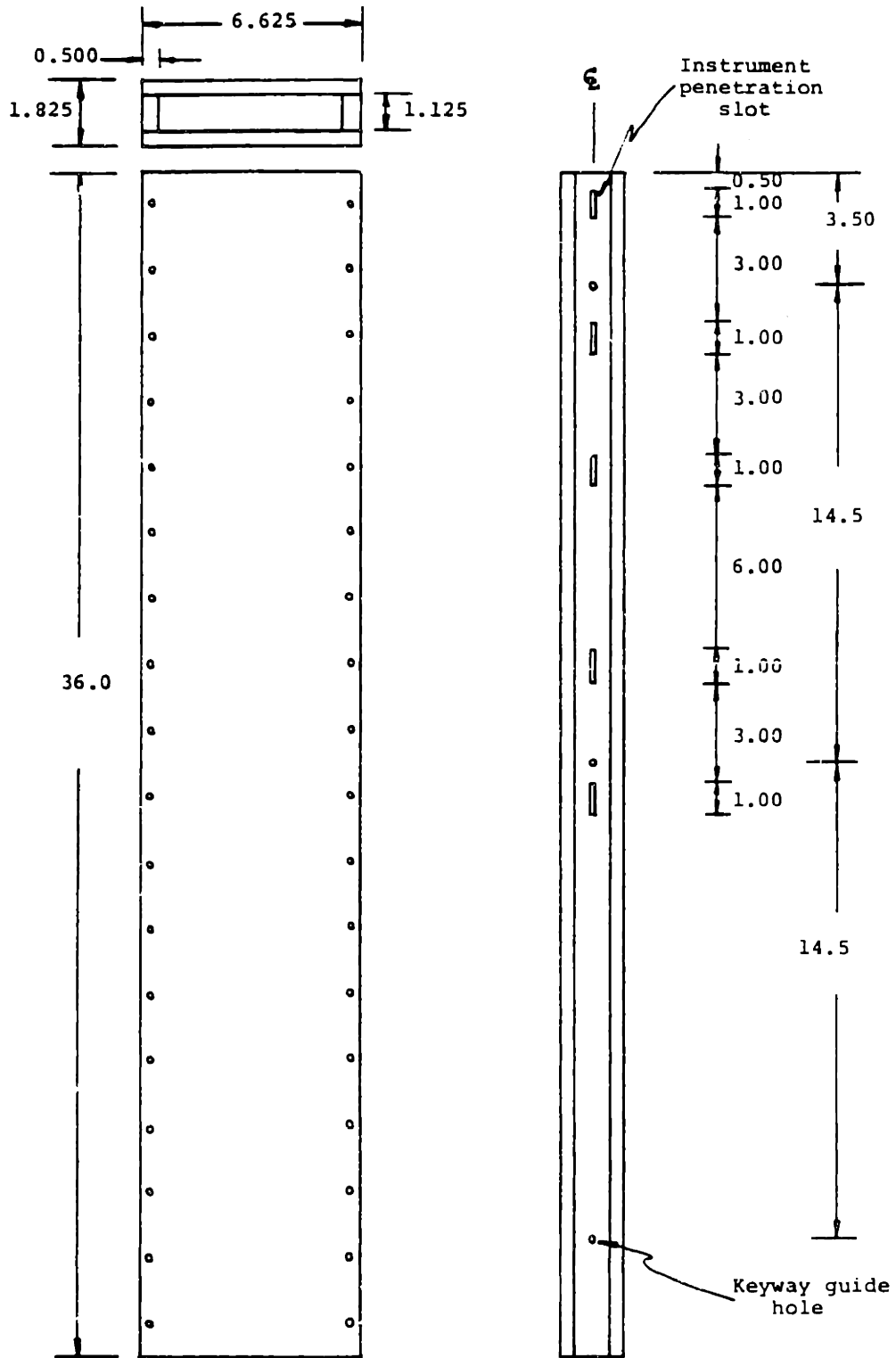


Figure B.1 Test section isometric.

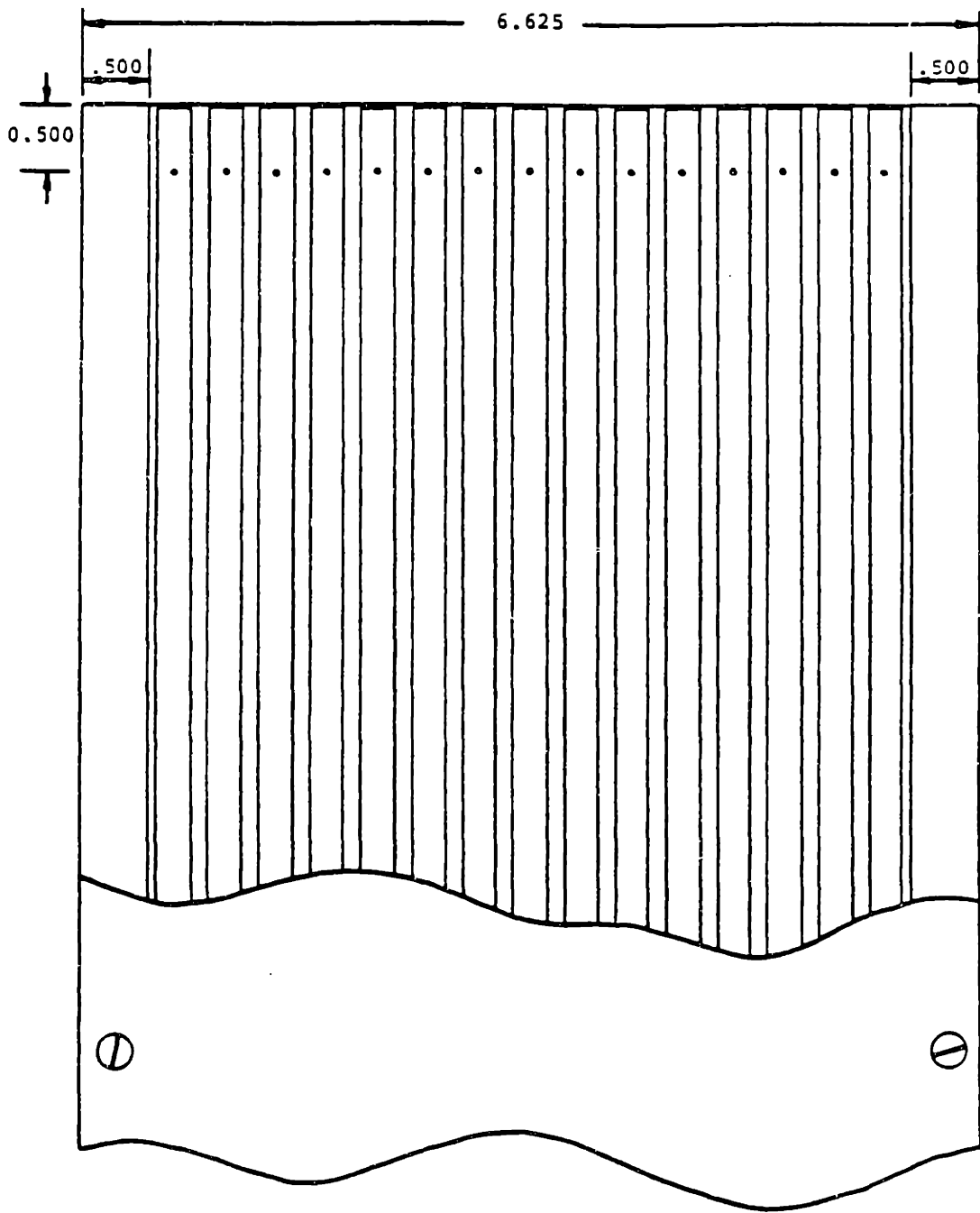


Figure B.2 Parallel test section--cutaway side view.

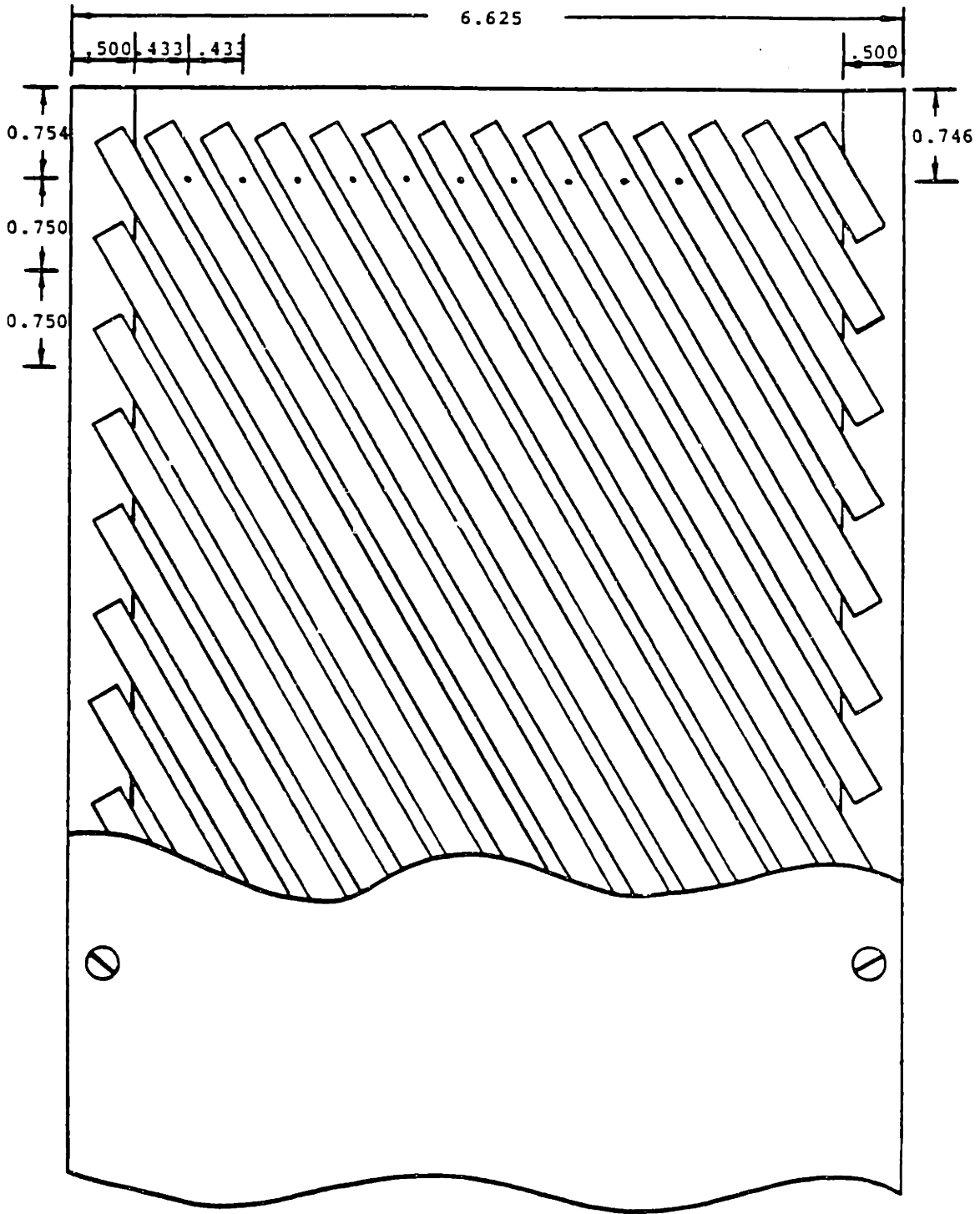


Figure B.3 30 degree test section--cutaway side view.

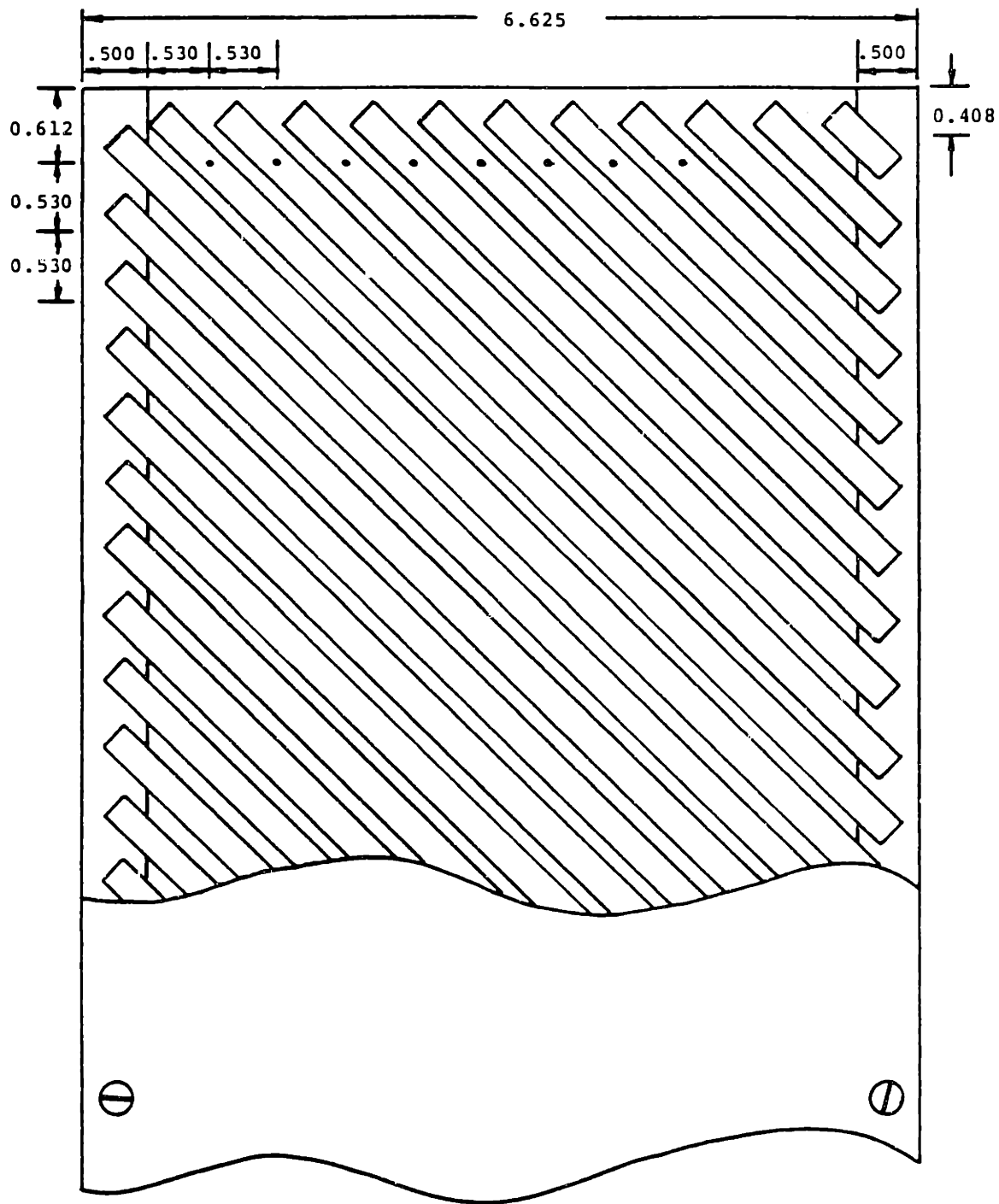


Figure B.4 45 degree test section--cutaway side view.

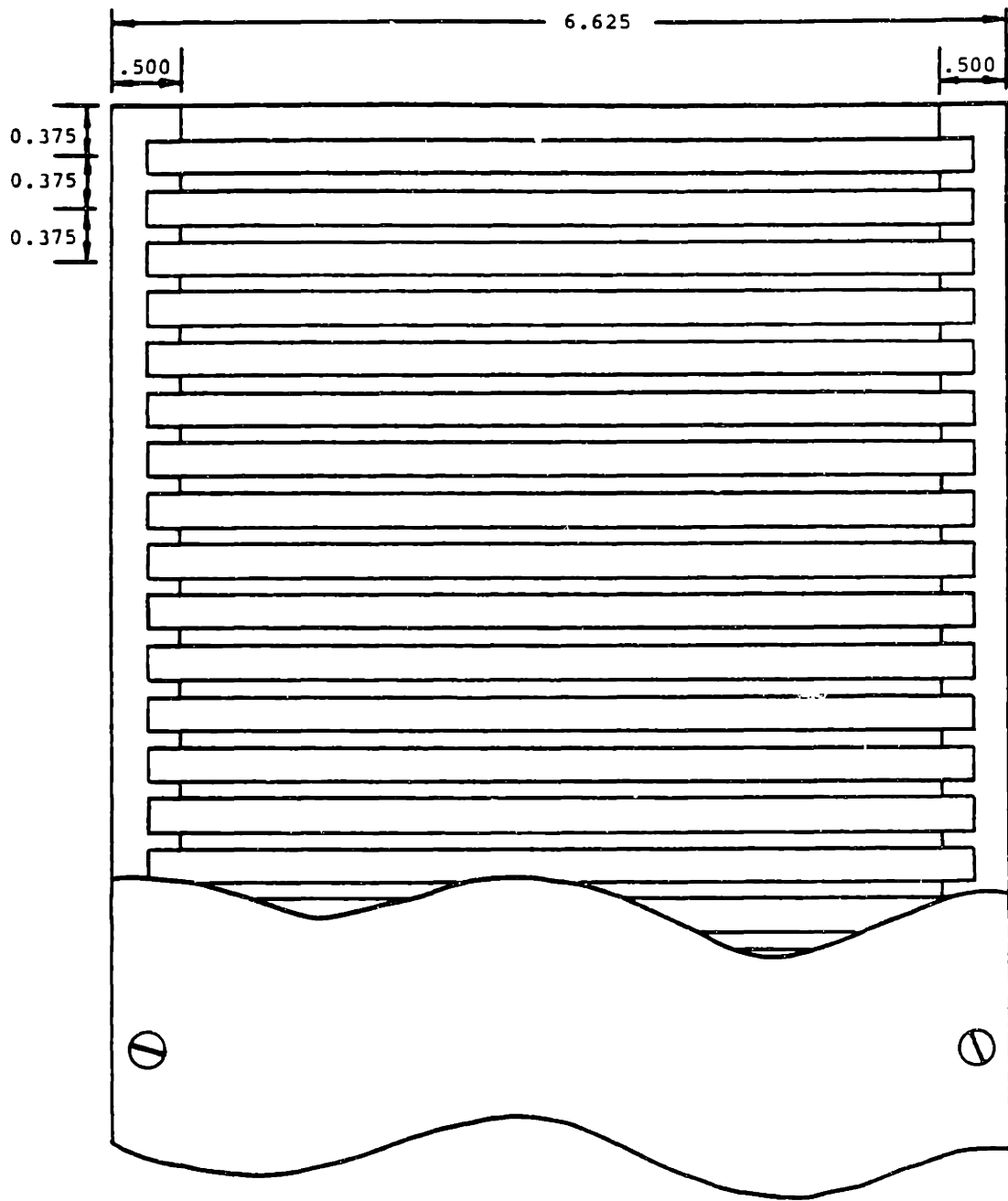
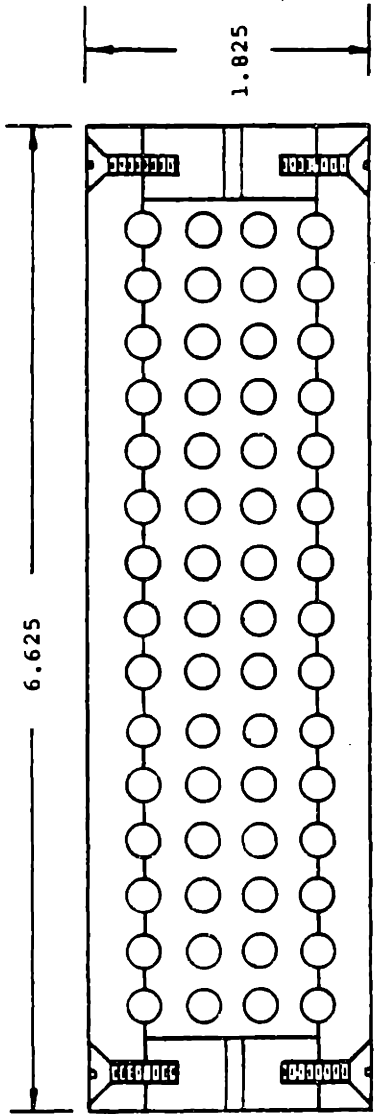
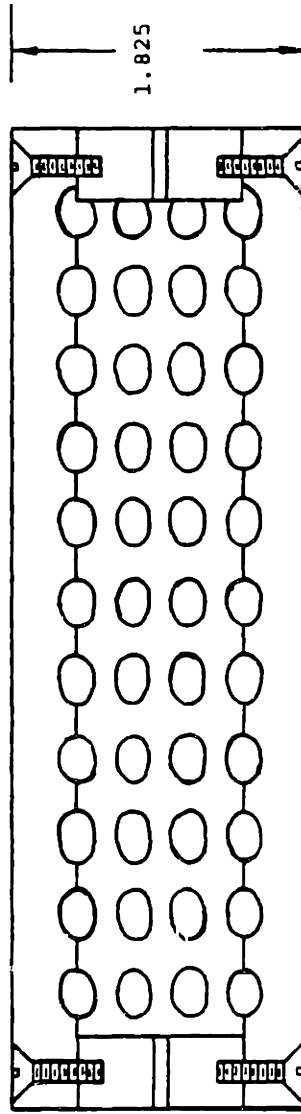


Figure B.5 Crossflow test section--cutaway side view.



(a)



(b)

Figure B.6 Cutaway top view--(a) parallel test section, (b) 45 degree test section.

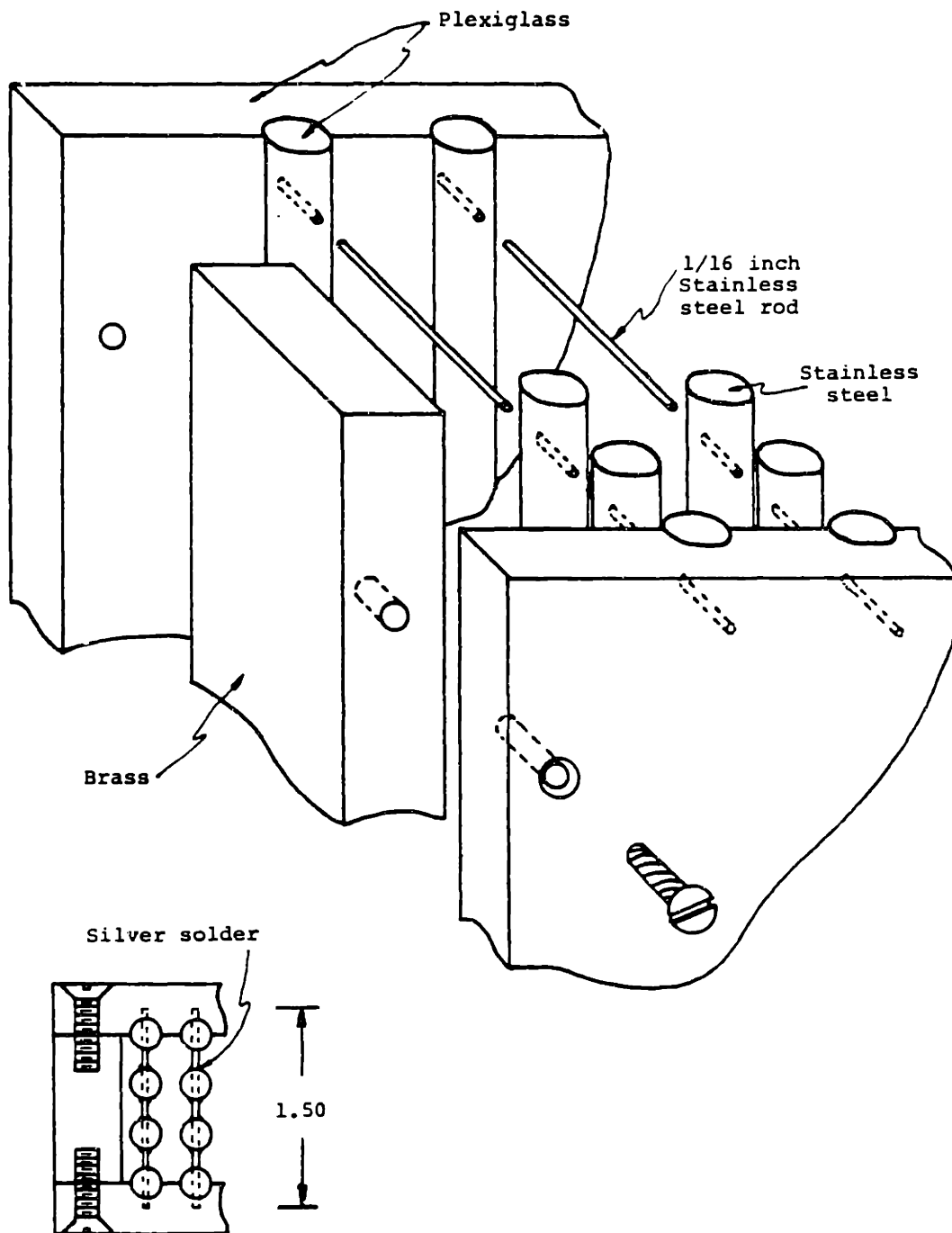


Figure B.7 Test section assembly.

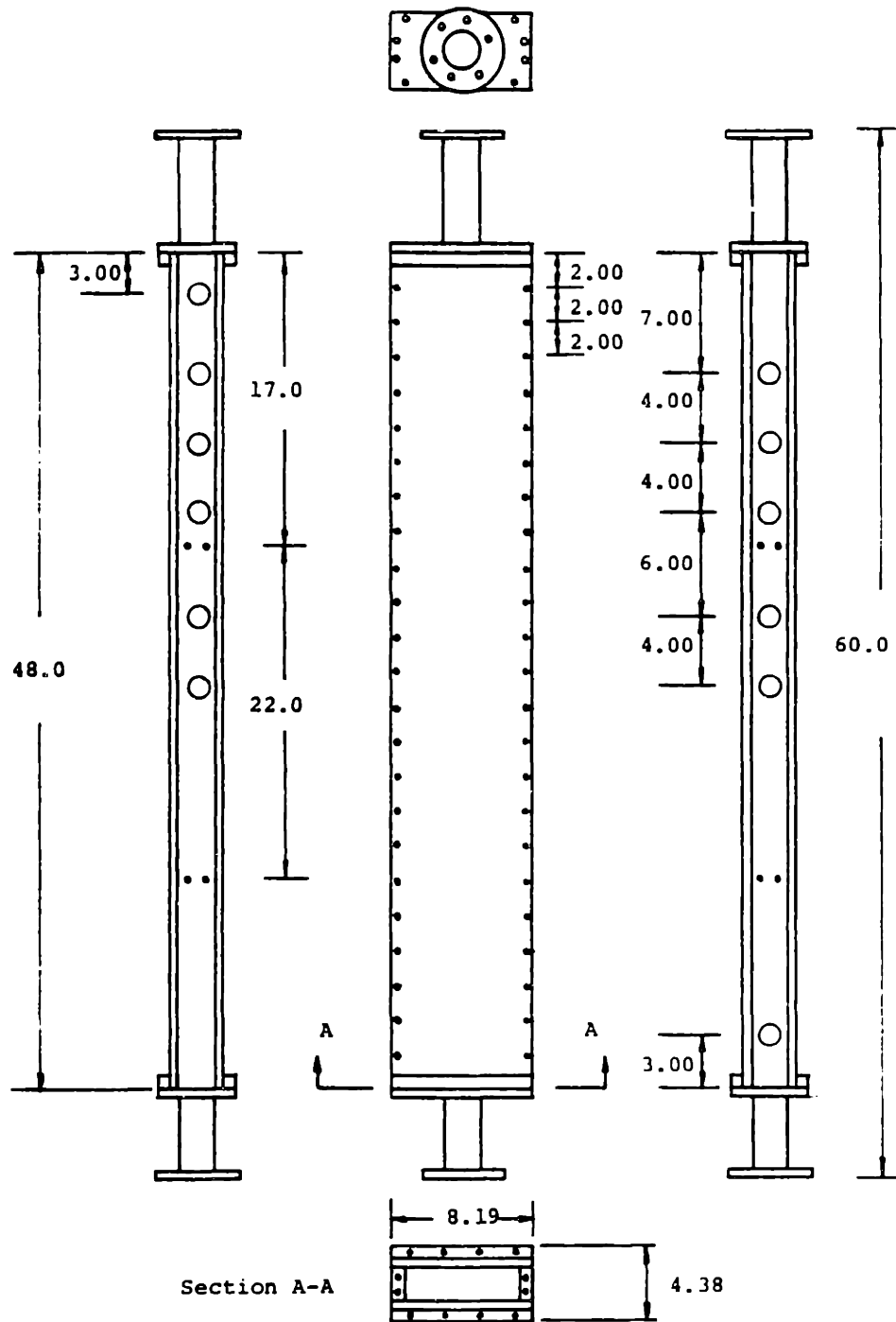


Figure B.8 Test duct isometric.

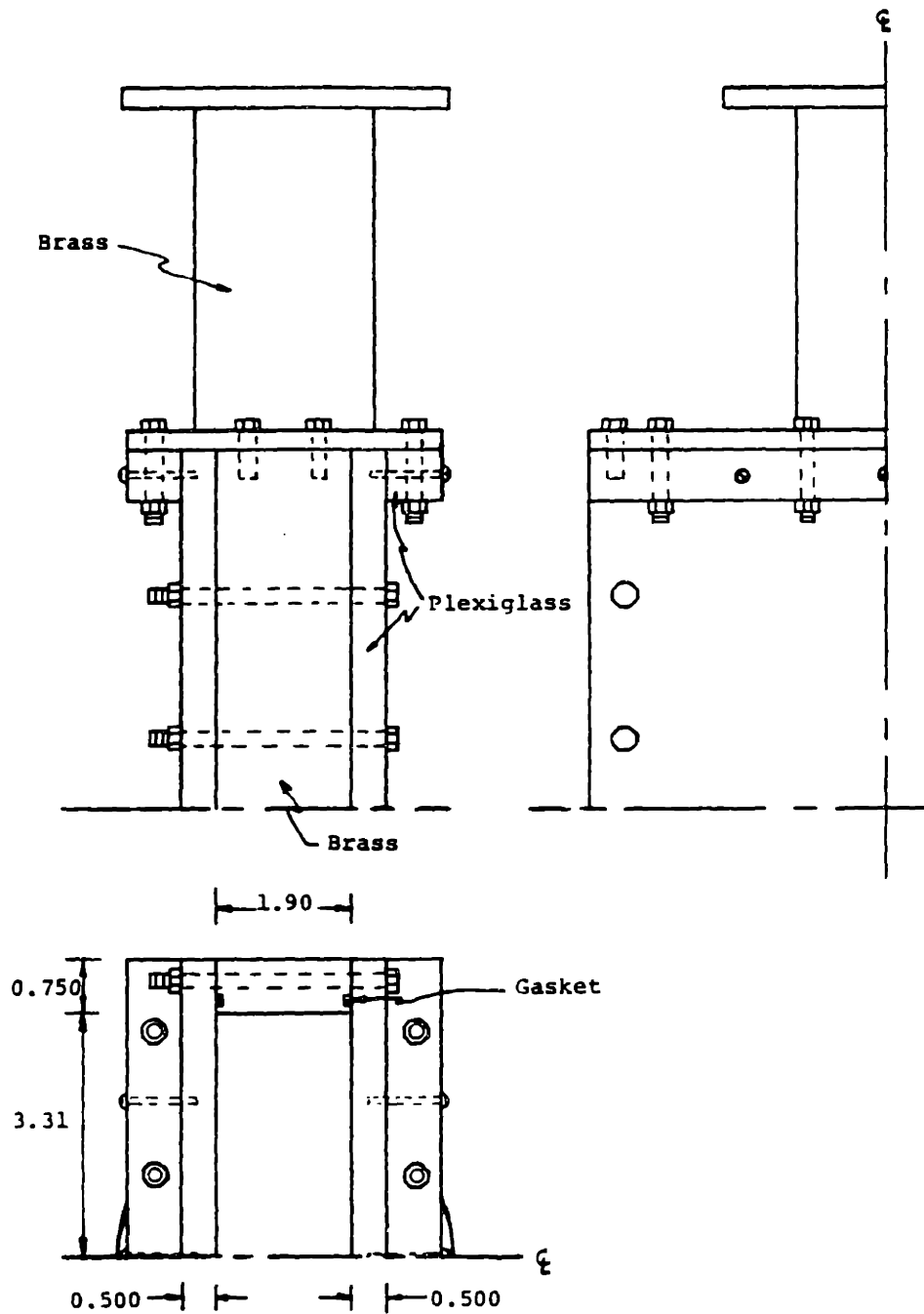


Figure B.9 Test duct isometric detail.

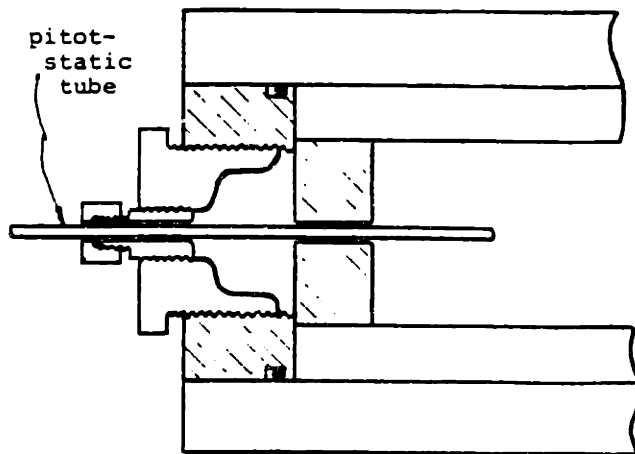
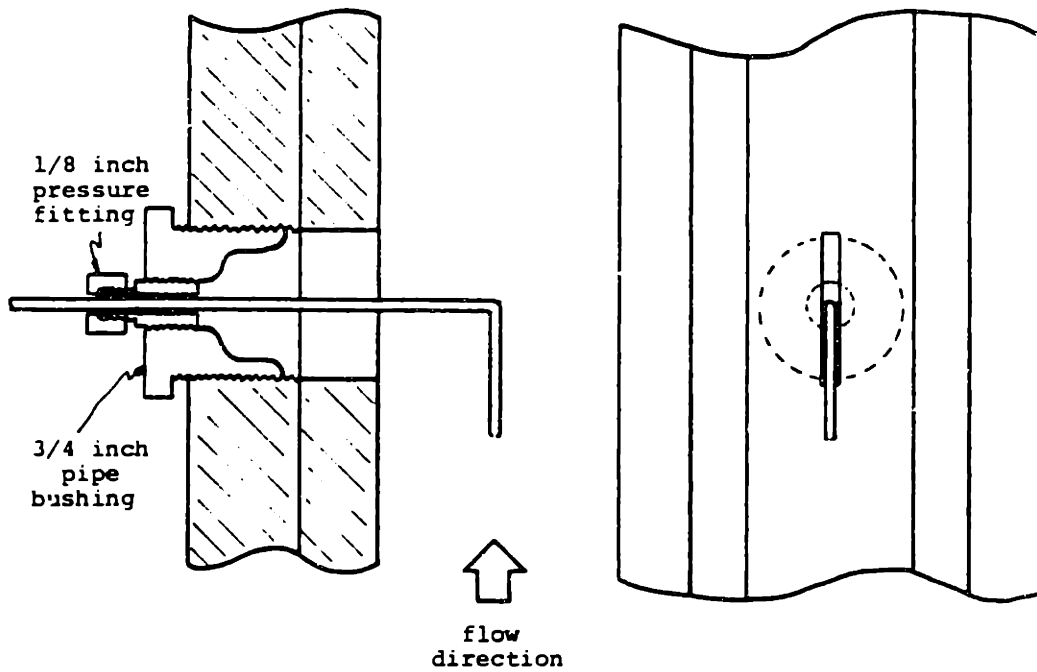


Figure B.10 Probe penetration detail.

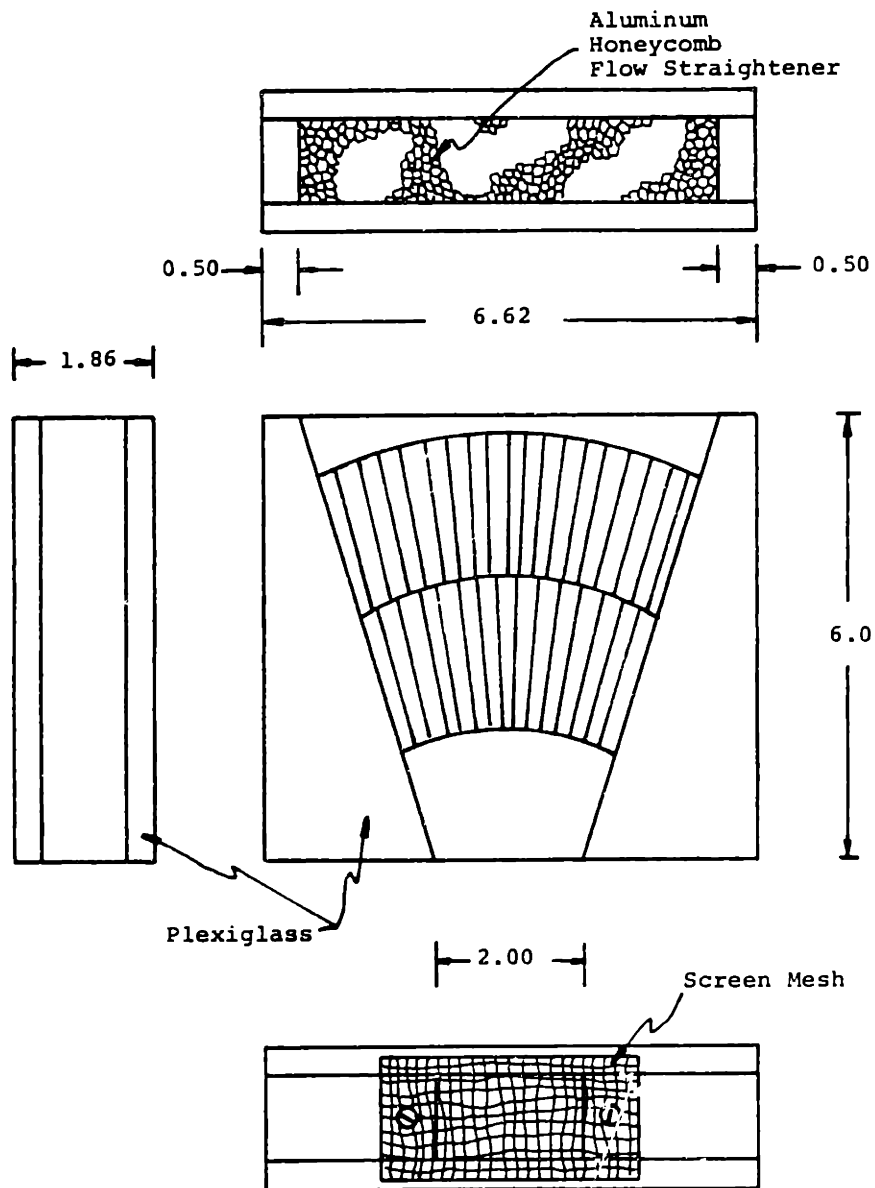


Figure B.11 Inlet flow diffuser/straightener.

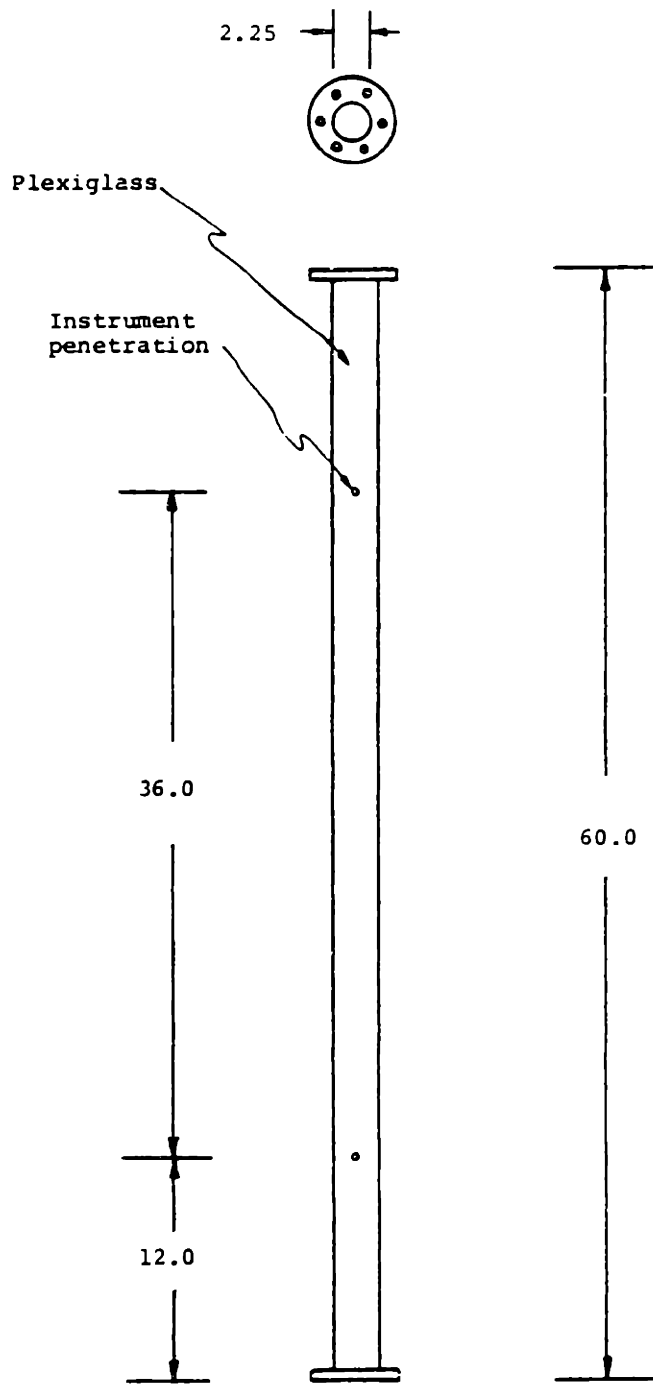


Figure B.12 Instrument calibration tube.

APPENDIX C
INSTRUMENT CALIBRATION

This appendix describes the calibration of the turbine flow meter, air orifice meter, air rotameters, and pitot-static tubes.

C.1 Turbine Meter Calibration

A turbine flow meter measures the liquid flow rate with a propeller which rotates at a frequency directly proportional to the flow rate. The meter measures the propeller frequency with an oscillating magnetic field. The measured frequency is converted to a D.C. voltage ranging from one volt at zero Hertz to five volts at 500 Hertz.

The Fischer-Porter turbine meter, model 10C1516, was factory calibrated from 13 to 144 gpm:

$$Q_l \text{ (gpm)} = \frac{60 f}{207.846 \text{ cycle/gal}} \quad (\text{C.1})$$

where f is the propeller frequency. This calibration is based on at least 15 straight pipe diameters before and 4 straight pipe diameters after the turbine meter. The resultant calibration in terms of output voltage V is

$$Q_l \text{ (gpm)} = 36.08 (V(\text{volts}) - 1.0) \quad (\text{C.2})$$

The meter calibration was confirmed and extended down to 4 gpm. The meter flow rate was confirmed by filling the test loop with water over a

measured time interval. Then the water in the loop was drained and weighed. Hence

$$Q_l = \frac{\text{Water Weight}}{\rho_l \Delta t} \quad (\text{C.3})$$

A comparison of the liquid flow rate determined from the turbine meter and Eq. (C.3) is shown in Fig. C.1. The data is accurate to within ± 3 percent of the factory calibration curve for flow rates down to 4 gpm. The resulting calibration curve is

$$Q_l \text{ (gpm)} = 36.08 (V(\text{volts}) - 0.996) \quad (\text{C.4})$$

where 0.996 is the actual zero reading of the turbine meter.

C.2 Orifice Meter Calibration

The flange-tap, sharp-edged orifice shown in Fig. C.2 measures the gas flow rate. The gas flow rate through the orifice is related to the pressure drop across the orifice by

$$\dot{m} = k\beta^2 A_{xs} \sqrt{2g_c \rho_g \Delta p} \quad (\text{C.5})$$

or

$$\dot{m} = 2.244 (k\beta^2) \sqrt{\rho_g (\text{lbm/ft}^3) \Delta p (\text{psi})} \quad (\text{C.6})$$

where $k\beta^2$ is a loss coefficient which is tabulated as a function of $\beta \triangleq D_{\text{orf}}/D_{\text{pipe}}$ and pipe Reynolds number, and $A_{xs} = 0.233 \text{ inch}^2$ for a pipe diameter of 2.067 inch.

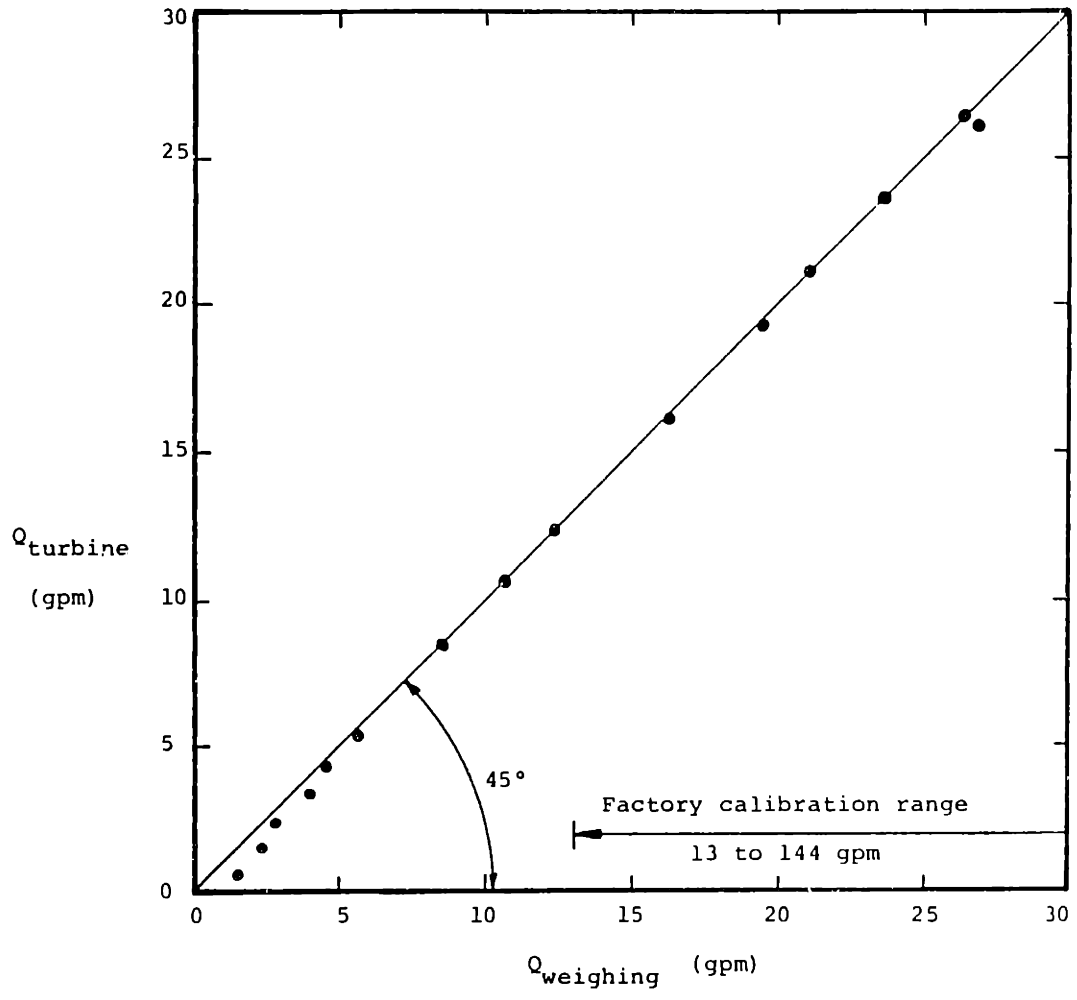


Figure C.1 Turbine flow meter calibration curve.

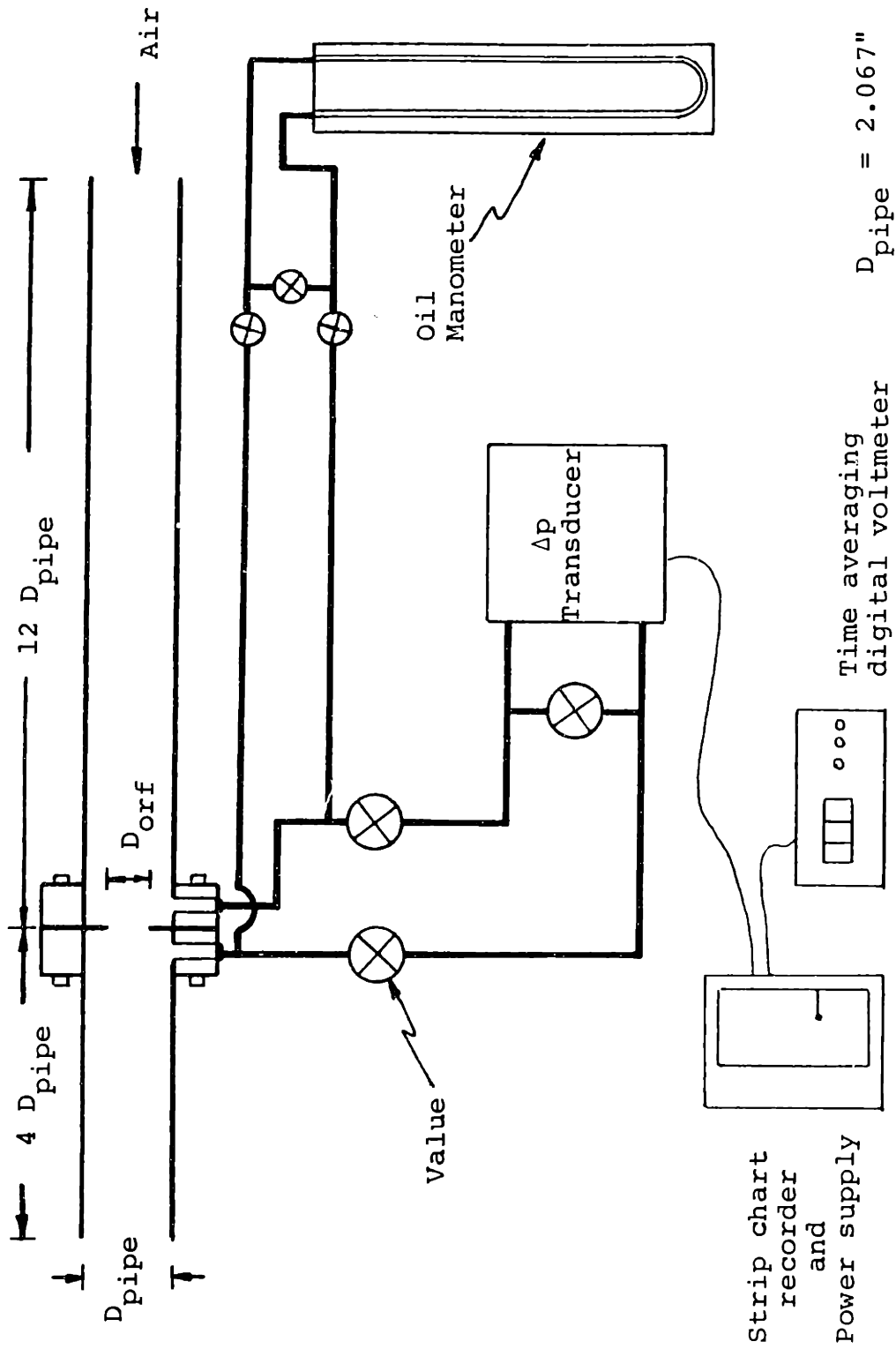


Figure C.2 Air orifice metering system.

For an ASME standard one inch flange-tap orifice meter with orifice diameter of 0.375, 1.00, and 1.45 inch, $k\beta^2$ in the Reynolds number range of 5,000 is 0.0199, 0.149, and 0.368, respectively. The air density at room temperature is

$$\rho_g \text{ (lbm/ft}^3\text{)} = 0.0749 \left(\frac{p_{us} \text{ (psi)} + 14.7}{14.7} \right) \quad (\text{C.7})$$

where p_{us} is the upstream gauge pressure. The resulting calibration curves

$$\dot{m} \text{ (lbm/sec)} = k' \sqrt{\Delta p \text{ (psi)}} \quad (\text{C.8})$$

for three upstream pressures are tabulated in Table C.1.

The differential pressure is measured either by a U-tube manometer or a Fischer-Porter electric differential pressure transmitter, model 50-DPF-100 and strip chart recorder.

The calibration curve for $D_{orf} = 0.375$ inch and $p_{us} = 20$ psig was checked by integral volume measurements. A material volume of air was collected and measured over a recorded time interval. The results are shown in Fig. C.3. Agreement with the calibration curve is good.

C.3 Rotameter Calibration

Two rotameters are used to measure gas flow rates below the range of the orifice meter. A rotameter is a vertical glass tube of gradually increasing cross-sectional area. A specific weight and size float is placed inside the tube. As flow passes through the tube the float rises until the area around the float is great enough so that the drag on the float just balances its weight. This elevation (cross-sectional area) is related to the flow rate through the tube.

TABLE C.1

Orifice Meter Calibration Curve

$$\dot{m} \text{ (lbm/sec)} = k' \sqrt{\Delta p \text{ (psi)}}$$

Orifice Diameter (Inch)	Upstream Pressure (psi)		
	20	30	40
0.375	$k' = 0.0188$	$k' = 0.0213$	$k' = 0.0236$
1.00	$k' = 0.1404$	$k' = 0.1594$	$k' = 0.1763$
1.45	$k' = 0.3472$	$k' = 0.3941$	$k' = 0.4320$

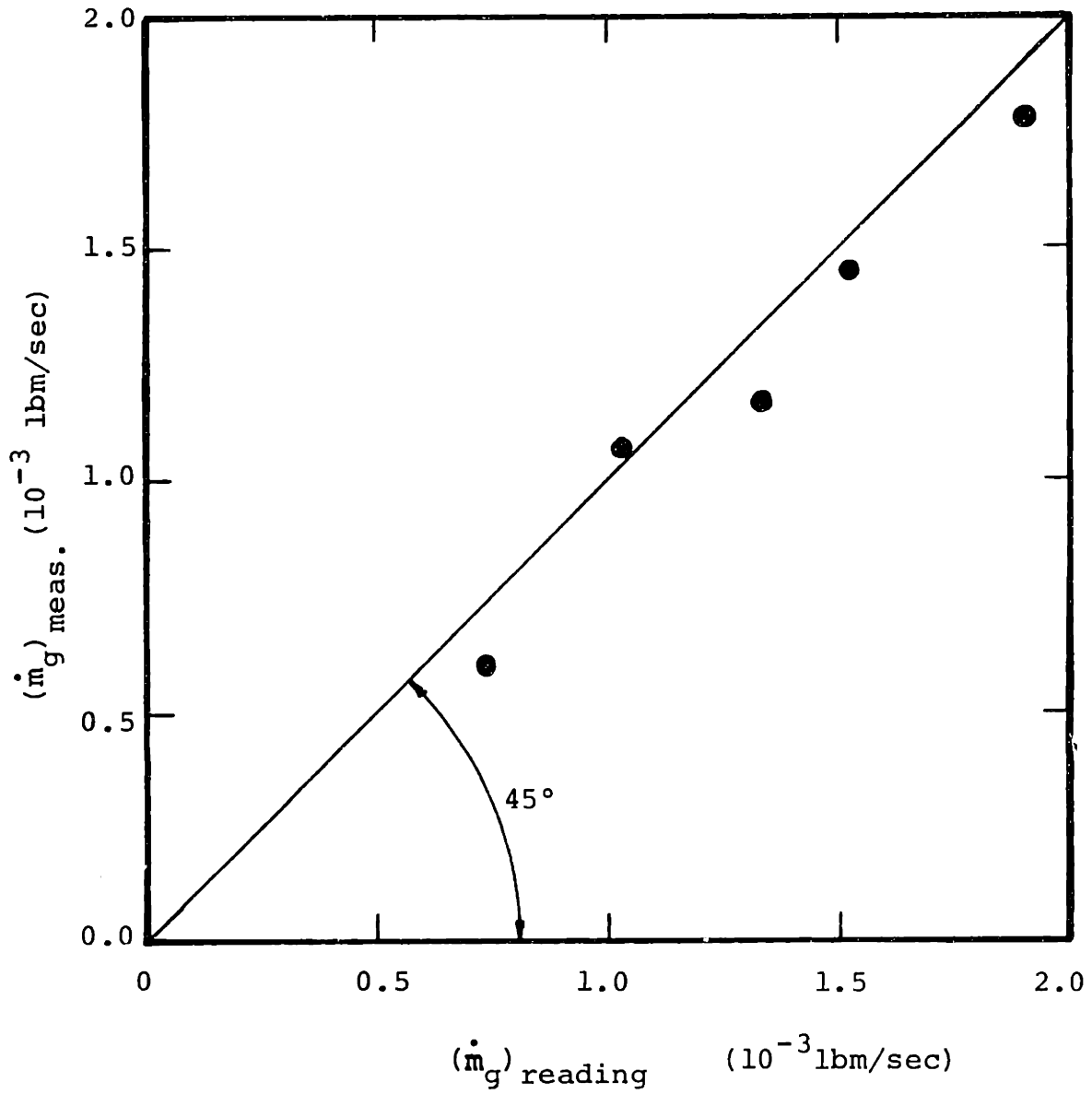


Figure C.3 Air orifice meter calibration curve.

The two rotameters used were a Fischer-Porter 1/8-12-G-5/84 (12FS), and 1/4-20-G-5/84 (20 FS). Both meters had been used previously and so were recalibrated with gas flow rates from integral volume measurements. Calibration curves for the two meters are shown in Fig. C.4 and C.5. The poor agreement with the original meter calibration is probably due to permanent sediment build up inside the tubes.

Expressions for the true mass flow rate can be written by using least square fits of Fig. C.4 and C.5; using the original calibration curves between the graduated take readings (RD) and mass flow rate:

$$\dot{m}_{\text{reading}} \text{ (lbm/sec)} = \frac{0.034 \text{ ft}^3/\text{min}}{60 \text{ sec/min}} \left(\frac{\text{RD}}{12} \right) \sqrt{\rho_g \text{ (lbm/ft}^3\text{)}} \quad (\text{C.9})$$

for the 12 FS meter, and

$$\dot{m}_{\text{reading}} \text{ (lbm/sec)} = \frac{0.65 \text{ ft}^3/\text{min}}{60 \text{ sec/min}} \left(\frac{\text{RD}}{20} \right) \sqrt{\rho_g \text{ (lbm/ft}^3\text{)}} \quad (\text{C.10})$$

for the 20 FS meter; and using Eq. (C.7). The resulting expressions are:

for the 12 FS meter

$$\dot{m}_{\text{true}} \text{ (lbm/sec)} = 4.57 \times 10^{-6} \text{ RD} \sqrt{\frac{P_{\text{us}} + 14.7}{14.7}} - 1.50 \times 10^{-5} \quad (\text{C.11})$$

where

$$2.0 \times 10^{-6} \leq \dot{m}_{\text{true}} \leq 6.9 \times 10^{-5}$$

and for the 20 FS meter

$$\dot{m}_{\text{true}} \text{ (lbm/sec)} = 2.36 \times 10^{-5} \text{ RD} \sqrt{\frac{P_{\text{us}} + 14.7}{14.7}} - 1.08 \times 10^{-4} \quad (\text{C.12})$$

where

$$3.0 \times 10^{-5} \leq \dot{m}_{\text{true}} \leq 5.9 \times 10^{-4}$$

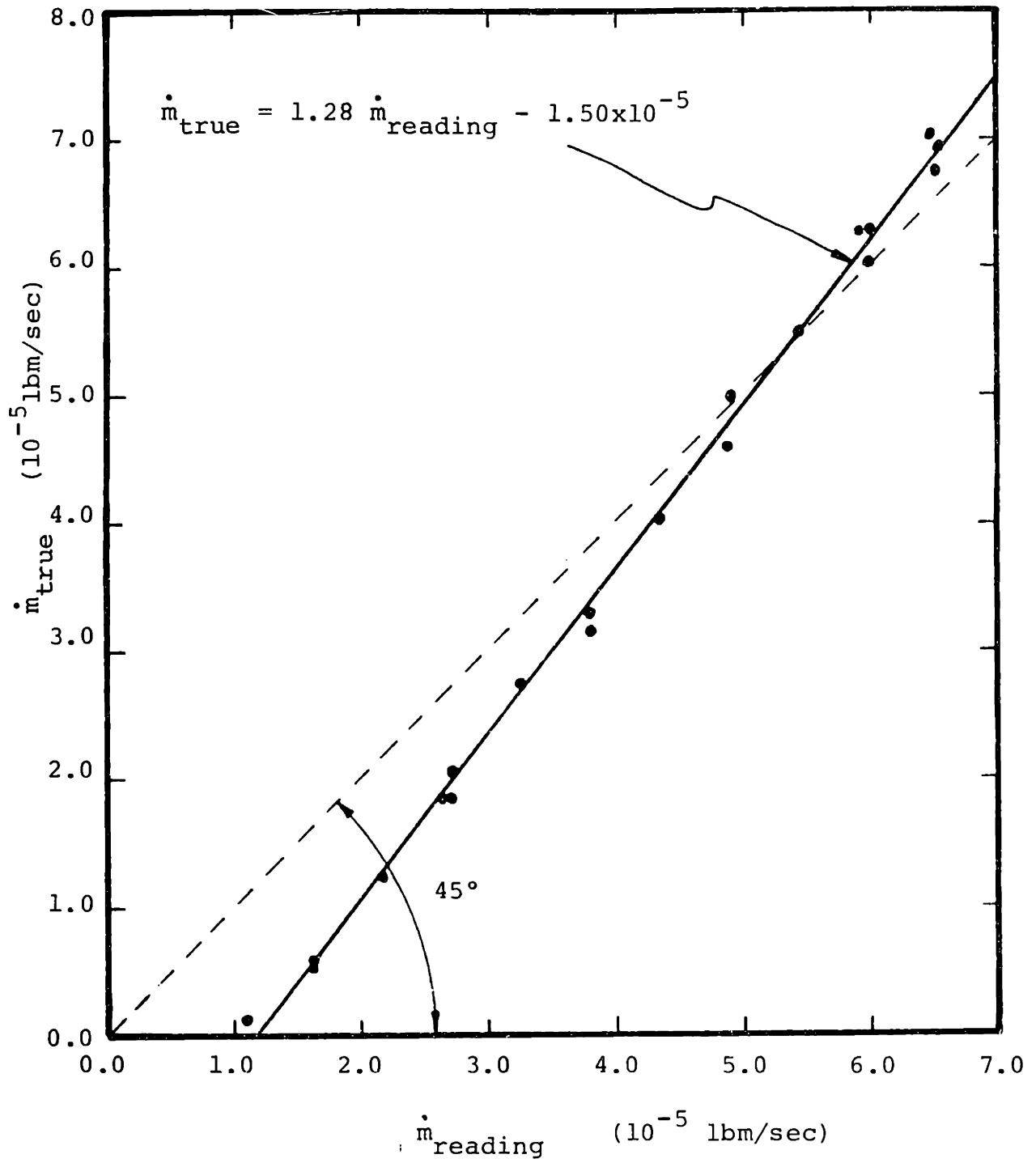


Figure C.4 12 FS rotameter calibration curve.

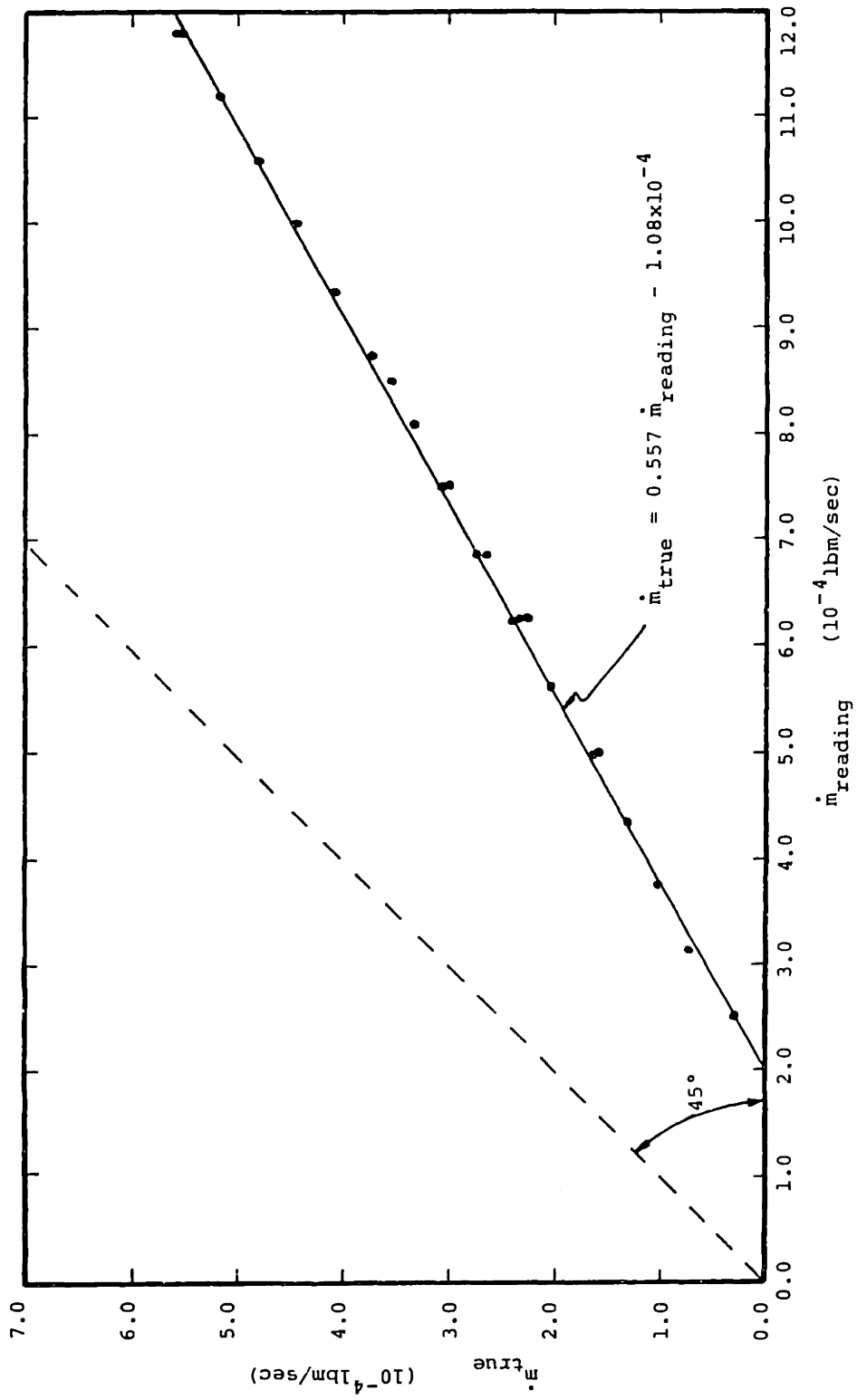


Figure C.5 20 FS rotameter calibration curve.

C.4 Pitot-Static Tube Calibration

Local velocity measurements are made with pitot-static tubes. A pitot-static tube is an L-shaped probe, constructed of two concentric tubes pointed in the direction of the flow. A hole at the probe tip measures the fluid stagnation pressure and three circumferential holes measure the static pressure. The difference between the stagnation and static pressure is the impact (dynamic) pressure of the fluid at the probe tip. The dynamic pressure equals the mean fluid kinetic energy when it is assumed that the fluid slows down isentropically

$$\Delta p_{\text{dyn}} = \frac{\rho_{\ell} v_{\ell}^2}{2} \quad (\text{C.13})$$

To correct for non-ideal effects (i.e., the probe tip shape and location of the static tapholes) a calibration constant C is introduced

$$\Delta p_{\text{dyn}} = \frac{1}{C^2} \frac{\rho_{\ell} v_{\ell}^2}{2} \quad (\text{C.14})$$

The constant C was determined for the 1/16 inch National Sensor pitot-static tubes used, by measuring velocity profiles in a round calibration tube (as shown in Fig. B.12). The integrated profiles were compared to the average tube velocity obtained from the turbine flow meter. Sample profiles are shown in Fig. C.6 and the calibration curve in Fig. C.7. The resulting value of C is 0.95, hence

$$v_{\ell} = 0.95 \sqrt{\frac{2\Delta p_{\text{dyn}}}{\rho_{\ell}}} = 11.6 \sqrt{\Delta p_{\text{dyn}} (\text{psi})} \quad (\text{C.15})$$

where the second equality is for $\rho_{\ell} = 62.2 \text{ lbm/ft}^3$

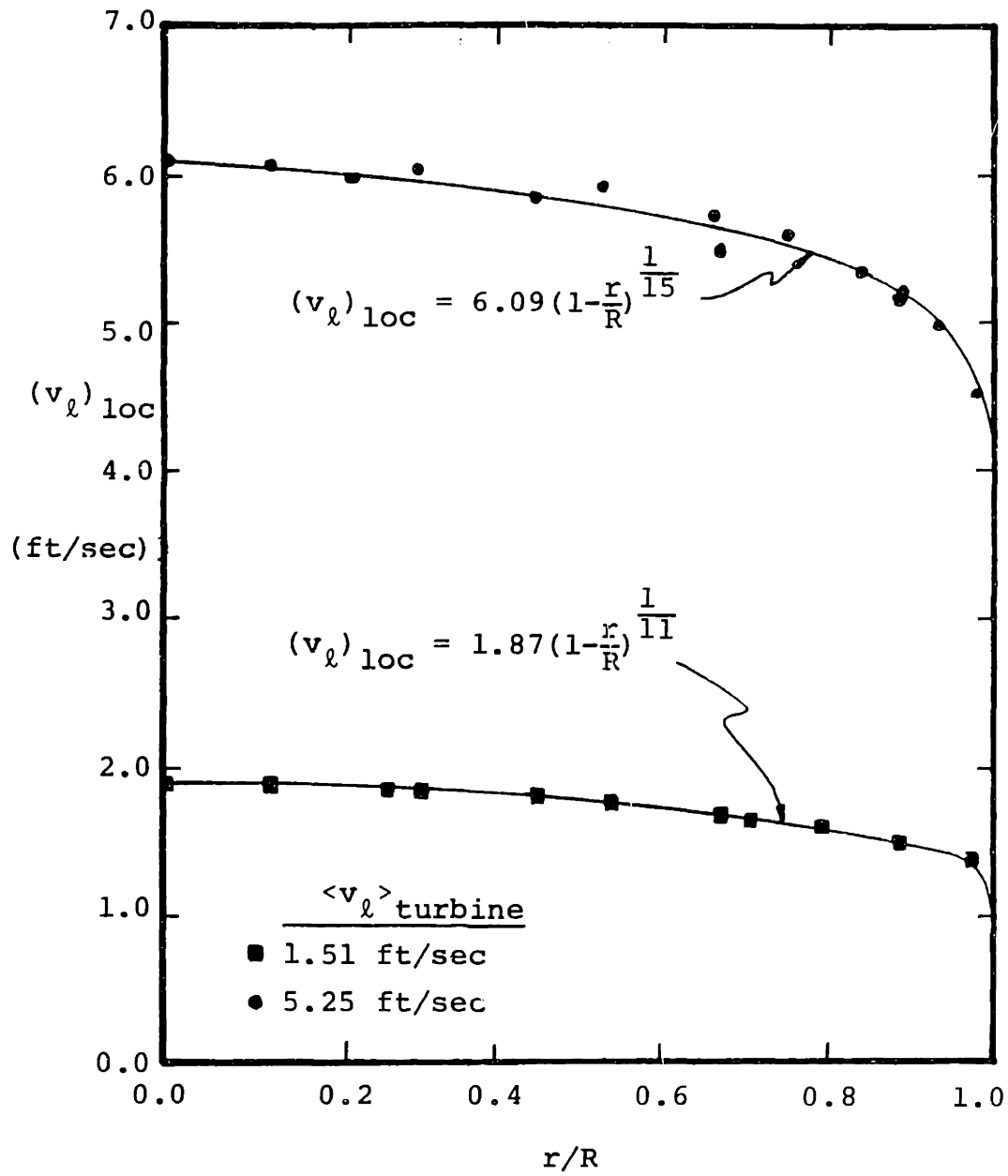


Figure C.6 Pitot-static tube calibration velocity profiles.

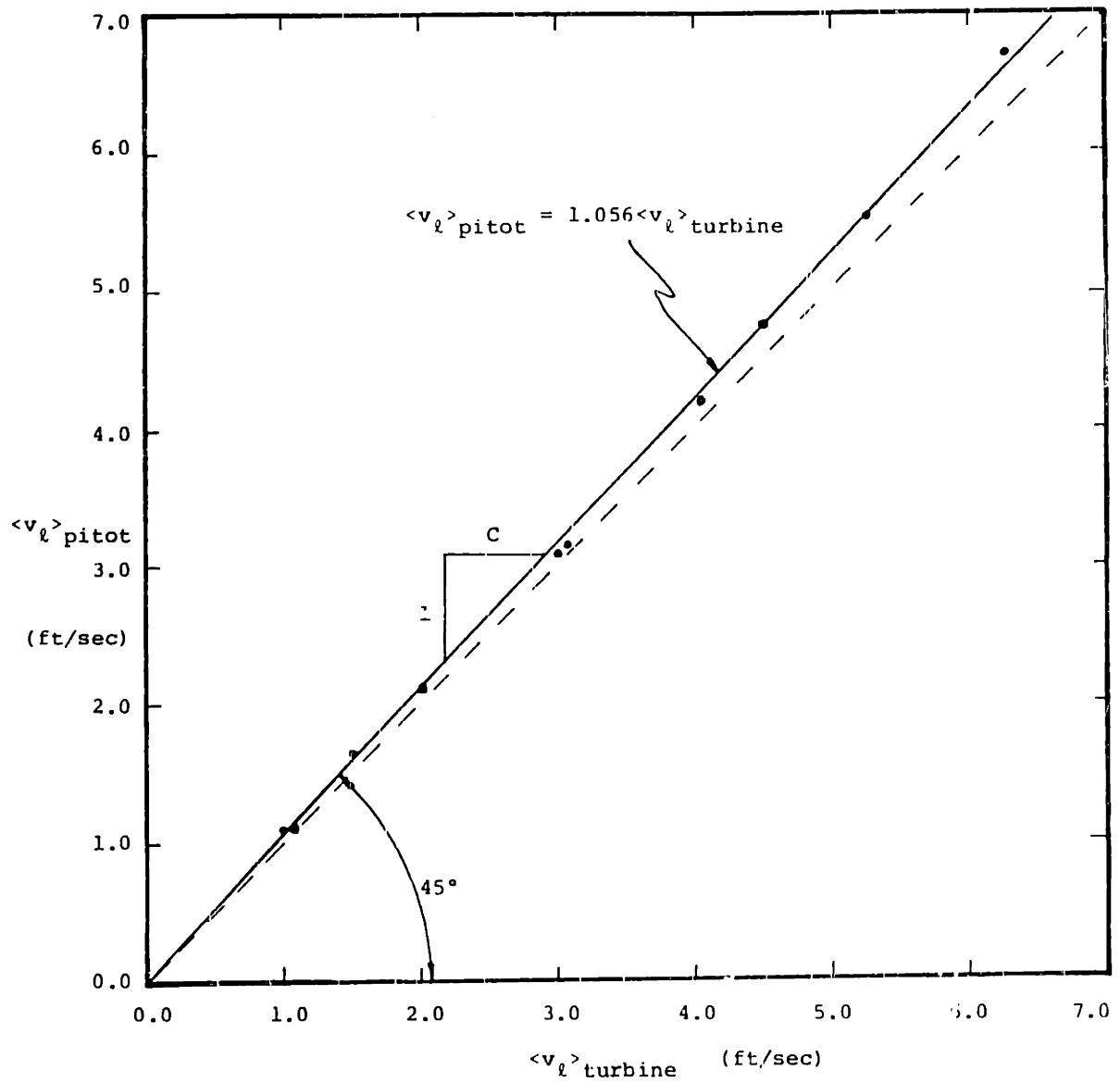


Figure C.7 Pitot-static tube calibration curve.

APPENDIX D

MODELS FOR CROSSFLOW MAINSTREAM VELOCITY

Photographic studies [V.2, W.3] of flows across rod arrays suggest a division of the flow field into two regions: a mainstream region in which irrotational flow weaves around the rods, and a drag region in which flow recirculates in vortices behind the rods (the first column of Fig. D.1). These observations suggest using the average velocity in the irrotational mainstream as the characteristic velocity for crossflow. Hence we define the average crossflow mainstream velocity, \underline{v}_{ms} , as the total volumetric flow rate Q , divided by the average mainstream flow area \bar{A}_{ms} , i.e.,

$$|\underline{v}_{ms}| \triangleq \frac{Q}{\bar{A}_{ms}} \quad (D.1)$$

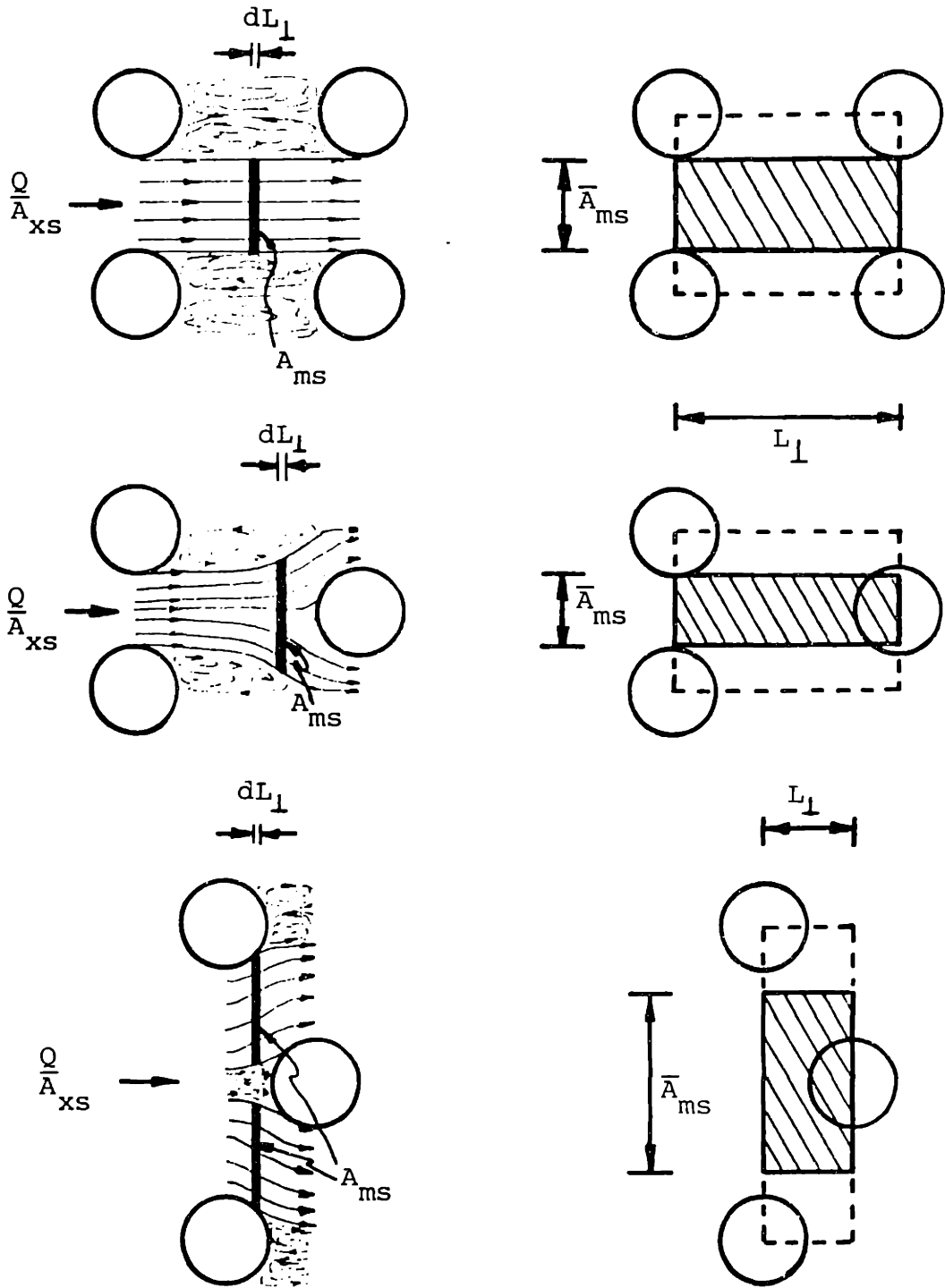
where

$$\bar{A}_{ms} \triangleq \frac{1}{L_{\perp}} \int_{L_{\perp}} A_{ms} dL_{\perp} \quad (D.2)$$

and L_{\perp} is the straight length in the average flow direction. The areas A_{ms} and \bar{A}_{ms} are shown graphically in Fig. D.1. Obviously \bar{A}_{ms} is not a uniquely defined geometric quantity, but requires a model describing the volume occupied by the mainstream flow.

The mainstream velocity, \underline{v}_{ms} , can be also expressed in terms of the volume average velocity, $\langle \underline{v} \rangle$, defined in Sec. 5.2.3,

$$|\langle \underline{v} \rangle| \triangleq \frac{Q}{A_{xs} \gamma_v} = \frac{Q}{\bar{A}_f} \quad (D.3)$$



$$\bar{A}_{ms} = \frac{1}{L_{\perp}} \int_{L_{\perp}} A_{ms} dL_{\perp}$$

Figure D.1 Definition of average mainstream flow area.

Eliminating Q between Eq. (D.1) and (D.2), giving

$$|\underline{v}_{ms}| = \frac{|\langle \underline{v} \rangle|}{\bar{A}_{ms}/\bar{A}_f} \quad (D.4)$$

It is analytically convenient to represent models for \underline{v}_{ms} in terms of a dimensionless fractional volume; therefore we define the crossflow mainstream porosity, δ_v , as

$$\begin{aligned} \delta_v &\triangleq \frac{\bar{A}_{ms}}{\bar{A}_f} = \frac{V_{ms}/L_{\perp}}{V_f/L_{\perp}} = \frac{V_{ms}}{V_f} \\ &= \frac{\text{Crossflow Mainstream Volume}}{\text{Fluid Volume}} \end{aligned} \quad (D.5)$$

Equation (D.4) now becomes simply

$$|\underline{v}_{ms}| = \frac{|\langle \underline{v} \rangle|}{\delta_v} \quad (D.6)$$

We present here five models for the mainstream velocity \underline{v}_{ms} , and corresponding analytical expression for the crossflow mainstream porosity, δ_v .

Most current crossflow correlations use as the characteristic velocity a velocity based on the minimum clearance area between rods (see Fig. D.2 (a)). We can generalize this characteristic velocity to be the average mainstream velocity by assuming the average mainstream area \bar{A}_{ms} , is the minimum clearance area. For an in-line array, then,

$$\bar{A}_{ms} = (S_T - d) L_{||} \quad (D.7)$$

and

$$\delta_v = \frac{\bar{A}_{ms}}{\bar{A}_f} = \frac{V_{ms}}{V_f} = \frac{(S_T - d)L_{||} S_L}{\gamma_v S_T S_L L_{||}} = \frac{1}{\gamma_v} \left(1 - \frac{d}{S_T}\right) \quad (D.8)$$

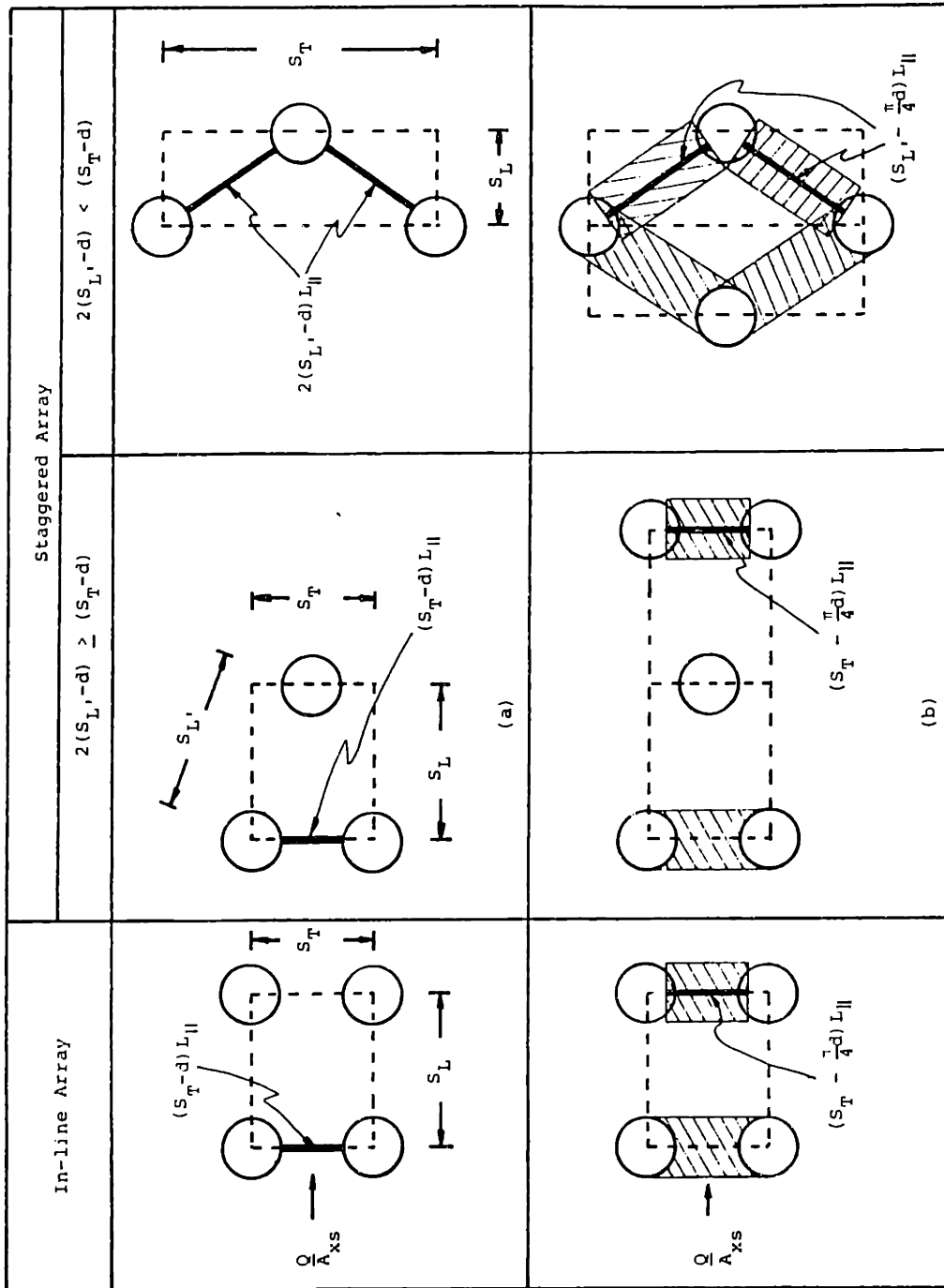


Figure D.2 Definition of (a) minimum and (b) average clearance area (model **A**) and **B**, respectively).

where $L_{||}$ is a unit length in the parallel flow direction and $(S_T - d)$ is the minimum clearance. For staggered arrays the minimum clearance may be either the transverse clearance between rods $2(S_T - d)$ or twice the diagonal clearance between rods $2(S_L' - d)$, whichever is smaller. This model shall be called model (A).

Model (B) is suggested by the crossflow correlation of VDI-Wärmeatlas [V.1]. VDI-Wärmeatlas uses the average area in the clearance region between rods to define the characteristic crossflow velocity. The clearance region, shown in Fig. D.2(b), is the region one rod diameter wide centered about the minimum clearance area. Assuming this average clearance area is the average mainstream area yields a second model for the average mainstream velocity. An in-line array, for example, gives

$$\bar{A}_{ms} = \left(S_T - \frac{\pi}{4} d \right) L_{||} \quad (D.9)$$

and

$$\delta_v = \frac{v_{ms}}{v_f} = \frac{\left(S_T - \frac{\pi}{4} d \right) L_{||} S_L}{\gamma_v S_T L_{||} S_L} = \frac{1}{\gamma_v} \left(1 - \frac{\pi d}{4 S_T} \right) \quad (D.10)$$

Model (C), proposed here, assumes the mainstream flow occupies a volume of constant cross-sectional area equal to the minimum clearance area, and path length as shown in Fig. D.3. Hence the average mainstream area is this volume divided by the straight path length L_{\perp} . For in-line arrays this model is identical to model (A) because the path length and straight length are equal. However for staggered arrays the inclusion of

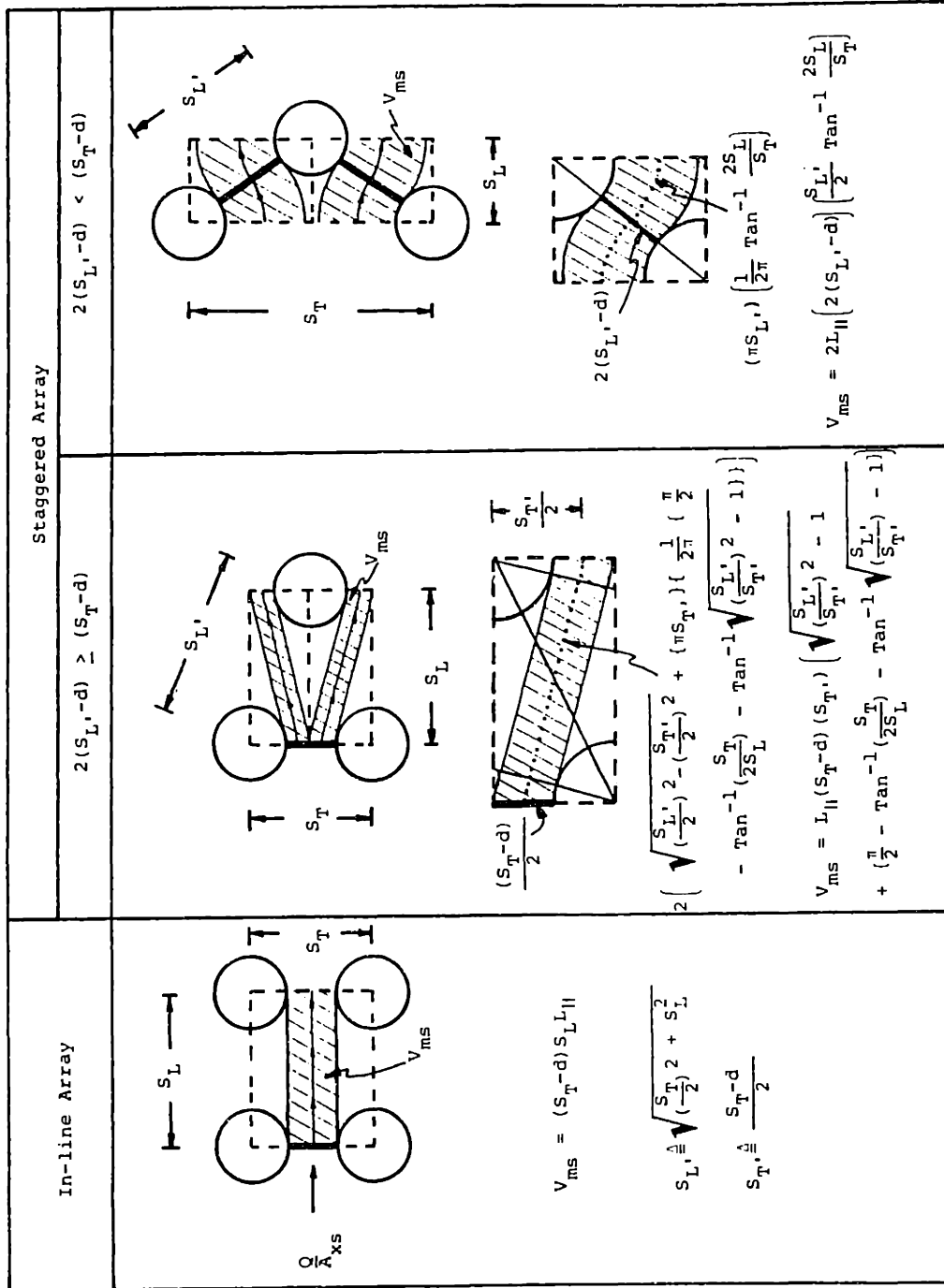


Figure D.3 Path length with constant minimum clearance area model for mainstem volume (model C).

a more realistic weaving path length reduces the average mainstream velocity relative to model (A). For example, for a tight longitudinal pitch staggered array

$$V_{ms} = (2(S_{L'} - d))(S_{L'} \tan^{-1} \frac{2S_L}{S_T})(L_{||}) \quad (D.11)$$

and

$$\begin{aligned} \delta_v \frac{V_{ms}}{V_f} &= \frac{2S_{L'} L_{||} (S_{L'} - d) \tan^{-1} \left(\frac{2S_L}{S_T} \right)}{\gamma_v S_T L_{||} S_L} \\ &= \frac{2}{\gamma_v} \left(\frac{S_{L'} - d}{S_L} \right) \left(\frac{S_{L'}}{S_L} \right) \tan^{-1} \left(\frac{2S_L}{S_T} \right) \end{aligned} \quad (D.12)$$

The above three models are plotted for the four equilateral, symmetric rod arrangements in Fig. D.4, D.5, and D.6.

The above models are well-defined and simple to evaluate for principal (symmetric) crossflow directions, however for varying directional crossflows (see Fig. 5.2(a)) an arrangement independent model is more appropriate. Therefore we define model (D) which approximates the crossflow mainstream porosity by the volume porosity

$$\delta_v = \gamma_v \quad (D.13)$$

This model has no real geometric basis, but nicely predicts the average trend of both models (A) and (C) as shown in Figure D.4 and D.5. The principal advantage of this model is it uniquely defines an average mainstream velocity, independent of the crossflow direction (rod arrangement).

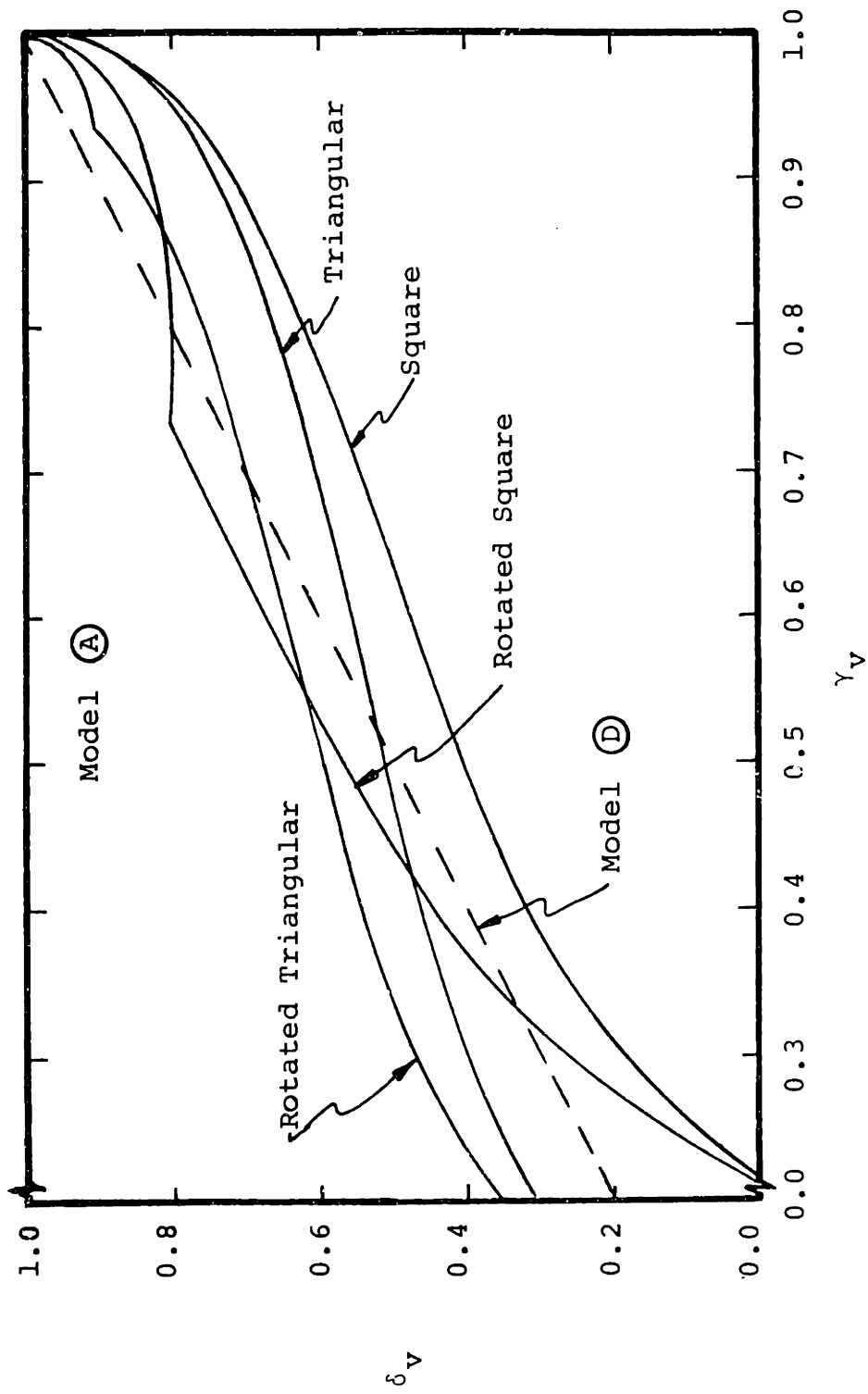


Figure D.4 Crossflow mainstream porosity model (A) for principal crossflow directions.

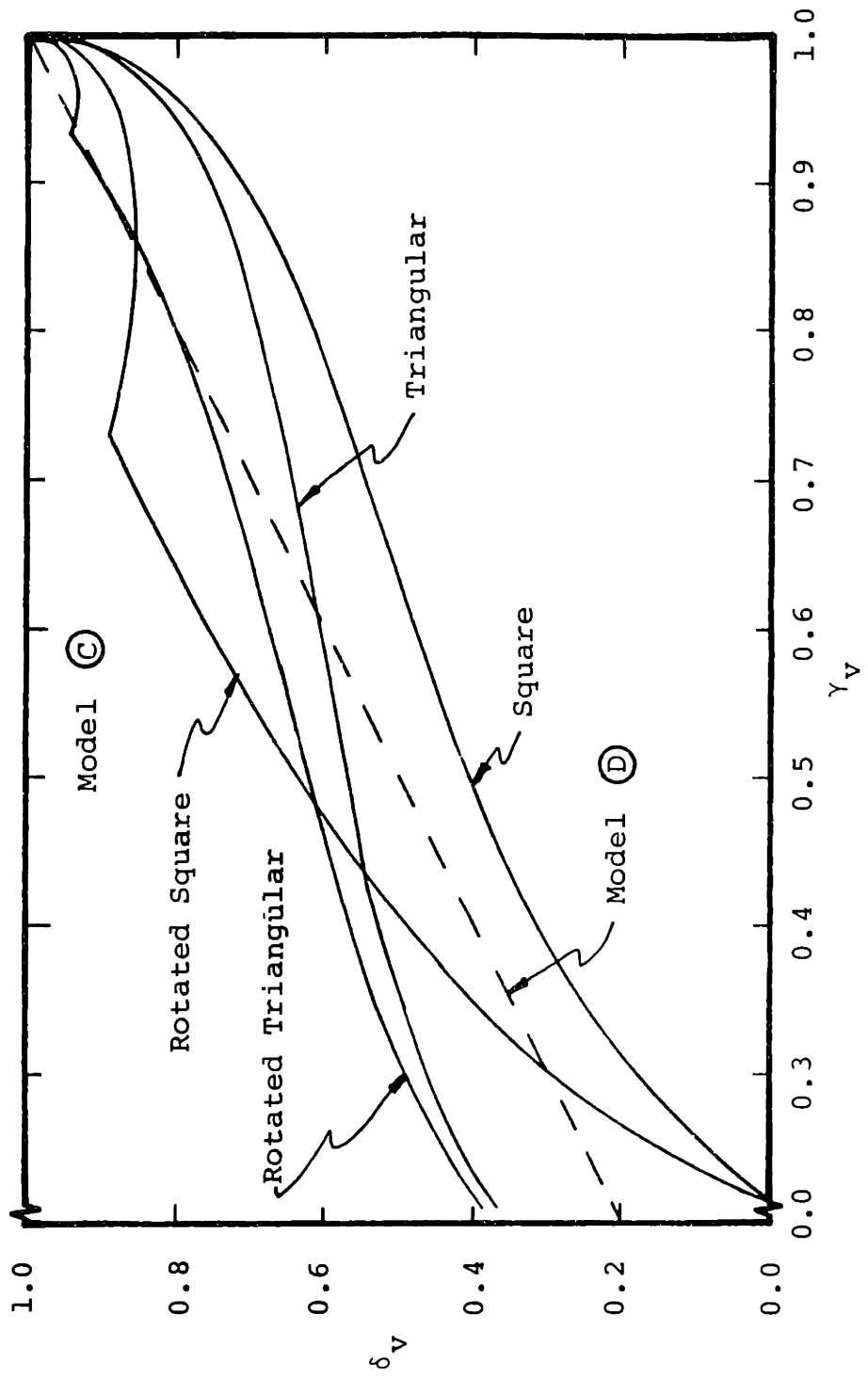


Figure D.5 Crossflow mainstream porosity model C for principal crossflow directions.

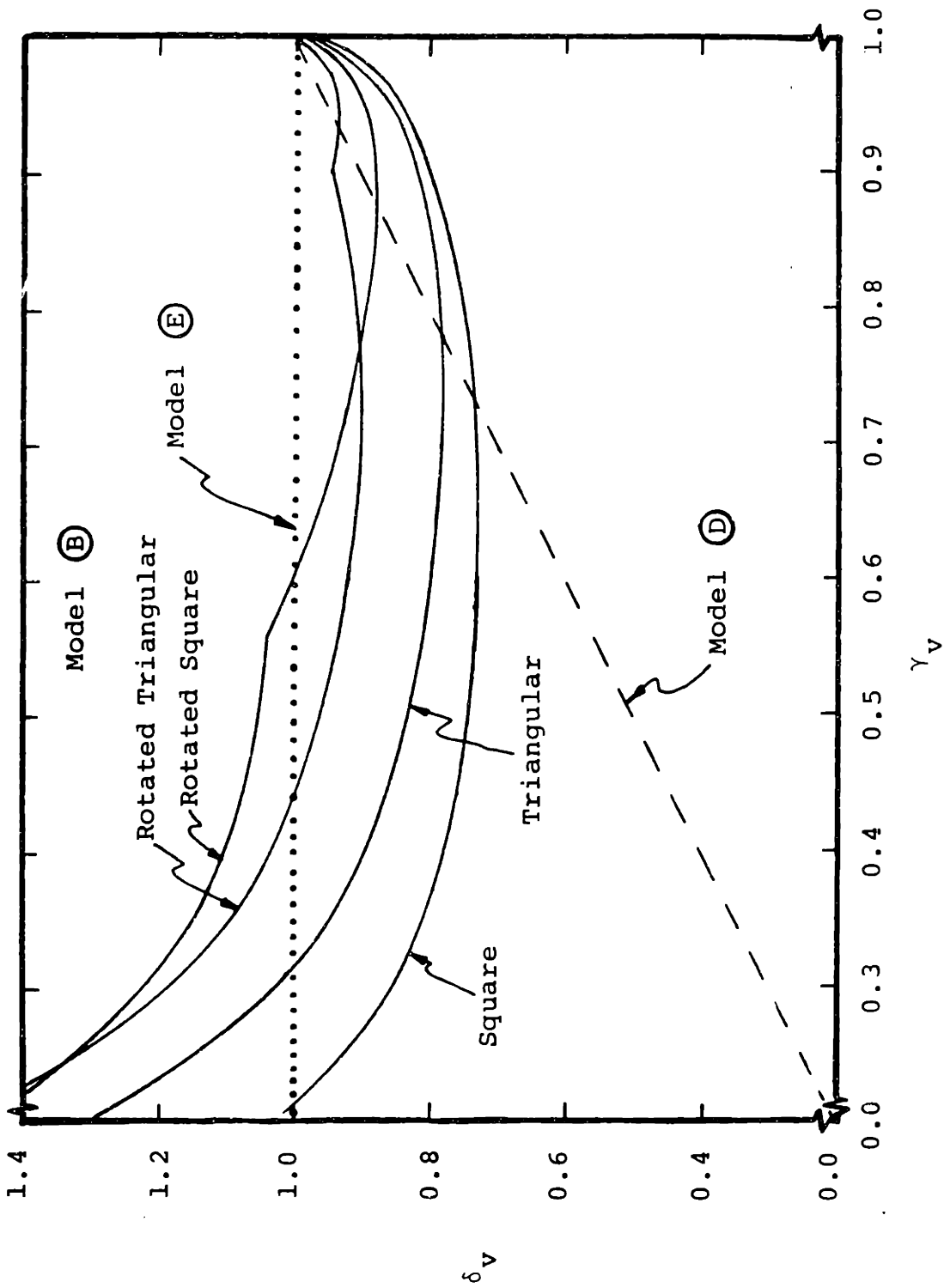


Figure D.6 Crossflow mainstream porosity model (B) for principal crossflow directions.

Last we introduce model (E), the limiting case where the average mainstream velocity is simply the volume-averaged velocity $\langle \underline{v} \rangle$, i.e.,

$$\delta_v = 1 \quad (\text{D.14})$$

As shown in Fig. D.6, this arrangement independent model is a closer approximation to model (B) than model (D).

Expressions for the crossflow mainstream porosity for the above models are summarized in Table D.1.

TABLE D.1

Models for Crossflow Mainstream Porosity, δ_V

$$S_{L'} = \frac{\Delta}{2} \sqrt{\left(\frac{S_T}{2}\right)^2 + S_L^2} \qquad S_{T'} = \frac{S_T + d}{2} \qquad \gamma_V = \left[1 - \frac{\pi}{4} \left(\frac{d}{S_T}\right) \left(\frac{d}{S_L}\right)\right]$$

Model	In-line Array	Staggered Array	Random Array
(A)	$\frac{1}{\gamma_V} \left(1 - \frac{d}{S_T}\right)$	$\frac{1}{\gamma_V} \left(1 - \frac{d}{S_T}\right)$ for $2(S_{L'} - d) \geq (S_T - d)$ $\frac{2}{\gamma_V} \left(\frac{S_{L'} - d}{S_T}\right)$ for $2(S_{L'} - d) < (S_T - d)$	--
(B)	$\frac{1}{\gamma_V} \left(1 - \frac{\pi d}{4 S_T}\right)$	$\frac{1}{\gamma_V} \left(1 - \frac{\pi d}{4 S_T}\right)$ for $2(S_{L'} - \frac{\pi}{4} d) \geq (S_T - d)$ $\frac{2}{\gamma_V} \left(\frac{S_{L'} - \frac{\pi}{4} d}{S_T}\right)$ for $2(S_{L'} - \frac{\pi}{4} d) < (S_T - d)$	--
(C)	$\frac{1}{\gamma_V} \left(1 - \frac{d}{S_T}\right)$	$\frac{1}{\gamma_V} \left(1 - \frac{d}{S_T}\right) \left(\frac{S_{T'}}{S_L}\right) \left[\sqrt{\left(\frac{S_{L'}}{S_{T'}}\right)^2 - 1} + \left(\frac{\pi}{2} - \tan^{-1}\left(\frac{S_T}{2S_L}\right) - \tan^{-1}\sqrt{\left(\frac{S_{L'}}{S_{T'}}\right)^2 - 1} \right) \right]$ for $2(S_{L'} - d) \geq (S_T - d)$ $\frac{2}{\gamma_V} \left(\frac{S_{L'} - d}{S_T}\right) \left(\frac{S_{L'}}{S_L}\right) \tan^{-1}\left(\frac{2S_L}{S_T}\right)$ for $2(S_{L'} - d) < (S_T - d)$	--
(D)	γ_V	γ_V	γ_V
(E)	1	1	1

APPENDIX E

SINGLE-PHASE FLOW RESISTANCE DATA

Tables E.1 through E.6 list the reduced single-phase flow resistance data for the 0, 30, 45, and 90 degree test sections.

Normalized flow resistance components

$$R_x^* \triangleq \frac{D_v^2}{\mu |\langle \underline{v} \rangle|} \frac{\Delta p_x}{L_x} \quad (E.1)$$

$$R_y^* \triangleq \frac{D_v^2}{\mu |\langle \underline{v} \rangle|} \frac{\Delta p_y}{L_y} \quad (E.2)$$

are tabulated versus fluid temperature, T, and Reynolds number

$$Re_v \triangleq \frac{\rho |\langle \underline{v} \rangle| D_v}{\mu} \quad (E.3)$$

where

$$|\langle \underline{v} \rangle| = \frac{\text{volumetric flow rate}}{\text{flow area}} = \frac{Q}{A_f}$$

$$D_v = \begin{cases} 0.418 \text{ inch (1.06 cm) for } 30^\circ, 45^\circ, \text{ and } 90^\circ \text{ test section} \\ 0.398 \text{ inch (1.01 cm) for } 0^\circ \text{ test section} \end{cases}$$

$$\rho = 62.3 \text{ lbm/ft}^3 \quad (0.998 \text{ g/cm}^3)$$

and the liquid viscosity is calculated for the measured fluid

temperature from the correlation [C.1]

$$\log \frac{\mu(T^\circ\text{C})}{\mu(20^\circ\text{C})} = \frac{1.3272(20 - T^\circ\text{C}) - 0.001053(T^\circ\text{C} - 20)^2}{T^\circ\text{C} + 105} \quad (E.4)$$

where

$$\mu(20^\circ\text{C}) = 2.424 \text{ lb/ft-hr (3.608 kg/m-hr)}$$

Estimated error bars of the measured variables are listed in Table E.7. The range of measured quantities were estimated from the precision of a single measurement (i.e., L , D_v) or fluctuation range of several measurements (i.e., Δp , $|\langle \underline{v} \rangle|$, T). The reduced data error bars are calculated assuming random error.

TABLE E.1

Flow Resistance for Parallel Test Section, Drag Component

$\theta = 0^\circ$

$L_x = 14$ inch (35.6 cm)

Re_v	T(°F)	R_x^*	Re_v	T(°F)	R_x^*
-	RUN 48	-	5,460	Assume	89.5
16,200		183	10,400	60°F	153
13,600	Assume	162	14,700		273
11,000	60°F	136	18,300		336
8,210		114	-	RUN 55	-
5,460		87.0	2,610		69.1
2,750		58.0	3,130	Assume	73.4
1,360		51.5	3,820	60°F	88.7
651		46.5	5,010		109
-	RUN 51	-	6,570		128
542		53.8	7,780		150
845		56.8	9,330		177
1,110	Assume	57.7	11,700		198
1,350	60°F	58.8	12,900		208
1,980		63.0	15,400		241
1,980		57.7	18,600		238
2,800		67.5	-	Run 60	-
4,080		80.4	1,580		65.8
5,420		93.5	3,130	Assume	81.1
7,660		121	5,460	60°F	112
10,300		157	7,780		143
12,400		170	10,300		178
15,000		201	11,600		194
18,500		240	14,800		232
2,820		66.8	18,500		276
3,980		80.8			
-	RUN 53	-			
1,350		54.6			

TABLE E.2

Flow Resistance for 30 Degree Test Section, Drag Component $\theta = 30^\circ$ $L_x = 10 \text{ inch (25.4 cm)}$

Re_v	T(°F)	R_x^*	Re_v	T(°F)	R_x^*
-	RUN 117	-	4,650	73	539
1,020	84	178	5,670	74	619
1,170	84	188	6,840	74	713
1,340	84	201	7,960	74	790
1,510	84	215	10,200	75	968
1,800	85	242	12,900	75	1,150
2,090	85	277	16,000	76	1,380
2,300	85	293	18,400	76	1,550
2,810	85	347	22,700	77	1,850
3,500	86	426	-	RUN 119	-
4,130	86	484	1,010	87	170
4,880	87	554	1,550	87	217
5,830	87	631	2,250	87	286
7,270	87	756	2,840	87	346
8,360	88	829	3,580	87	416
9,650	88	926	5,000	87	537
10,600	88	1,000	8,580	87	816
13,700	89	1,250	12,700	87	1,120
15,100	89	1,340	18,600	88	1,510
17,900	90	1,540	25,900	88	2,020
20,600	90	1,730	-	RUN 120	-
23,100	90	1,930	5,350	88	578
26,600	91	2,150	7,670	88	768
14,800	91	1,340	6,520	89	683
8,040	92	833	8,620	89	847
4,070	92	475	10,400	89	970
-	RUN 118	-	11,600	90	1,070
1,260	72	195	12,700	90	1,160
1,540	72	223	14,800	90	1,310
1,830	72	258	16,300	90	1,410
2,010	72	282	18,200	91	1,540
2,600	72	360	19,600	91	1,640
3,360	73	442	21,900	91	1,760
3,910	73	482	24,400	92	1,940
			27,100	92	2,110

TABLE E.3

Flow Resistance for 30 Degree Test Section, Lift Component

$\theta = 30^\circ$

$L_y = 3.46 \text{ inch (8.80 cm)}$

Re_v	T(°F)	R_y^*	Re_v	T(°F)	R_y^*
-	RUN 121	-	18,200	80	1,770
1,150	69	86.3	19,500	80	1,870
1,410	69	105	21,200	81	2,030
1,810	69	139	22,600	81	2,140
1,110	70	89	23,800	81	2,230
1,390	70	106	7,700	82	789
1,810	70	142	4,470	82	453
2,110	70	180	-	RUN 123	-
2,660	71	235	1,260	66	100
3,060	71	280	1,520	66	121
3,640	72	337	1,930	66	164
4,260	72	404	2,400	66	213
4,870	72	463	2,830	66	265
5,760	72	543	3,310	67	314
7,020	73	654	3,800	67	378
7,790	74	738	4,050	67	401
9,760	74	925	4,610	67	462
-	RUN 122	-	5,470	68	553
1,170	75	115	6,370	68	649
1,530	75	120	7,390	69	743
1,720	75	147	8,290	69	831
2,220	75	200	9,330	70	926
2,700	75	257	10,300	70	1,030
3,300	75	329	11,300	70	1,100
4,010	75	403	12,200	71	1,210
4,560	76	465	13,500	71	1,310
5,300	76	512	14,400	72	1,380
5,980	76	618	15,400	72	1,490
6,830	77	697	16,300	72	1,550
7,600	77	776	17,500	72	1,680
8,360	77	861	18,400	73	1,760
9,460	78	964	19,600	73	1,880
11,100	78	1,110	20,500	73	1,970
12,700	78	1,260	21,800	73	2,070
13,600	79	1,350	8,140	74	808
14,700	79	1,430	4,490	75	434
15,900	80	1,540	2,500	75	230
16,700	80	1,620	1,990	75	175
			1,670	76	148

TABLE E.4

Flow Resistance for 45 Degree Test Section, Drag Component

$\theta = 45^\circ$

$L_x = 10 \text{ inch (25.4 cm)}$

Re_v	T(°F)	R_x^*	Re_v	T(°F)	R_x^*
-	RUN 100	-	12,800	91	3,490
1,310	79	646	13,000	91	3,530
2,020	79	606	13,500	91	3,670
2,740	79	827	16,800	93	4,460
4,090	80	1,067	20,400	94	5,280
5,330	80	1,474	24,200	94	6,140
6,500	81	1,763	-	RUN 102	-
7,820	81	2,078	1,080	77	468
9,010	82	2,357	1,517	78	625
10,100	83	2,626	2,300	78	928
11,500	84	2,873	2,660	79	1,053
12,300	84	3,140	3,380	80	1,275
13,900	85	3,349	4,320	80	1,525
17,000	85	3,773	8,120	81	2,390
21,700	85	4,456	9,370	82	2,729
-	RUN 101	-	11,500	83	3,215
1,000	87	488	13,900	84	3,750
3,281	88	1,304	21,400	84	5,320
1,830	88	782	-	RUN 103	-
2,665	89	1,048	1,130	88	495
5,945	89	1,821	1,450	89	623
7,324	90	2,256	1,740	90	728
8,900	90	2,630	3,060	91	1,160
10,200	90	2,870	4,920	92	1,690
11,700	91	3,220			

TABLE E.5

Flow Resistance for 45 Degree Test Section, Lift Component

$\theta = 45^\circ$

$L_y = 2.65 \text{ inch (6.73 cm)}$

Re_v	T(°F)	R_y^*	Re_v	T(°F)	R_y^*
-	RUN 96	-	2,670	94	773
1,060	65	229	4,250	94	1,200
1,550	65	388	6,190	94	1,670
1,850	66	493	7,190	94	1,990
3,130	66	848	7,910	94	2,040
3,590	66	976	9,500	95	2,420
4,520	67	1,190	10,900	96	2,682
5,340	67	1,363	11,900	96	2,960
6,630	68	1,620	13,500	97	3,240
9,140	69	2,060	14,100	97	3,360
9,660	70	2,290	19,600	97	4,360
13,900	70	2,940	24,900	98	5,500
17,600	70	3,650	-	RUN 99	-
-	RUN 97	-	2,740	79	725
1,030	83	285	2,100	80	557
1,840	84	526	1,540	81	399
2,700	84	791	1,180	82	297
4,480	85	1,270	1,430	84	361
5,590	85	1,520	2,080	85	558
6,870	85	1,820	2,660	85	716
8,910	85	2,270	6,490	86	1,590
9,970	87	2,520	11,700	86	2,590
12,200	88	2,940	15,600	87	3,250
12,600	88	2,990	18,200	87	3,660
15,600	89	3,610	22,200	88	4,260
17,900	90	4,060	4,260	88	1,100
22,800	90	4,930	1,070	89	256
-	RUN 98	-	1,150	92	279
1,947	93	569			

TABLE E.6

Flow Resistance for Crossflow Test Section, Drag Component

$\theta = 90^\circ$

$L_x = 14 \text{ inch (35.6 cm)}$

Re_v	T(°F)	R_x^*	Re_v	T(°F)	R_x^*
-	RUN 108	-	19,100	84	8,930
2,450	73	1,780	-	RUN 110	-
3,420	73	2,330	1,040	72	740
4,460	74	2,920	1,090	72	777
5,430	74	3,370	1,320	73	928
6,510	75	3,870	1,510	74	1,080
7,610	75	4,320	1,820	74	1,350
8,850	76	4,880	2,060	75	1,550
9,470	77	5,140	4,050	76	2,640
11,700	78	6,010	6,230	77	3,610
12,800	78	6,490	8,290	78	4,520
14,700	79	7,210	10,500	79	5,450
17,930	79	8,340	13,300	80	6,680
-	RUN 109	-	16,400	80	7,830
1,050	78	796	18,100	80	8,440
1,150	78	890	-	RUN 111	-
2,100	78	1,620	1,070	77	824
3,220	79	2,290	1,470	77	1,130
4,280	80	2,860	2,100	78	1,560
5,390	80	3,310	2,620	78	1,910
6,990	81	4,030	2,850	79	2,050
8,690	82	4,740	3,220	79	2,250
10,200	82	5,410	3,450	80	2,390
12,300	83	6,250	3,740	80	2,530
15,000	84	7,310	6,530	81	3,780
18,000	84	8,400	12,000	81	6,080

TABLE E.7

Estimated Measurement Error Bars

Variable	Relative Error (%)
D_v	± 3.0
$\mu(T)$	± 1.3
$ \langle \underline{v} \rangle $	± 0.5
L_x	± 1.3
L_y	± 2.0
$\rho(T)$	± 0.33
Δp	± 2.0
Re_v	± 3.3
R_x^*	± 5.1
R_y^*	± 5.3

APPENDIX F

SINGLE BUBBLE VELOCITY AND TRAJECTORY DATA

Bubble velocities and trajectories were measured by recording the time of flight, starting, and termination points for a bubble of known volume. The measured variables are shown in Fig. F.1. The bubble trajectory is

$$\phi_b = \text{Tan}^{-1} \left(\frac{y_2 - y_1}{x_2 - x_1} \right) \quad (\text{F.1})$$

The bubble velocity is

$$\left| \langle \frac{v}{g} \rangle \right| = \sqrt{\frac{(y_2 - y_1)^2 + (x_2 - x_1)^2}{\Delta t}} \quad (\text{F.2})$$

The bubble equivalent diameter is

$$D_b = \left(\frac{6V_b}{\pi} \right)^{1/3} \quad (\text{F.3})$$

The bubble velocity for the test duct (infinite medium), parallel, and crossflow test sections are tabulated in Tables F.1, F.2, and F.3. The bubble velocity and trajectory for the 45 degree test section at liquid velocities of zero, 0.36 and 0.56 ft/sec (zero, 0.11, and 0.17 m/sec) are given in Tables F.4 through F.8.

The tabulated data are given in English units. They may be converted to SI units by:

$$v \text{ (m/sec)} = 0.3048 v \text{ (ft/sec)} \quad (\text{F.4})$$

$$D_b \text{ (cm)} = 2.54 D_b \text{ (inch)} \quad (\text{F.5})$$

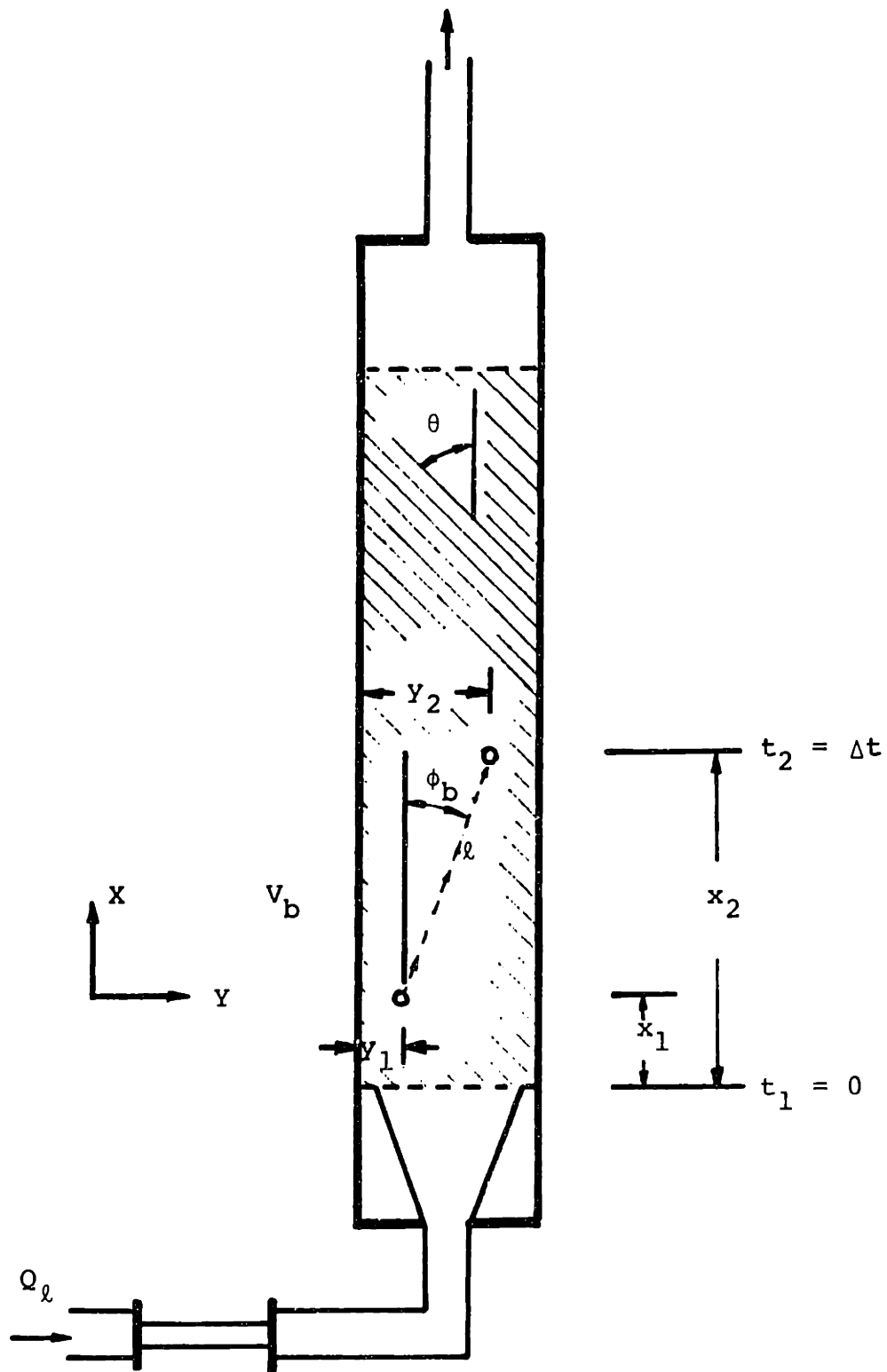


Figure F.1 Measured quantities for determining bubble velocity and trajectory.

TABLE F.1

Bubble Velocity in Test Duct

$$|\langle \underline{v}_g \rangle| = 0 \quad \phi_b = 0^\circ$$

D_b (inch)	$ \langle \underline{v}_g \rangle $ (ft/sec)	D_b (inch)	$ \langle \underline{v}_g \rangle $ (ft/sec)
0.03	0.28	0.27	0.71
0.06	0.98	0.27	0.74
0.06	0.94	0.28	0.72
0.08	0.87	0.29	0.76
0.08	0.90	0.30	0.74
0.11	0.85	0.30	0.75
0.11	0.78	0.30	0.73
0.12	0.62	0.31	0.76
0.12	0.82	0.31	0.74
0.12	0.84	0.31	0.76
0.12	0.83	0.32	0.78
0.13	0.63	0.32	0.76
0.13	0.81	0.32	0.73
0.14	0.67	0.32	0.75
0.15	0.69	0.32	0.73
0.16	0.68	0.33	0.77
0.18	0.67	0.33	0.76
0.18	0.70	0.33	0.75
0.18	0.67	0.34	0.76
0.20	0.69	0.34	0.73
0.20	0.68	0.34	0.75
0.20	0.69	0.34	0.76
0.20	0.68	0.34	0.74
0.20	0.69	0.35	0.77
0.21	0.69	0.36	0.75
0.22	0.70	0.36	0.79
0.22	0.69	0.38	0.78
0.23	0.71	0.38	0.79
0.23	0.71	0.39	0.79
0.24	0.72	0.39	0.79
0.26	0.71	0.41	0.82
0.26	0.72	0.42	0.82
0.26	0.71	0.43	0.82

TABLE F.2

Bubble Velocity in Parallel Test Section

$$\left| \langle \underline{v}_{-g} \rangle \right| = 0$$

$$\phi_b = 0^\circ$$

D_b (inch)	$\left \langle \underline{v}_{-g} \rangle \right $ (ft/sec)	D_b (inch)	$\left \langle \underline{v}_{-g} \rangle \right $ (ft/sec)
0.03	0.20	0.24	0.65
0.03	0.24	0.25	0.66
0.03	0.30	0.26	0.63
0.03	0.22	0.26	0.75
0.03	0.21	0.26	0.71
0.06	0.74	0.26	0.75
0.06	0.70	0.27	0.75
0.06	0.80	0.27	0.77
0.08	0.74	0.28	0.73
0.08	0.78	0.28	0.78
0.08	0.74	0.28	0.78
0.08	0.75	0.30	0.77
0.11	0.70	0.30	0.78
0.11	0.74	0.30	0.80
0.12	0.64	0.31	0.78
0.12	0.72	0.31	0.82
0.12	0.64	0.32	0.80
0.12	0.66	0.32	0.82
0.12	0.71	0.32	0.88
0.12	0.73	0.33	0.88
0.12	0.74	0.34	0.87
0.12	0.70	0.34	0.84
0.14	0.57	0.35	0.83
0.16	0.57	0.35	0.92
0.16	0.55	0.36	0.72
0.19	0.58	0.39	0.92
0.20	0.57	0.39	0.92
0.21	0.59	0.39	0.90
0.22	0.64	0.40	0.90
0.24	0.63	0.41	0.94
0.24	0.66		

TABLE F.3

Bubble Velocity in Crossflow Test Section

$$\left\langle \frac{v}{-g} \right\rangle = 0$$

$$\phi_b = 0^\circ$$

D_b (inch)	$\left\langle \frac{v}{-g} \right\rangle$ (ft/sec)	D_b (inch)	$\left\langle \frac{v}{-g} \right\rangle$ (ft/sec)
0.03	0.22	0.23	0.58
0.03	0.23	0.24	0.64
0.06	0.51	0.25	0.63
0.08	0.51	0.25	0.59
0.08	0.57	0.27	0.61
0.09	0.49	0.28	0.60
0.11	0.56	0.29	0.62
0.11	0.51	0.29	0.64
0.12	0.54	0.30	0.63
0.12	0.54	0.30	0.64
0.12	0.55	0.31	0.61
0.12	0.53	0.31	0.62
0.12	0.56	0.32	0.65
0.13	0.57	0.32	0.65
0.15	0.63	0.32	0.63
0.15	0.58	0.33	0.65
0.16	0.58	0.33	0.63
0.16	0.57	0.34	0.64
0.17	0.55	0.35	0.62
0.19	0.61	0.36	0.61
0.20	0.61	0.36	0.65
0.21	0.59	0.36	0.60
0.21	0.58	0.37	0.66
0.22	0.57	0.39	0.68
0.22	0.61	0.41	0.71
0.22	0.60	0.42	0.70
0.22	0.58	0.43	0.74
0.23	0.63		

TABLE F.4

Bubble Trajectory in 45 Degree Test Section : $|\langle \underline{v}_\ell \rangle| = 0$

D_b (inch)	ϕ_b (degree)	D_b (inch)	ϕ_b (degree)
0.03	0.0	0.24	4.0
0.08	-1.3	0.25	9.7
0.10	-2.1	0.25	8.0
0.10	-1.4	0.25	10.7
0.10	-1.1	0.25	10.3
0.11	-0.8	0.25	7.7
0.11	-0.3	0.25	4.6
0.11	-1.9	0.26	7.5
0.11	-0.2	0.26	10.5
0.12	-0.1	0.26	10.5
0.13	-3.5	0.26	6.5
0.14	-0.9	0.27	12.2
0.16	-4.6	0.27	10.0
0.17	-3.0	0.28	6.8
0.17	-2.8	0.28	9.2
0.18	-3.5	0.30	7.2
0.18	-3.0	0.31	7.6
0.18	-2.9	0.31	9.0
0.20	-3.3	0.32	7.0
0.21	-2.6	0.32	6.2
0.21	-1.4	0.33	5.0
0.22	9.8	0.33	4.5
0.22	7.7	0.33	3.9
0.22	4.4	0.33	7.6

TABLE F.5

Bubble Velocity in 45 Degree Test Section: $|\langle \underline{v}_g \rangle| = 0$

D_b (inch)	$ \langle \underline{v}_g \rangle $ (ft/sec)	D_b (inch)	$ \langle \underline{v}_g \rangle $ (ft/sec)
0.06	0.51	0.22	0.40
0.08	0.50	0.24	0.63
0.08	0.64	0.25	0.65
0.10	0.51	0.25	0.64
0.10	0.52	0.25	0.54
0.10	0.53	0.25	0.50
0.11	0.46	0.25	0.62
0.11	0.50	0.25	0.64
0.11	0.54	0.26	0.62
0.11	0.52	0.26	0.61
0.12	0.62	0.26	0.62
0.12	0.52	0.26	0.60
0.13	0.53	0.26	0.59
0.14	0.55	0.27	0.53
0.16	0.54	0.27	0.64
0.17	0.57	0.28	0.60
0.17	0.56	0.30	0.61
0.18	0.56	0.31	0.63
0.18	0.55	0.31	0.62
0.18	0.58	0.32	0.59
0.20	0.58	0.32	0.64
0.21	0.57	0.33	0.66
0.21	0.59	0.33	0.62
0.22	0.61	0.33	0.66
0.22	0.54	0.35	0.59

TABLE F.6

Bubble Trajectory in 45 Degree Test Section: $|\langle v_{\underline{z}} \rangle| = 0.36$ ft/sec

D_b (inch)	ϕ_b (degree)	D_b (inch)	ϕ_b (degree)
0.16	9.7	0.26	9.9
0.17	9.1	0.27	11.1
0.19	12.0	0.27	9.8
0.20	12.3	0.27	11.4
0.21	11.7	0.28	10.9
0.21	8.1	0.28	10.2
0.22	11.4	0.28	10.5
0.22	11.4	0.28	10.0
0.22	12.2	0.28	10.5
0.23	12.0	0.28	11.2
0.23	12.1	0.29	11.5
0.24	12.1	0.29	10.5
0.24	11.3	0.29	10.9
0.24	7.6	0.29	6.9
0.24	10.5	0.29	12.0
0.25	10.3	0.30	10.3
0.26	10.7	0.30	6.3
0.26	9.6	0.32	7.8

TABLE F.7

Bubble Trajectory in 45 Degree Test Section: $|\langle v_{-l} \rangle| = 0.56$ ft/sec

D_b (inch)	ϕ_b (degree)	D_b (inch)	ϕ_b (degree)
0.14	6.6	0.27	13.2
0.15	8.7	0.28	12.0
0.16	9.1	0.28	13.9
0.16	10.6	0.28	12.5
0.19	10.8	0.29	14.1
0.19	11.7	0.29	11.3
0.20	13.6	0.29	12.0
0.20	14.6	0.29	8.7
0.22	13.3	0.29	14.1
0.23	6.8	0.29	8.2
0.23	12.3	0.30	13.5
0.23	11.8	0.31	13.3
0.24	14.4	0.32	12.3
0.25	14.1	0.33	14.6
0.26	12.7		

TABLE F.8

Bubble Velocity in 45 Degree Test Section: $|\langle v_{-l} \rangle| > 0$

$ \langle v_{-l} \rangle $ (ft/sec)	D_b (inch)	$ \langle v_{-g} \rangle $ (ft/sec)
0.36 	0.28	1.33
	0.28	1.34
	0.28	1.19
	0.28	1.32
	0.28	1.36
	0.29	1.27
	0.29	1.36
0.56 	0.27	1.58
	0.28	1.32
	0.28	1.35
	0.29	1.57
	0.29	1.35
	0.29	1.38
	0.29	1.69

APPENDIX G

DERIVATION OF MULTIPLE BUBBLE DRAG MODEL

Ishii [1.3, I.5] has developed a model for the drag coefficient of multiple bubbles in an infinite medium based on modifying single bubble drag correlations. To follow is a derivation of Ishii's multiple bubble model starting with his single bubble model.

G.1 Single Bubble Model

Ishii single bubble model for drag in an infinite medium is

$$|F_{D\infty}| = C_{D\infty} [Re_{b\infty}] a_p \frac{\rho_l |v_{r\infty}|^2}{2} \quad (G.1)$$

$$C_{D\infty} = \begin{cases} \frac{24}{Re_{b\infty}} (1 + 0.1 Re_b^{0.75}) & N_\mu \leq \frac{36\sqrt{2}}{(Re_{b\infty}^{VD})^2} (1 + 0.1 (Re_{b\infty}^{VD})^{0.75}) \\ \frac{2}{3} D_b \sqrt{\frac{g(\rho_l - \rho_g)}{\sigma}} & \text{elsewhere} \\ \frac{8}{3} & D_b \geq 4 \sqrt{\frac{\sigma}{g(\rho_l - \rho_g)}} \end{cases} \quad (G.2)$$

where

$$Re_{b\infty} \triangleq \frac{\rho_l D_b |v_{r\infty}|}{\mu_l} \quad (G.3)$$

$$N_\mu \triangleq \hat{M}^{1/4} = \frac{\mu_l}{\left\{ \rho_l \sigma \sqrt{\frac{\sigma}{g(\rho_l - \rho_g)}} \right\}^{1/2}} \quad (G.4)$$

$$a_p \triangleq \frac{3}{2} \frac{1}{D_b}$$

In Eq. (G.2) the first equality is the viscous bubble regime, the

second is the distorted bubble regime, and the third capped bubble regime. The viscous-distorted transition point

$$N_{\mu} = \frac{36\sqrt{2}}{(Re_{b_{\infty}}^{VD})^2} (1 + 0.1(Re_{b_{\infty}}^{VD})^{0.75}) \quad (G.5)$$

was obtained by using continuity of the relative velocity and consequently the drag coefficient at the transition point. First a relation between relative velocity and bubble diameter is obtained in the distorted regime for buoyancy driven flow, $|F_{D_{\infty}}| = (\rho_{\ell} - \rho_g)g$. From Eq. (G.1)

$$C_{D_{\infty}}^D = \frac{2|F_{D_{\infty}}|}{a_p \rho_{\ell} |v_{r_{\infty}}|^2} = \frac{4D_b(\rho_{\ell} - \rho_g)g}{3\rho_{\ell} |v_{r_{\infty}}|^2} \quad (G.6)$$

Equating with $C_{D_{\infty}}^D$ of Eq. (G.2) and solving for the Reynolds number gives

$$Re_{b_{\infty}} = D_b \frac{\sqrt{2}}{N_{\mu}} \sqrt{\frac{g(\rho_{\ell} - \rho_g)}{\sigma}} \quad (G.7)$$

Now equating the viscous and distorted drag coefficients

$$C_{D_{\infty}}^V [Re_{b_{\infty}}^{VD}] = C_{D_{\infty}}^D [Re_{b_{\infty}}^{VD}] \quad (G.8)$$

evaluating Eq. (G.7) at the viscous-distorted limit and eliminating D_b^{VD} in favor of $Re_{b_{\infty}}^{VD}$, gives Eq. (G.5).

Conversely, the transition bubble diameter D_b^{VD} can be found by eliminating the transition Reynolds number $Re_{b_{\infty}}^{VD}$, thus

$$\left(D_b^{VD} \sqrt{\frac{g(\rho_{\ell} - \rho_g)}{\sigma}} \right)^2 = 18\sqrt{2} N_{\mu} \left\{ 1 + 0.1 \left(\frac{\sqrt{2}}{N_{\mu}} D_b^{VD} \sqrt{\frac{g(\rho_{\ell} - \rho_g)}{\sigma}} \right)^{0.75} \right\} \quad (G.9)$$

An explicit approximation of Eq (G.9) is

$$D_b^{VD} \sqrt{\frac{g(\rho_l - \rho_g)}{\sigma}} \approx 5.42 N_\mu^{1/3} \quad (G.10)$$

G.2 Multiple Bubble Model

The multiple bubble drag coefficient is defined by

$$|F_{-D',\infty}| = C_{D',\infty} [Re_{b',\infty}] a_p \frac{\rho_l |v_{-r',\infty}|^2}{2} \quad (G.11)$$

where the prime denotes multiple bubbles. Dividing Eq. (G.11) by (G.1) gives a useful identity

$$C_{D',\infty} [Re_{b',\infty}] = C_{D,\infty} [Re_{b,\infty}] \left| \frac{v_{-r,\infty}}{v_{-r',\infty}} \right|^2 \left| \frac{F_{-D',\infty}}{F_{-D,\infty}} \right| \quad (G.12)$$

G.2.1 Viscous Regime

The first equality of Eq. (G.2) is for viscous single bubbles. Ishii hypothesizes that a similarity between single and multiple bubble systems can be drawn when the liquid viscosity is replaced by the mixture viscosity μ_m , thus

$$C_{D',\infty}^V [Re_{b',\infty}] = \frac{24}{Re_{b',\infty}} \left(\frac{\mu_m}{\mu_l} \right) \left(1 + 0.1 \left(Re_{b',\infty} \frac{\mu_l}{\mu_m} \right)^{0.75} \right) \quad (G.13)$$

The justification of using mixture viscosity similarity is that as a bubble moves through a dispersed two-phase medium it causes translation and rotation of the medium in the neighborhood of the bubble. The addition of discrete bubbles in the liquid makes the surrounding medium appear more rigid, increasing the resistance to motion. This increased resistance is accounted for by the higher viscosity of the mixture relative to that for the liquid alone, i.e.,

$$\frac{\mu_m}{\mu_l} = \left(1 - \frac{\langle \alpha \rangle}{\alpha_m}\right)^{-2.5} \alpha_m \left(\frac{\mu_g + 0.4 \mu_l}{\mu_g + \mu_l}\right) \quad (G.14)$$

where α_m is the maximum packing void fraction. Equation (G.14) derived by Ishii [I.4] is an interpolation between linear and power correlations for the mixture viscosity for fluid and solid particles, respectively. For bubbly, gas-liquid flow $\mu_g \ll \mu_l$ and $\alpha_m = 1$, so Eq. (G.14) reduces to

$$\frac{\mu_m}{\mu_l} = \frac{1}{1 - \langle \alpha \rangle} \quad (G.15)$$

G.2.2 Distorted Regime

The drag coefficient for a single distorted bubble is independent of $|\underline{v}_{r\infty}|$ and μ_l (second equality of Eq. (G.2)). For multiple bubbles it is assumed that the drag is also independent of relative velocity and viscosity. Thus for a given bubble diameter

$$\frac{C_{D,\infty}^D [Re_{b,\infty}]}{C_{D\infty}^D [Re_{b\infty}]} = \text{Constant} = \frac{C_{D,\infty}^D [Re_{b,\infty}^{VD}]}{C_{D\infty}^D [Re_{b\infty}^{VD}]} = \frac{C_{D,\infty}^V [Re_{b,\infty}^{VD}]}{C_{D\infty}^V [Re_{b\infty}^{VD}]} \quad (G.16)$$

where the last equality is obtained by requiring continuity at the transition point.

By evaluating the drag coefficient ratio at the viscous-distorted transition point with the viscous regime correlations, the distorted multiple bubble drag can be calculated from

$$C_{D,\infty}^D [Re_{b,\infty}] = \frac{2}{3} D_b \sqrt{\frac{g(\rho_l - \rho_g)}{\sigma}} \frac{C_{D,\infty}^V [Re_{b,\infty}^{VD}]}{C_{D\infty}^V [Re_{b\infty}^{VD}]} \quad (G.17)$$

Explicit expressions for the viscous-distorted transition can be developed to simplify Eq. (G.17). Dividing Eq. (G.13) by Eq. (G.2) for the viscous regime, gives

$$\frac{C_{D'_{\infty}}^V [Re_{b'_{\infty}}]}{C_{D_{\infty}}^V [Re_{b_{\infty}}]} = \left| \frac{v_{r_{\infty}}}{v_{r'_{\infty}}} \right| \left(\frac{\mu_m}{\mu_l} \right) \frac{1 + 0.1 \left(Re_{b_{\infty}} \left| \frac{v_{r'_{\infty}}}{v_{r_{\infty}}} \right| \left(\frac{\mu_l}{\mu_m} \right) \right)^{0.75}}{1 + 0.1 (Re_{b_{\infty}})^{0.75}} \quad (G.18)$$

An alternate expression can be obtained from Eq. (G.12)

$$\frac{C_{D'_{\infty}}^V [Re_{b'_{\infty}}]}{C_{D_{\infty}}^V [Re_{b_{\infty}}]} = \left| \frac{v_{r_{\infty}}}{v_{r'_{\infty}}} \right|^2 \left| \frac{F_{D'_{\infty}}}{F_{D_{\infty}}} \right| \quad (G.19)$$

For an infinite medium the drag force is buoyancy controlled, so

$$\left| \frac{F_{D'_{\infty}}}{F_{D_{\infty}}} \right| = \frac{(1 - \langle \alpha \rangle)(\rho_l - \rho_g)g}{(\rho_l - \rho_g)g} = (1 - \langle \alpha \rangle) \quad (G.20)$$

Substituting Eq. (G.20) into Eq. (G.19), equating Eq. (G.18) to (G.19), and solving for $\left| \frac{v_{r'_{\infty}}}{v_{r_{\infty}}} \right|$ gives

$$\left| \frac{v_{r'_{\infty}}}{v_{r_{\infty}}} \right| = \frac{1}{(1 - \langle \alpha \rangle)} \left(\frac{\mu_m}{\mu_l} \right) \frac{1 + 0.1 \left(Re_{b_{\infty}} \left| \frac{v_{r'_{\infty}}}{v_{r_{\infty}}} \right| \left(\frac{\mu_l}{\mu_m} \right) \right)^{0.75}}{1 + 0.1 (Re_{b_{\infty}})^{0.75}} \quad (G.21)$$

This implicit expression can be approximated explicitly by noting that the implicit term is dominant only at high $Re_{b_{\infty}}$. Substituting the limit

$$\text{Limit}_{Re_{b_{\infty}} \rightarrow \infty} \left| \frac{v_{r'_{\infty}}}{v_{r_{\infty}}} \right| = (1 - \langle \alpha \rangle)^{4/7} \left(\frac{\mu_l}{\mu_m} \right)^{1/7} \quad (G.22)$$

into Eq. (G.21)

$$\left| \frac{v_{r'_{\infty}}}{v_{r_{\infty}}} \right| = \frac{1}{(1 - \langle \alpha \rangle)} \left(\frac{\mu_m}{\mu_l} \right) \frac{1 + 0.1 \text{Re}_{b_{\infty}}^{0.75} \left(\sqrt{1 - \langle \alpha \rangle} \frac{\mu_l}{\mu_m} \right)^{6/7}}{1 + 0.1 \text{Re}_{b_{\infty}}^{0.75}} \quad (\text{G.23})$$

Finally substituting back into Eq. (G.19) and evaluating at the transition point gives the drag coefficient ratio at the viscous-distorted transition

$$\frac{C_{D'_{\infty}}^V [\text{Re}_{b'_{\infty}}^{\text{VD}}]}{C_{D_{\infty}}^V [\text{Re}_{b_{\infty}}^{\text{VD}}]} = \left\{ \frac{1 + 0.1 (\text{Re}_{b_{\infty}}^{\text{VD}})^{0.75} f'[\alpha]^{6/7}}{f'[\alpha] (1 + 0.1 (\text{Re}_{b_{\infty}}^{\text{VD}})^{0.75})} \right\}^2 \quad (\text{G.24})$$

where

$$f'[\alpha] = \sqrt{1 - \langle \alpha \rangle} \left(\frac{\mu_l}{\mu_m} \right) \quad (\text{G.25})$$

or for bubbly flow

$$f'[\alpha] = (1 - \langle \alpha \rangle)^{1.5} \quad (\text{G.26})$$

All that remains is an expression for $\text{Re}_{b_{\infty}}^{\text{VD}}$. Ishii uses the approximation that $\text{Re}_{b_{\infty}}^{\text{VD}} \approx \text{Re}_{b_{\infty}}^{\text{VN}}$ where VN is the viscous-Newton transition point. The Newton regime is the high Reynolds number drag limit for a solid sphere, i.e.,

$$C_{D_{\infty}}^{\text{N}} [\text{Re}_{b_{\infty}}^{\text{N}}] = 0.45 \quad (\text{G.27})$$

Equating the viscous and Newton drag coefficients (Eq. (G.27) to (G.13)) and, solving for the transition Reynolds number yields $\text{Re}_{b_{\infty}}^{\text{VN}} = 1,006$. Finally substituting $\text{Re}_{b_{\infty}}^{\text{VN}}$ into Eq. (G.24) and subsequently Eq. (G.24) into Eq. (G.17) gives

$$C_{D'_{\infty}}^{\text{D}} [\text{Re}_{b'_{\infty}}] = D_b \sqrt{\frac{g(\rho_l - \rho_g)}{\sigma}} \left\{ \frac{1 + 17.86 f'[\alpha]^{6/7}}{18.86 f'[\alpha]} \right\}^2 \quad (\text{G.28})$$

A more precise expression for $Re_{b\infty}^{VD}$ can be obtained by solving Eq. (G.5) explicitly for $Re_{b\infty}^{VD}$. Using the explicit approximation employed for D_b^{VD} , (substituting Eq. (G.10) into Eq. (G.7)), gives

$$Re_{b\infty}^{VD} = \frac{7.66}{N_{\mu}^{2/3}} \quad (G.29)$$

Consequently the distorted regime drag coefficient becomes

$$C_{D',\infty}^D [Re_{b',\infty}] = \frac{2}{3} D_b \sqrt{\frac{g(\rho_l - \rho_g)}{\sigma}} \left\{ \frac{1 + \frac{0.460}{\sqrt{N_{\mu}}} f'[\alpha]^{6/7}}{f'[\alpha] \left(1 + \frac{0.460}{\sqrt{N_{\mu}}}\right)} \right\}^2 \quad (G.30)$$

G.2.3 Churn-Turbulent Regime

As the bubble diameter increases the wake of one bubble will not only influence the surrounding liquid but also influence the motion of neighboring bubbles directly. This interaction between bubbles creates a continuous churning, hence the name churn-turbulent regime. Ishii models this regime by hypothesizing that drag is governed by that for the largest bubble, i.e., capped bubble, where the characteristic velocity between phases is the drift velocity $|\underline{v}_{gj}|$,

$$|\underline{v}_{gj}| = (1 - \langle \alpha \rangle) |\underline{v}_{r',\infty}| \quad (G.31)$$

Thus the drag force becomes

$$|\underline{F}_{D',\infty}| = C_{D\infty}^C [Re_{b\infty}] a_p \frac{\rho_l |\underline{v}_{gj}|^2}{2} \quad (G.32)$$

Substituting Eq. (G.31) into Eq. (G.32) and comparing with the definition of multiple drag coefficient, Eq. (G.11) gives

$$C_{D',\infty}^C [Re_{b',\infty}] = \frac{8}{3} (1 - \langle \alpha \rangle)^2 \quad (G.33)$$

G.3 Summary

The drag coefficient for multiple bubble flow in an infinite medium is summarized in Table G.1. In Table G.1 the ranges are expressed in terms of bubble diameter and the expressions for μ_m/μ_l (Eq. (G.15)) and $f'[\alpha]$ (Eq. (G.26)) have been substituted in.

TABLE G.1

Multiple Bubble Drag Coefficient

$$|F_{D,\infty}| = C_{D,\infty}^a \rho \frac{|v_{r,\infty}|^2}{2}$$

Drag Coefficient		Range
$C_{D,\infty}^V = \frac{24}{(1 - \langle\alpha\rangle) Re_{b,\infty}} \{1 + 0.1[(1 - \langle\alpha\rangle) Re_{b,\infty}]^{0.75}\}$		$D_b < D_b^{VD}$
$C_{D,\infty}^D = \frac{2}{3} D_b \sqrt{\frac{g(\rho_l - \rho_g)}{\sigma}}$	$\left[\frac{1 + \frac{0.460}{\sqrt{N_\mu}} (1 - \langle\alpha\rangle)^{9/7}}{(1 - \langle\alpha\rangle)^{3/2} (1.0 + \frac{0.460}{\sqrt{N_\mu}})} \right]^2$	$D_b^{VD} < D_b < D_b^{DC}$
$C_{D,\infty}^C = \frac{8}{3} (1 - \langle\alpha\rangle)^2$		$D_b^{DC} < D_b$
<p>where: $D_b^{VD} \approx 5.42 N_\mu^{1/3} \sqrt{\frac{\sigma}{g(\rho_l - \rho_g)}}$</p>		
$D_b^{DC} = 4 \sqrt{\frac{\sigma}{g(\rho_l - \rho_g)}} (1 - \langle\alpha\rangle)^5$	$\left[\frac{1 + \frac{0.460}{\sqrt{N_\mu}}}{1 + \frac{0.460}{\sqrt{N_\mu}} (1 - \langle\alpha\rangle)^{9/7}} \right]^2$	

APPENDIX H
THERMIT-2 MODIFICATIONS

Several modifications to the THERMIT-2, [K.3] a two-fluid thermal-hydraulic computer code, were required for simulations of the inclined rod array experiment to be performed. The following is a list of the modifications made. Full documentation of the modifications is given in Ref. [T.5].

- Inclusion of air properties option for the gas phase.
- Implemented the capability for inclined rods with respect to the principal coordinate system of the code. This modification allowed calculation of flow resistance for a rod array at an inclined angle to the numerical mesh coordinate system.
- Generalized the body force (gravity) vector to all coordinate directions. Previously gravity was restricted to the z-component direction.
- Generalized the input requirements so cell specific quantities could be input for all geometric variables (not restricted to a single input for a single column of cells or all cells).
- Revised the interfacial drag model to employ the magnitude of the total relative velocity vector (See Sec. 6.5 for details).

APPENDIX I

BUBBLE VELOCITY AND TRAJECTORY CALCULATIONS

I.1 Isotropic Model

The following is a sample calculation of the bubble trajectory and velocity using the isotropic model of Sec. 6.5.2,

$$\begin{aligned} \underline{F}_D &= F_{D||} \underline{e}_{||} + F_{D\perp} \underline{e}_{\perp} \\ &= C_{D\perp} a_p \frac{\rho_l |\underline{v}_r|}{2} v_{r||} \underline{e}_{||} + C_{D\perp} a_p \frac{\rho_l |\underline{v}_r|}{2} v_{r\perp} \underline{e}_{\perp} \end{aligned} \quad (I.1)$$

$$\begin{aligned} \underline{v}_r &= v_{r||} \underline{e}_{||} + v_{r\perp} \underline{e}_{\perp} \\ &= (\langle v_{g||} \rangle - \langle v_{l||} \rangle) \underline{e}_{||} + (\langle v_{g\perp} \rangle - \langle v_{l\perp} \rangle) \underline{e}_{\perp} \end{aligned} \quad (I.2)$$

The inclination of the driving force ψ , is

$$\tan \psi = \frac{F_{D\perp}}{F_{D||}} = \frac{F_{R\perp} + F_{G\perp}}{F_{R||} + F_{G||}} \quad (I.3)$$

The sample calculation flow conditions are:

$D_v = 0.0388 \text{ ft}$	$ \langle \underline{v}_l \rangle = 1 \text{ ft/sec}$
$\theta = 45^\circ$	$\rho_l = 62.22 \text{ lbm/ft}^3$
$\langle \alpha \rangle = 0.0$	$\rho_g = 0.0749 \text{ lbm/ft}^3$
$D_b = 0.02 \text{ ft}$	$\mu_g = 5.78 \times 10^{-4} \text{ lbm/ft sec}$
	$\sigma = 5 \times 10^{-3} \text{ lbf/ft}$

Then

$$a_p \frac{\Delta}{2D_b} = 70.2 \text{ ft}^{-1} \quad \text{Re}_v \frac{\Delta}{\mu_l} = \frac{\rho_l D_v |\langle \underline{v}_l \rangle|}{\mu_l} = 4,180$$

The buoyancy force is:

$$\begin{aligned} F_{G||} &= (1 - \langle \alpha \rangle)(\rho_l - \rho_g)g \cos \theta = 44.0 \text{ lbf/ft}^3 \\ F_{G\perp} &= (1 - \langle \alpha \rangle)(\rho_l - \rho_g)g \sin \theta = 44.0 \text{ lbf/ft}^3 \end{aligned} \quad (I.4)$$

The flow resistance obtained from the fits in Table 5.6, is:

$$R_x^* (45^\circ) = 1.42 (Re_v)^{0.837} = 1,520 \quad (I.5)$$

$$R_y^* (45^\circ) = 1.19 (Re_v)^{0.827} = 1,170$$

Assuming the presence of a bubble has a negligible effect on the single-phase flow resistance the bubble resistance force becomes

$$F_{R||} = \frac{\mu_l |\langle \underline{v}_l \rangle|}{D_v^2} (R_x^* \cos \theta - R_y^* \sin \theta) = 2.95 \text{ lbf/ft}^3 \quad (I.6)$$

$$F_{R\perp} = \frac{\mu_l |\langle \underline{v}_l \rangle|}{D_v^2} (R_x^* \sin \theta + R_y^* \cos \theta) = 22.7 \text{ lbf/ft}^3$$

Finally summing Eqs. (I.4) and (I.5) gives

$$\begin{aligned} F_{D||} &= 47.0 \text{ lbf/ft}^3 \\ F_{D\perp} &= 66.7 \text{ lbf/ft}^3 \\ |\underline{F}_D| &= 80.3 \text{ lbf/ft}^3 \end{aligned} \quad (I.7)$$

and substituting the above into Eq. (I.3) gives $\psi = 54.8^\circ$, or

$$(\psi - \theta) = 9.8^\circ \quad (I.8)$$

Now solving Eq. (I.1) for the relative velocity components yields

$$v_{r||} = \frac{F_{D||}}{\sqrt{\frac{\rho_l}{2} a_p C_{D\perp} |\underline{F}_D|}} \quad (I.9)$$

$$v_{r\perp} = \frac{F_D}{\sqrt{\frac{\rho_l}{2} a_p C_{D\perp} |\underline{F}_D|}} \quad (I.10)$$

The crossflow drag coefficient is

$$C_{D\perp} = C_{D\infty} \left[Re_{b\perp} \left| \frac{\underline{v}_{r\infty}}{\underline{v}_{r\perp}} \right| \right] \left| \frac{\underline{v}_{r\infty}}{\underline{v}_{r\perp}} \right|^2 \quad (I.11)$$

For $D_b = 0.02$ ft,

$$\frac{D_b}{\bar{L}_{\text{gap}}} = \frac{0.020}{0.018} = 1.13 > 0.6 \quad (\text{I.12})$$

so from the piecewise relative velocity ratio approximation (Eq. (6.41))

$$\left| \frac{v_{r\perp}}{v_{r\infty}} \right| = 0.85 \quad (\text{I.13})$$

Also since

$$0.0070 \text{ ft} = D_b^{\text{VD}} < D_b < D_b^{\text{DC}} = 0.036 \quad (\text{I.14})$$

the distorted regime infinite medium drag coefficient is used in Eq.

(I.11) yielding

$$C_D = \frac{2}{3} D_b \sqrt{\frac{g(\rho_l - \rho_g)}{\sigma}} \left| \frac{v_{r\infty}}{v_{r\perp}} \right|^2 = 2.06 \quad (\text{I.15})$$

Now evaluating Eqs. (I.9) and (I.10) gives

$$\begin{aligned} v_{r\parallel} &= 0.438 \text{ ft/sec} \\ v_{r\perp} &= 0.622 \text{ ft/sec} \end{aligned} \quad (\text{I.16})$$

Using Eq. (I.2) to solve for the bubble velocity components gives

$$\begin{aligned} \langle v_{g\parallel} \rangle &= v_{r\parallel} + \langle v_{l\parallel} \rangle \\ &= v_{r\parallel} + |\langle v_{-l} \rangle| \cos \theta = 1.15 \text{ ft/sec} \\ \langle v_{g\perp} \rangle &= v_{r\perp} + \langle v_{l\perp} \rangle \\ &= v_{r\perp} + |\langle v_{-l} \rangle| \sin \theta = 1.33 \text{ ft/sec} \end{aligned} \quad (\text{I.17})$$

Finally the bubble velocity is

$$|\langle v_{-g} \rangle| = \sqrt{\langle v_{g\parallel} \rangle^2 + \langle v_{g\perp} \rangle^2} = 1.75 \text{ ft/sec} \quad (\text{I.18})$$

and the bubble trajectory is

$$\theta_g = \text{Tan}^{-1} \left(\frac{v_{g\perp}}{v_{g\parallel}} \right) = 49.1^\circ \quad (\text{I.19})$$

or

$$\phi_b = \theta_g - \theta = 4.1^\circ \quad (\text{I.20})$$

The angles $(\psi - \theta) = 9.8^\circ$ and $\phi_b = 4.1^\circ$ can be seen in Fig. I.1 for $|\langle v_{\perp} \rangle| = 1$ ft/sec.

I.2 Two-Region Model

A program was written to calculate the bubble trajectory and velocity for the two-region model given in Table 6.4. Table I.1 summarizes the input and output variables and Table I.2 gives a listing of the program.

The bubble trajectory ϕ_b , calculated with the two-region model is also shown in Fig. I.1.

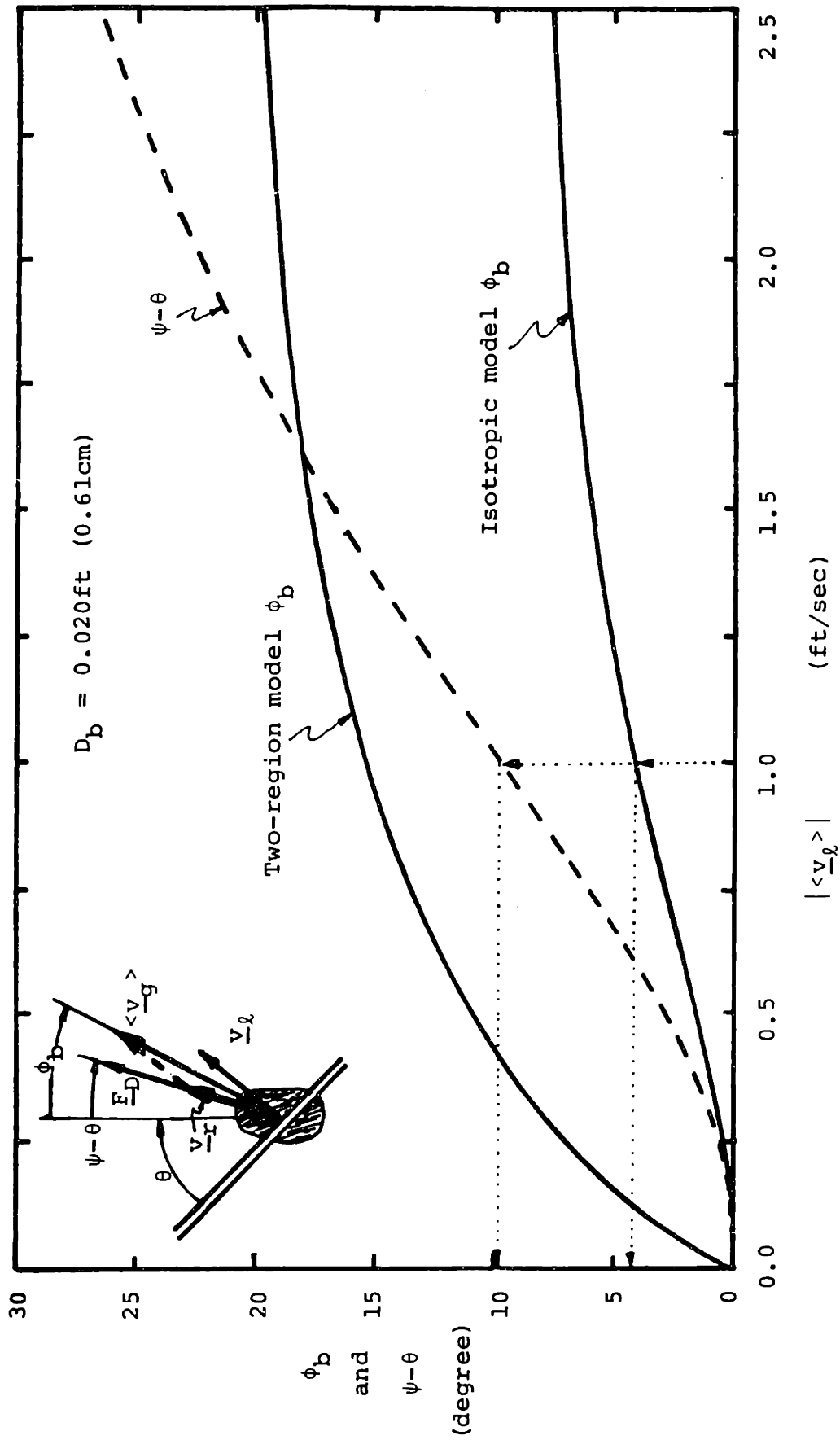


Figure I.1 Isotropic and two-region model for $D_b = 0.02 \text{ ft } (0.61 \text{ cm})$.

TABLE I.1

Two-Region Model Program Input/Output

Line	Variable
	<u>Input</u>
1	ires, iblam ires = 1: 45 degree flow resistance fits = 2: 30 degree flow resistance fits iblam = 0: Step function model = 1: Mainstream region ($\lambda = 0$) = 2: Recirculating region ($\lambda = 1$)
2	std, sld, thgrav, ra std: Transverse pitch to diameter, S_T/d sld: Longitudinal pitch to diameter, S_L/d dia: Rod diameter, d (ft) thgrav: Array inclination from vertical, θ (degree) ra = 1: Square array
3	viscl, rhol, rhog, surten viscl: Liquid viscosity, μ_l (lbm/ft sec) rhol: Liquid density, ρ_l (lbm/ft ³) rhog: Gas density, ρ_g (lbm/ft ³) surten: Surface tension, σ (lb _f /ft)
4	rel, thl, db rel: Liquid Reynolds number, Re_v thl: Liquid flow inclination, $\langle \theta_l \rangle$ (degree) db: Bubble diameter, D_b (ft)
	<u>Restart</u>
1	rel, db rel \geq 0: New liquid Reynolds number, Re_v \leq 0: End run db: New bubble diameter, D_b (ft)
	<u>Output</u>
1	rel, db, vg, phig rel: Liquid Reynolds number, Re_v db: Bubble diameter, D_b (ft) vg: Bubble velocity, $ \langle \underline{v}_g \rangle $ (ft/sec) phig: Bubble trajectory, ϕ_b (degree)

TABLE I.2

Two-Region Model Program Listing

```

common/geo/sld,std,dia,thgrav,ra,dv,gam,delv,gavgdv
common/flow/rel,thl
common/prop/viscl,rhol,rhog,surten,delrho,visn,dhat,dbt1dv
common/const/pi,grav,gcon,rad,nin,nout,ires,iblam
pi = 3.14159
grav = 32.174
gcon = 32.174
rad = 57.296
nin = 5
nout = 6
read(nin,1000) ires,iblam
write(nout,2001) ires,iblam
read(nin,1000) std,sld,dia,thgrav,ra
write(nout,2010) std,sld,dia,thgrav,ra
read(nin,1000) viscl,rhol,rhog,surten
write(nout,2010) viscl,rhol,rhog,surten
read(nin,1000) rel,thl,db
write(nout,2010) rel,thl,db
1000 format(v)
2001 format(1x,"input:",8i5)
2010 format(1x,"input:",8f12.6)
thgrav = thgrav/rad
thl = thl/rad
gam = 1. - pi/(4.*sld*std)
dv = dia*gam/(1. - gam)
delv = (1. - 1./std)/gam
delrho = rhol-rhog
dhat = sqrt(surten*gcon/(grav*delrho))
visn = viscl/sqrt(rhol*surten*gcon*dhat)
dbt1 = 5.42*dhat*visn**0.33333
dbt1dv = dbt1/dv
gavgdv = dia*(std-gam)/dv
alp = 0.0
50 continue
call velgas(db,vg,thg)
phig = (thg - thgrav)*rad
write(nout,2003)
2003 format(1x,/)
write(nout,2004) rel,db,vg,phig
write(nout,2003)
2004 format(10x,5f10.5)
200 continue
write(0,2005)
2005 format(1x,"input new rel,db")
read(0,1000) rel,db
c write(nout,2010) rel,db
if(rel.ge.0.0) go to 50
stop
end
subroutine velgas(db,vg,thg)
common/geo/sld,std,dia,thgrav,ra,dv,gam,delv,gavgdv
common/flow/rel,thl
common/prop/viscl,rhol,rhog,surten,delrho,visn,dhat,dbt1dv
common/const/pi,grav,gcon,rad,nin,nout,ires,iblam
dbdv = db/dv
if(dbdv.gt.1.0) write(nout,2015)
2015 format(1x,37hBubble diameter > hydraulic diameter.)
dprojdb = 1.0
ap = 1.5*dprojdb*dprojdb/db
c forces

```

TABLE I.2 (continued)

Two-Region Model Program Listing

```

fgrav = delrho*grav*(1.-alp)/gcon
fgrav1 = fgrav*cos(thgrav)
fgrav2 = fgrav*sin(thgrav)
if(ires.eq.0) call resis(rel,th1,r1,r2)
if(ires.eq.1) call rexp45(rel,0.7854,r1,r2)
if(ires.eq.2) call rexp30(rel,0.5236,r1,r2)
fac = rel*viscl*viscl/(rho1*dv*dv*dv*gcon)
fr1 = r1*fac
fr2 = r2*fac
fd1 = fr1 + fgrav1
fd2 = fr2 + fgrav2
if(dbdv.ge.dbt1dv) go to 200
c      viscous regime
fac = 2.*rho1*db*db*gcon/(ap*viscl*viscl)
v1iv = vvv(dbdv,1.0)
v2iv = vvv(dbdv,gavgdv)
visclm = 1. - alp
reb = 100
rebold = reb
lmax = 20
do 50 l = 1,lmax
reb = 0.5*(reb + rebold)
recdv1 = 24.*(1.+0.1*(reb*visclm/v1iv)**0.75)/(v1iv*visclm)
recdv2 = 24.*(1.+0.1*(reb*visclm/v2iv)**0.75)/(v2iv*visclm)
rebold = reb
reb = fac*sqrt(fd1*fd1/(recdv1*recdv1)+fd2*fd2/(recdv2*recdv2))
if(abs(1.-reb/rebold).le.0.01)go to 100
50 continue
write(nout,2000)
2000 format(1x,39h Viscous regime iteration not converge.)
100 cd1 = recdv1/reb
cd2 = recdv2/reb
go to 500
200 continue
c      distorted regime
v1id = vvv(dbt1dv,1.0)
v2id = vvv(dbt1dv,gavgdv)
if(dbdv.gt.0.6) v1id = 1.12
if(dbdv/gavgdv.gt.0.6) v2id = 0.85
psi = 0.460/sqrt(v1id)
ftnalp = 1.0/sqrt(1. - alp)
fac = psi*v1id**0.75
cd1 = 0.6667*db/dhat*((1. + fac*ftnalp**0.8571)/
a      (ftnalp*v1id*(1. + fac)))**2
fac = psi*v2id**0.75
cd2 = 0.6667*db/dhat*((1. + fac*ftnalp**0.8571)/
a      (ftnalp*v2id*(1. + fac)))**2
c      capped regime
v1ic = vvc(dbdv)
v2ic = v1ic
if(dbdv.gt.0.6) v1ic = 1.12
if(dbdv/gavgdv.gt.0.6) v2ic = 0.85
cdc1 = 2.6667*((1.-alp)/v1ic)**2
cdc2 = 2.6667*((1.-alp)/v2ic)**2
if(cdc1.gt.cdc1) cd1 = cdc1
if(cdc2.gt.cdc2) cd2 = cdc2
500 continue
c      relative velocity of mainstream region
cdm = cd2
if(fd2.lt.0.1*fd1) cdm = cd1

```


TABLE I.2 (continued)

Two-Region Model Program Listing

```

fcd1 = fd1/cdm
fcd2 = fd2/cdm
vr = sqrt(2.*gcon*sqrt(fcd1*fcd1 + fcd2*fcd2)/(ap*rhol))
reb = rhol*vr*db/viscl
fac = 0.5*rhol*vr*ap/gcon
vr1 = fcd1/fac
vr2 = fcd2/fac
xi = 1/delv
if(iblam.eq.3) xi = 1.0
vl = rel*viscl/(rhol*dv)
c   gas velocity
vgm1 = vr1 + vl*cos(thl)
vgm2 = vr2 + xi*vl*sin(thl)
thg = atan2(vgm2,vgm1)
thd = atan2(fd2,fd1)
thdout = thd*rad
vgm = sqrt(vgm1*vgm1 + vgm2*vgm2)
thgout = thg*rad
c   write(nout,2010) vgm,thgout,cd1,cd2,cdm,fd1,fd2,thdout
c   write(nout,2010) vgm1,vgm2,xi,vl,reb
2010 format(1x,"output",8f12.5)
c   relative velocity of recirculation region
cdr = 1.0e+8
if(fd2.lt.0.1*fd1) cdr = cd1
fcd1 = fd1/cdr
fcd2 = fd2/cdr

vr = sqrt(2.*gcon*sqrt(fcd1*fcd1 + fcd2*fcd2)/(ap*rhol))
reb = rhol*vr*db/viscl
fac = 0.5*rhol*vr*ap/gcon
vr1 = fcd1/fac
vr2 = fcd2/fac
c   gas velocity
vgr1 = vr1 + vl*cos(thl)
vgr2 = vr2
thg = atan2(vgr2,vgr1)
vgr = sqrt(vgr1*vgr1 + vgr2*vgr2)
thgout = thg*rad
c   write(nout,2010) vgr,thgout,cdr,vgr1,vgr2,blam
call blamda(dbdv,blam)
vg1 = (1-blam)*vgm1 + blam*vgr1
vg2 = (1-blam)*vgm2 + blam*vgr2
vg = sqrt(vg1*vg1 + vg2*vg2)
thg = atan2(vg2,vg1)
return
end
function vvv(dbdv,gapdv)
vvv = 1. - dbdv/(0.9*gapdv)
if(dbdv.le.0.6) return
vvv = 0.12*gapdv*gapdv/(dbdv*dbdv)
return
end
function vvc(dbdv)
vvc = 1.0
if(dbdv.le.0.125) return
vvc = 1.13*exp(-dbdv)
if(dbdv.le.0.6) return
vvc = 0.496*sqrt(1./dbdv)
return
end

```

TABLE I.2 (continued)

Two-Region Model Program Listing

```

subroutine rexp45(rel,thl,r1,r2)
  rx =169.
  ry = 62.4
  if (rel.lt.300) go to 100
  rx = 1.42*rel**0.837
  ry = 0.0936*rel**1.14
  if(rel.lt.3370) go to 100
  ry = 1.19*rel**0.827
  if(rel.lt.4500.) go to 100
  rx = 1.46*rel**0.823
100 continue
  r1 = rx*cos(thl) - ry*sin(thl)
  r2= rx*sin(thl) + ry*cos(thl)
  return
end
subroutine rexp30(rel,thl,r1,r2)
  rx = 56.7
  ry = 19.6
  if(rel.lt.300) go to 100
  rx = 0.858*rel**0.759
  ry = 0.0223*rel**1.18
  if(rel.lt.4360) go to 100
  ry = 0.134*rel**0.966
  if(rel.lt.5230) go to 100
  rx = 0.604*rel**0.80
100 continue
  r1 = rx*cos(thl) - ry*sin(thl)
  r2 = rx*sin(thl) + ry*cos(thl)
  return
end
subroutine resis(rel,thl,r1,r2)
common/geo/sld,std,dia,thgrav,ra,dv,gam,delv,gavgdv
return
end
subroutine blamda(dbdv,blam)
common/const/pi,grav,gcon,rad,nin,nout,ires,iblam
common/geo/sld,std,dia,thgrav,ra,dv,gam,delv,gavgdv
blam = 1.0
if(iblam.eq.2) go to 10
blam = 0.0
if(iblam.eq.1) go to 10
if(iblam.eq.3) go to 10
if(dbdv.lt.dia/(2.*dv)) blam = 1.0
10 return
end

```

REFERENCES

- [A.1] Aris, R., Vectors, Tensors, and the Basic Equations of Fluid Mechanics, Prentice-Hall (1963).
- [A.2] Album of Photographs on file with Prof. N.E. Todreas, MIT, Cambridge, MA (1983).
- [B.1] Banerjee, S. and Chan, A.M.C., "Separated Flow Models-I," Int. J. Multiphase Flow, Vol. 6, pp 1-24 (1980).
- [B.2] Butterworth, D., "The Development of a Model for Three Dimensional Flow in Tube Bundles," Int. J. Heat Transfer, Vol. 21, pp 256-258 (1978).
- [B.3] Blasius, H., Forschungsarbeiten, Vol. 131, No.1, (1913).
- [B.4] Böttgenbach, H., "Messungen von Strömungsfeldern in engen Stäbbündeln zur Überprüfung einer anisotropen Strömungsfeld theorie," Koktrorarbeit Ruhr-Universität, Bochum (1977).
- [B.5] Bouré, J. and Delhaye, J.M., "General Equations and Two-Phase Flow Modeling," Handbook of Multiphase Systems, G. Hatsroni, Ed, Hemisphere Publishing (1982).
- [B.6] Boissier, A. et al., E.D.F. Bulletin de la Direction des Études et Recherches, Série A, Nucleaire, Hydraulique, Thermique No.2/3 (1971).
- [B.7] Böttgenbach, H. "Strömungswiderstand son quer-und längsangeströmten Stäbbündeln," Atomkernenergie (ATKE) Bd. 26, Lfg 4 (1975).
- [B.8] Burshall, W.J. and Loftin, L.K., Jr., "Experimental Investigation of the Pressure Distribution about a Yawed Circular Cylinder in the Critical Reynolds Number Range," NACA-TN-2463, Sept. (1951).
- [B.9] Brockett, G.F. and Johnson, R.T., "Single-Phase and Two-Phase Flow Measurement Techniques for Reactor Safety Studies," ERRI-195 July (1976).
- [B.10] Baush, M. and Lahey, R.T., Jr., "The Measurement of Two-Dimensional Phase Separation Phenomena," NUREG/CR-1936, Feb. (1981).

- [C.1] CRC Handbook of Chemistry and Physics, 59 Ed., R.C. Weast, Editor, CRC Press Inc. (1978).
- [C.2] Chilton, T.H. and Geneaux, R.P., "Pressure Drop Across Tube Bank," AICHE Trans., Vol. 29, pp 161-172 (1933).
- [C.3] Cliff, R. et al., Bubbles, Drop, and Particles, Academic Press (1978).
- [C.4] COBRA-TF: Computer Code under development at Battelle Pacific Northwest Lab., sponsored by NRC.
- [D.1] Drew, D.A. and Lahey, R.T., Jr., "Application of General Constitutive Principles to the Derivation of Multidimensional Two-Phase Flow Equations," Int. J. Multiphase Flow, Vol 5, pp 243-264 (1979).
- [E.1] Ebeling-Koning, D.B. et al. "Hydrodynamic Prediction of Multidimensional Single- and Two-Phase Flow in Rod Arrays, Progress Report No. 1," DOE/ER/12075-1PR, MIT, Jan. (1983).
- [G.1] Groehn, H.G. "Influence of the Yaw Angle on Heat Transfer and Pressure Drop of the Bundle Heat Exchangers," Heat Transfer, Vol. 6, pp 203-208, 7th IHTC, Munchen (1982).
- [G.2] Gunter, A.Y. and Shaw, W.A., "A general Correlation of Friction Factors of Various Types of Surfaces in Crossflow," ASME Trans., Vol. 67, pp 643-660 (1945).
- [G.3] Grimison, E.D., "Correlation and Utilization of New Data on Flow Resistance and Heat Transfer for Crossflow of Gases Over Tube Banks," ASME Trans., Vol. 59, pp 583-594 (1937).
- [G.4] Groehn, H.G., "Thermal Hydraulic Investigation of Yawed Tube Bundle Heat Exchangers," Heat Exchangers S. Kakaç et al., Ed, Hemisphere Publishing, pp 97-109 (1981).
- [G.5] Groehn H.G., "Modelluntersuchungen Zum Einfluss des Neigungswinkels der Rohre..." Fahrestagung Kerntechnik '82, Tagungsbersicht (1982).
- [G.6] Gorchakov, M.K. et al. "Anisotropiya Koehffitsienta Treniya v Poristyxh Telakh, Sostoyashchikh iz Puchkov Sternhnej," FEI-446 (1973).

- [G.7] Griffith, P., "The Prediction of Low-Quality Boiling Voids," ASME Paper No. 63-HT-20 (1963).
- [H.1] Hoerner, S.F. Fluid-Dynamic Drag, Published by author, Hoerner Fluid Dynamics, 2 King Lane Bricktown, N.J. 08723 (1965).
- [H.2] Hewitt, G.F., Measurement of Two-Phase Flow Parameters, Academic Press (1978).
- [H.3] Haas, U. et al. Chem-Ing-Tech, Vol. 44, pp 1060-1068 (1972).
- [I.1] Ishii, M., Thermo-Fluid Dynamic Theory of Two-Phase Flow, Eyrolles, Paris (1975).
- [I.2] Idel'chik, I.E., "Handbook of Hydraulic Resistance," ACE-TR-6630 (1960).
- [I.3] Ishii, M. and Zuber, N., "Drag Coefficient and Relative Velocity in Bubbly, Droplet or Particulate Flows," AICHE Journal, Vol. 25, No. 5, pp 843-855 (1979).
- [I.4] Ishii, M., "One-Dimensional Drift-Flux Model and Constitutive Equations for Relative Motion Between Phases in Various Two-Phase Flow Regime," ANL-77-47, (1977).
- [I.5] Ishii, M. and Mishima, K., "Study of Two-Fluid Model and Interfacial Area," ANL-80-111 (1980).
- [J.1] Jakob, M., "Heat Transfer and Flow Resistance Crossflow of Gas Over Tube Banks--Discussions," ASME Trans., Vol. 60, pp 381-392 (1938).
- [K.1] Krudsen, J.G. and Katz, D.L., Fluid Dynamics and Heat Transfer, McGraw-Hill (1958).
- [K.2] Kazakevich, F.P. "Influence of Angle of Approach of a Gas Steam on the Aerodynamic Resistance of a Tube Bundle," Izu. Vses. Insti. Imoni F.E. Dzerzhimkogo, Vol. 8, pp 7-12 (1952).
- [K.3] Kelly, J.E. "Development of a Two-Fluid, Two-Phase Model for a Light Water Reactor Subchannel Analysis," Ph.D. thesis, Department of Nuclear Engineering, MIT, Cambridge, MA (1980).

- [L.1] LeTourneau, B.W. and Bergles, A.E., "Two-Phase Flow Instrumentation," ASME Publication (1969).
- [L.2] Lahey, R.T., Jr. et al. "An Evaluation of Interfacial Drag Models for Bubbly Two-Phase Flow," ASME Nonequilibrium Interfacial Transport Process (1979).
- [M.1] McAdams, W.H., Heat Transmission, 3rd Ed., McGraw-Hill, p 155 (1954).
- [M.2] Marek, J. et al., "Heat Transfer and Pressure Drop Performance of Rod Bundles Arranged in Square Arrays," Int. J. Heat Mass Transfer, Vol. 16 pp 2215-2228 (1973).
- [M.3] Möller, S.V., "Un Modelo Constitutivo Para o Escoamento Através de Um Arranjo de Barras de Seção Circular," M.Sc. Thesis, Universidade Federal do Rio de Janeiro (1979).
- [M.4] Michjew, M.A., "Grundlagen der Wärmeübertragung," VEB Verlag Technik, Berlin (1961).
- [O.1] Osakabe, M. and Adachi, H., "Characteristic of Two-Phase Slanting Flow in Rod Bundle," J. of Nuclear Science and Technology, Vol. 19, No. 6, pp 504-506 (1982).
- [P.1] Peebles, F.N. and Garber, H.J., Chem. Eng Progr., Vol. 49, pp 88-97 (1953).
- [R.1] Rehme, K., "Simple Method of Predicting Friction Factors of Turbulent Flow in Non-circular Channels," J. of Heat Mass Transfer, Vol. 16, pp 933-950 (1973).
- [R.2] Rehme, K., "Pressure Drop Performance of Rod Bundles in Hexagonal Arrangements," J. Heat Mass Transfer, Vol. 15, pp 2499-2517 (1972).
- [R.3] Reed, W.H. and Stewart, H.B., "THERMIT: A Computer Program for Three-Dimensional Thermal-Hydraulic Analysis of Light Water Reactor Cores," ERRI-NP-2032 (1981).
- [S.1] Sha, W.T. et al., "COMMIX-1: A Three-Dimensional Transient Single-Phase Component Computer Program for Thermal Hydraulic Analysis," ANL-77-96 (1978).
- [S.2] Sha, W.T. et al., "Local Volume-Averaged Transport Equations for Multiphase Flow in Regions Containing Distributed Solid Structures," ANL-81-69 (1981).

- [S.3] Sha, W.T. and Chao, B.T., "Local Volume-Averaged Transport Equations for Single-Phase Flow in Regions Containing Fixed, Dispersed Heat Generating Solids," ANL-80-124, (1980).
- [S.4] Sparrow, E.M. and Loeffler, A.L., Jr., "Longitudinal Laminar Flow Between Cylinders Arranged in Regular Array," AICHE Journal, Vol. 5, No. 3, pp 325-330 (1959).
- [S.5] Stonecypher, T.E., "Dynamic and Thermal Non-Equilibrium in Two-Phase Flow in Rocket Nozzles," Report No. P-10-17, Rhom and Haas Company, Huntsville, Alabama (1960).
- [T.1] Taborek, J. "Ideal Tube Bank Correlations for Heat Transfer and Pressure Drop," Thermal and Hydraulic Design of Heat Exchangers, Vol. 3, Hemisphere Publishing (1983).
- [T.2] Todreas, N.E. and Coëffé, Y., "Formulation of the Fluid-Solid Interaction Force for Multidimensional, Two-Phase Flow within Tube Arrays," Nucl. Eng. and Design, Vol. 58, pp 383-391 (1980).
- [T.3] TRAC-PIA: An Advanced Best-Estimate Computer Program for PWR LOCA Analysis; LA-7777-MS; Los Alamos Scientific Laboratory (1979).
- [T.4] Thurgood, M.J. and Kelly, J.M., "COBRA-TF Model Description, Dec. 1979," Presented at NRC Advance Code Review Group Meeting, Silver Spring, Maryland, Jan. (1980).
- [T.5] THERMIT-SG: Modifications to THERMIT-2 on file with Rachel Morton, Nuclear Engineering Computer Librarian, MIT, Cambridge, MA (1983).
- [U.1] The URSULA-2 Computer Program, Vol. 1 and 2, EPRI-NP-1315 (1980).
- [V.1] VDI-Wärmeatlas, 3. Auflage, VDI-Verlag, Dusseldorf, Ld 1 (1977).
- [V.2] Van Dyke, M., An Album of Fluid Motion, Parabolic Press, Stanford (1982).
- [W.1] Whitaker, S., "Fluid Motion in Porous Media," Industrial and Engineering Chemistry, Vol. 61, No. 12, pp 14-28 (1969).

- [W.2] Williams, C.L. and Green, S.J., "Thermal and Hydraulic Aspects of PWR Steam Generators," Presented at ANS/ASME International Topical Meeting on Nuclear Reactor Thermal-Hydraulic, Saratoga Springs, New York, Oct. 5-8 (1980).
- [W.3] Wallis, R.P., "Photographic Study of Fluid Flow Between Bank of Tubes," Engineering, Vol. 148, pp 423-426 (1939).
- [W.4] Wiemer, P., Untersuchungen uber den Zugwiderstand von Wasserrohrkesseln. Diss. TH Aachen (1937).
- [W.5] White, F.M., Viscous Fluid Flow, McGraw-Hill (1974).
- [W.6] Wallis, G.B., "The Separated Flow Model of Two-Phase Flow," EPRI NP-275 (1976).
- [W.7] Wallis, G.B., One-Dimensional Two-Phase Flow, McGraw-Hill (1969).
- [Z.1] Zūkauskas, A. and Ulinskas, R., "Banks of Plain and Finned Tubes," Thermal and Hydraulic Design of Heat Exchangers, Vol. 2, Hemisphere Publishing (1983).
- [Z.2] Zūkauskas, A., "Heat Transfer from Tubes in Crossflow," Advances in Heat Transfer, Vol. 8, J.P. Hartnett et al., Ed, Academic Press (1972).

BIOGRAPHICAL NOTE

Derek B. Ebeling-Koning was born in Aruba, Netherlands Antilles, on September 26, 1955. The author grew up on Eastern Long Island, New York, and graduated valedictorian from Tilton School, Tilton, New Hampshire, in June 1973. In September 1973, he enrolled at Rensselaer Polytechnic Institute and graduated cum Laude in May 1977, receiving his Bachelor of Science in Nuclear Engineering with a minor in Economics. Upon graduation he worked at Exxon Nuclear Company in Richland, Washington, for the summer of 1977, as a junior engineer with the Nuclear Reactor Safety Group.

In September 1977, the author entered graduate studies at the Massachusetts Institute of Technology and received his Master of Science in Nuclear Engineering in February 1979. During the summer of 1980, after beginning his doctoral studies, he was employed at Northeast Utilities in Berlin, Connecticut, with the Safety Analysis Group. In September 1983, he received his Doctor of Philosophy in Nuclear Engineering and subsequently entered employment at Westinghouse Nuclear Technology Division in Monroeville, Pennsylvania.

During his graduate studies the author received the Sherman R. Knapp Fellowship and U.S. Department of Energy Nuclear Science and Engineering and Health Physics Fellowship. The author is a member of Tau Beta Pi Association and an associate member of Sigma Xi. He is also a member of the American Nuclear Society and the American Society of Mechanical Engineers.